FLOW FIELD CHARACTERISTICS AROUND BLUFF PARACHUTE CANOPIES

by

C.Q.SHEN

A Thesis Submitted to the University of Leicester
for the Degree of Doctor of Philosophy

June 1987

FLOW FIELD CHARACTERISTICS AROUND BLUFF PARACHUTE CANOPIES

by

C. Q. SHEN

ABSTRACT

The objectives of the present investigation are to determine the nature of the flow field around bluff parachute canopies, considering the effects of canopy shape parameters on this flow field and hence on the resulting aerodynamic forces and moments which are developed on the canopy surface.

In order to relate the flow field developed around bluff parachute canopies to their aerodynamic characteristics, a series of experiments in the Leicester University wind tunnel has been conducted on a family of particularly significant canopy shapes. These cross-shaped canopies have excellent drag and stability characteristics if arm ratios of about 4:1 are selected.

Flow visualisation, using both helium bubbles and wool tufts, was used to determine the flow field around the canopy. The most probable description of the wake flow is chains of irregularly-shaped vortex loops which move at about 0.7 times the undisturbed free stream velocity. Aerodynamic forces and moments measured on the various canopies correspond with the observed flow characteristics. Statistical correlation analyses made with hot wire anemometers in their wake indicate the periodic structure of the wakes formed behind these bluff bodies and reveal their basic similarities. Strouhal numbers of about 0.15 were obtained in the wake formed behind an imporous rigid hemispherical canopy. These are increased as canopy porosity is made larger.

A useful comparison between a semi-theoretical blockage correction applied to aerodynamic forces and test results was obtained from an ancillary test programme conducted under water in a large cross-sectional area ship tank.

ACKNOWLEDGEMENTS

First and foremost the author would like to express sincere and particular thanks to her supervisor Dr. D.J. Cockrell for his patience and great guidance, help and encouragement throughout this research over two and half years.

She also wishes to thank Mr. P.S. Barwell and Mr. P.D. Williams for assisting in the design and construction of the experimental apparatus and helping in the test programme and thanks to Mr. P. Smith for his excellent photographs. She is specially appreciative of the kindness and encouragement from Mr. P.S. Barwell.

Many thanks are also offered to Mr. D. Pratt, Miss N.I. Berridge and Mrs. J.P. Meredith for the tracings; to Dr. A.C. Baxter for assisting with the Micro-computer Test Program; to Mr. R. Harwood for co-operating in ship tank tests and to Professor N.B. Jones and his research groups for providing their sophisticated fast fourier-transform equipment.

The author gratefully acknowledges all the facilities which were provided by the Engineering Department led by Professor G.D.S. MacLellan and the friendly help from all his staff involved, particularly in the Secretariat and Workshop of the Engineering Department, University of Leicester.

The author would like to extend sincere thanks to the Chinese Government and the British Council for the financial

support in her research work in the U.K., and special thanks to the University of Leicester for making it possible for her to register for the Ph.D. Degree.

Finally, she wishes to thank Irvin Great Britain Ltd. for their interest and encouragement. All the test models used were supplied by them.

CONTENTS

NOMENCLATURE

Unsubscripted Variables

D	Drag force parallel to the direction of free stream velocity (N)
d	Diameter of the body (M)
F	Vector force
F	Magnitude of the force (N)
f	Frequency of periodic motion (Hz)
g	Gravitational acceleration (m/sec^2)
L	Lift force perpendicular to the direction of free stream velocity (N); Length of cross-shaped canopy arm (m)
l	Length or distance (m)
M	Moment (Nm)
m	Mass of the body (kg)
N	Normal aerodynamic force (N)
R	Resultant aerodynamic force (N)
Re	Reynolds number
S	Cross-Sectional area (m^2)
St	Strouhal number
T	Tangential force (N); periodicity (sec)
U	Root mean square velocity in the wake behind the parachute (m/sec); Reference flow velocity, such as that of the free stream at infinity (m/sec)
V	Vector velocity in the flow field
V	Magnitude of velocity in the flow field (m/sec)
v	Voltage output from hot-wire anemometer
W	Width of cross-shaped canopy arm (m)
X,Y,Z	Co-ordinate system axis

α	Angle of attack (degree); Added mass tensor
β	The angle between the axis of the system and the direction of the gravitational force (degree)
Φ	Velocity potential function
Γ	Vorticity
λ	Nominal porosity of canopy fabric (cu.ft/sq.ft/sec)
ν	Kinematic viscosity of the fluid m^2/sec
ρ	Fluid density (kg/m^3)
τ	Time delay (sec)
ω	Angular frequency (rad./sec)

Subscripted Variables

C_D	Drag coefficient
C_L	Lift coefficient
C_N	Normal force coefficient
C_M	Pitching moment coefficient
C_{Mc}	Pitching moment coefficient about confluence point of suspension lines
C_T	Tangential force coefficient
C_{To}	Tangential force coefficient at zero angle of attack
D_o	Nominal diameter of the canopy (m) $D_o = (4S_o/\pi)^{1/2}$
D_p	Projected diameter of the canopy (m)
F_a	Inertia force caused by the flow unsteadiness
F_s	Aerodynamic force in steady flow
l_s	Length of suspension line (m)
l_f	Length of the parachute in flight (m)
M_o	Pitching moment about canopy apex (Nm)
M_C	Pitching moment about confluence point of suspension lines (Nm)

M_G	Pitching moment about centroid of the combined parachute and payload.
R_A	Arm ratio of cross-shaped canopy $R_A=L/W$
R_s	Suspension line ratio, for cross-shaped canopy $R_s=l_s/L$
S_o	Nominal surface area of the parachute canopy (m^2)
S_p	Projected area of the parachute canopy (m^2)
X_p	Distance between the canopy apex and the centre of pressure (m)
U_∞	Velocity of the free stream at infinity (m/sec)
α_c	The maximum angle of attack at which the canopy can inflate properly without collapse (collapse angle of attack) (degree)
α_{eq}	Statically stable equilibrium angle of attack at which the canopy both is in equilibrium and is statically stable (degree)
λ_e	Effective porosity of canopy fabric
λ_g	Geometric porosity of canopy

LIST OF FIGURES

LIST OF TABLES

1 INTRODUCTION

Parachutes are widely applied as decelerators, for example to aircraft landing, to individual or to capsule escape from aircraft, to atmospheric re-entry, to vehicle stabilization, to cargo delivery and to airborne troop manoeuvres. All of these examples depend on the parachute and payload system possessing good stability characteristics, a relatively high drag coefficient and a reliable structural strength. An optimal design of the parachute for minimum weight and volume together with reliable deployment and inflation which imply that it must possess sufficient drag, stability and strength to withstand impact loads is currently based on a mixture of analysis, experimentation and empiricism.

A great deal of research on the prediction of parachute stability and performance is based on the experimental knowledge of aerodynamic characteristics which has taken place during the last 50 years, but very little work has been done to determine and appreciate the nature of the flow field around parachute canopies.

In his aerodynamics of parachutes AGARDograph Cockrell[1.1] (1987) had described the complexities of the unsteady flow field around bluff parachute canopies, saying that it caused difficulties in both the planning and the execution of experimental programmes. Even if the aerodynamic forces which are developed are assumed to be steady they are, in fact, average values of time-varying quantities which fluctuate with unsteady wake formed downstream. Appreciation of such flow features are among the aims of the present research.

Both because of these complexities and because of recent advances in analytical techniques, the experimental study of flow field which develops around parachute canopies has received all too little attention from those considering the aerodynamics of parachutes.

1.1 Potential Fluid Flow Solutions

Ibrahim[1.2,1.3](1965,1967) has used a conformal mapping technique to develop a potential solution to the flow around a fully-inflated parachute canopy. Klimas[1.4,1.5,1.6] (1972,1977) has modelled the parachute surface using linear vortex rings. In the Klimas' model the effects of canopy porosity were included. In solutions developed by both Ibrahim and Klimas it was necessary to assume that no wake was formed behind the bluff parachute canopy. Because they were neglecting this main flow feature, their solutions did not agree well with experimental data. A realistic representation of the flow in the vicinity of a parachute canopy must include a consideration of the wake. As a development of aerofoil theory Roberts[1.7](1974) and Reddy & Roberts[1.8](1975) assumed the existence of a starting vortex, locating it at a point which was exterior to the skirt area. They used the conformal mapping method as a basis for determining forces during the canopy inflation process. As with all methods of analysis, good experimental data were required with which to validate their model, but at that time these were not easy to find.

An identifiable region of vorticity in an otherwise ideal fluid flow field with which to represent the wake shed by a bluff body such as a parachute canopy has more recently been considered by Ashurst[1.9], Meyer & Purvis[1.10](1984), Shirayama & Kuwahara[1.11,1.12] (1985,1986), Strickland[1.13] (1986), and McCoy & Werme[1.14](1986). In their modelling each of these considered the viscous rotational real flow field in which the parachute is immersed as if it were a potential flow field for which the total velocity potential function Φ was given by the sum of three superimposed fields, i.e

$$\Phi = \Phi_1 + \Phi_2 + \Phi_3$$

where

Φ_1 represents free stream velocity potential function;

Φ_2 represents the discrete or continuous vortices which are bound to the parachute surface;

and

Φ_3 represents the free discrete vortices which simulate the wake arising as a consequence of flow separation.

Milne Thomson[1.15](1963) in "Theoretical Hydrodynamics" shows that in a potential flow the velocity at any point is given by

$$V = \nabla\Phi$$

and since

$$\mathrm{div}\ V = 0$$

Laplace's equation

$$\nabla^2\Phi = 0$$

is valid for the flow. The boundary condition for this equation is:

$$v_n = n(\partial\Phi/\partial n) = V_s.n_s = 0$$

where

v_n — Velocity component normal to the boundary surface,

V_s — Velocity component tangential to the boundary surface, and

n_s — Normal direction of the boundary surface.

Effects caused by fabric porosity can be included in this velocity potential model, as Klimas showed. In order to evaluate the velocity potential Φ_3 it is necessary to model the essentially non-steady processes which occur in the near wake immediately downstream of the bluff parachute canopy that is, to model the vortex formation process.

"It is at this point that we are handicapped by the fact that experimental techniques are, at this moment, lagging behind the advance of theory."(ref1.16) And we do not know enough about the flow which is to be modelled, such as the period over which vortices are formed in the wake and what influences this period. The most important objective of this research programme is to accumulate information about the nature of the wakes formed behind bluff three-dimensional bodies, as this is indispensable to the realistic formulation of any theoretical model of these wakes.

Although a great deal is known about the nature of the wake formed by two-dimensional bluff bodies, the requirement to satisfy Kelvin's theorem means that the wake behind an axisymmetric body, such as a disc, must differ considerably from that formed by the equivalent two-dimensional body possessing the same cross-sectional shape.

1.2 The Fluctuating Aerodynamic Forces Developed on Parachute Canopies

Doherr & Saliaris[1.17] (1981) have proposed that the aerodynamic force F, which is developed on parachute canopies can be considered to be the sum of three terms:

$$F = F_s + \Delta F + F_a$$

where

F_s — Mean value of the corresponding aerodynamic force in steady flow,

ΔF — Amplitude of force fluctuations about this mean value,

F_a — Inertia force caused by the flow unsteadiness.

It is known that the mean aerodynamic force F_s plays an essential part in the determination of the parachute's dynamic stability characteristics and in its rate of descent. Experimental data required as inputs to the equation of motion developed variously by White & Wolf[1.18,1.19] (1968), Doherr & Saliaris[1.17], Tory & Ayres[1.20](1977) and by Eaton[1.21](1983) can be determined from model tests such as those conducted by Heinrich & Haak[1.22](1971), by Doherr & Schmerwitz[1.23](1971), by Hume[1.24](1973), or by Leicester research students such as Yavuz[1.25](1982) and Jorgensen[1.26](1982). The latter collaborated with each other to determine the characteristic mean non-dimensional aerodynamic coefficients and added mass coefficients used in the Cockrell & Doherr[1.27](1981) six-degree of freedom equations of motion. For this growing application of aerodynamic forces and moments developed on parachute canopies considerable experimental data are needed, and for these bluff body models constrained in wind tunnels or similar test facilities, blockage constraint effects must be considered.

The inertia force F_a developed on a parachute, like any other immersed bluff body is caused by the flow unsteadiness. It is not dependent on the rate of change in the momentum of the parachute itself but on that of the surrounding fluid. Since the mass of this displaced fluid is of the same order of that of the parachute which is immersed in it, this is not a negligible term for a canopy and

$$F_a = d(\alpha V)/dt$$

where α represents the twenty-one different components of the added mass tensor which Cockrell[1.1] and others have described.

The added mass coefficients for parachute-shaped bodies were the first calculated theoretically by Ibrahim[1.2] who assumed potential flow and neglected the effect of the wake. Subsequently they have been determined experimentally, first by Yavuz and Cockrell[1.28](1981). The significant difference between these results shows that it is important to consider the influence of the wake caused by the separation of the real fluid flow behind the bluff parachute canopy. A more recent investigation conducted by Cockrell, Shen, Harwood and Baxter[1.29](1986) has confirmed this point.

In his Ph.D thesis Jorgensen described the aerodynamic forces and moments developed on parachute canopies as varying stochastically. Doherr[1.30,1.31] (1975,1981) has described the importance that the frequency and amplitude of the fluctuating aerodynamic force ΔF may have on dynamic stability effects. Little is known about the frequency and amplitude of the aerodynamic forces developed on parachute canopies. Such a variation is clearly related to vortex shedding in their wakes, and to the porosity of the canopies themselves. It is also important to understand fluctuating forces better when seeking to predict the structural strength and the inflation reliability of parachute canopies.

1.3 The Effects of Porosity on the Aerodynamic Forces Developed on Parachute Canopies

Cross parachute canopies have been specifically considered because they are simple to manufacture and possess excellent drag and stability characteristics. They are widely applied to the deceleration and stabilization of aircraft, racing cars, and weaponry, particularly where their propensity to rotate is not an important design feature. Niccum, Haak & Gutenkauf[1.32](1965) suggested that there is a general decline in tangential aerodynamic force components with increasing cloth porosity. When Ludtke[1.33](1972) investigated the spinning characteristics of cross parachutes he made a similar observation. However, Jorgensen, from more limited flow visualization tests, argued that their aerodynamic behaviour depended solely on their arm ratio and any effects caused by porosity variation of their fabric were not significant. Using similar cross-shaped canopy models, the author has made intensive force measurements and flow visualization tests in both a wind tunnel and a large ship tank. Effects of openness of the canopy caused by variation in the arm ratio and of the porosity of the canopy material were both seen to be significant in determining the drag and the stability characteristics of cross parachute canopies. Flow separation points around the parachute canopies are not fixed at the intersection points of two arms, as Jorgensen had stated. Their location has been shown to vary extensively.

1.4 The Summary of Objectives

The summary of objectives for the current research programme is therefore:

(1) To determine the nature of the flow field around parachute canopies, so that it might serve as an input for vortex sheet methods of analysis;

(2) To consider the causes of the fluctuating aerodynamic forces developed when otherwise steady flow separates from bluff parachute canopies;

(3) To show the effects of canopy shape and porosity on the aerodynamic characteristics developed on a specific type of canopy, the cross canopy, considering the reasons for these effects;

(4) To develop in wind tunnel tests appropriate methods of flow visualization, together with mean and fluctuating force measurement, considering the importance of any blockage effects that such bluff bodies may cause.

2 THE WAKE CHARACTERISTICS BEHIND BLUFF BODIES

A HISTORICAL SURVEY

2.1 Two Important Dimensionless Parameters

The main flow characteristics associated with the wake which forms behind bluff bodies are flow separation and its consequent periodic fluctuation. Consideration of two dimensionless dynamic similarity parameters, Reynolds number Re and Strouhal number St is necessary for proper analytical and experimental observation.

By determining the ratio of inertia to viscous forces in the flow, the Reynolds number considers the effects of the viscosity of the fluid in which the bluff body is immersed.

$$Re = \frac{Ud}{\upsilon}$$

U __ Reference flow velocity, such as that of the free stream at infinity

d __ Chracteristic length of bluff body, such as its diameter.

υ __ Kinematic viscosity of the fluid.

The Strouhal number St represents the characteristics of periodic phenomena occurring in the wake.

$$St = \frac{df}{U}$$

f __ Characteristic frequency of vortex shedding from the bluff body.

2.2 The Wake Behind Two-Dimensional Bluff Bodies

Since experimental and theoretical investigations of the fluid field around three-dimensional bluff bodies are much more difficult than those around two-dimensional bodies, periodic phenomena in the wake behind the latter have been regarded as an appropriate introduction to the former.

The periodic nature of the wake behind a circular cylinder as shown in fig.2.1 was first systematically investigated in 1878 by Strouhal[2.1]. Two rows of vortices, termed a vortex street, are formed behind the cylinder. The first descriptions of such a flow were made by Mallock[2.2](1907) and Benard[2.3](1908, 1913).

Later von Karman[2.4](1911) and von Karman & Rubach[2.5](1912) idealized the flow behind the cylinders into a representation in a potential flow field of two series of discrete concentrated vortices along parallel lines, whose direction of rotation along one line is opposed to that along the other. Along one row these vortices are positioned half way between two vortices in the other row, as shown in fig.2.2. They analysed the double row of vortices generated by a cylinder, establishing a stability criterion for the double row. The average drag force D developed by the cylinder can be obtained from the consideration of the momentum defect in the wake,

$$D = \frac{2\pi k^2 \rho}{a} + \frac{2\pi k \rho b}{a}(U-2V)$$

where

k __ Strength of each concentrated vortex

b, a __ Distances shown in fig.2.2

U __ Free-stream velocity

V __ Velocity with which the vortex street moves

The latter can be expressed as:

$$V = \frac{\pi k}{a}\tanh\frac{\pi b}{a}$$

The frequency of vortex shedding is given by:

$$f = \frac{U-V}{a}$$

Von Karman's stability criterion is $b = 0.281a$

Only if $b=0.281a$ is the double row of vortices stable. Such an idealized stable double row configuration is called a von Karman vortex street. Subsequently, this phenomenon has been accorded a great deal of attention.

By means of flow visualization and measurements of frequency and speed with which the vortices pass downstream, Fage & Johansen[2.6,2.7] (1927), Relf & Simmons[2.8] (1924), and others have continued the consideration of the wake behind two-dimensional bodies. Primarily, theoretical studies have been concerned with elaboration of the stability analysis for alternate rows of vortices. Goldstein[2.9](1938) has summarized most of the early research in this field.

In a real fluid field a double row of vortices may follow a transition region which is formed just behind the bluff body. Motion becomes irregular further downstream and because the flow is turbulent the double row diffuses. The double row of vortices does not form exactly on two parallel rows, but the trails tend to widen, as is shown in fig.2.3.

Another characteristic phenomenon is a vortex pair formed behind a cylinder at very low Reynolds numbers. This has been reported by a number of authors. Rubach[2,10] (1914), Homann[2.11] (1936) and others[2.12,2.13,2.14] have shown excellent photographs which indicate that a vortex pair appears at Reynolds numbers smaller than about 40. This vortex pair changes slightly with the shape of the bluff body and with the degree of turbulence in the stream. As Reynolds numbers increase the vortex pair elongates and this is illustrated in fig.2.4.

The wakes which form behind cylinders have been modelled as stable von Karman vortex streets, but little further progress has been achieved with the analysis of these flows.

In 1950 Rosenhead[2.15] suggested a reappraisal of the flow field, proposing in 1953 that the stable double row of vortices is limited to a certain Reynolds number range. Delany & Sorensen[2.16](1953), Roshko[2.17,2.18] (1954,1955) and others[2.19,2.20,2.21] all observed that stable and well-defined von Karman vortex streets occurred only in a small range of Reynolds numbers from about 40 to 150.

The Reynolds numbers between 150 and 300 constitute a transition range. In that range the flow behind the cylinder becomes turbulent and any stable vortex street tends to be irregular.

In this irregular range, at which the Reynolds numbers are in the range from 300 to about $5\text{x}10^5$, periodic vortex formation still occurs but the vortices are composed of turbulently fluctuating fluid. At higher Reynolds numbers still these vortices are destroyed by turbulent diffusion, and further downstream a turbulent wake with no evident periodic motion is established.

In spite of all these investigations the mechanism by which the vortex street is formed from the free vortex layers discharged from the bluff body is still not clear. The field around two-dimensional bluff bodies, which move with uniform velocities through viscous incompressible fluids, presents an unsteady flow problem which is still receiving consideration. However, it does not now appear to offer a pertinent introduction to the flow field around an immersed three-dimensional bluff body.

2.3 The Wake Behind Three-Dimensional Bluff Bodies

The flow fields established in the wake behind three-dimensional bluff bodies are very complex. In the periodic discharge of vorticity they are similar to those formed behind two-dimensional bluff bodies. However, an important difference is the formation of vortex rings, or loops, instead of the double row of vortices or the vortex pair which form behind two-dimensional bluff bodies.

The first flow visualizations performed around spheres and square plates, both in air and in water, were reported by Eden[2.22] in 1912. Nisi & Porter[2.23](1923) investigated the velocity distribution in the eddies formed behind spheres, and Ermisch[2.24](1927) measured the static pressure over the surface of a sphere and also photographed the flow in its wake. Simmons & Dewey[2.25](1931) observed vortex movement formed in the wake of circular plates. Over a limited range of Reynolds numbers they tried to find so-called permanent vortex rings standing in the wake, just like the vortex pair which formed behind two-dimensional bluff bodies at very low Reynolds numbers, but they were unsuccessful in this endeavour.

Von Karman & Levi-Civita[2.26](1922) reported that they had found two trailing vortices which were similar to the horseshoe vortex in Prandtl's lifting-line theory. Schiller & Schimedel[2.27](1928) and Stanton & Marshall[2.28](1930) separately adopted flow visualization methods to investigate the wake formed behind a sphere and a disc. Schiller & Schimedel presented flow patterns formed behind a sphere and these have been reproduced in fig.2.5. Combining their results with Rosenhead's[2.29] paper(1930), in which it was predicted that the wake formed behind circular plates could only consist of vortex rings, Stanton & Marshall found that although flows were periodic at Reynolds numbers larger than about 195, permanent vortex rings appeared to be stable at Reynolds numbers which were less than this value. Moller[2.30](1938), Taneda[2.31](1956) and Achenbach[2.32](1974) all discovered permanent vortex rings to be formed behind spheres at Reynolds numbers below 400. In order to obtain data on the formation and structure of these vortices, Magarvey & Maclatchy[2.33](1965) experimentally investigated the wake formed by a liquid sphere at Reynolds numbers between 200 and 500. In this wake the vortices were first continuously distorted by the backflowing fluid and then broke away, to reappear later.

It is not possible to generalize a two-dimensional von Karman vortex street into any form of three-dimensional wake. Reviewing both the investigations contributed by Levy & Forsdyke[2.34,2.35] (1927,1928) and Thomson's[2.36] earlier conclusions, Rosenhead predicted that the only possibility for the flow in the wake formed behind a three-dimensional bluff body was a sequence of irregularly-shaped vortex loops, or vortex rings, which were discharged downstream and which passed some plane of symmetry whose orientation in space was purely random. In any particular case its orientation would be determined by the position of the point at which the vortex sheet broke away, due to instability, from what Rosenhead referred to as a sheath of discontinuity.

After Winny[2.37](1934) first measured the frequency of vortex shedding experimentally, Cometta[2.19](1957) obtained quantitative results for the periodic discharge from three-dimensional bluff bodies at Reynolds numbers from $2x10^3$ to $4x10^4$. These are shown graphically in fig.2.6. For a certain range of sphere size a lower critical Reynolds number of about $7.4x10^3$ was observed, at which the wake structure changed suddenly without any detectable corresponding change in the drag. He suggested that this phenomenon occurred due to a transition from laminar to turbulent flow in the free vortex layer, in a similar manner to that in the wake formed behind two-dimensional bluff bodies over a range of Reynolds numbers from 150 to 300. Because the mechanism by which vortex loops are shed was incompletely understood, Cometta could not explain this phenomenon with any certainty.

During the last twenty years, a new interest in the flow field behind three-dimensional bluff bodies of various shapes has arisen. This has been stimulated by various contemporary engineering design problems, such as the design of road vehicles and tall buildings. Fail, Lawford & Eyer[2.38](1957) conducted low-speed wind tunnel experiments on the wake characteristics formed behind flat plates with various cross sections and aspect ratios which were held normal to the air stream. A sketch of the flow pattern formed behind a circular plate, shown in fig.2.7, drawn from the results which they obtained reveals the closed bubble pattern.

Later, Carmody[2.39](1964) developed an analytical method by which he established a similar formation. This was based on his own measurements of mean pressure distribution. Bearman[2.40] in 1980, explained that the main feature of the flow around an axisymmetric bluff body is the wake cavity formed immediately downstream.

MacLennan & Vincent[2.41](1982), used the concept of this wake structure to investigate the transport of airborne material in the wake of flat plates. However, Nakamura & Ohya$^{2.42}$(1986) criticized this earlier work. They argued that there were stronger periodic and less stable wake characteristics formed behind three-dimensional bluff bodies than there were behind two-dimensional bluff bodies. Much of the evidence which is now available supports their view point.

Calvert$^{2.43,2.44}$(1967) has investigated the flow field around cones having various apex angles. He has also investigated the aerodynamic characteristics and accompanying flow field for an inclined disc. The wake behind the former was almost identical to that of the closed bubble shown in fig.2.7. However, the wake behind the latter appeared to be strongly periodic with unstable vortex shedding. These vortices were in the form of a chain of irregularly-linked rings, moving downstream at about 0.6 of the free-stream velocity. The shedding frequency of these vortices increased with the angle of attack at which the disc was inclined. Since Calvert suggested that the flow pattern at zero angle of attack was similar to that of inclined ones, he disagreed with the closed bubble wake structure, which had been proposed earlier.

A relationship between the Strouhal and Reynolds numbers for a sphere, at Reynolds numbers from $6x10^3$ to about $5x10^6$, was observed by Achenbach$^{2.45,2.32}$ (1972,1974). Both in a water tank and a wind tunnel a higher critical Reynolds number of about $3.7x10^5$, at which the drag changed rapidly, was observed. The schematic representation of the vortex configuration in the wake shown in fig.2.8 was based on his flow visualization. The signals from four hot wires, located in the wake and 90 degrees apart, indicated a rotating separation point on the sphere surface.

Taneda[2.46](1978) conducted flow visualization studies around a sphere. For these studies at Reynolds numbers between 10^4 and 10^6 he used surface oil flow, smoke and a tuft-grid mounted in the wind tunnel. Below the critical Reynolds number the sphere wake performed a progressive wave motion, its wave length being about 4.5 times the sphere diameter. Above the critical Reynolds number the wake formed a pair of streamwise line vortices, as shown in fig.2.9. This vortex pair rotated slowly and randomly. At Reynolds numbers ranging from about 400 to 10^6 the sphere wake was not axisymmetric. Taneda predicted that a sphere placed in a uniform flow would be subjected to a fluctuating side force whose direction was completely random.

On the other hand, Pao & Kao[2.47](1977), from their observations at Reynolds numbers from $4x10^3$ to $2x10^4$ of the flow of a weakly-stratified liquid, argued that the sphere wake formed two branches of helical vortices which continuously unwound in opposite senses to one another, as shown in fig.2.10. Because of Thomson's Circulation Theory a number of people have opposed the concept of this double helical vortex wake structure.

Xia & Bearman[2.48](1983) in a wind tunnel investigated the wake formed behind an axisymmetric body with a slanted base and an ellipsoidal nose. Again, their smoke visualization and hot-wire correlation measurements presented evidence of an unstable wake, forming behind a three-dimensional body.

An experimental investigation conducted by Nakamura & Ohya(1986) consisted of flow visualization and velocity and pressure distribution measurements for flows around square prisms of various lengths. It supported Taneda's observations of the wake structure shed by bluff three-dimensional bodies. The plane of vortex shedding from these bodies was observed to rotate slowly and irregularly.

Although there have been many published reports dealing with wakes formed behind three-dimensional bluff bodies, the formation of these wakes is still only partially understood.

2.4. The Wake Formed behind a Parachute

Numerous investigations have been conducted in order to explain the nature of the wake which is formed behind rigid bluff bodies. However, there seems to be very little experimental data to describe the flow field formed around a parachute-shaped body, whether it is rigid or flexible. If the body is flexible it is not easy to conduct the necessary flow field experiments.

In 1956 Pounder[2.49] mapped the steady-state flow field for various shapes of canopies. He injected neutrally-buoyant helium-filled soap bubbles into the stream, but he did not appear to have obtained much data of any lasting value. In order to obtain a qualitative description, a number of experiments have been conducted, from some of which misleading conclusions have been drawn. Babish & Hunter[2.50](1965) investigated two-dimensional rigid models whose shapes represented those of inflated parachute canopies. Dereng[2.51](1973) arranged a flow visualization test in a wind tunnel for the field around a simple canopy gore. Although very interesting photographs were obtained from these tests the results have contributed little to the understanding of the wake structure which is formed behind a real parachute canopy.

Klimas[2.52](1973) and Klimas & Rogers[2.53](1977) used the helium bubble visualization method which Pounder had introduced. Furthermore, they developed a sophisticated computer-based data-processing scheme by which bubble traces taken from high-speed cine camera film frames were plotted and the velocity calculated. Although they presented the velocity distribution around a flexible parachute canopy during the inflation process, there was no discussion of the data which they obtained.

Lingard[2.54](1977) adopted this method of data processing, both in a water tank and a wind tunnel, to survey the flow field formed around parachute canopies during the inflation process. According to his observations, a narrow wake developed up to the maximum over-inflation shape, but vortex shedding from the canopy only occurred when the canopy reached its maximum over-inflation shape.

Although several authors have attempted to visualize the flow field during the inflation of canopies, few experimental data have been published.

In a wind tunnel Jorgensen[1.26] studied the pressure distributions developed on both a 3:1 arm ratio cross or cruciform parachute canopy and a hemispherical canopy. He complemented these measurements with some smoke and wool tuft flow visualization tests. From a spectral density analysis which he made of the fluctuating forces and moments developed on the canopies, he found that the frequency of fluctuations in the aerodynamic forces developed on the hemispherical canopy (projected diameter d=0.553m) was about 20 Hz at a free stream velocity of 17.5 m/sec. He drew a sketch of the flow around a hemispherical parachute canopy which was similar to Fail et al's closed bubble pattern around a flat plate, for which the drag coefficient was similar to that of the canopy.

He also generalized the flow field around all cross parachute canopies as an attached flow over a large portion of the canopy surface. He described steady jets of air passing though large gaps formed between the arms, and no vortex shedding occurring in the wake. He concluded that the reason why cross parachute canopies exhibit desirable static stability characteristics is because of the attached flow over the four arms, and that variation of the canopy fabric porosity had little effect on their aerodynamic behaviors. Later evidence by Shen & Cockrell[2.55](1986) opposes this latter conclusion.

It is clear that there is still much to learn about the flow field which surrounds a flexible bluff body such as a parachute canopy.

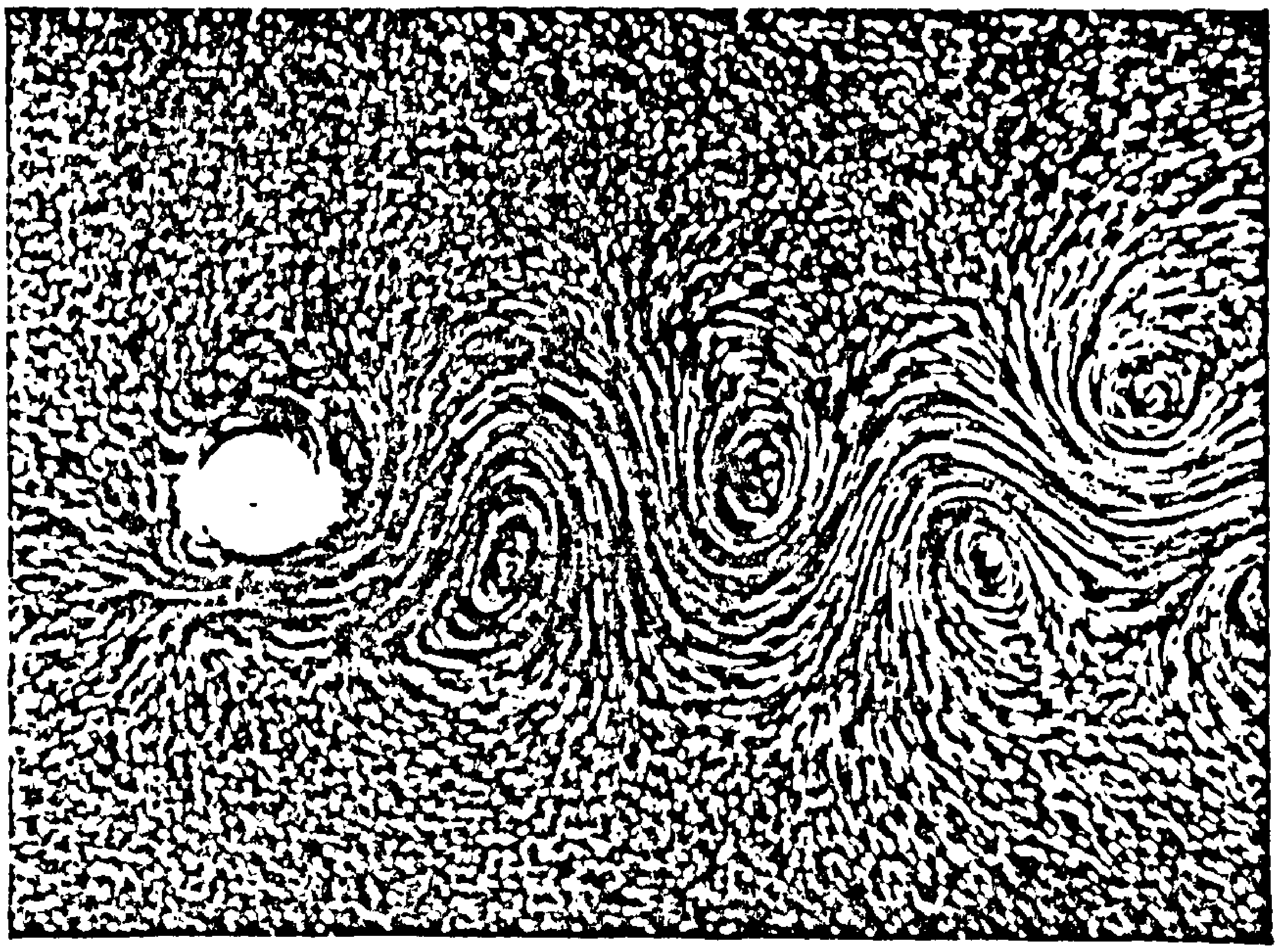

Fig.2.1 A Double Row of Vortices Behind a Cylinder (from Milne-Thomson, L.)

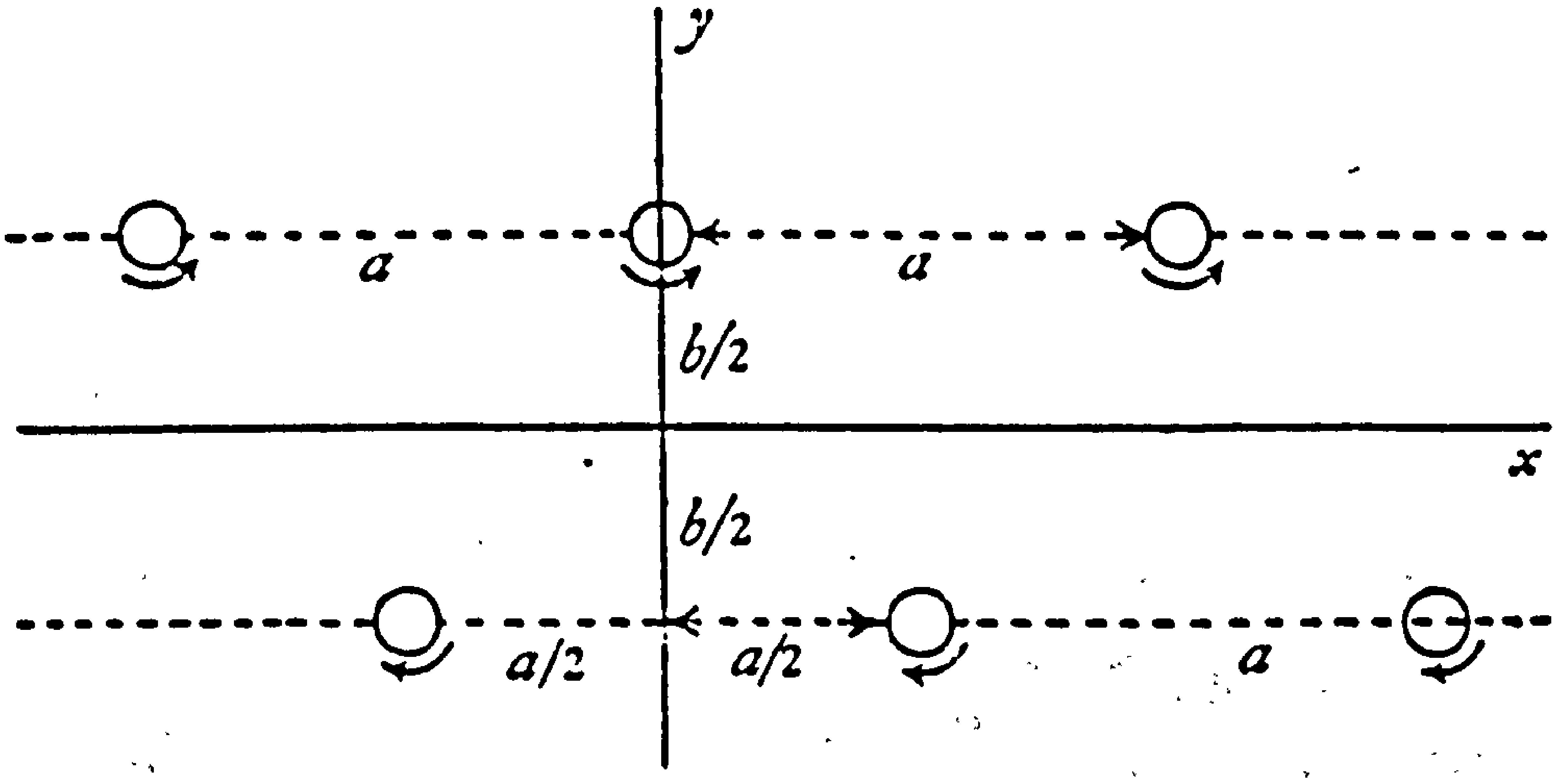

Fig.2.2 Karman Vortex Street

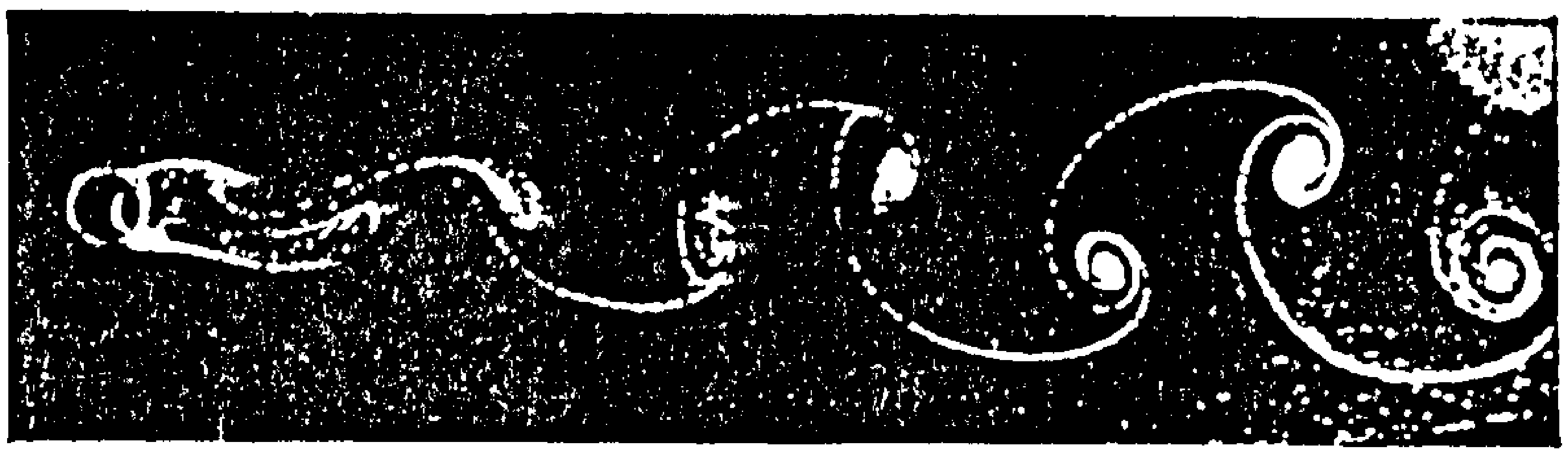

Fig.2.3 Trail of Double Row

(from Goldstein,S.)

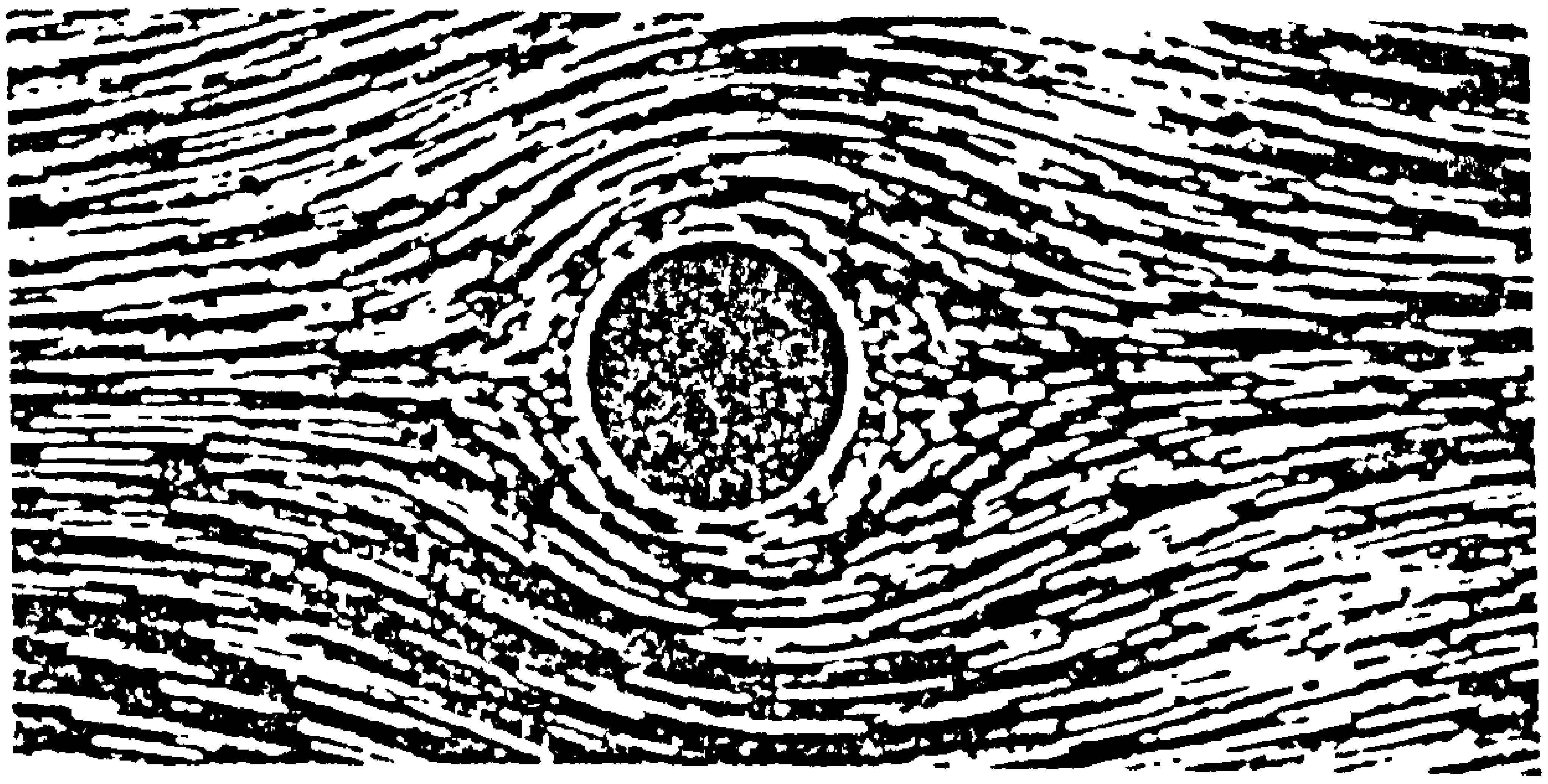

Re = 3.9 (from Goldstein,S.)

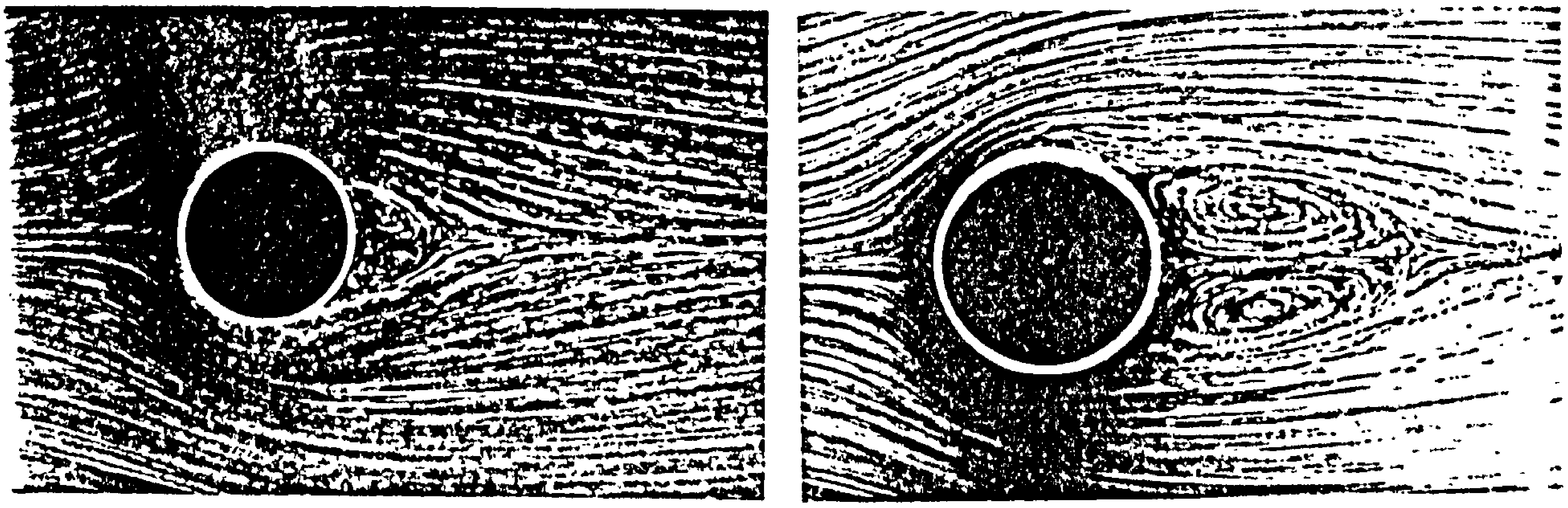

Re = 13.1 (from Van Dyke,M.[2.56]) Re = 26

Fig.2.4 Vortex Pair Elongated with Increase of Reynolds Number

(from Goldstein,S.)

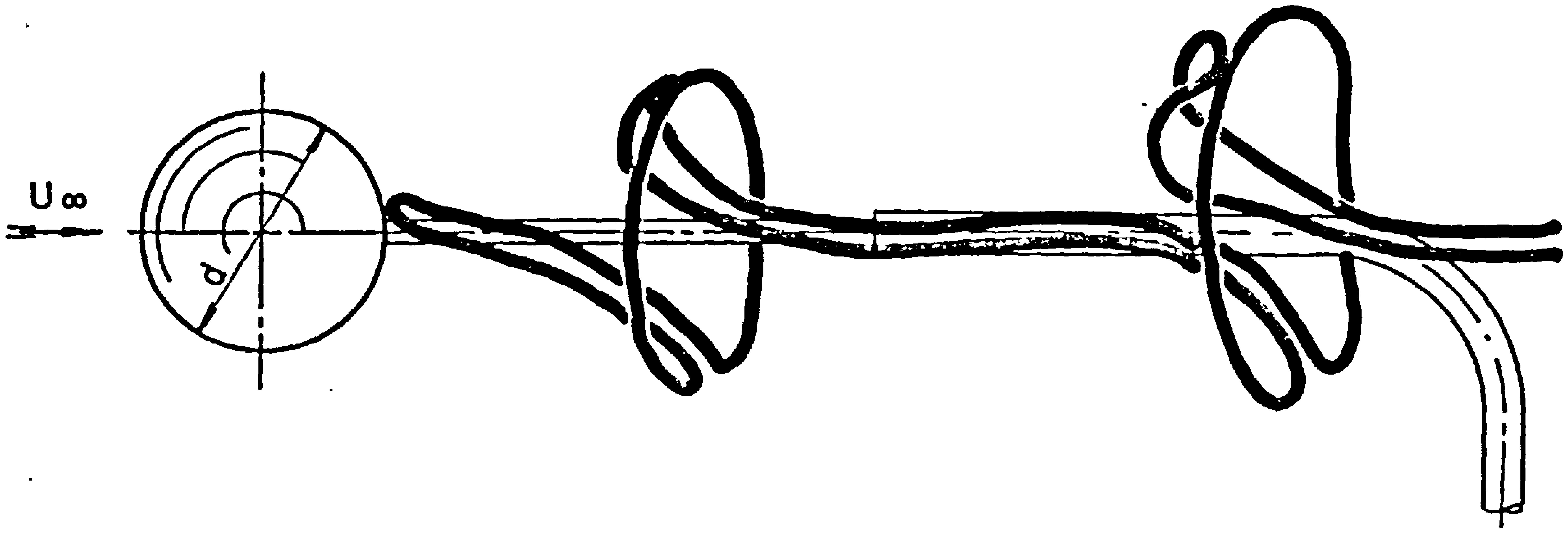

Fig.2.5 Schematic Representation of the Wake Behind a Sphere

(reproduced by Cometta,C.)

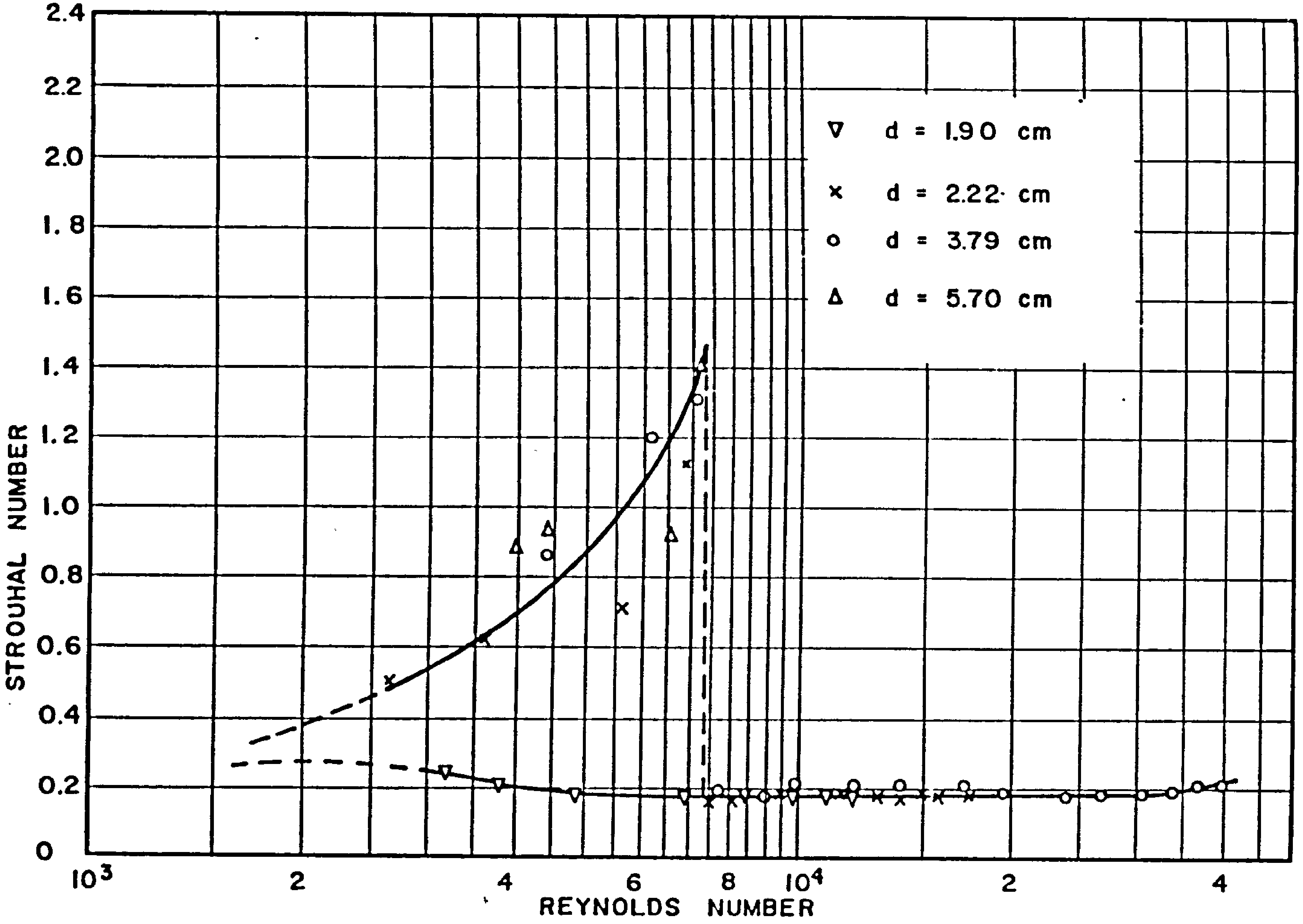

Fig.2.6 Strouhal Number vs. Reynolds Number for a Sphere

(from Cometta,C.)

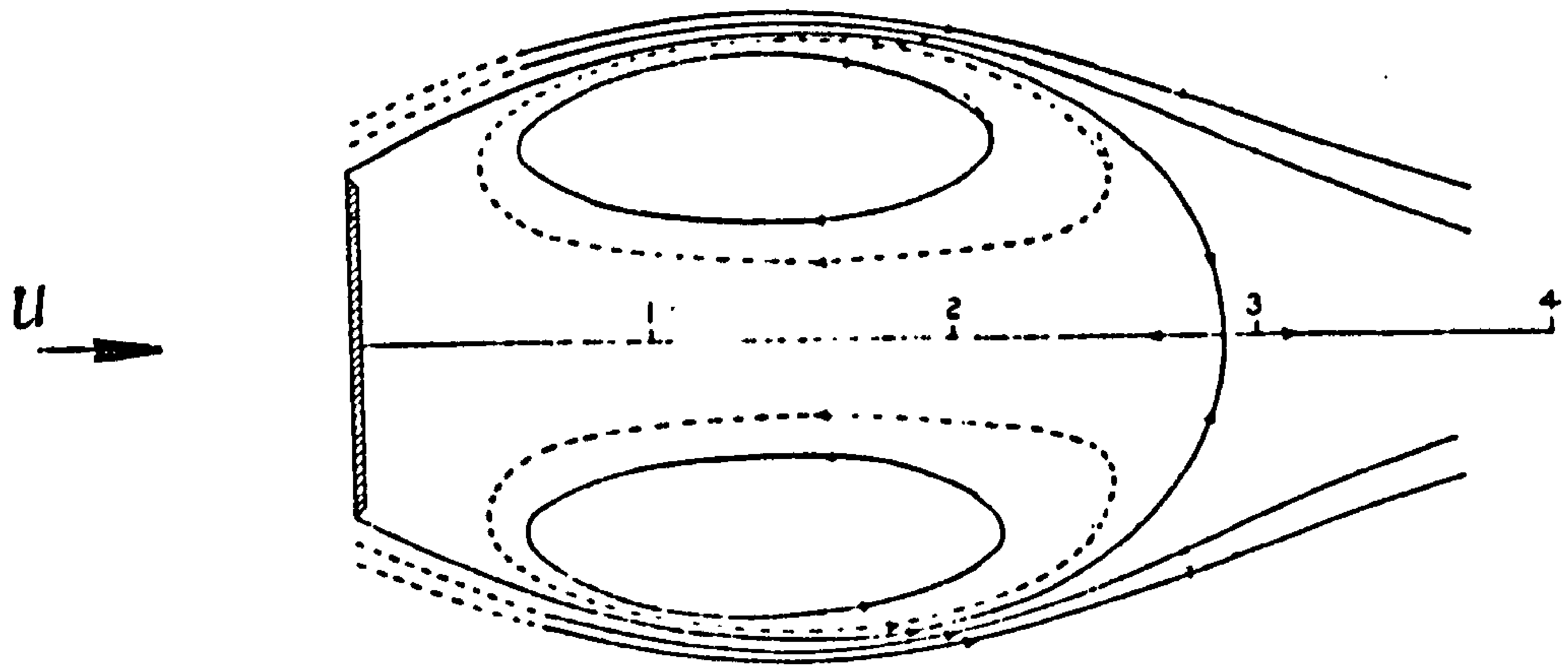

Fig.2.7 Schematic Representation of the Wake Behind a Flat Plate

(from Fail et al)

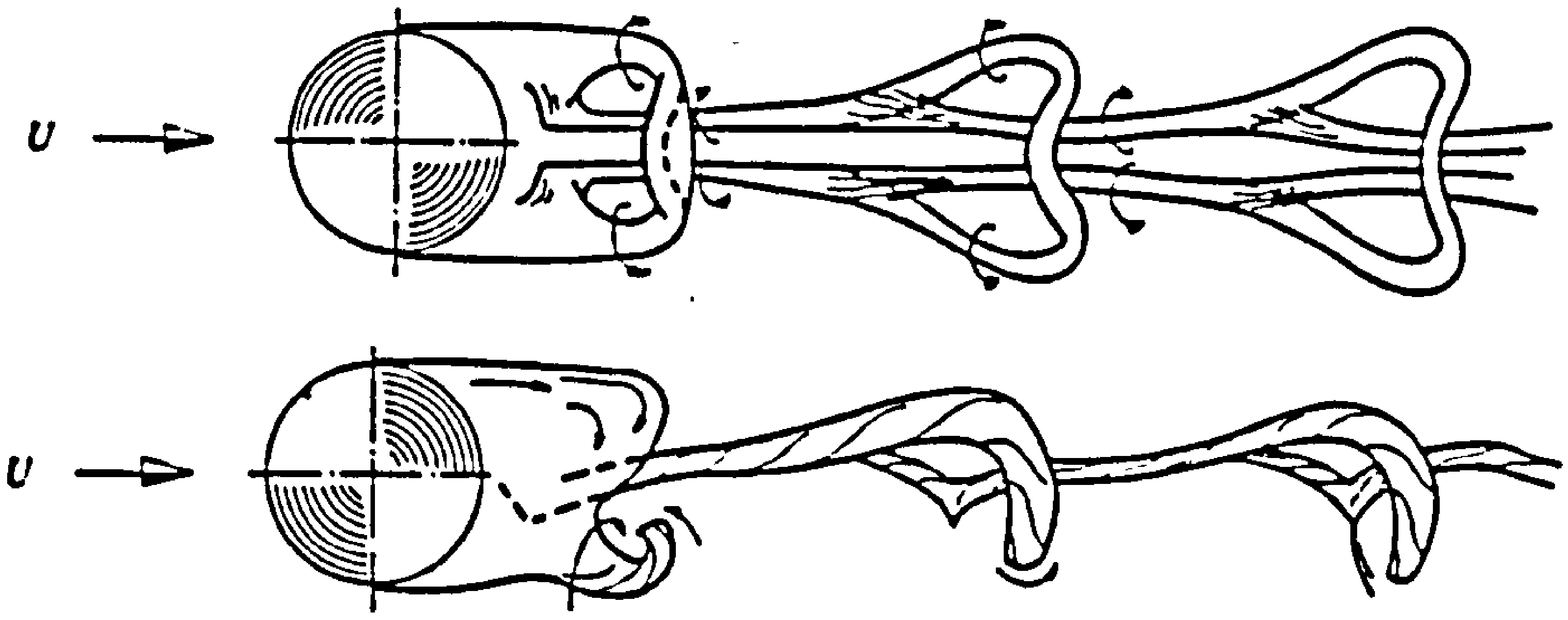

Fig.2.8 Schematic Representation of the Wake Behind a Sphere

(from Achenbach)

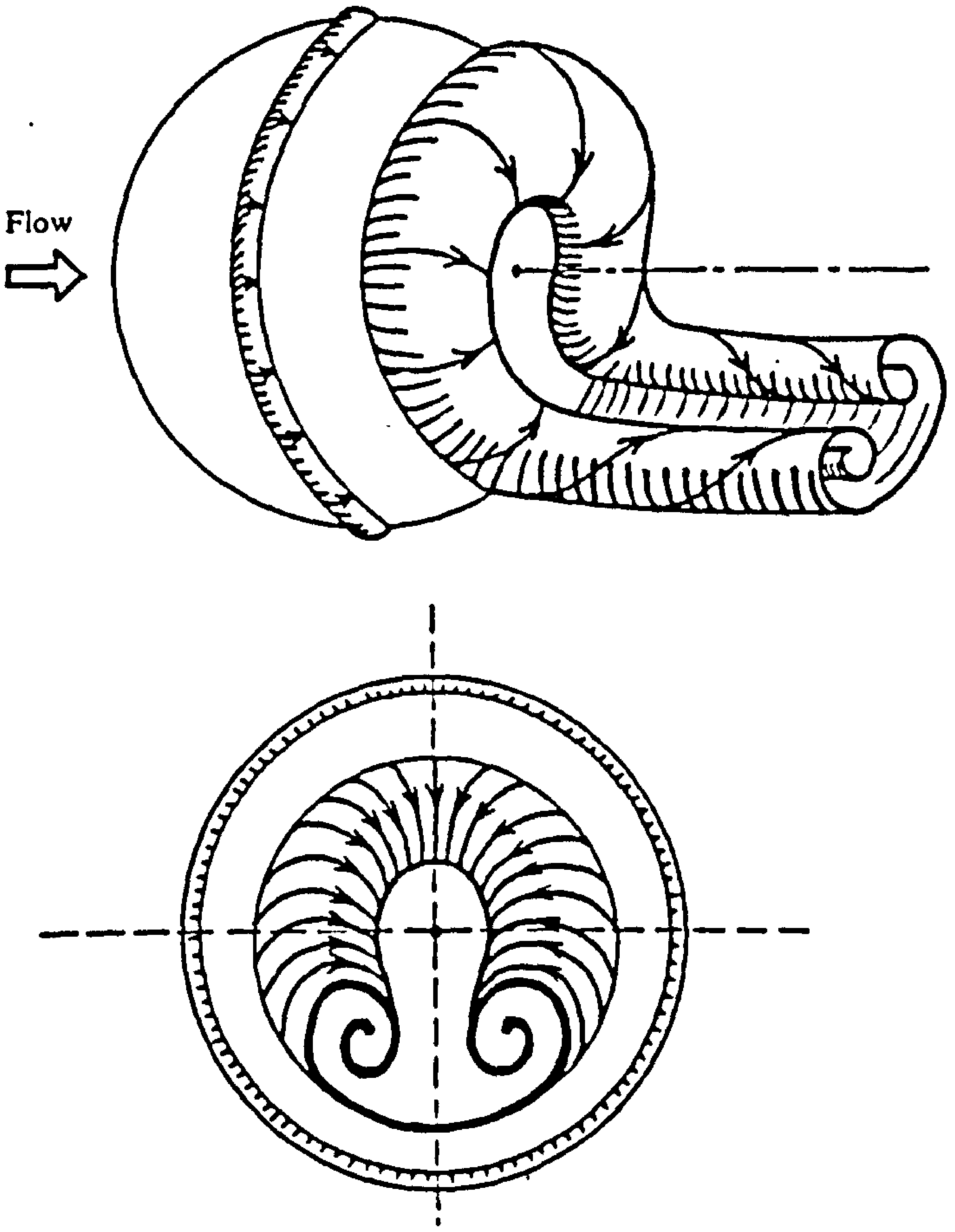

Fig.2.9 Schematic Representation of the Wake Behind a Sphere

(from Taneda)

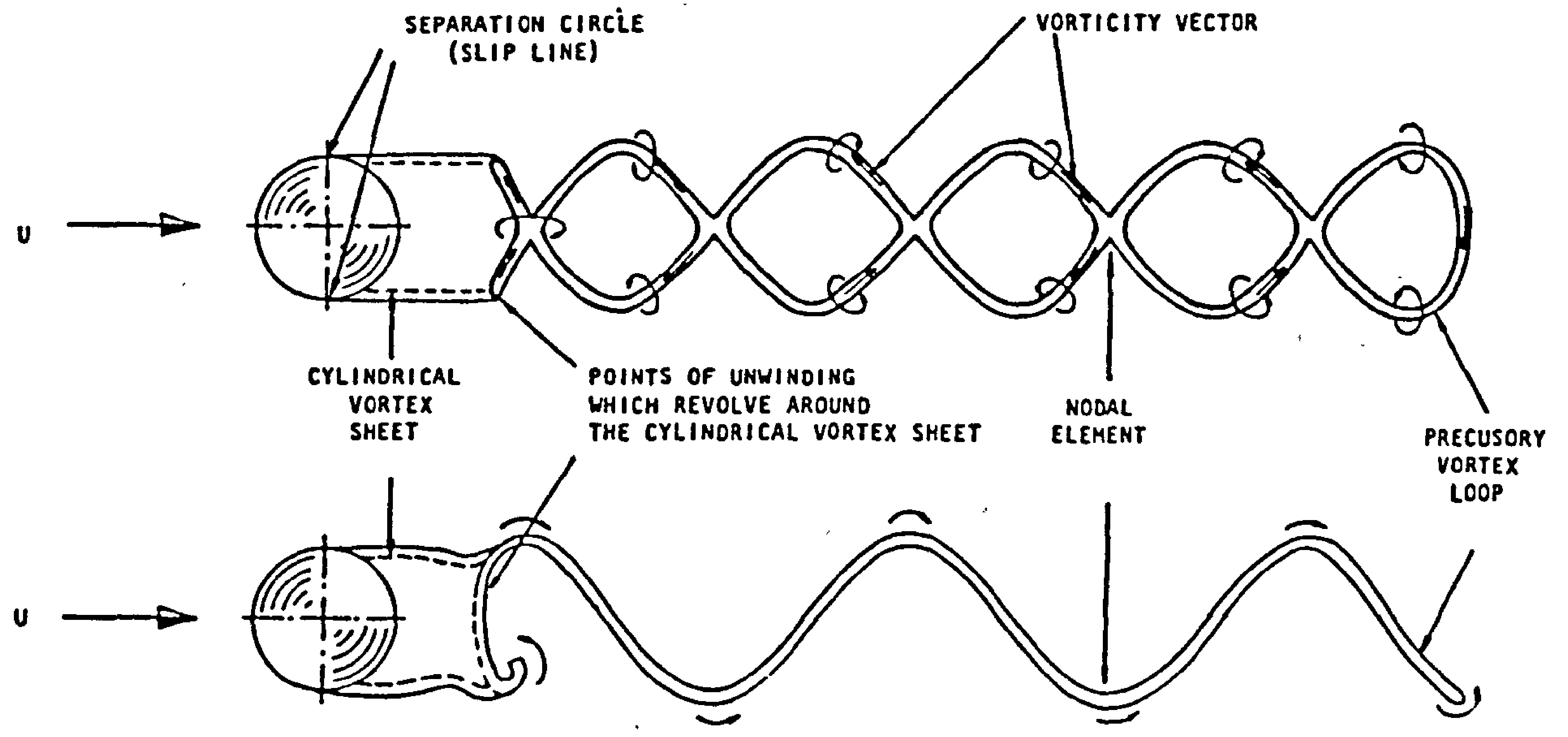

Fig.2.10 Two-Helical Vortex Wake Structure
for a Sphere

(from Pao & Kao)

3 EXPERIMENTAL PROGRAMME

3.1 Introduction

In order to relate the flow field which develops around parachute canopies to their aerodynamic characteristics, a series of experiments was conducted on a family of canopies possessing a particular and significant shape; cross or cruciform canopies. These canopies possessed different fabric porosities and arm ratios, resulting in a variation of their geometrical open area.

The experiments consisted of force and moment measurements together with correlation studies made in their wakes using hot-wire anemometers. Flow visualisation, using neutrally-buoyant helium-filled soap bubbles and wool tufts, was also undertaken. The work was mainly conducted in the Leicester University Charles Wilson Wind Tunnel, though part of the programme was conducted under water in the Ship Tank at the Institute of Higher Education, Southampton.

3.2 Co-ordinate System and Aerodynamic Coefficients for A Parachute Model

3.2.1 Co-ordinate System

The co-ordinate system adopted is fixed to the canopy and is shown in Fig.3.1. The origin O is chosen to be on the parachute's axis of symmetry. The conventionally-positive direction of the tangential aerodynamic force component T is in the opposite sense to the positive direction of axis OX and the conventionally-positive direction of the normal aerodynamic force component N is in the opposite sense to the positive direction of axis OZ. The centre of pressure P is considered as a point on the axis of symmetry through which the line of action of the total aerodynamic reaction R acts, where $R = (T^2 + N^2)^{1/2}$. X_p is the distance from the origin O to the centre of pressure P. A conventionally-positive aerodynamic force will produce a negative pitching moment about the suspension line confluence point C. Since the latter is located close to the centroid of the combined parachute and payload system the pitching moment coefficient about this confluence point is effectively that about the system centroid. This latter is required for the estimation of stability characteristics.

3.2.2 Aerodynamic Coefficients and Static Stability Criteria

3.2.2.1 Non-Dimensional Aerodynamic Force Coefficients

The drag force D and lift L are force components which are respectively parallel and perpendicular to the direction of the resultant air-flow. From Fig.3.1, the relationships between T, N and D, L are as follows:

$$T = D\cos\alpha - L\sin\alpha \qquad (3\text{-}1)$$

$$N = D\sin\alpha + L\cos\alpha \qquad (3\text{-}2)$$

Where α denotes the canopy angle of attack.

At low speeds relative to the speed of sound, aerodynamic force and moment coefficients for parachute canopies are defined as follows:

$$C_T = \frac{T}{0.5\rho U^2 S_0} = f_1(\alpha, Re) \tag{3-3}$$

$$C_N = \frac{N}{0.5\rho U^2 S_0} = f_2(\alpha, Re) \tag{3-4}$$

$$C_D = \frac{D}{0.5\rho U^2 S_0} = f_3(\alpha, Re) \tag{3-5}$$

$$C_L = \frac{L}{0.5\rho U^2 S_0} = f_4(\alpha, Re) \tag{3-6}$$

$$C_M = \frac{M}{0.5\rho U^2 S_0 D_0} = f_5(\alpha, Re) \tag{3-7}$$

where ρ — Air density (kg/m^3)

U — Resultant free stream velocity relative to the origin O (m/s)

S_0 — Characteristic area, chosen as surface area of parachute canopy (m^2)

D_0 — Characteristic length, generally chosen as the nominal diameter of the canopy (m)

$$D_0 = \sqrt{(4S_0/\pi)}$$

Re — Reynolds numbers

3.2.2.2 Parachute Stability

The degree of stability or instability of any system which is in equilibrium is measured by determining the magnitude and direction of its response to small disturbances. When considering parachute stability and instability, motion in pitch is assumed unless otherwise stated.

In aeronautical engineering applications the stability of a system is normally subdivided into static stability and dynamic stability. Static stability is solely concerned with the direction of the moment about the centroid which is developed on the system as a direct consequence of its displacement from equilibrium, that is, does this moment act to restore the system to equilibrium or to amplify the initial disturbance? Dynamic stability, which can only be determined from a full dynamic analysis, is concerned with the amplitude and the degree of damping which the disturbed system develops in its return to its equilibrium state.

Doherr and Saliaris[1.17] have shown that for a parachute to be dynamically stable in pitch it must necessarily exhibit static stability. Conversely, if it is strongly statically stable in pitch it must also be dynamically stable. Only if it is weakly statically stable in pitch is it not clear whether the parachute will be stable or unstable dynamically. Because of the significance of the static stability in pitch which the parachute possesses, it was solely considered, to the exclusion of the corresponding dynamic stability characteristics, in this experimental programme on parachute stability.

3.2.2.3 Static Stability Criterion

Consider a parachute to be rigidly-connected to its payload. The aerodynamic force developed on the payload is assumed to be negligible compared with that on the canopy. The aerodynamic and gravitational forces and moment acting on the parachute and payload are shown in Fig.3.2. For equilibrium:

$$N = mg\sin\beta \qquad (3\text{-}8)$$

$$T = mg\cos\beta \qquad (3\text{-}9)$$

Where m __ Mass of parachute-payload system (kg)

β __ The angle between the axis of the system and the direction of the gravitational force

Thus at the equilibrium condition,

$$N = 0$$

$$M_G \simeq M_C = -N(l_f - X_p) = 0$$

and $\sin\beta = 0$, $\beta = 0$, $\cos\beta = 1$

so that

$$T = mg \qquad (3\text{-}10)$$

If the derivative of the pitching moment about the suspension line confluence point with respect to the angle of attack $dC_{Mc}/d\alpha$ is negative, then when it is disturbed from the equilibrium state the parachute develops an aerodynamic restoring moment. Such a parachute possesses static stability. The static stability criterion in pitch is therefore that at equilibrium

$$dC_{M_G}/d\alpha < 0$$

or $$dC_N/d\alpha > 0$$

The angle of attack at which the canopy is both in equilibrium and statically stable is known as the statically stable angle of attack α_{eq}.

3.3 Parachute Models

Twenty-seven different cross parachute models were considered, each with the same nominal surface area of $0.108m^2$. Their configurations are shown in Fig.3.3 and their structural and geometrical characteristics are listed in Table A.1 of Appendix A

The arm ratio R_A of a cross-shaped canopy is defined as the ratio of arm length to the arm width, as shown in Fig.3.3. The suspension line ratio R_s is the ratio of the length of the suspension line, fixed to the canopy skirt, to the arm length.

Three different definitions can be adopted for canopy porosity. As its name implies, the geometric porosity λ_g is defined as the ratio of the total canopy open area to the total surface area of the canopy, inclusive of any apex vent area. The nominal porosity λ is a measure of the volumetric flow rate of air through a unit area of cloth at a stated differential pressure (10 inches of water in Britain). The dimensionless effective porosity λ_e, used in Table A.2 in Appendix A, is the ratio of the average velocity through the porous surface to the free stream velocity relative to the canopy.

In order to compare aerodynamic characteristics of the cross parachute with the conventional round or hemispherical parachute, both rigid and flexible hemispherical parachute canopy models with different geometrical porosities were also tested in the wind tunnel. Their configurations are shown in Figs.3.4 and 3.5 and Table A.3 of Appendix A.

3.4 Experimental Facilities and Their Arrangement

3.4.1 Measurements of Mean Aerodynamic Forces

3.4.1.1 Wind Tunnel Tests

Force measurements were mainly made in the horizontal return-flow atmospheric pressure wind tunnel, with closed working section of a cross-sectional area 1.14m by 0.84m (3.75ft x 2.75ft), at Reynolds numbers between 1×10^5 and 5×10^5. The turbulence intensity was lower than 0.5%. The models were mounted by means of a supporting sting on a three component balance, as shown in Fig.3.6.

To reduce the interference caused by the supporting sting on the flow field surrounding the parachute canopy, the suspension system was downstream of the canopy models. The sting was shrouded by a streamlined body, as shown in

Fig.3.7, to reduce its drag to a minimum.

The aerodynamic forces and moment developed on the parachute canopy were transmitted to the sting at two points, the apex of the canopy and the suspension line confluence point. Heinrich & Haak[1.22] indicated that the normal force at the latter point was negligible.

The supporting sting was attached to the three-component balance manufactured by Plint and Partners Ltd. and illustrated in Fig.3.8. This was located on the back wall of the wind tunnel. The aerodynamic forces and moment were balanced by three constrained forces NA, NF and DG, determined by strain gauges which were mounted on the aft lift, fore lift and drag spring cantilevers respectively as shown in Fig.3.9 . From the force diagram shown in Fig.3.10 the drag D, lift L and pitching moment M_O about the origin O can be determined as follows:

$$D = DG \tag{3-11}$$

$$L = (NA + NF) \tag{3-12}$$

$$M_O = -(NA - NF) \times \frac{0.127}{2} + N \times A_0 \tag{3-13}$$

Combining equations (3-13) and (3-2)

$$M_O = -(NA - NF) \times \frac{0.127}{2} + (D\sin\alpha + L\cos\alpha) \times A_0$$

The location of the centre pressure can then be determined,

$$X_p = |M_O/N| \tag{3-14}$$

The pitching moment about the suspension line confluence point C is

$$M_C = -N(l_f - x_p) \qquad (3\text{-}15)$$

where l_f is the length measured along the axis of symmetry of the inflated parachute.

Amplified signals from the strain gauges mounted on the balance together with a pressure transducer signal from a manometer manufactured by Air Instrument Resources Ltd (which detected the working section dynamic pressure) were fed into a BBC micro-computer which recorded, calculated and displayed the aerodynamic coefficients C_T, C_N and C_{Mc} as functions of the measured angle of attack and Reynolds number. Both the structure diagram for this computer program and the full program are listed in Appendix B.

It was assumed that the effects of the shrouded supporting sting on the calculated results could be neutralized by subtracting any aerodynamic and gravitational forces, which were developed on the sting in the absence of the parachute canopy, from those which were obtained at the same angle of attack when the parachute models were present.

3.4.1.2 Ship Tank Tests

As part of an experimental programme conducted by Cockrell, Shen, Harwood and Baxter[1.29] in 1986, tests were performed in a Ship Tank on parachute canopies fully immersed in water. When these canopies had been tested in the Leicester University Wind Tunnel the blockage area ratio, based on the projected area of canopy, was some 6% ~ 8% and although corrections were made by Maskell's[3.1] method to the measured drag coefficient, it was considered desirable to measure the canopy drag coefficient in an environment in which the blockage constraint was negligible.

The canopy models were immersed in the stationary water and mounted via a strain-gauged sting to the towing carriage shown in Fig.3.11. This carriage could travel with a constant velocity of some 1.5m/sec. down the 61m (200ft) length of the 3.66m x 1.83m (12ft x 6ft) tank in which the blockage factor was only about 1.0%. The test Reynolds number was about the same as that in the wind tunnel, ie. 3.0×10^5, based on the nominal diameter of the canopy model.

Just as for the wind tunnel tests the strain-gauged sting was shrouded by a cylindrical tube, to minimise the aerodynamic forces developed on it. The strain-gauged sting was attached to a U-shaped clamp on the circular turntable device shown in Fig 3.12. This latter was mounted on to a square frame which was attached to the ship tank towing carriage. Adjustment of the angle of attack could be made either by turning the sting in the U-shaped clamp or by rotation of the circular turntable device.

Aerodynamic forces developed on the parachute were determined from measurements of two groups of strain gauges mounted along cross sections 1-1 and 2-2 on the sting shown in Fig.3.13. There are six force and moment components F_x, F_y, F_z, M_x, M_y, M_z which can be considered to be developed on this sting. Constrained bending and torsional moments caused by these aerodynamic forces and moments at section 1-1 are M_{1x}, M_{1z}, T_{1y}, and at section 2-2 are M_{2x}, M_{2z}, T_{2y}. Bending moments were measured by strain gauges which were arranged as Fig.3.14, and torsional moments by strain gauges arranged as Fig.3.15.

The constrained moments at section 1-1 are:

$$M_{1x} = -F_z Y_1 + M_x \tag{3-16}$$

$$M_{1z} = F_y X_c + M_z + F_x Y_1 \tag{3-17}$$

$$T_{1y} = -F_z X_c + M_y \tag{3-18}$$

The constrained moments at section 2-2 are:

$$M_{2x} = -F_z Y_2 + M_x \tag{3-19}$$

$$M_{2z} = F_y X_c + M_z + F_x Y_2 \tag{3-20}$$

$$T_{2y} = T_{1y} = -F_z X_c + M_y \tag{3-21}$$

Since

$$Y_1 - Y_2 = l_{12}$$

By subtracting (3-19) from (3-16):

$$M_{1x} - M_{2x} = -F_z l_{12}$$

then

$$F_z = - \frac{M_{1x}-M_{2x}}{l_{12}} \qquad (3\text{-}22)$$

By subtracting (3-20) from (3-17):

$$M_{1z} - M_{2z} = F_x l_{12}$$

$$Fx = \frac{M_{1z}-M_{2z}}{l_{12}} \qquad (3\text{-}23)$$

F_x is the tangential force T developed on the parachute. The normal force N is equal to $(F_y{}^2 + F_z{}^2)^{1/2}$. Since the angle of attack α is formed in the plane XOZ, $F_y = 0$ and the normal force N is equal to F_z. To avoid having to make repairs during the test program, each strain gauge bridge was duplicated and both sets of readings were recorded simultaneously.

From equation(3-21)

$$X_c = - \frac{T_y-M_y}{F_z}$$

Assuming the centre of pressure lies at a distance X_p along the axis of symmetry from the origin O, and $M_x=0$, $M_y=0$, $M_z=0$, then the general point C becomes the centre of pressure P, so that

$$x_p = - \frac{T_Y}{F_z} \qquad (3\text{-}24)$$

The relative velocity of the fluid is that of the towing carriage which travels down the ship tank. Amplified signals from the strain gauges and from a revolution counter on a towing carriage wheel were fed into a Reseach Machines micro-computer. The data reduction program was essentially similar to the one used for the wind tunnel tests.

3.4.2 Flow Visualisation Methods

Flow visualisation studies at Reynolds numbers between 1.0×10^5 and 2.0×10^5, were conducted in the same wind tunnel which had been used for force measurements. Both wool tufts and neutrally-buoyant soap bubbles were used to visualise the flow field surrounding the parachute canopies. The former were used to check the symmetry of the wake about the canopy axis, and the latter to appreciate the nature of the whole flow field.

3.4.2.1 Wool tufts

Wool tufts were arranged downstream of the parachute model as illustrated in Fig.3.16. Here their purpose was to show wake movement with time at certain cross-sectional locations. The tufts grid, located some 0.5 to 1.0 canopy projected diameters downstream, consisted of a wooden frame on which 1 mm diameter metal wire formed a 25mm square grid from the nodal points of which the wool tufts, of length some 50 mm, were hung.

Location of the tuft grid was selected to be where the tufts had the most strongly-fluctuating movement. A motor-driven camera with a flash gun was set downstream of this grid to record the movement of the tufts. The exposure was 0.001 second.

3.4.2.2 Helium Bubble Visualisation

The flow field surrounding the parachute was visualised using small neutrally-buoyant, helium-filled, soap bubbles which were introduced upstream of the canopies as shown in Fig.3.17. If smoke had been used rather than helium-filled bubbles to visualise the flow field around the parachutes the test speed of the wind tunnel would have been limited by the diffusion of the smoke to less than 2m/s, at which speed the parachute canopy cannot inflate properly. Using neutrally-buoyant soap bubbles enables the range of test Reynolds numbers to be much higher than it can be with smoke visualisation. Additionally, the soap film is highly reflective and thus helium-filled neutrally-buoyant soap bubbles are very good for photographic purposes.

The bubble generator head is shown in Fig.3.18. It comprises three concentric tubes arranged so that compressed helium is used to fill the bubble which can than be blown away from the head by a suitable compressed gas, such as air or carbon dioxide. A bubble generator console controls the quantities of helium, gas and soap solution.

Bubbles were illuminated against a black background with a shrouded parallel light source downstream. A 16 mm cine camera with an operating speed from 12 to 80 frames per second, or else a video recorder camera, were located outside the wind tunnel, so that the flow could be photographed through a glass window. The cine camera was set at an aperture of f=2.5 and a frame speed of 12 frames/sec. Before each series of runs the view in the camera was calibrated by photographing a ruler marked in 50 mm multiplies in both the horizontal and the vertical directions.

An appropriate bubble size was chosen with which clear photographs were obtained without any accumulation of bubble solution on the parachute models. In order to increase the stiffness of the supporting sting and so reduce the effects of model vibration on the flow pattern, three thin suspension wires 0.5 mm in diameter, were fixed between the sting and the wall of the wind tunnel.

3.4.3 Measurements of Periodic Characteristics in the Wake Formed behind Parachute Canopies

Both the mean and the fluctuating velocity in the wake were measured using a constant temperature hot-wire anemometer (1050 series) manufactured by TS1 Incorporated. Two hot-wire probes were placed normal to the flow in the upstream direction, so that they could be traversed through the wake, along radii or the axis, as shown in Fig.3.19.

The hot-wire transducer probe, which is arranged in a Wheatstone bridge as shown in Fig.3.20, is a resistance element with a high temperature coefficient, at an elevated temperature. The basic calibration between the voltage output v from the hot-wire anemometer and the velocity V is formed by King's law:

$$v^2 = a + bV^{1/2} \qquad (3\text{-}25)$$

This can be expressed in the form:

$$\frac{V}{U_\infty} = \left[\frac{(v^2 - v_o^2)}{(v_\infty^2 - v_o^2)}\right]^2$$

where a,b__ constant coefficient

v_o __ value of v at V=0

v_∞ __ value of v at $V=U_\infty$

In order to obtain the analysis of the waveform, frequency, and phase relationship of the periodic velocity in the wake the outputs from two hot-wire anemometers were passed through a Fast Fourier-Transform (FFT) Analyser (CF-900 series) manufactured by ONO SOKK1 Co. Ltd.

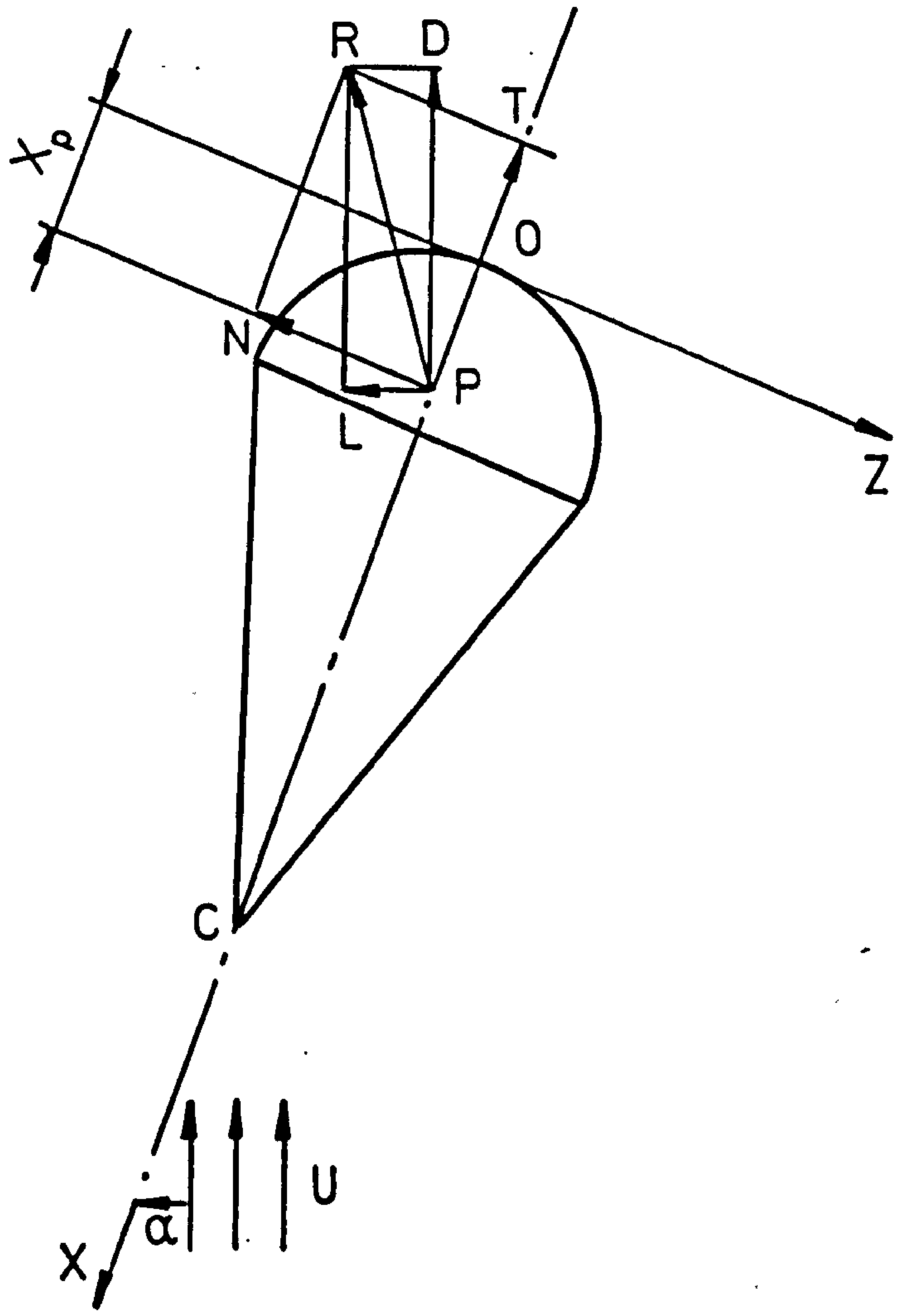

Fig.3.1. Co-ordinate system

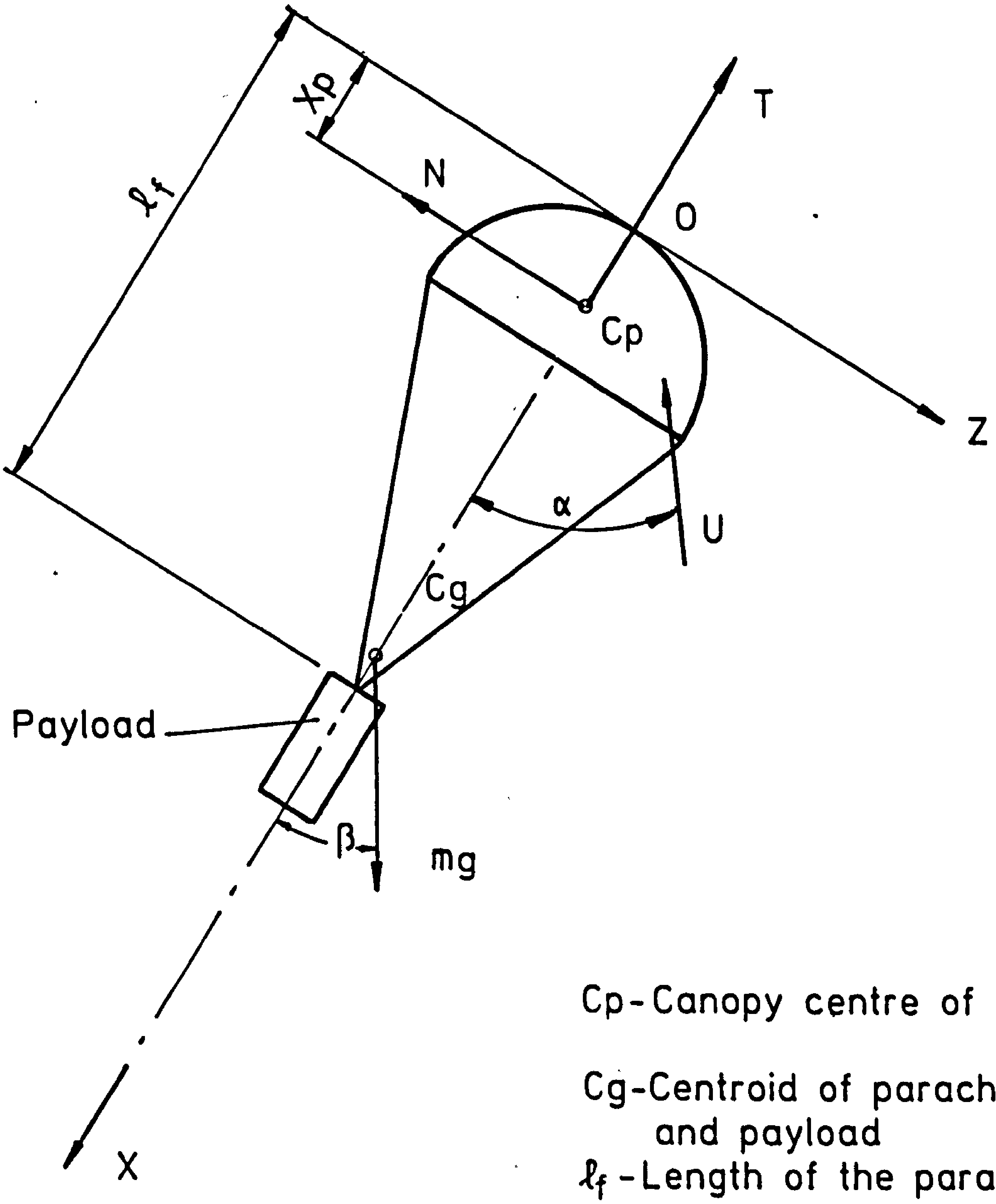

Cp - Canopy centre of pressure

Cg - Centroid of parachute
and payload

ℓ_f - Length of the parachute
in flight

Fig. 3.2 Forces and moments developed on a descending parachute and payload

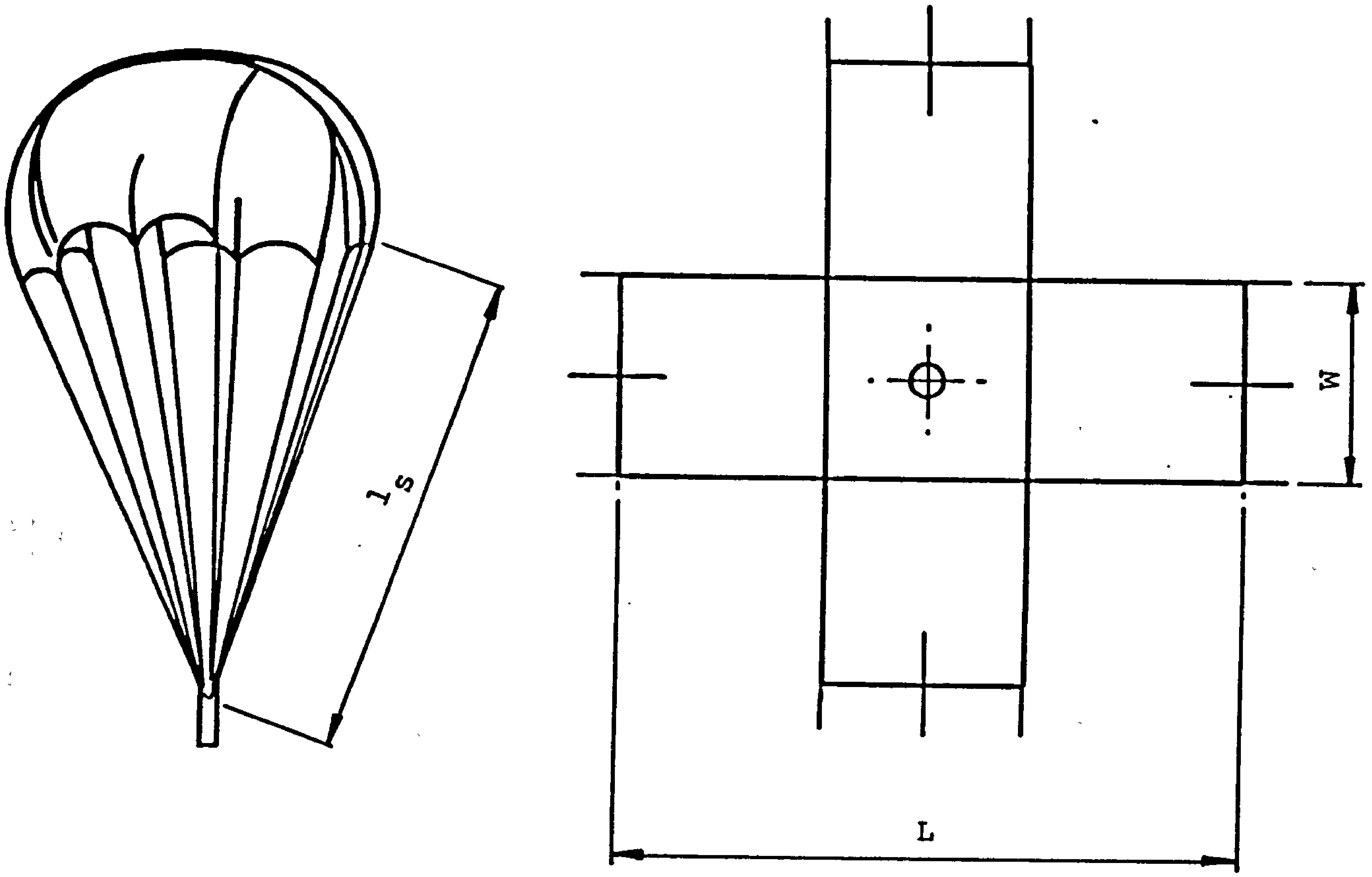

Arm ratio $R_A = L/W$

Suspension line ratio $R_S = l_S/L$

Fig. 3.3 Cross parachute model configurations

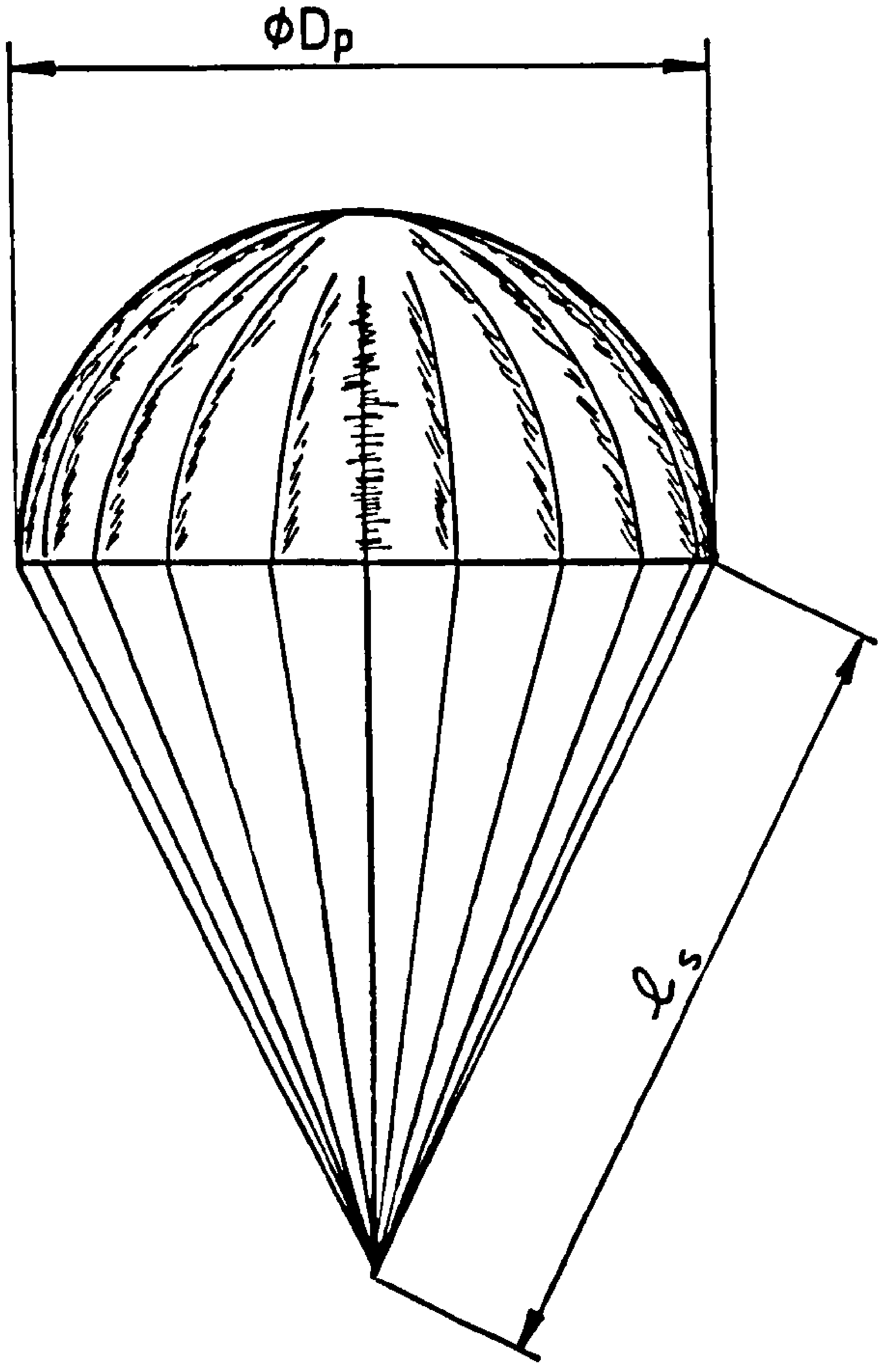

$$D_o = \frac{\text{Perimeter of parachute skirt}}{\pi}$$

$$R_s = \ell_s / D_o$$

$$S_o = \frac{\pi D_o^2}{2}$$

Fig. 3.4 Configuration of the flexible hemispherical parachute canopy model

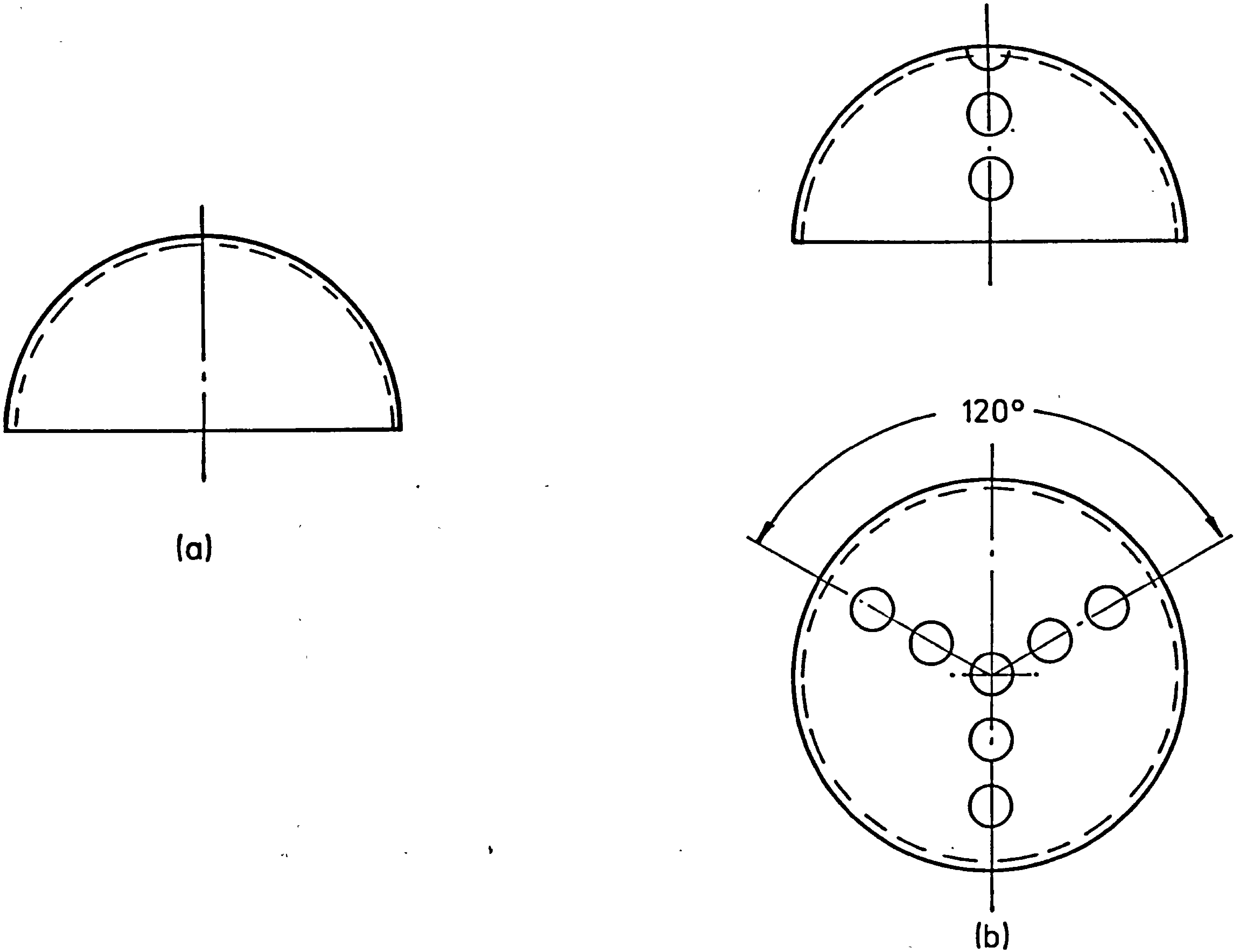

Fig. 3.5 Simulation of porosity for rigid hemispherical parachute models

(a) without porosity (b) with geometrical porosity

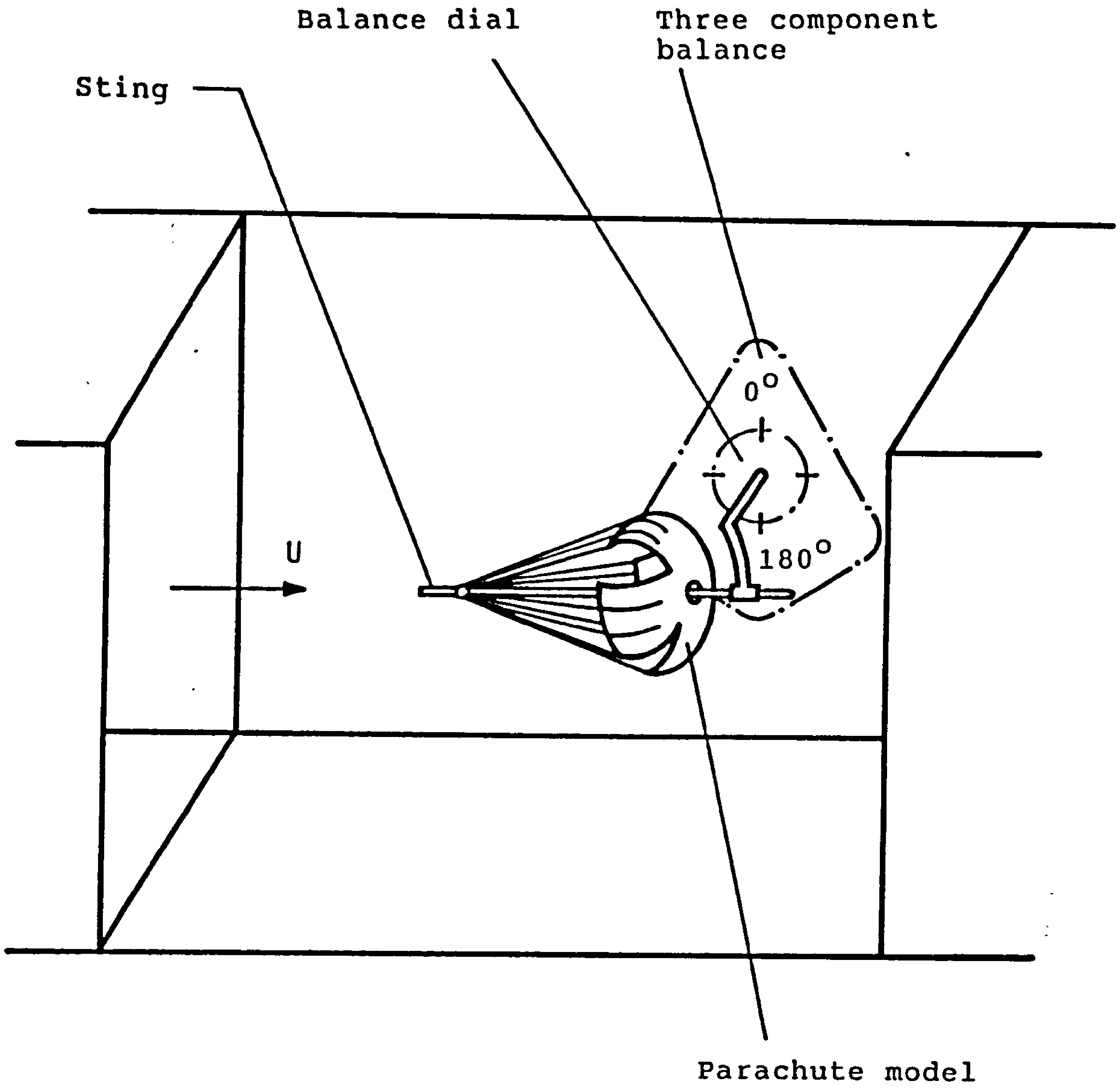

Fig. 3.6 Model suspension

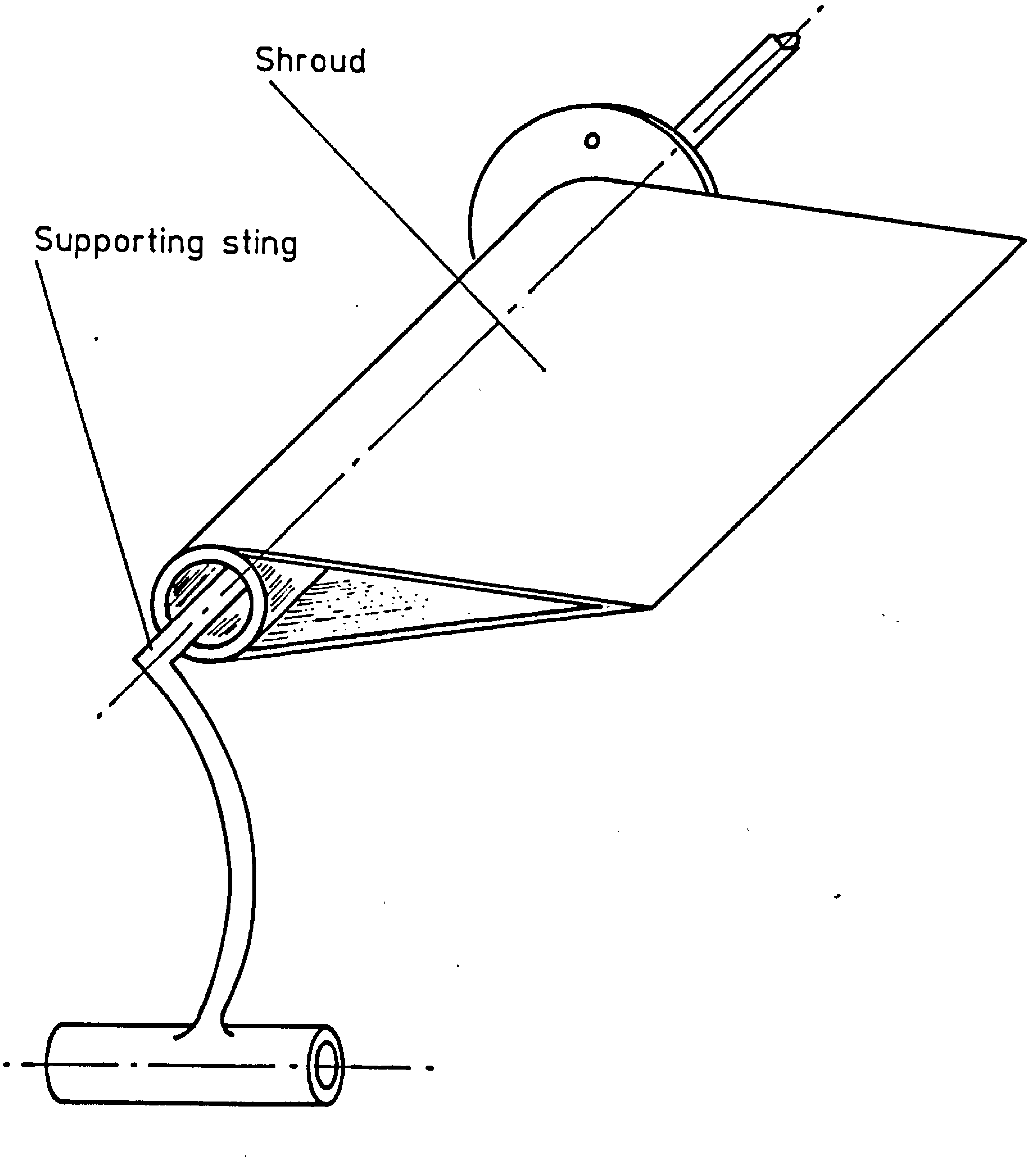

Fig. 3.7 Supporting sting with shroud

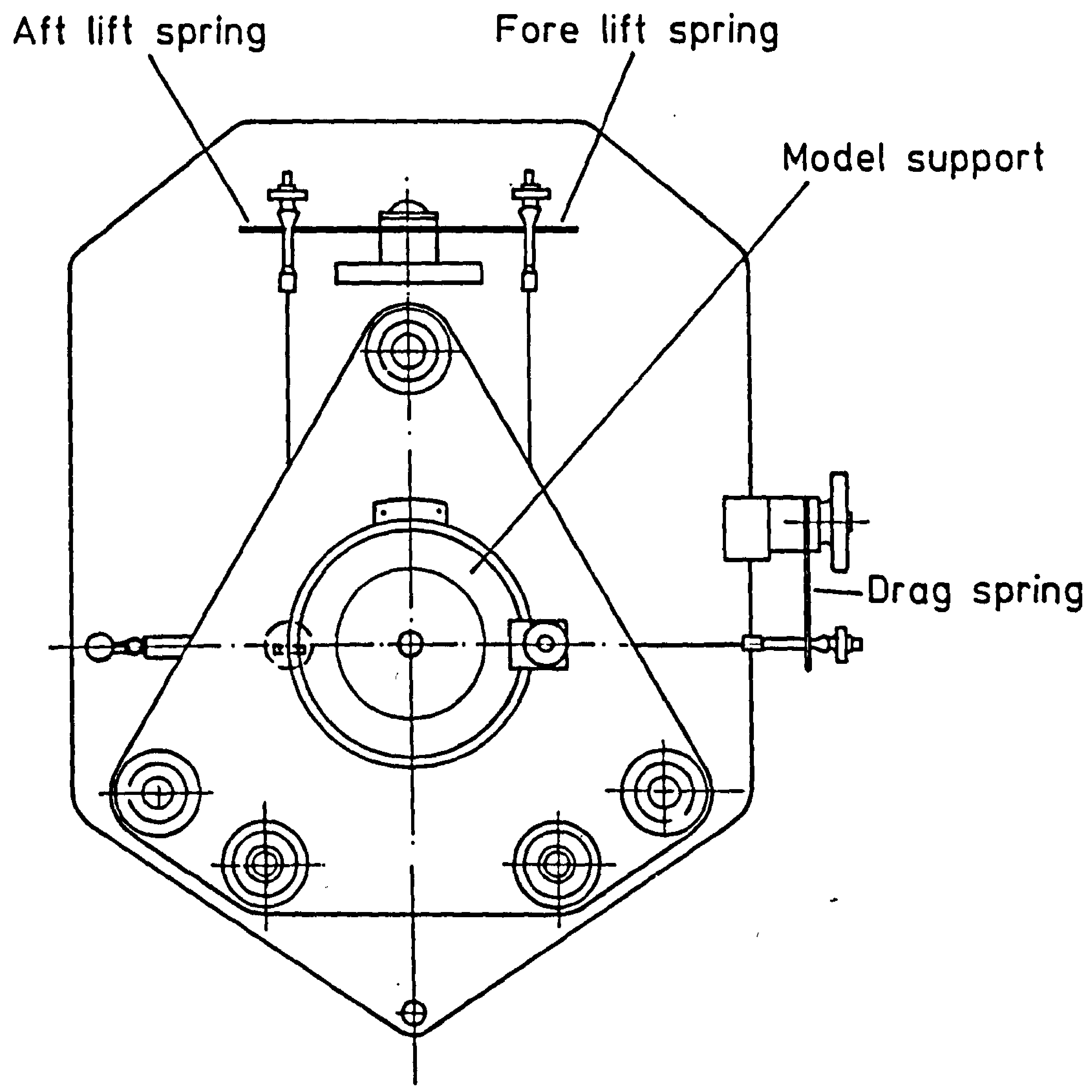

Fig. 3.8 Plint and Partners three-component wind tunnel balance

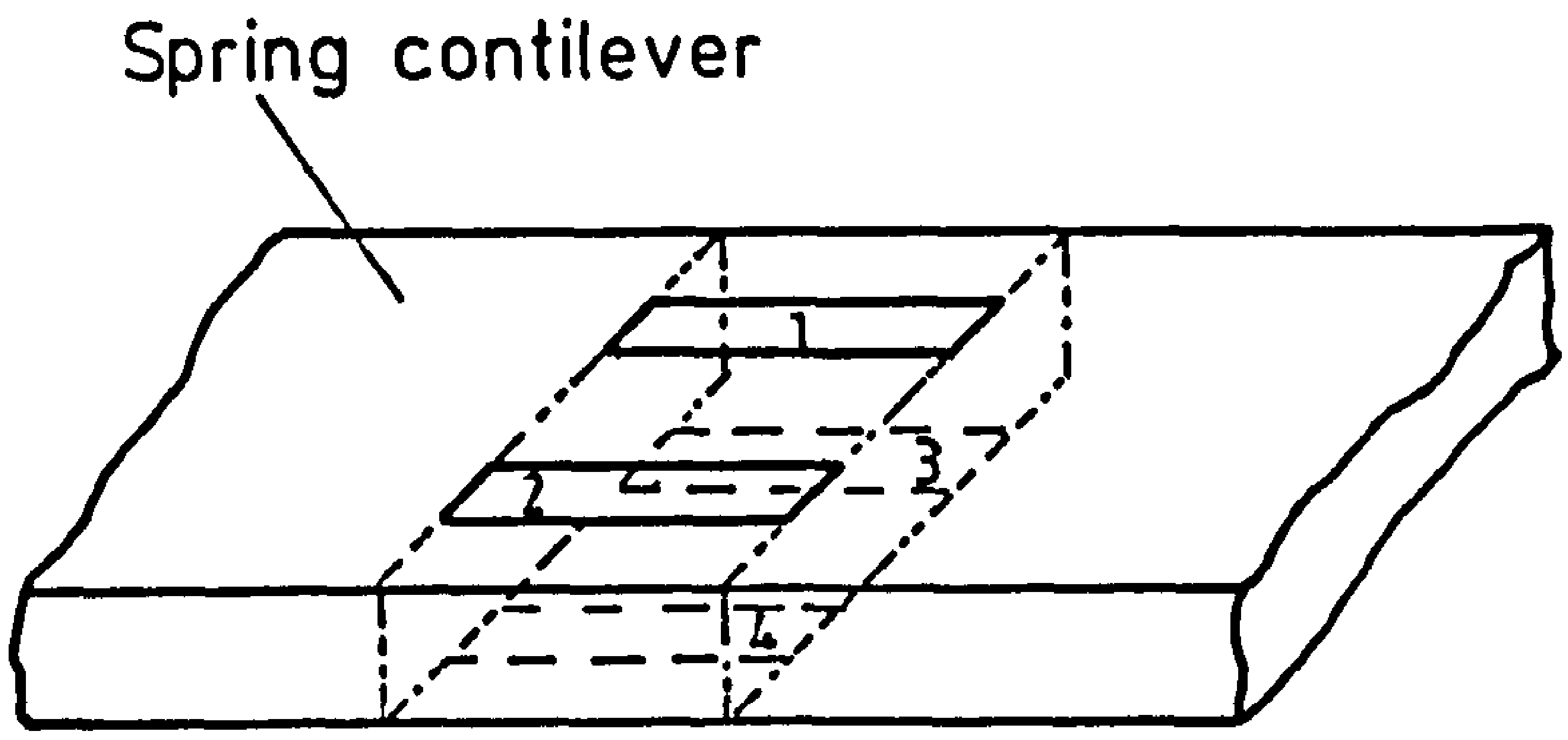

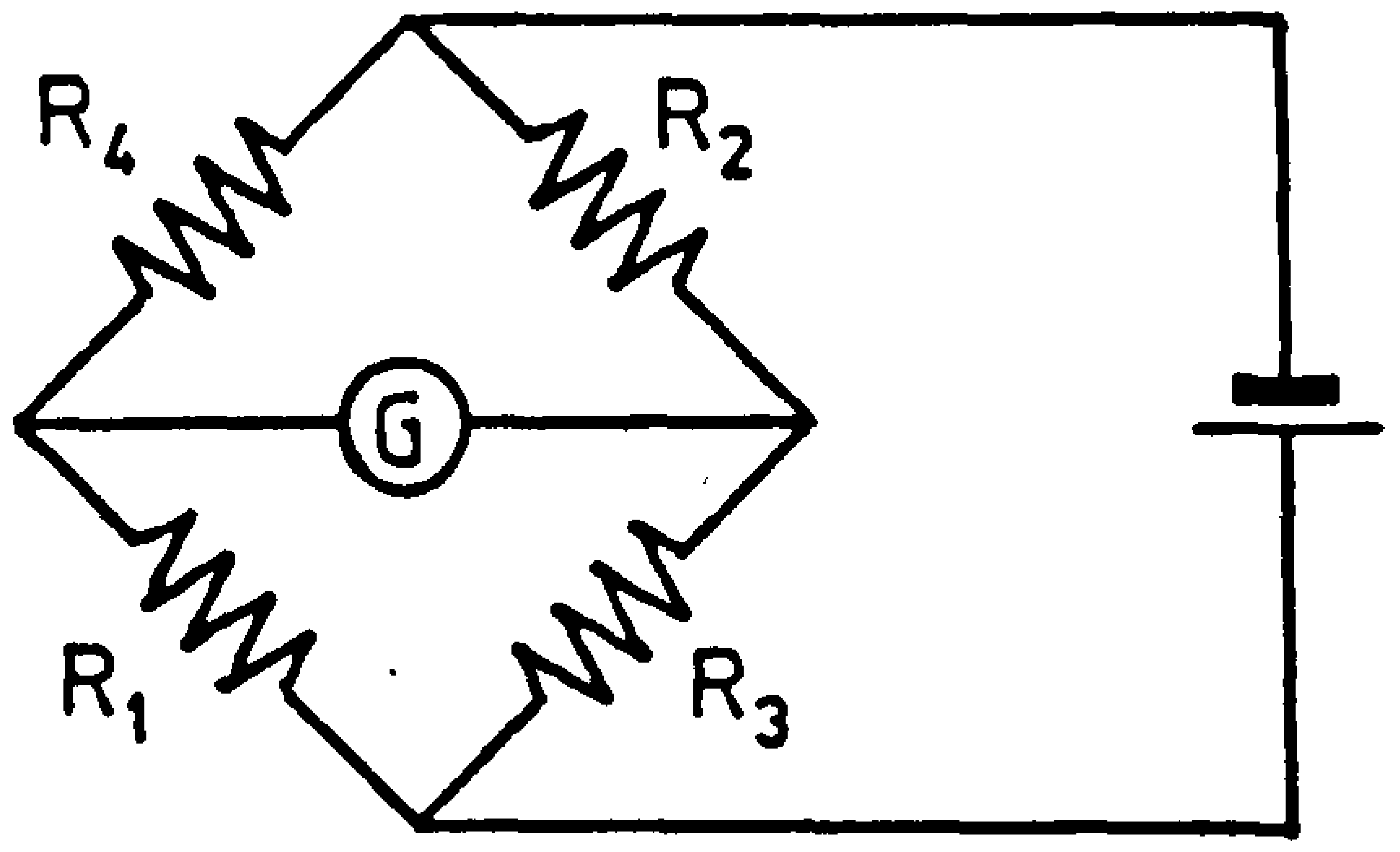

Fig. 3.9 Arrangement of wheatstone bridge on spring contilevers of three component balance

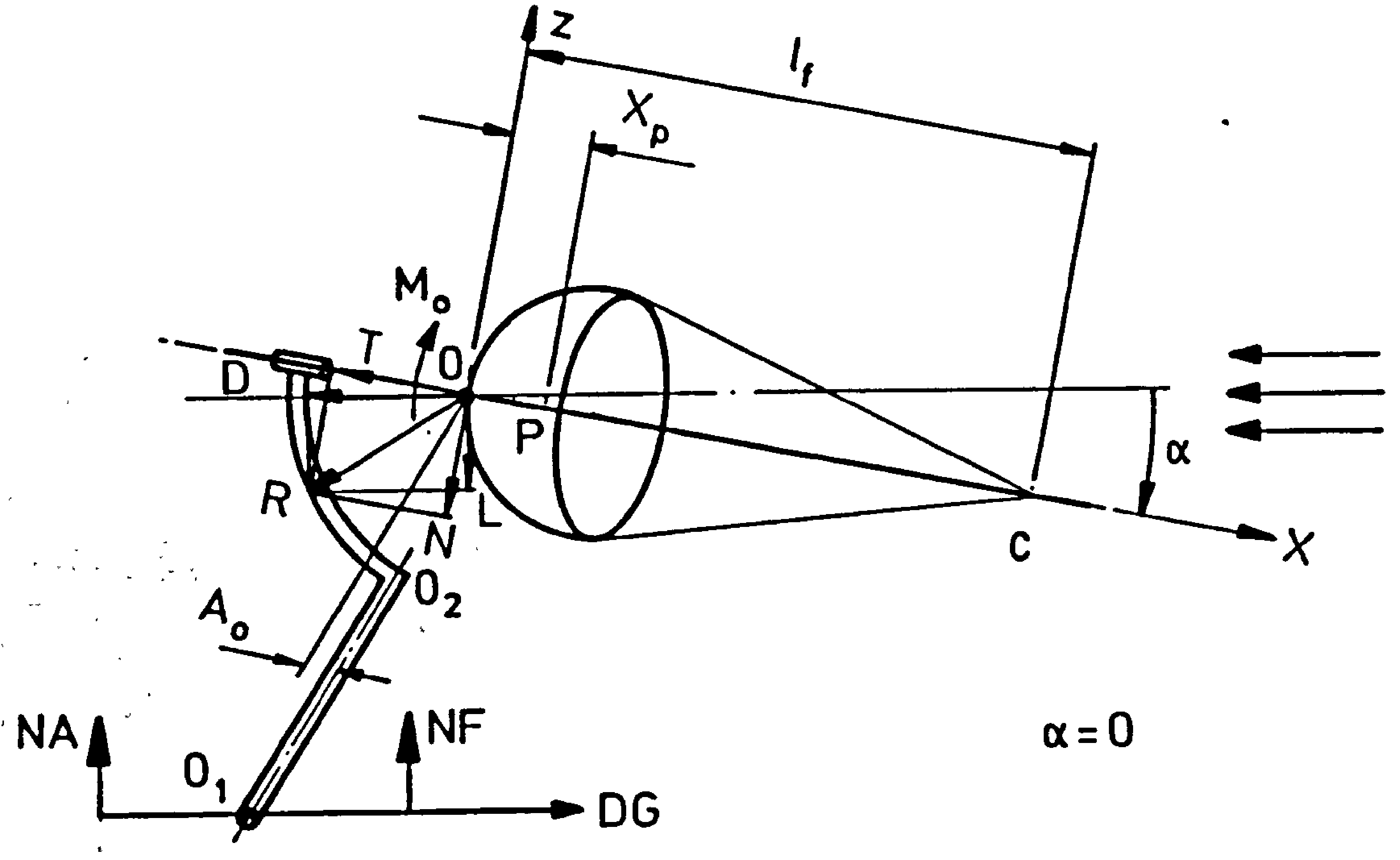

Fig. 3.10 Force diagram in wind tunnel test

Fig. 3.11 Towing Carriage Travels along the Ship Tank

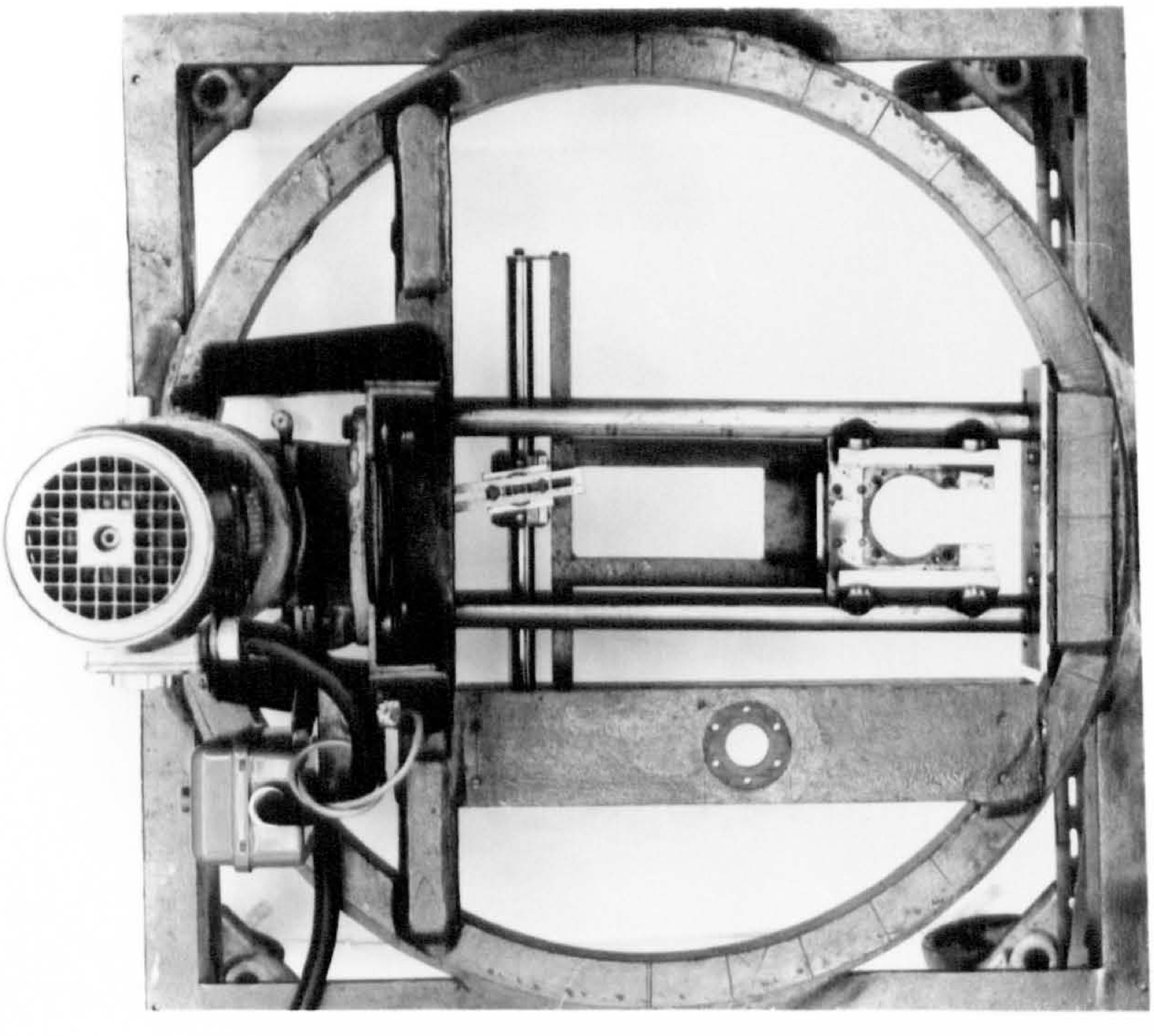

Fig. 3.12 Circular Turnable Device on a Square Support Frame

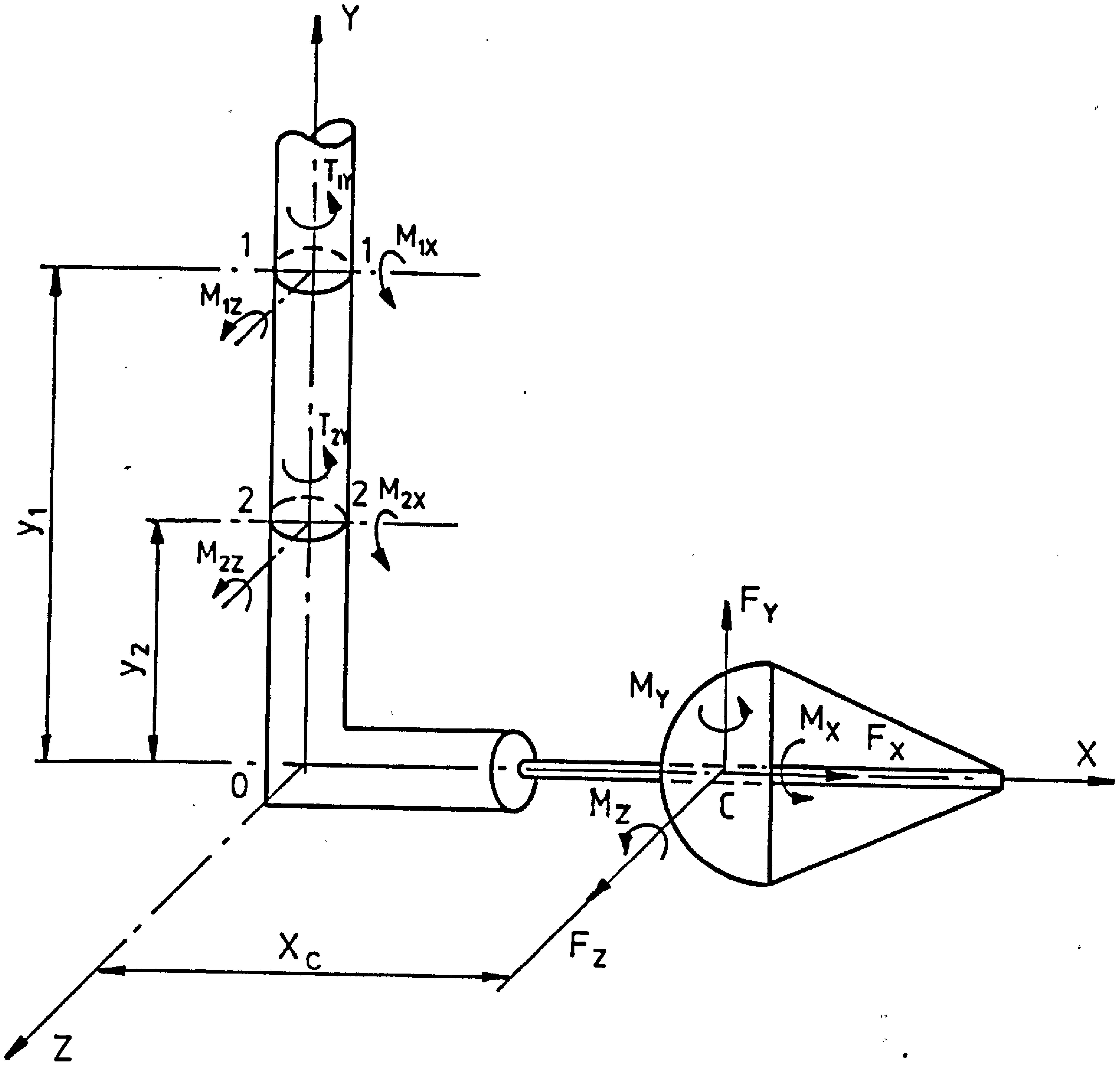

Fig. 3.13 Force diagram in ship tank test

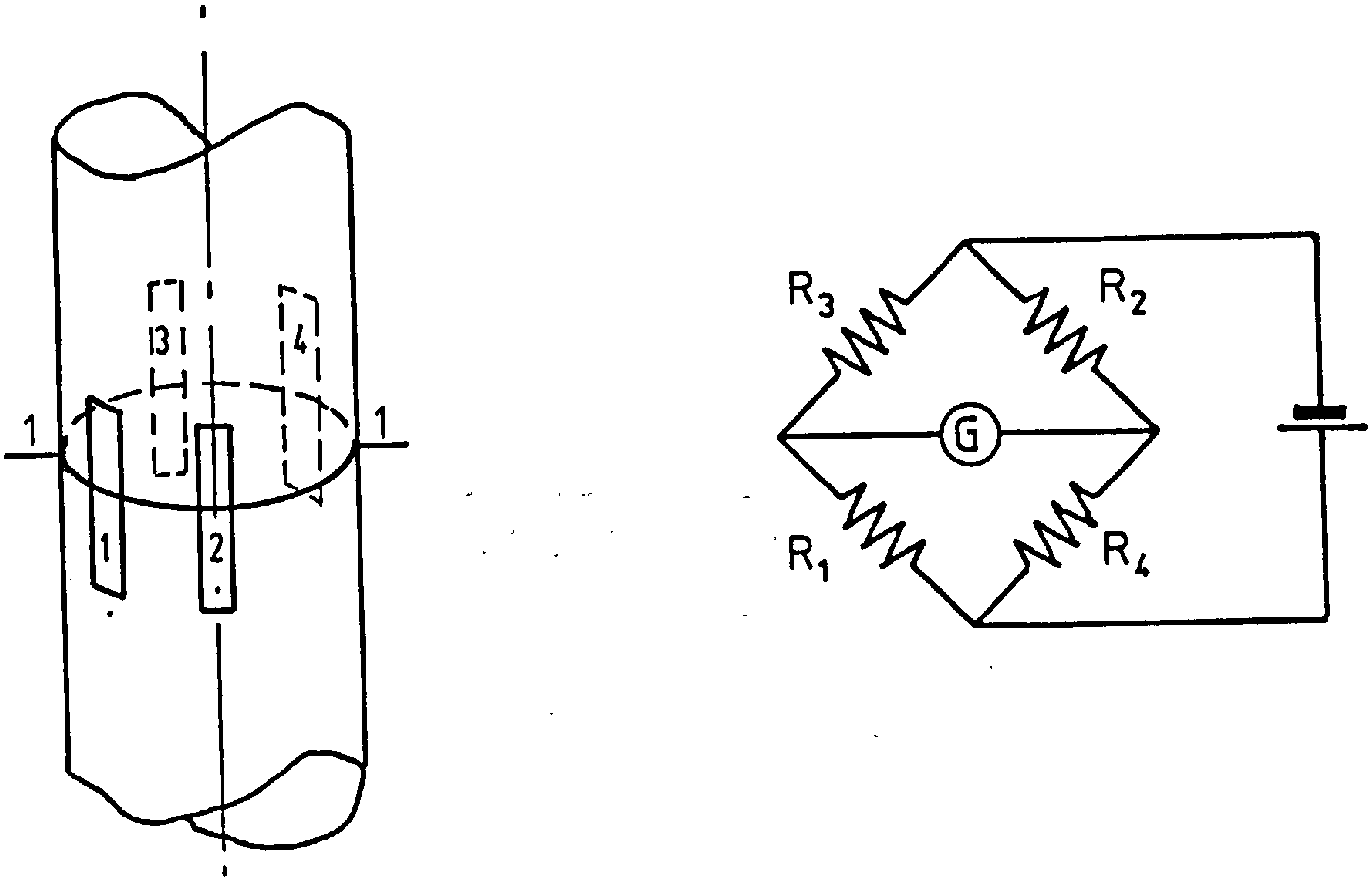

Fig. 3.14 Wheatstone bridge arrangement of strain gauges for sting bending moment measurements

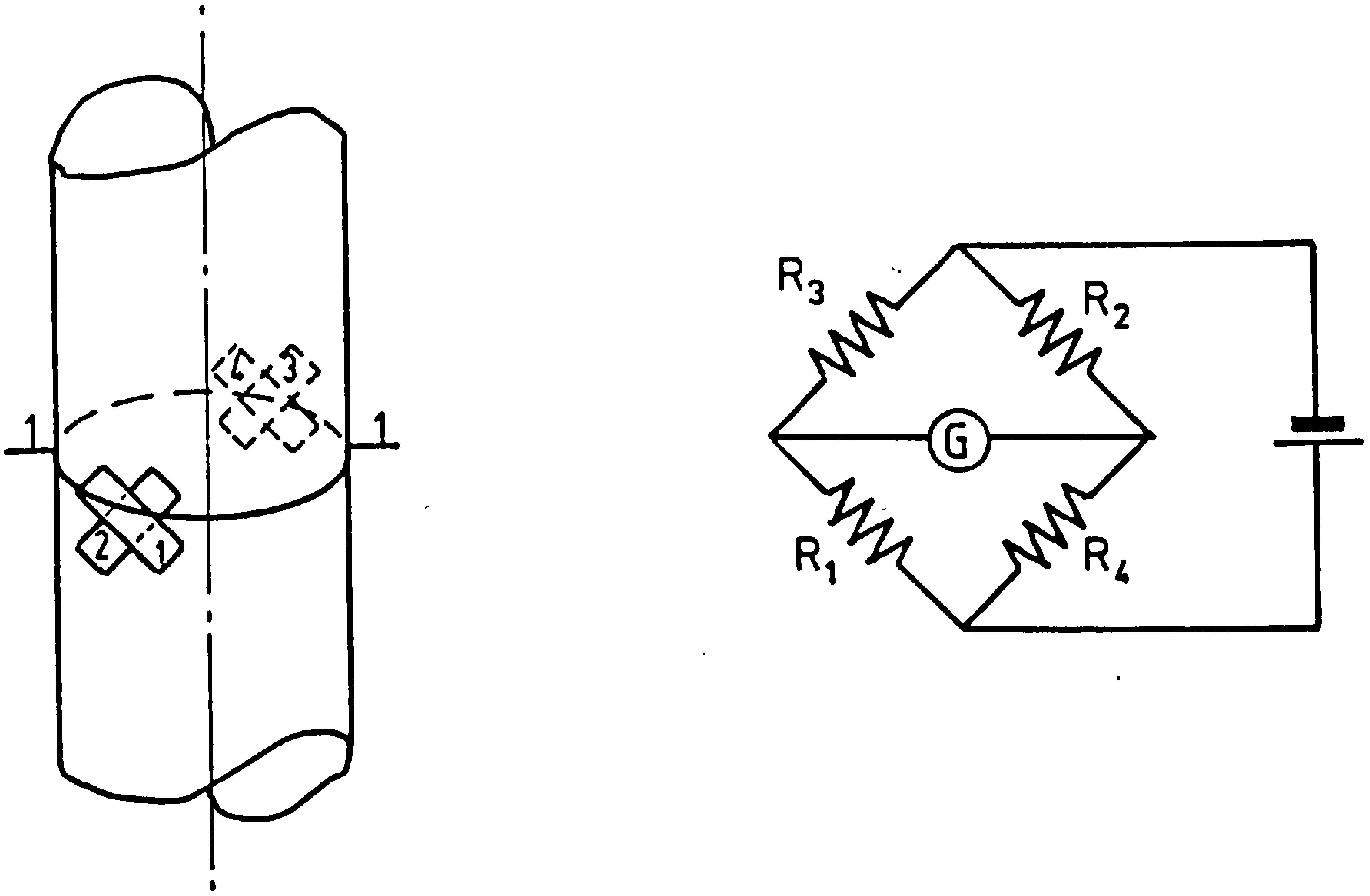

Fig. 3.15 Wheatstone bridge arrangement of strain gauges for sting torsional moment measurements

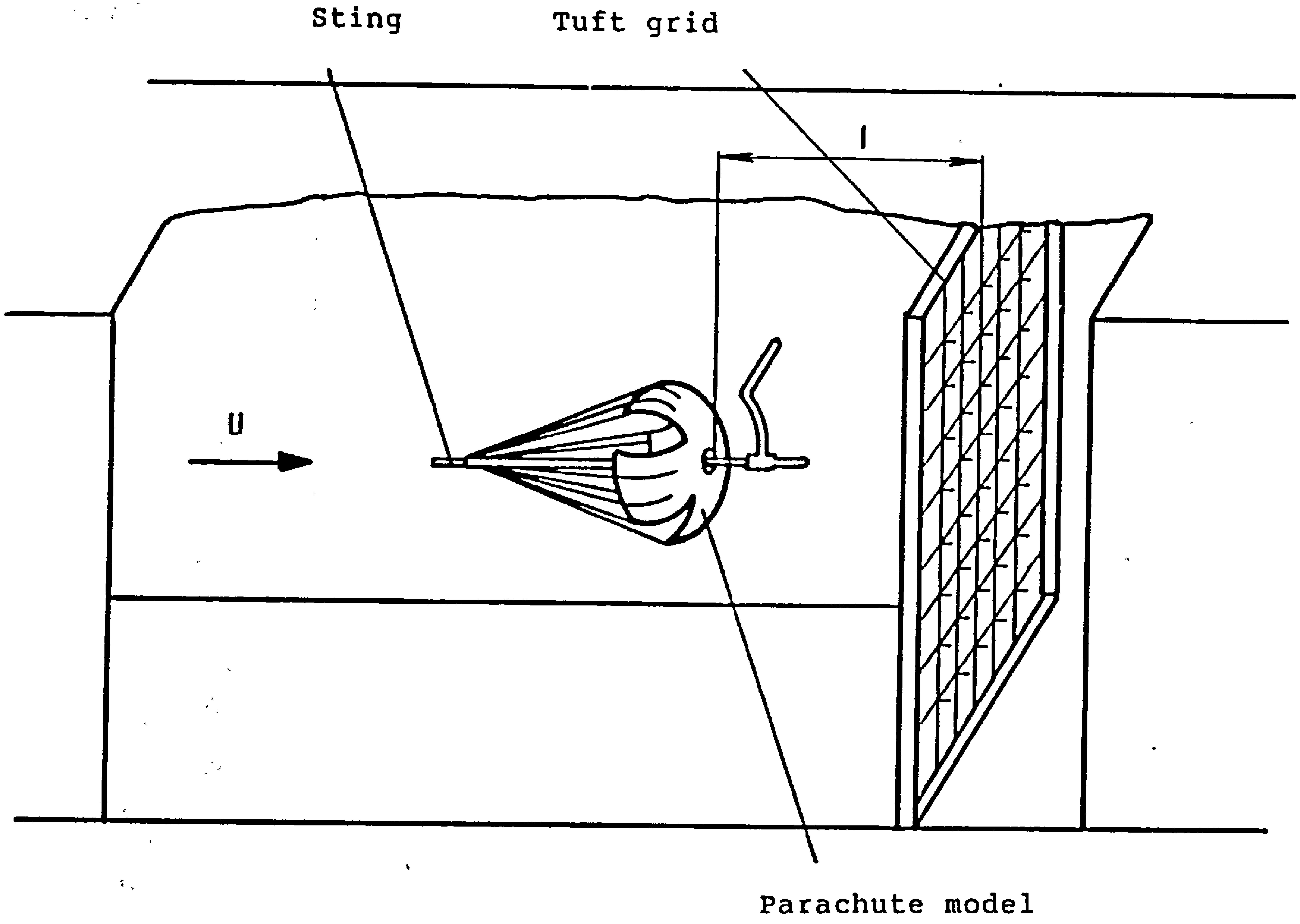

Fig. 3.16 Experimental arrangement for Wool-tuft visualisation

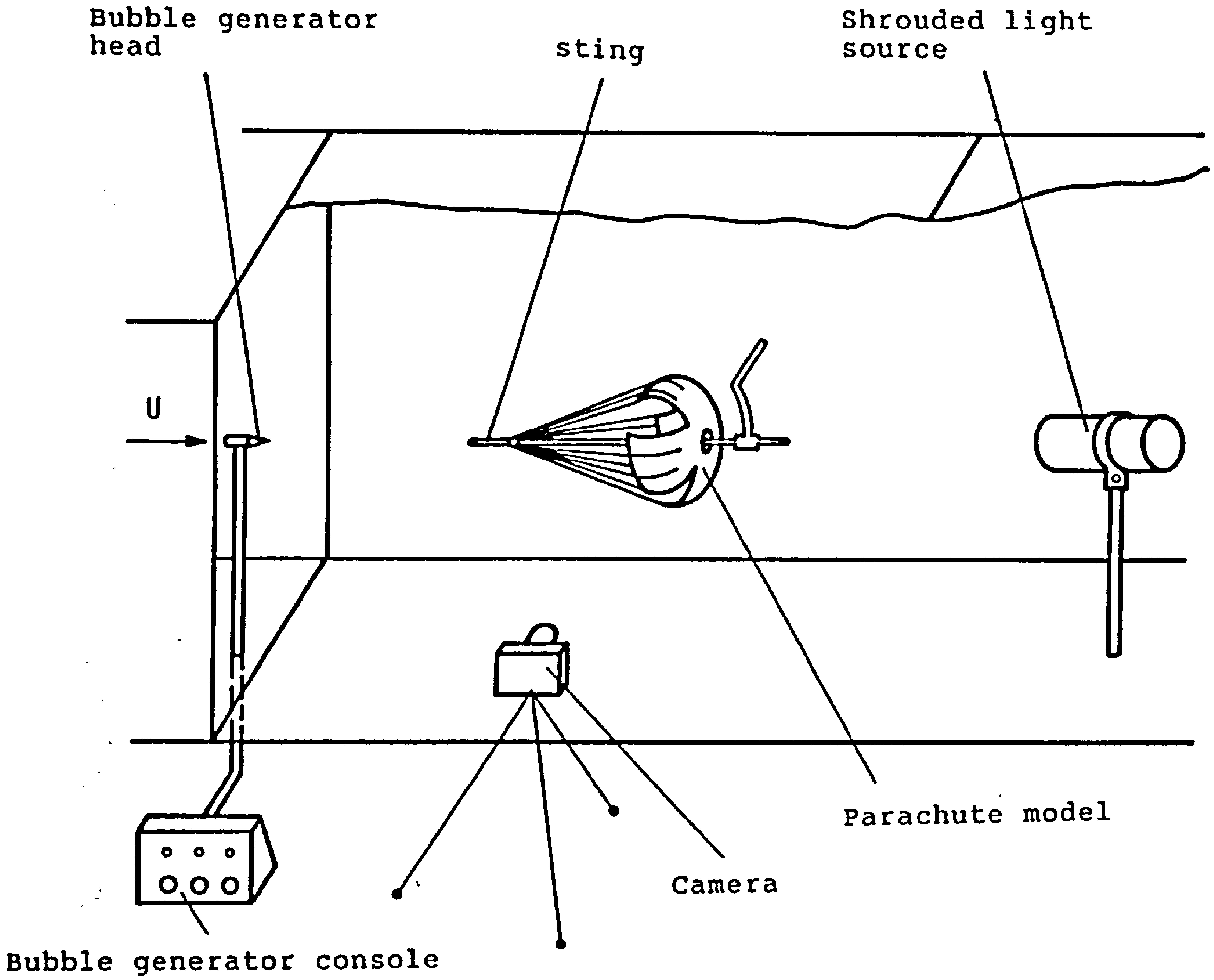

Fig. 3.17 Experimental arrangement for helium bubble visualisation

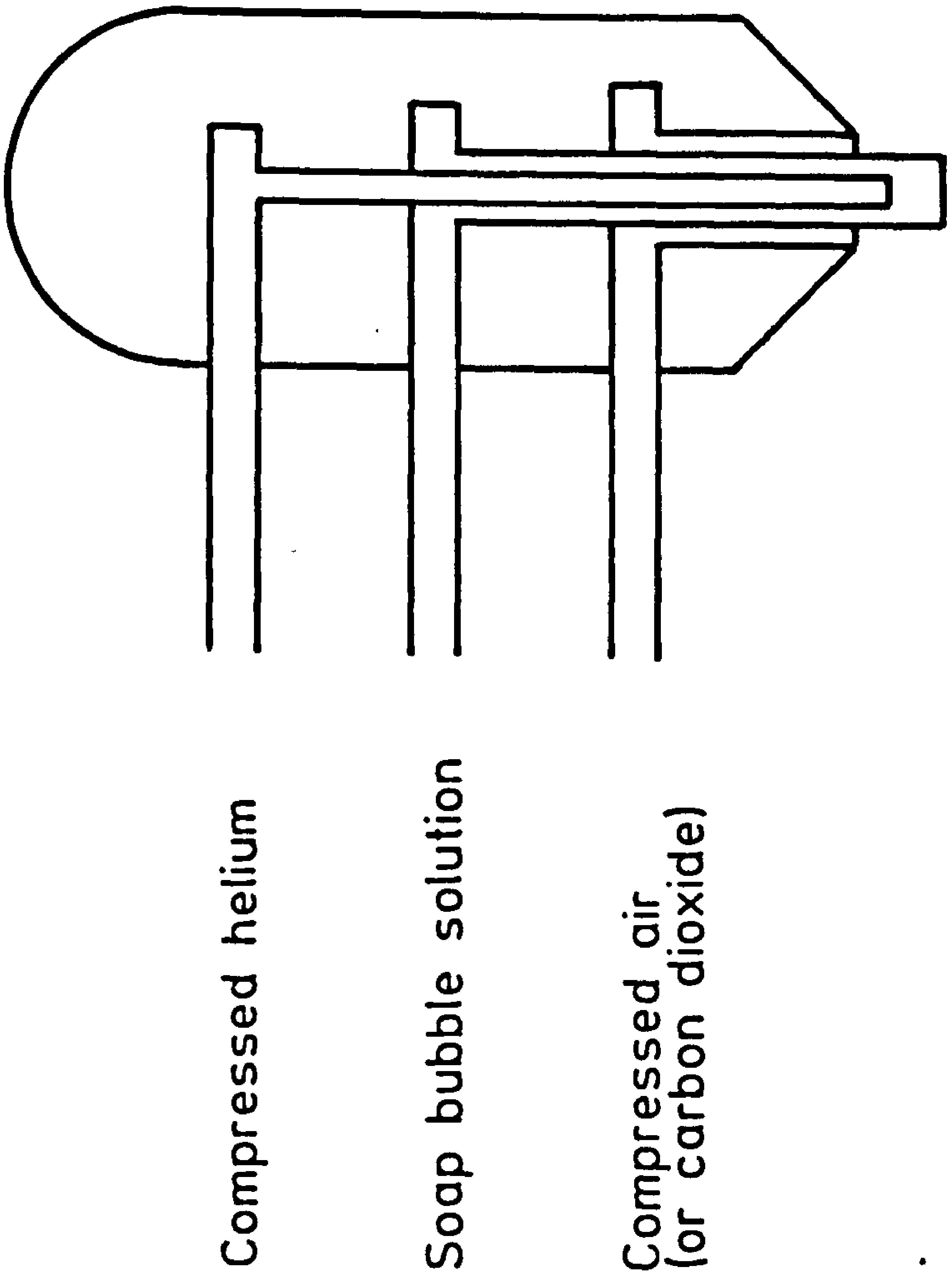

Fig. 3.18 Schematic diagram of bubble generator head

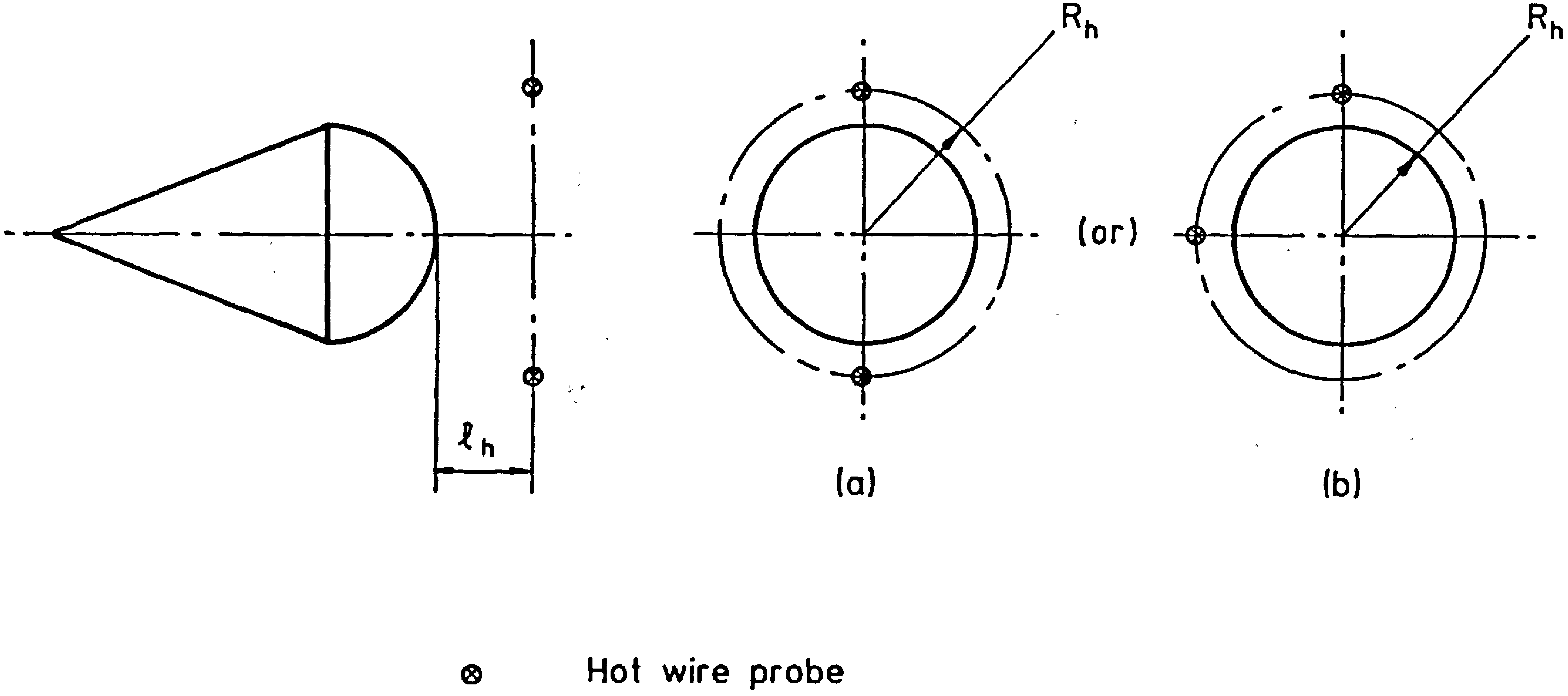

Fig. 3.19 The schematic arrangement of hot wire probe
(a) 180° apart between two hot wire probes
(b) 90° apart between two hot wire probes

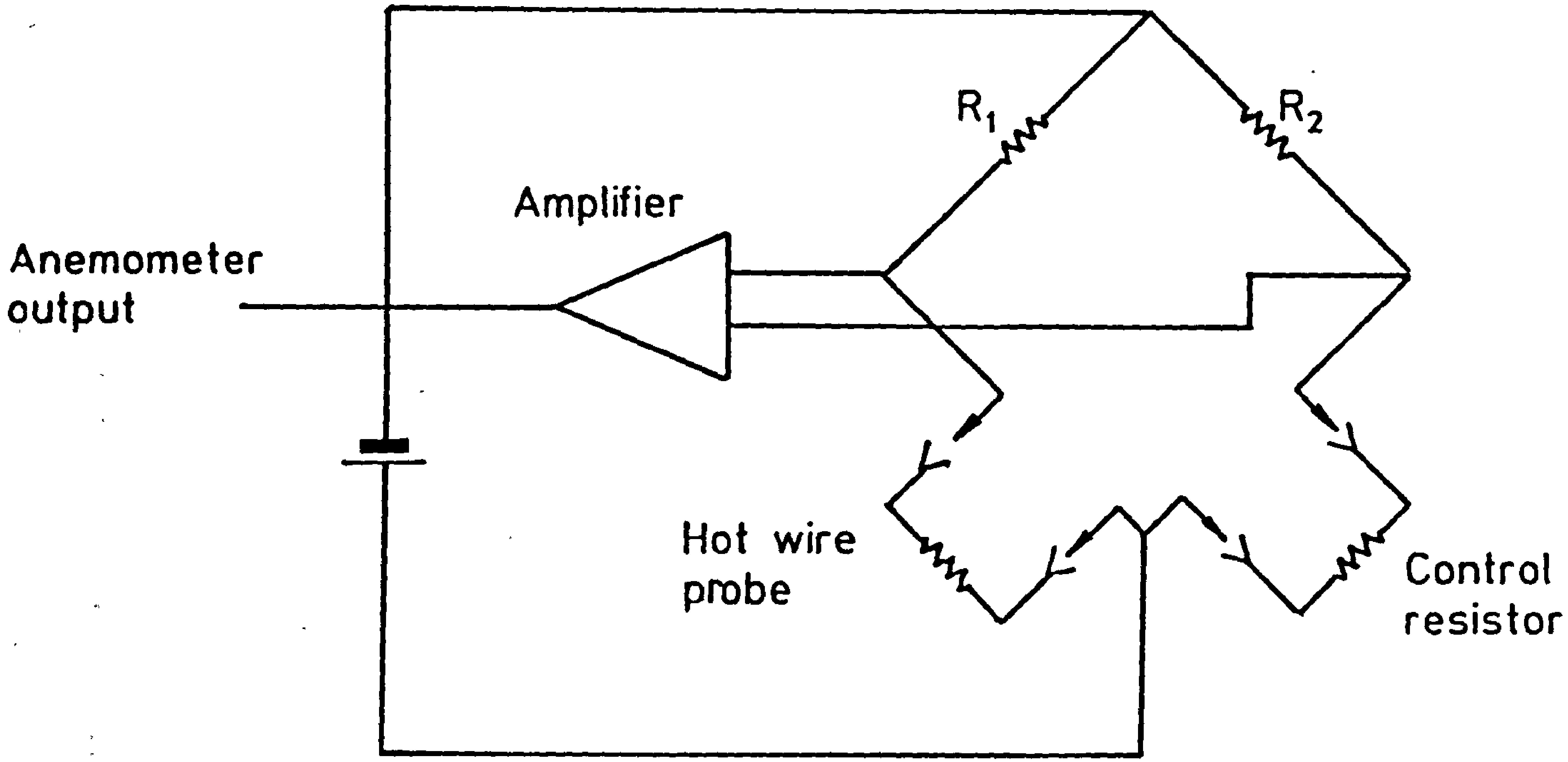

Fig. 3.20 Hot wire anemometer function schematic

4 RESULTS OBTAINED AND THEIR INTERPRETATION

4.1 Main Aerodynamic Behaviour from the Force Measurements

Measurements of the aerodynamic forces developed on all twenty-seven cross parachute canopies and three hemispherical canopies were obtained from tests conducted in the wind tunnel. At the beginning of each run the angle of attack was made equal to zero, then successively increased by five degree (or sometimes smaller) increments, moving the dial of the balance (see Fig.3.6 and Fig.3.8) until the highest positive angle of attack was achieved which would still permit the parachute to inflate properly. The angle of attack was then successively decreased to the corresponding highest negative angle of attack, then it was increased again back to zero degrees.

The aerodynamic force measurements made in the ship tank were investigated on four different cross parachute models. The first of them was imporous, having arm ratio of 4:1. The remaining three were of 3:1 arm ratio, having nominal porosities in air of 0, 13, and 23 cu.ft/sq.ft/sec. The range of angles of attack tested were between -10 degrees and +10 degrees, at five degree increments.

Values for the tangential force coefficients at zero angle of attack C_{T0}; the statically stable equilibrium angle of attack α_{eq} at which the canopies are both in equilibrium and are statically stable; the maximum angle of attack α_c at which the canopies can inflate properly without collapse; together with the sign of the change of the pitching moment coefficient about the suspension line confluence point C with the angle of attack, $dC_{MC}/d\alpha$, at zero angle of attack both in wind tunnel and ship tank; are all listed in Table 4.1. The total results for force measurements of cross parachute canopies in the wind tunnel are given in the Appendix C (Table C.1 to Table C.30). On none of the values listed and plotted later have blockage corrections been applied.

4.2 Blockage Effects

The blockage area ratio, or blockage factor, which is the ratio of canopy projected area to cross-sectional area of the wind tunnel or ship tank test facility, was between 6% and 8% in the wind tunnel. This is a significant blockage constraint. Cockrell[1.1] shows the necessity for the correction of blockage constraint when considering the drag coefficient of parachute canopies, giving Maskell's method for acceptable corrections. Maskell's correction can be expressed as

$$\frac{\Delta C_D}{C_D} = -2.77 C_D \frac{S_p}{S}$$

where S_p — the projected area of test body.

S — the cross-sectional area of the fluid stream.

Since the blockage factors obtained in the ship tank tests were only 1%, any differences obtained between the results in the wind tunnel and in the ship tank, other than those arising from canopy porosity, can be assumed to be caused by blockage in the wind tunnel. The recalculated values using the data obtained from the wind tunnel corrected for blockage by Maskell's method and listed in Table 4.2 are of very similar magnitude to the data obtained from the ship tank tests, though they overestimate the blockage correction required for the 4:1 arm ratio cross canopy, which has the largest projected area. This indicates that for blockage area ratios of less than 8%, Maskell's correction appears to be acceptable.

4.3 Effect of Canopy Characteristics on the Tangential Force Coefficient

4.3.1 Tangential Force Coefficients are Basically Dependent on the Geometrical Structure of Canopies

As shown in Table 4.1, different geometrical shapes, e.g. hemispherical and cross-shaped parachute canopies, certainly possess different tangential force coefficients C_T. The same basic shape of canopy but with different geometrical characteristics, such as arm ratio or geometric porosity formed by some open area on the canopy surface, can also result in different values of C_T. Fig.4.1 to Fig.4.3 indicate that the tangential force coefficient at zero angle of attack C_{T0} increases as the canopy arm ratio increases from 2.4:1 to 4:1. Table A.1 shows that with the increase in arm ratio there is also an increase in the canopy projected area S_p for a constant nominal surface area S_0. This is the primary cause of the drag increase; the secondary one, which can be seen by flow visualisation, is that the wake is widened by the air flow through the gaps between the canopy arms. This is shown in Fig.4.4 and is discussed in detail in Chapter 5.

Clearly, cross-shaped canopies having high arm ratios are effective drag producers, but they do have a disadvantage. They tend to collapse at lower angles of attack than do smaller arm ratio cross canopies and this is shown in Table 4.1. That is the reason why in Fig.4.1 to Fig.4.3 for a canopy having an arm ratio 4:1 C_T decreases more rapidly with increasing angle of attack than it does for a cross-shaped canopy with a smaller arm ratio. Table 4.1 and Fig.4.5 and Fig.4.6 also show that among all the cross parachute canopies tested the largest value of C_{T0} was developed by an imporous cross parachute with an arm ratio R_A of 4:1 and a suspension line ratio R_S of 2:1. In contrast, the smallest value of C_{T0} was developed by a highly porous parachute which also had an arm ratio R_A of 4:1 but which had a suspension line ratio R_S of 0.67:1. High values of porosity and large gaps between the arms of cross parachute canopies cause poor inflation characteristics.

Fig.4.7 shows the tangential force coefficient for a rigid hemispherical parachute canopy with geometric porosity equal to 12% is lower than that without porosity. The tangential force coefficient at zero angle of attack C_{T0} for a flexible imporous hemispherical parachute canopy differs only marginally from that developed on the rigid hemispherical canopy model.

4.3.2 The Effects of Canopy Fabric Porosity on Tangential Force Coefficient

Experimental results indicate that as the porosity of a fabric canopy increases then C_{T0} is reduced accordingly. These are shown in Fig.4.8 to Fig.4.10. This observed result differs from one reported in 1981 by Jorgensen[1.26]. Figs.4.5 and 4.6 show that for very porous cross-shaped canopies fabric porosity plays a more significant role in determining the magnitude of the tangential force characteristics than the variation of arm ratio. The flow visualisation studies shown in Figs.4.11 and 4.12, which will be discussed in more detail in chapter 5, indicate that this consequence of canopy porosity is caused by flow variation occurring around the canopy.

4.3.3 Other Tangential Force Characteristics

From Figs.4.13 to 4.18 it is seen that the tangential force coefficient increases as the suspension line ratio is made larger. Observations show that the canopy projected area increases with the suspension line ratio and this is the reason for the increase in tangential force coefficient. However, the figures make clear that this increase is less marked when the suspension line ratio exceeds 2:1.

Over the Reynolds numbers from 1.0×10^5 to 5.0×10^5 Fig.4.19 indicates that for cross-shaped canopies the measured tangential force coefficient increases by less than 10%. From results obtained by Ludtke[4.1] on full-scale parachute canopies it is apparent that Reynolds numbers effects are even less significant at higher Reynolds numbers. For any shape of full-scale parachute canopies at Reynolds numbers which are above 10^6 the Reynolds number variation is considered to have a negligible effect on the values of the tangential force coefficient or the drag coefficient. Although there are hardly any experimental data to show the variation of other force coefficients (e.g. C_N; C_L) with Reynolds numbers above 10^6 little variation in these characteristics would be anticipated.

Structural non-uniformities which occur, such as lack of suspension line symmetry, can cause any parachute canopy with a symmetrical configuration to rotate about its axis of symmetry. Cross parachute canopies, having four large air gaps formed between their arms, will very readily rotate. The results of tangential force measurement for a model with and without rotation are shown in Fig.4.20. They indicate that when cross parachute canopies rotate their tangential force coefficients are only marginally higher than when there is no rotation. From the flow visualisation shown in Fig.4.21 it is difficult to see any significant change in the flow characteristics caused by rotation.

4.4 Effects of Canopy Characteristics on Parachute Stability in Pitch

As discussed in section 3.2, two parameters which describe parachute static stability characteristics in pitch are $dC_N/d\alpha$ (or $dC_{Mc}/d\alpha$) at zero angle of attack, and the statically-stable equilibrium angle of attack α_{eq}. They are strongly dependent on both the parachute geometrical structure for example, arm ratio, and the fabric and geometric porosity. Relevant relationships are shown in Figs.4.22 to 4.36. The arm ratio and the canopy porosity determine the ability of the air to pass through the canopy, from the under to the upper side and this is discussed in chapter 5.

The statically stable equilibrium angles of attack are shown in Figs.4.22 and 4.23 to be functions of both the canopy arm ratio R_A and its porosity λ. An inspection of Figs.4.24 to 4.29 shows that $dC_N/d\alpha$ at $\alpha=0$ becomes increasingly positive, hence the static stability is increased as either the arm ratio or the porosity is made larger, In these figures sudden changes in the sign of $dC_N/d\alpha$ can be seen, when a stable canopy becomes an unstable canopy. Sometimes a small variation of fabric porosity can have dramatic effect on a parachute's static stability and this had been discussed elsewhere by Shen and Cockrell[4.2]. If a parachute canopy is not strongly statically stable in pitch, e.g. a 3:1 arm ratio cross parachute with an effective porosity of 6%, the magnitude of $[dC_N/d\alpha]_{\alpha=0}$ can qualitatively be influenced by the test medium, as shown in Fig.4.37. In air flow, canopy (a) is of negligible porosity, canopy (b) is of medium porosity and canopy (c) is very porous. Whether measured in air or in water the characteristics of canopy (a) demonstrate static instability in pitch. Correspondingly, both in air and in water canopy (c) exhibits static stability. However, canopy (b) exhibits static stability in air but static instability in water. The reason for this variation in static stability is that the effective porosity of a canopy, that is the ratio of the average velocity through the canopy to the free stream velocity related to the canopy is different in water from what it is in air and this difference will be further discussed in chapter 5.

The variation of suspension line length clearly affects the tangential aerodynamic component force but, as Figs.4.38 to 4.40 show, it has little effect on the static stability in pitch.

Canopy rotation caused by constructional unsymmetries while marginally increasing the parachute drag, does not change the static stability characteristics, as Fig.4.41 shows.

Although the static instability of hemispherical parachute canopies can be reduced by increasing their porosity, it is clear from Table 4.3 that their static stability at zero angle of attack can not be achieved. Cross parachute canopies with arm ratios that are greater than 3:1 however, combine the stabilising effects which follow from the high rate of flow between the arms with relatively high drag characteristics, so they are widely adopted.

4.5 Periodic Phenomena in the Wake

4.5.1 Results Obtained from Flow Visualisation

Flow visualisation studies were made on nine cross parachute models having different fabric porosity λ and arm ratios but with the same suspension line ratio R_s of 1.33:1. Hemispherical parachute canopy models with different geometrical porosity were also used. First will be described the physical reasons why the aerodynamic characteristics of canopy change with its structural parameters as a consequence of the flow field variations. The observed width of the wake behind a rigid imporous hemispherical parachute canopy is about twice its projected diameter, reducing in width as the porosity increases. The width of wake behind a flexible relatively imporous hemispherical canopy is some 1.7 canopy projected diameters, rather less than that behind the rigid canopy. This reduction occurs because the canopy is flexible and therefore its inflated shape is never exactly hemispherical. The drag of these canopies is clearly related to their wake width. Further, the pattern of flow around stable and instable canopies differs and this will be discussed in chapter 5.

Secondly, flow visualisation also indicates that periodic phenomena occur in the wake formed behind parachute canopies and this is shown in Fig.4.42. Both the periodicity and the velocity with which vortices move in the wake can be determined from cine film and then converted to Strouhal numbers and average velocity ratios U/U_∞, as listed in Table 4.4. The wake formed behind the rigid and imporous hemispherical canopy appears to be the most strongly periodic. Periodic characteristics presented in the wakes formed behind an imporous cross-shaped canopy of arm ratio

4:1 and a porous cross-shaped canopy of arm ratio 3:1 are not sufficiently clear for their frequencies to be determined, though periodic motion can be observed hidden in the large eddy structure which is caused by the flow through the gaps between the canopy arms.

The wool tufts visualisation shown in Fig.4.43 was obtained using a motor-driven camera. It reveals that the wakes formed behind symmetrical parachute canopies are not themselves symmetrical. Vortex loops present in the wake appear to be randomly orientated.

4.5.2 Results Obtained from Hot-Wire Measurements

An inspection of periodic phenomena observed in the wakes formed behind various parachute canopies indicate that they are basically similar, whether the canopies are flexible or rigid. When flexible and very porous canopy are selected it can become difficult to observe any periodic nature in the flow as has already been stated for cross-shaped canopies.

In order to study the formation and structure of the wakes formed behind parachute canopies, extensive velocity fluctuation measurements were made behind a rigid parachute canopy having a diameter of 0.153 m. Two hot wire sensors were set in the wake behind this canopy, either 90^o apart or 180^o apart, as shown in Fig.3.19. The two signals from the hot-wire anemometers were simultaneously recorded and correlated, using the Fast Fourier Transform Analyser. From this statistical analysis, made at test Reynolds numbers ranging between 3 x 10^4 and 2.0 x 10^5, everywhere in the wake periodic phenomena could be seen except exactly on the axis of symmetry. These phenomena extended for a radial distance of some two projected canopy diameters.

The method of analysis is as follows. If the two signals from the hot-wire anemometers are x(t) and y(t), the power spectral density function describes the distribution of energy over the total frequency range and within a frequency band Δf, expressed as follows.

$$G_x(f) = \lim_{\Delta f \to \infty} \lim_{T \to \infty} \frac{1}{T\Delta f} \int_0^T x^2(t,f,\Delta f)dt$$

$$G_y(f) = \lim_{\Delta f \to \infty} \lim_{T \to \infty} \frac{1}{T\Delta f} \int_0^T y^2(t,f,\Delta f)dt$$

i.e. the mean square value within a frequency band Δf over the total frequency range.

Spectra measured indicate that the peak frequency varies somewhat with time, as shown in Fig.4.44, but if an average is taken, consistent and repeatable results can be obtained. This average was used in the consequent calculation of Strouhal numbers. Fig.4.45 shows the average power spectra obtained for two hot wires spaced 180^o apart at a radial distance of two projected diameters and some 1.2 projected diameters downstream of the canopy skirt. Fig.4.46 is a cross-spectral density function plot. The peak frequency does not vary from place to place in the wake, and it can be observed throughout the wake, but the clearest signals are observed 1.2 to 2.0 projected diameters downstream of the canopy at a radial location of some 2.0 projected diameters. As shown in Fig.4.47, the closer measurements are made to the canopy axis of symmetry, the broader the peak becomes until on the axis the peak frequency can no longer be detected.

Waveforms of the fluctuating velocity and its auto-correlation function from two hot wires 180^{o} apart are shown in Fig.4.48 and Fig.4.49 respectively. The cross-correlation function obtained between the two signals indicates that their phase difference is approximately 180^{o}, and does not vary significantly with time. This will be discussed in chapter 5. The phase difference can also be obtained from the waveforms shown in Fig.4.48

The results obtained from the two hot wires placed 90^{o} apart in the wake indicate similar spectra and their phase difference was observed to be between 50^{o} to 150^{o}. This can also be seen from the two waveforms shown in Fig.4.50. Their cross-correlation function shown in Fig 5.4 will also be discussed in chapter 5. It seems two signals 90^{o} apart do not correlate as well as two signals 180^{o} apart.

The mean velocity distributions along the radius obtained at various distances behind the canopy skirt are shown in Fig.4.51. In this figure U is the root mean square velocity and U_{∞} is free stream velocity. Reversed velocity behind parachute was not detected.

The results of this investigation of periodic flow phenomena are in relatively good agreement with the flow visualisation studies, as is shown in Table 4.4. Some of the Strouhal numbers determined by other investigators in the wake formed by various three-dimensional bodies, together with those in the present investigation are listed in Table 4.5.

In the present study the observed Strouhal number over the Reynolds number range between 3×10^4 and 2×10^5 shown in Fig.4.52 is 0.15 with a variation of 5%. Over this range of Reynolds numbers a negligible change in Strouhal numbers occurred. The results differ from that of 0.61 observed by Jorgensen.

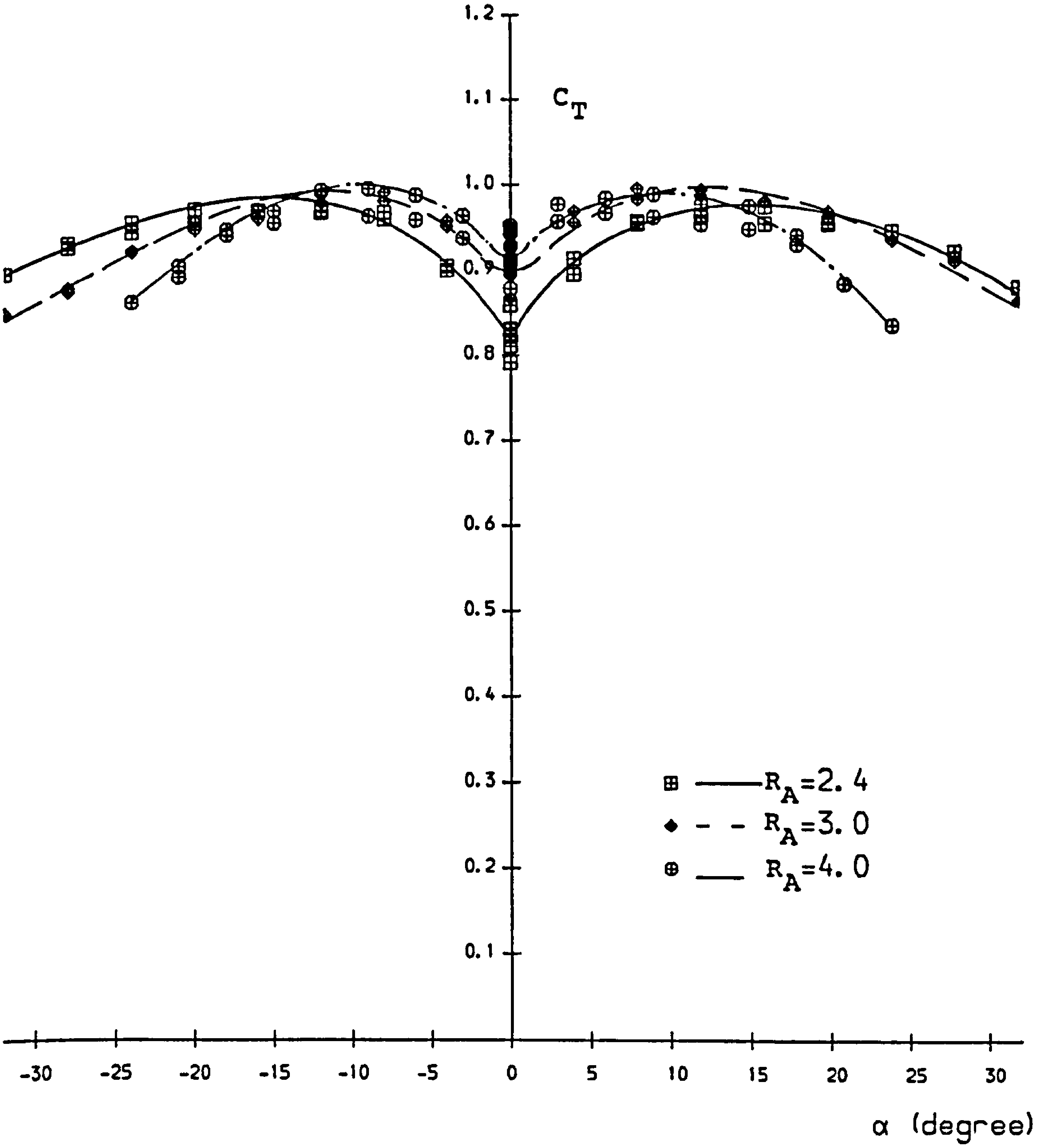

Fig. 4.1 Tangent Force Coefficient versus Angle of Attack for Various Arm Ratios R_A

Nominal Porosity (cu.ft/sq.ft/sec) $\lambda=0$

Suspension Line Ratio $R_S=1.33$

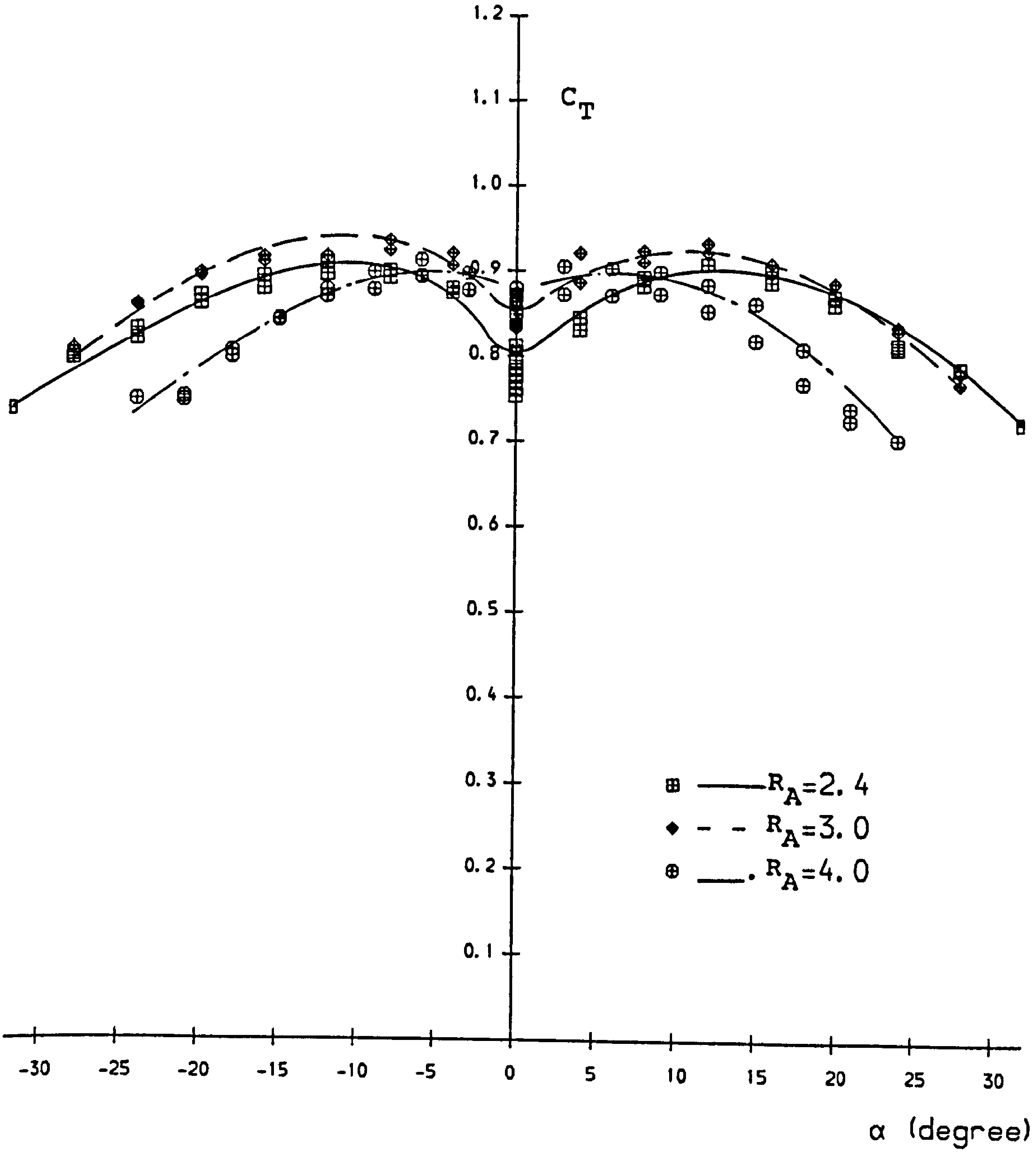

Fig. 4.2 Tangent Force Coefficient versus Angle of Attack for Various Arm Ratios R_A

Nominal Porosity (cu.ft/sq.ft/sec) λ=13
Suspension Line Ratio R_s=1.33

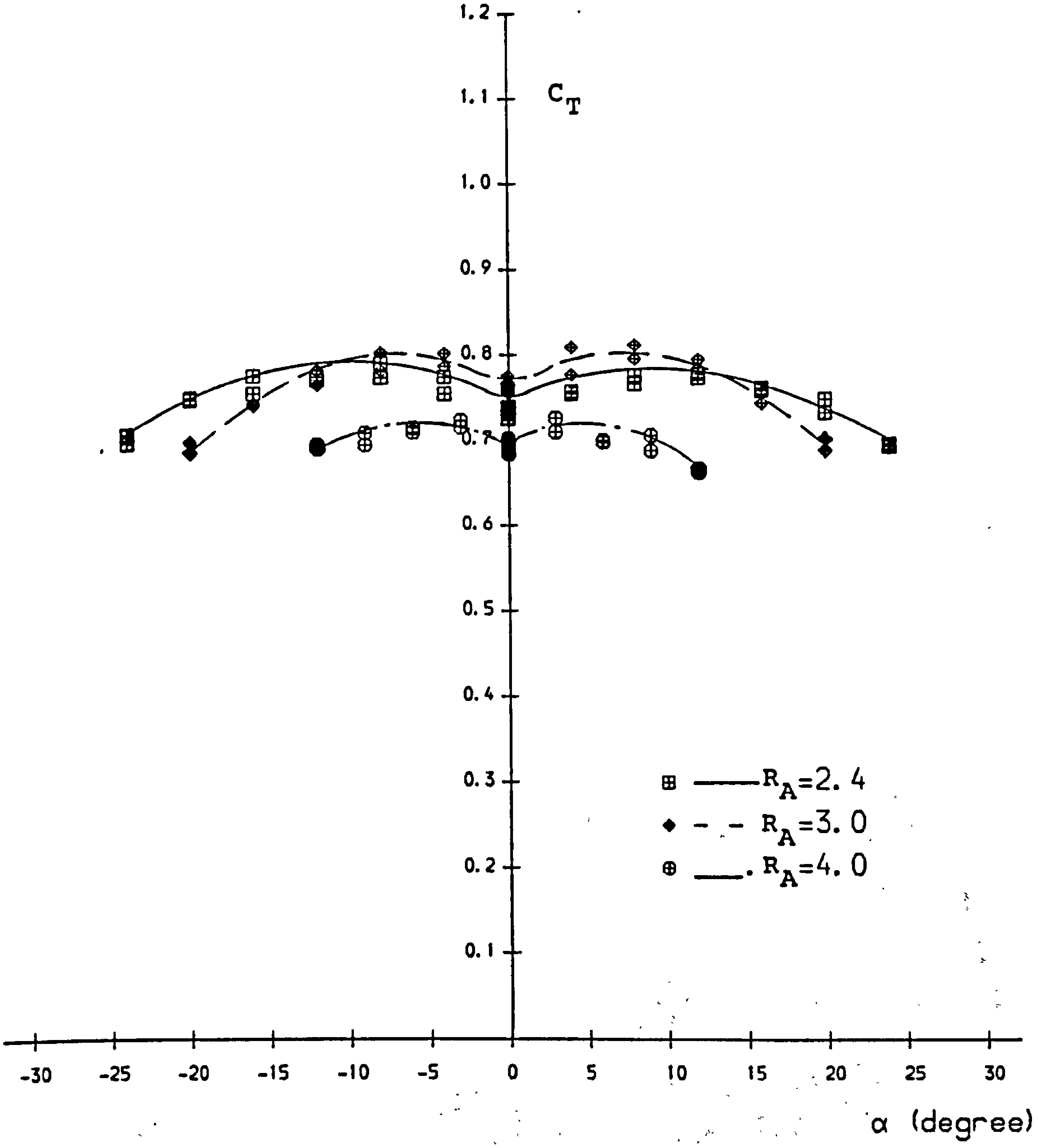

Fig. 4.3 Tangent Force Coefficient versus Angle of Attack for Various Arm Ratios R_A

Nominal Porosity (cu.ft/sq.ft/sec) $\lambda=23$
Suspension Line Ratio $R_s=1.33$

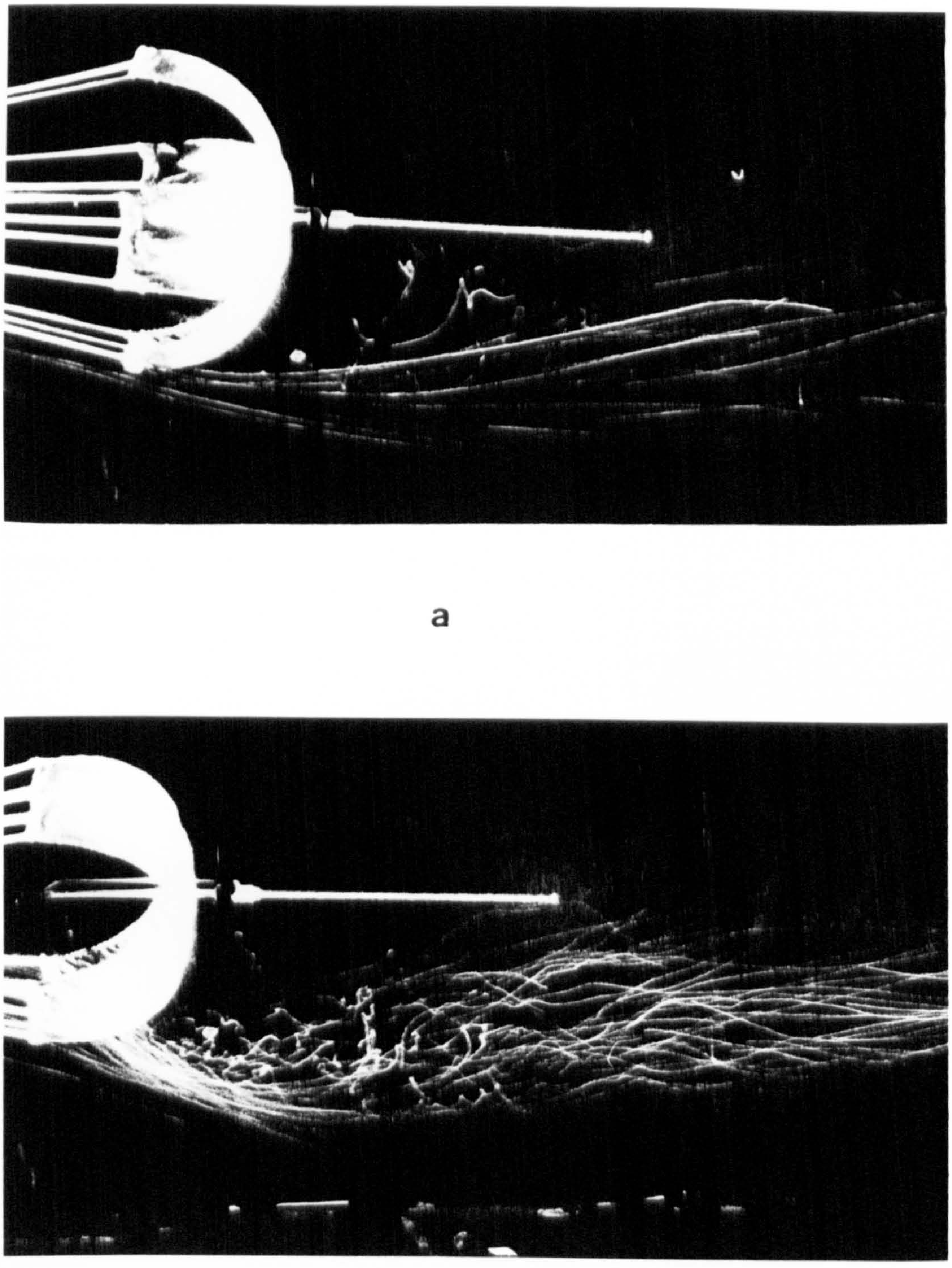

Fig. 4.4 The Flow Field around an Imporous Cross-Shaped Canopy with Arm Ratio 4:1

(a) Flow over an Arm
(b) Flow though a Gap

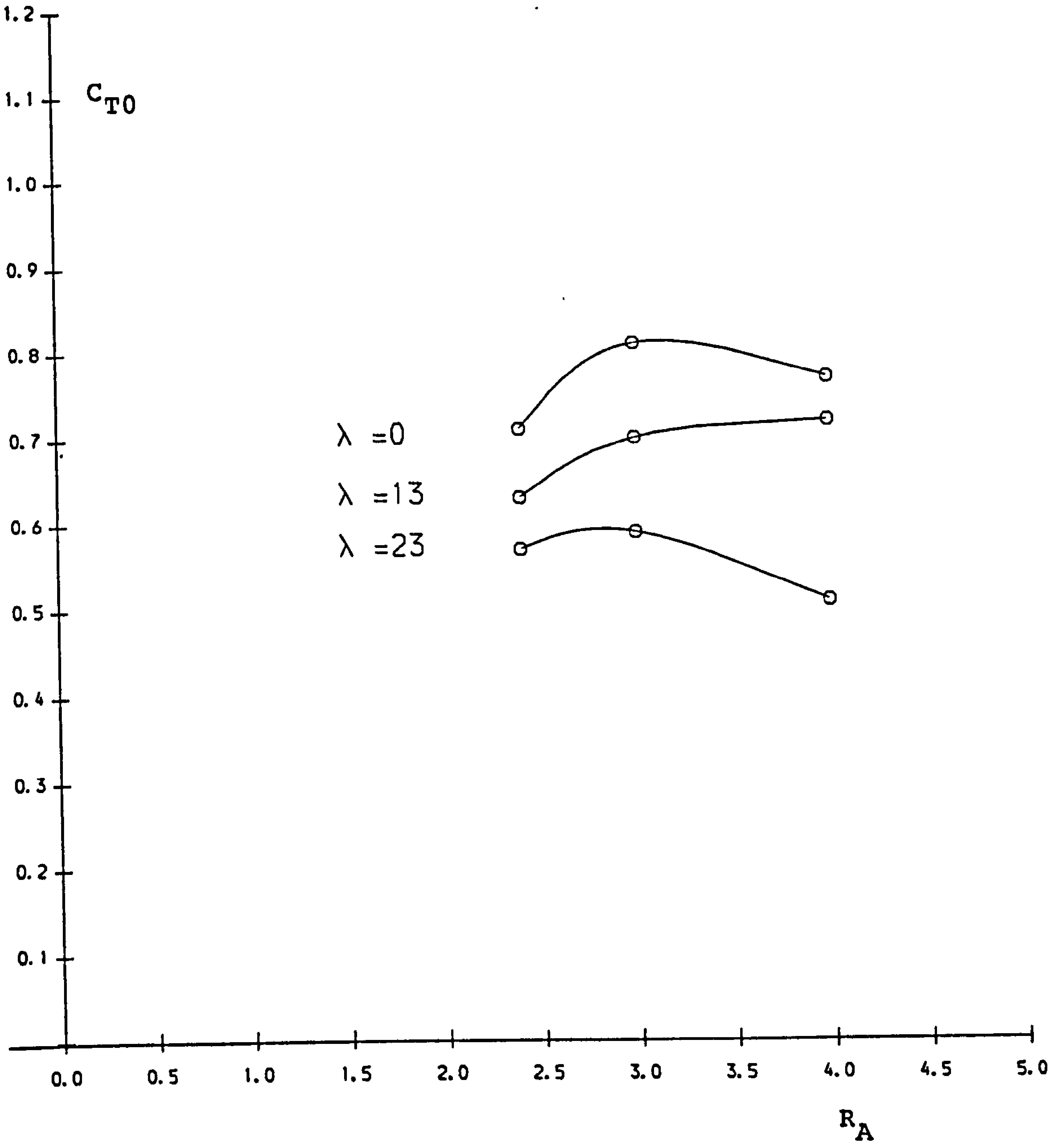

Fig. 4.5 Variation of Tangential Force Coefficient at Zero Angle of Attack C_{T0} with Arm Ratios R_A for Canopies Varying Porosities λ (cu.ft/sq.ft/sec)

Suspension Line Ratio R_s=0.667

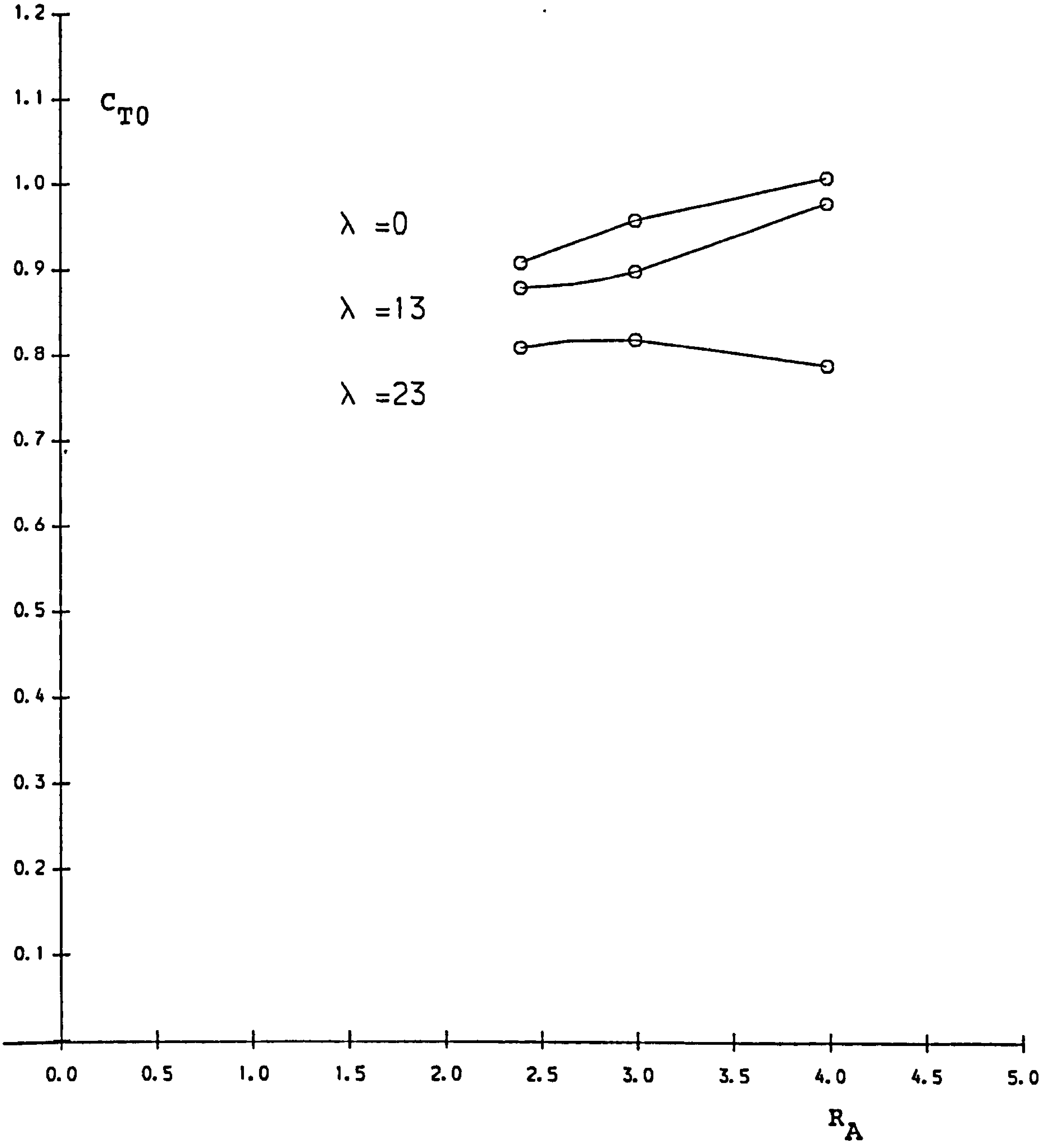

Fig. 4.6 Variation of Tangential Force Coefficient at Zero Angle of Attack C_{T0} with Arm Ratios R_A for Canopies Varying Porosities λ (cu.ft/sq.ft/sec)

Suspension Line Ratio R_s=2.0

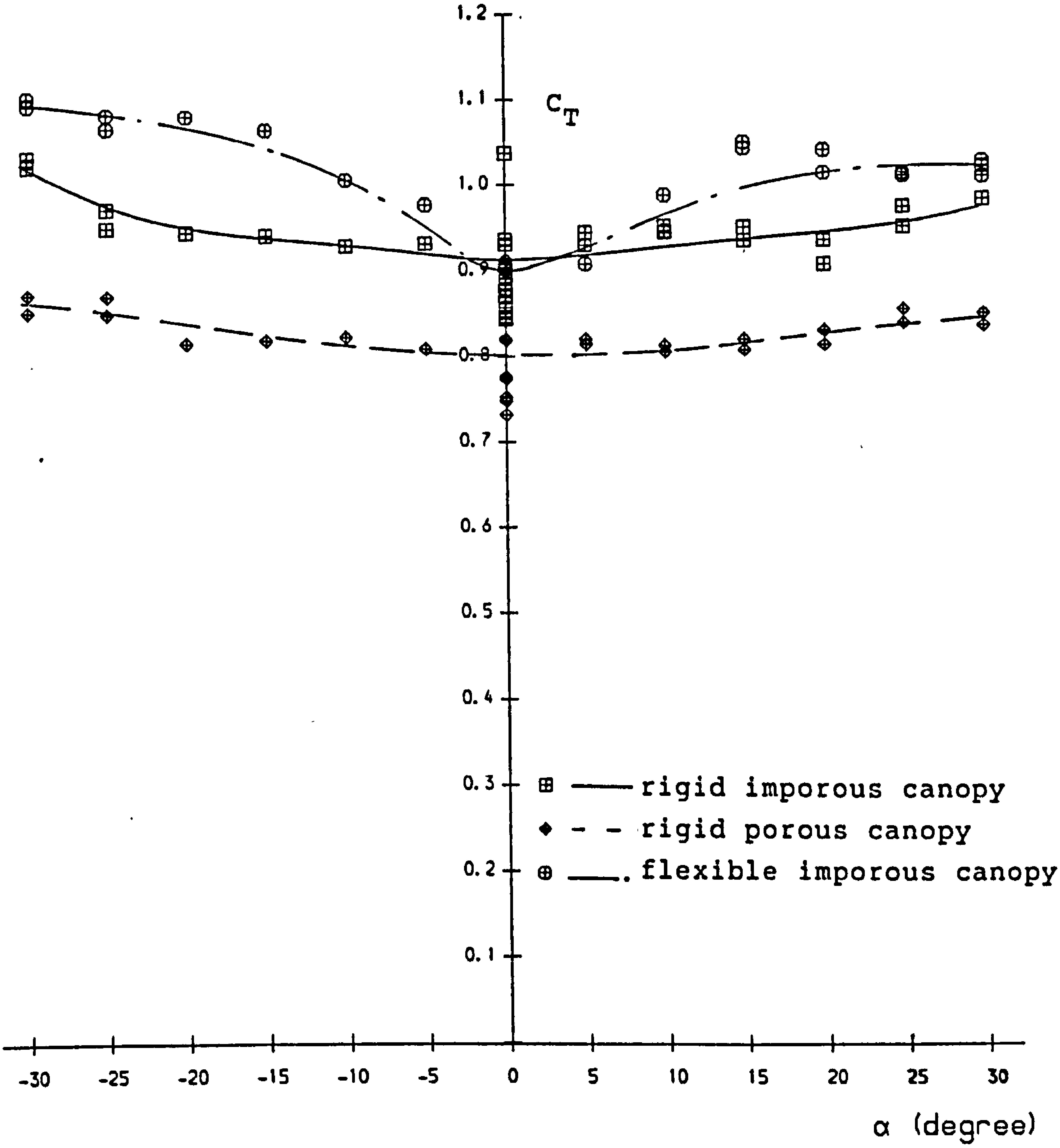

Fig. 4.7 Tangent Force Coefficient versus Angle of Attack for Hemispherical Parachutes

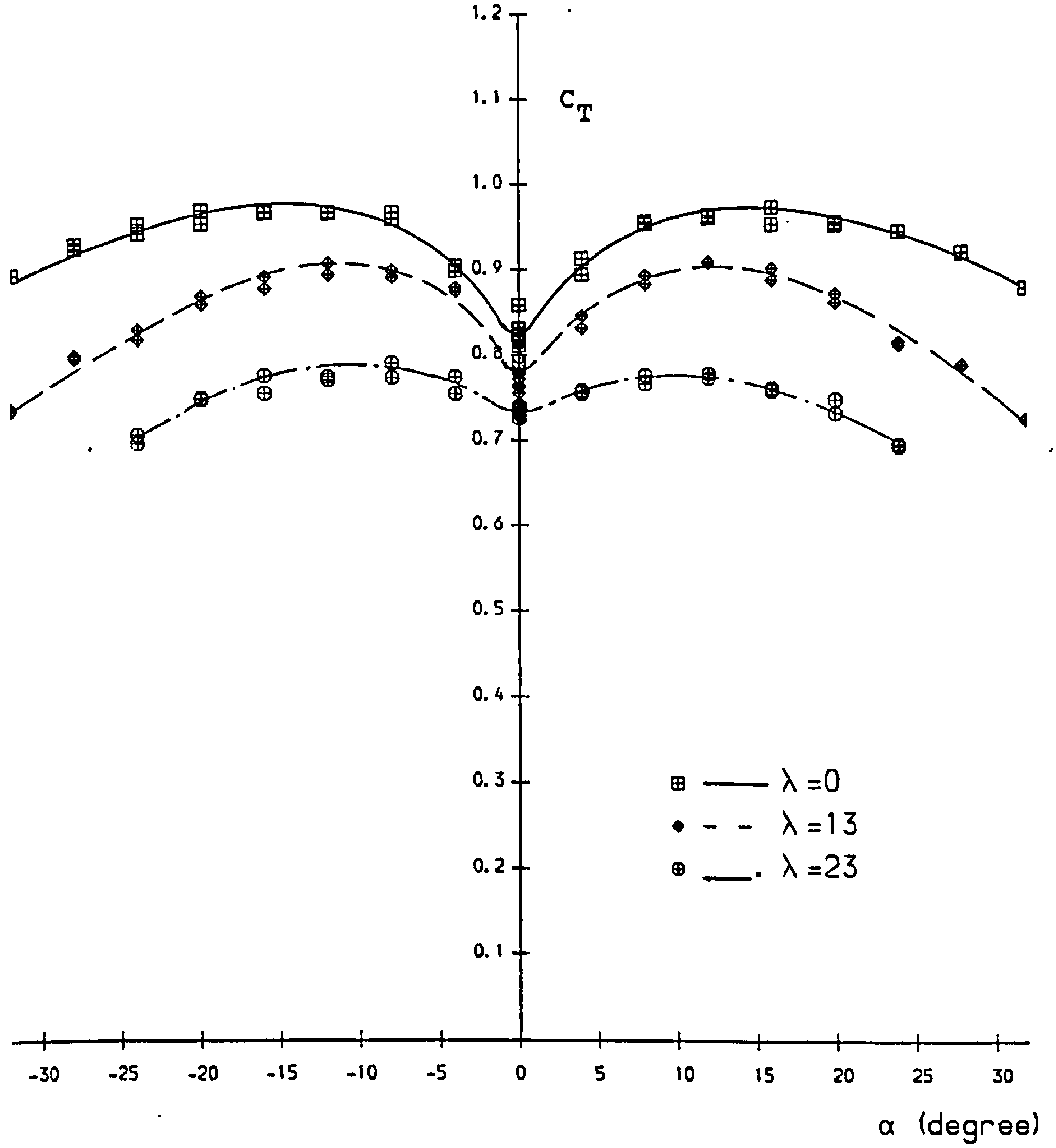

Fig. 4.8 Tangent Force Coefficient versus Angle of Attack for Various Nominal Porosities λ(cu.ft/sq.ft/sec)

Arm Ratio R_A=2.4
Suspension Line Ratio R_s=1.33

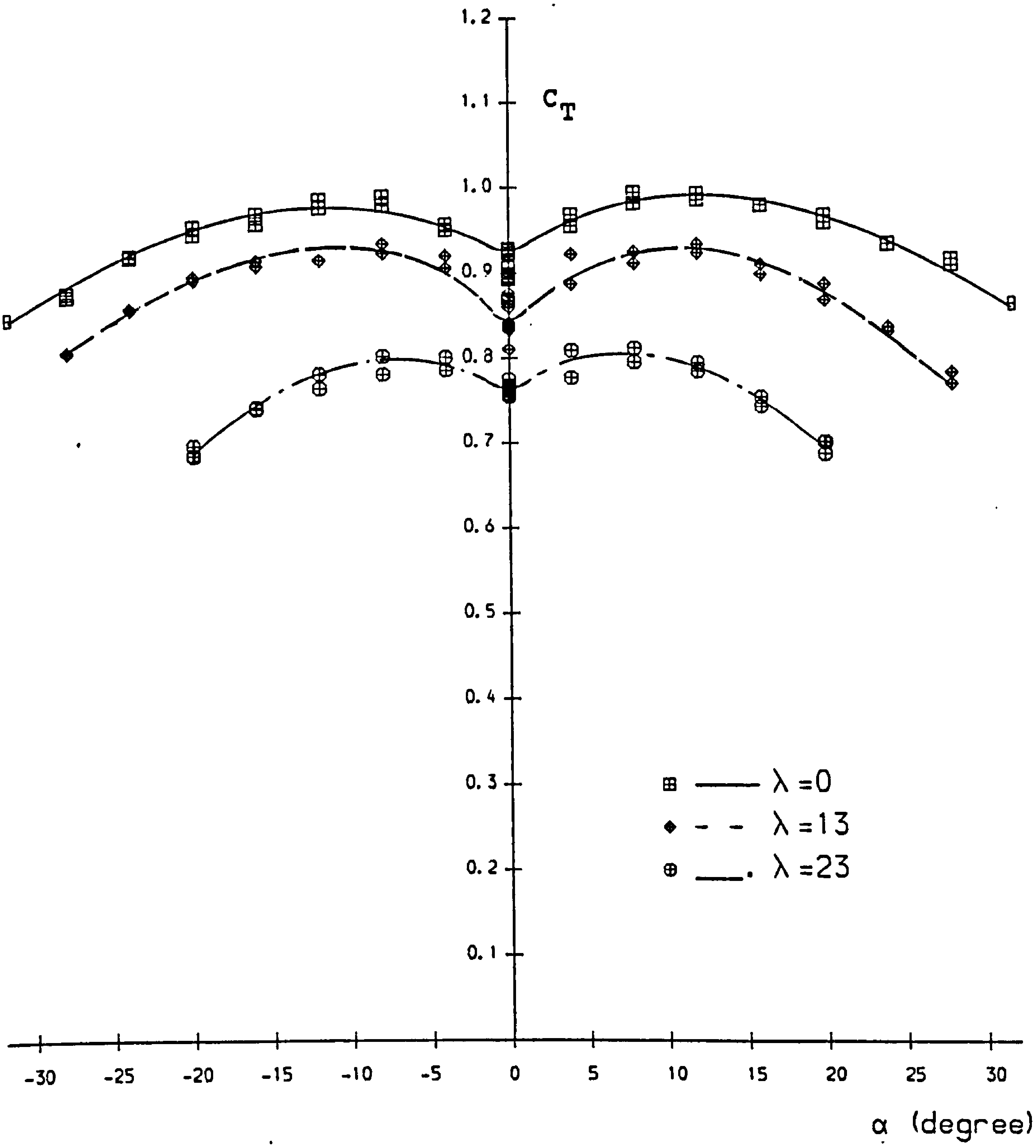

Fig. 4.9 Tangent Force Coefficient versus Angle of Attack for Various Nominal Porosities λ(cu.ft/sq.ft/sec)

Arm Ratio R_A=3.0
Suspension Line Ratio R_S=1.33

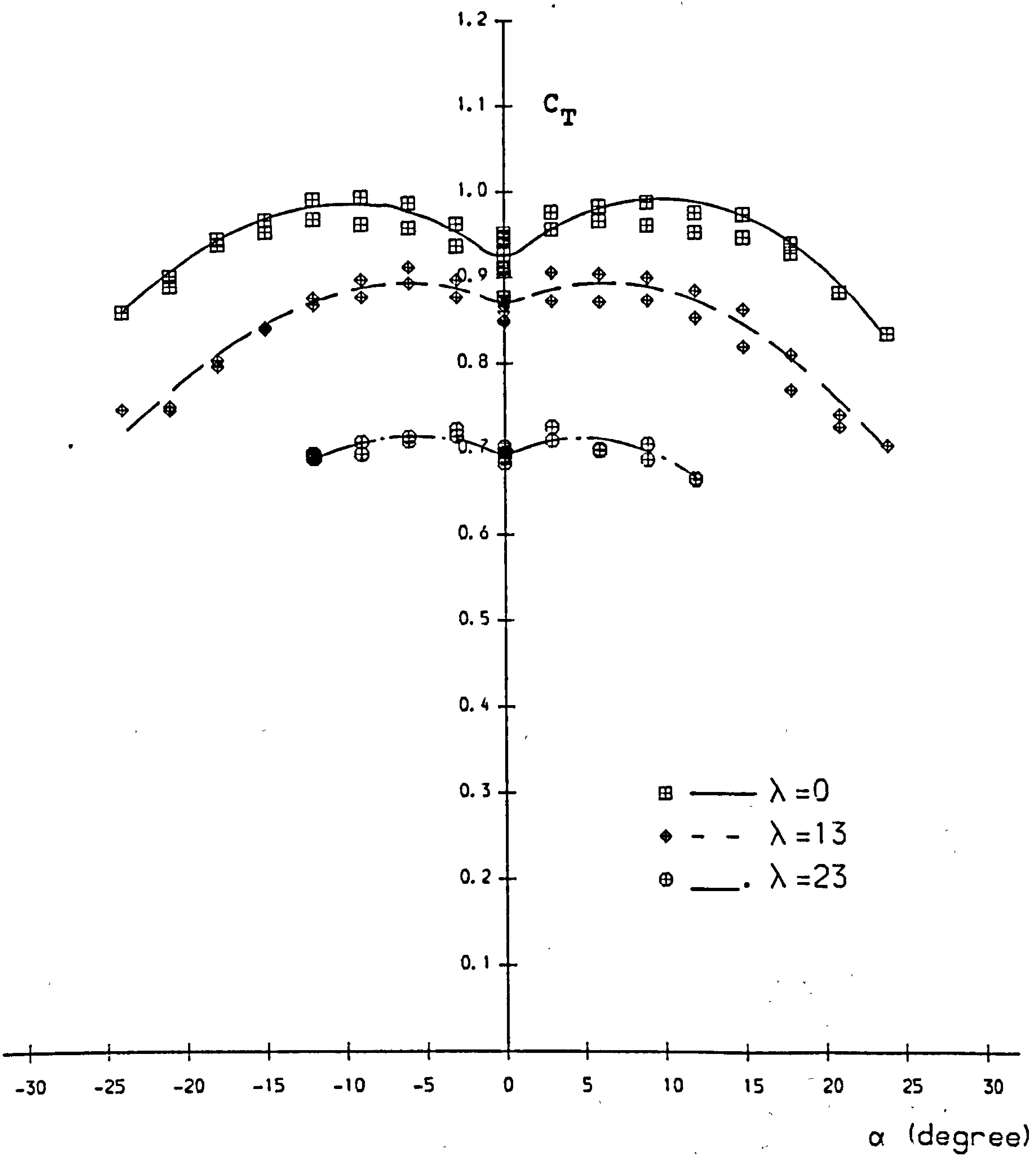

Fig. 4.10 Tangent Force Coefficient versus Angle of Attack for Various Nominal Porosities λ (cu.ft/sq.ft/sec)

Arm Ratio $R_A=4.0$
Suspension Line Ratio $R_S=1.33$

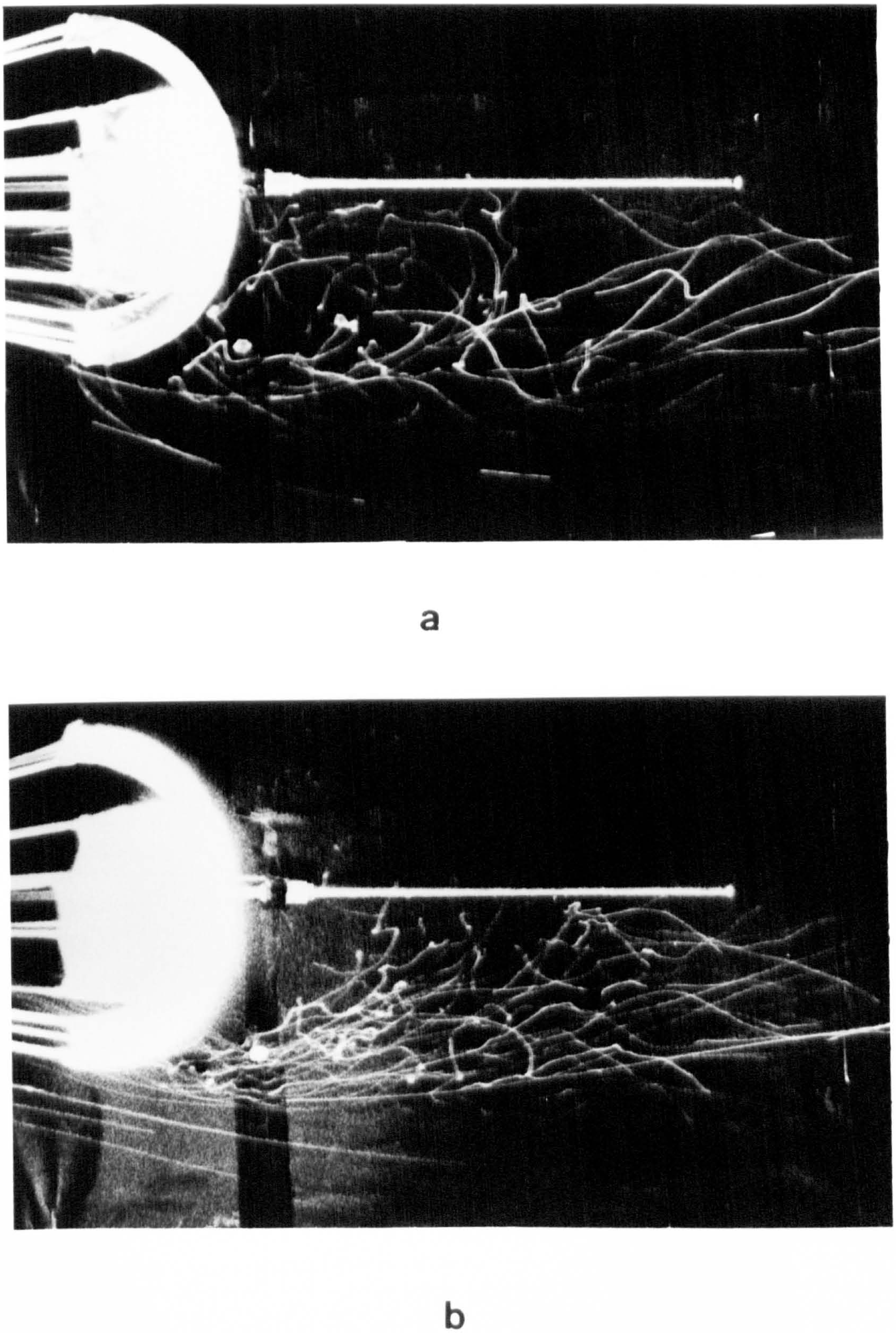

Fig. 4.11 The Flow Field around Cross-Shaped Canopies with Arm Ratio 3:1

(a) Fabric Porosity: 0 cu.ft/sq.ft/sec

(b) Fabric Porosity: 23 cu.ft/sq.ft/sec

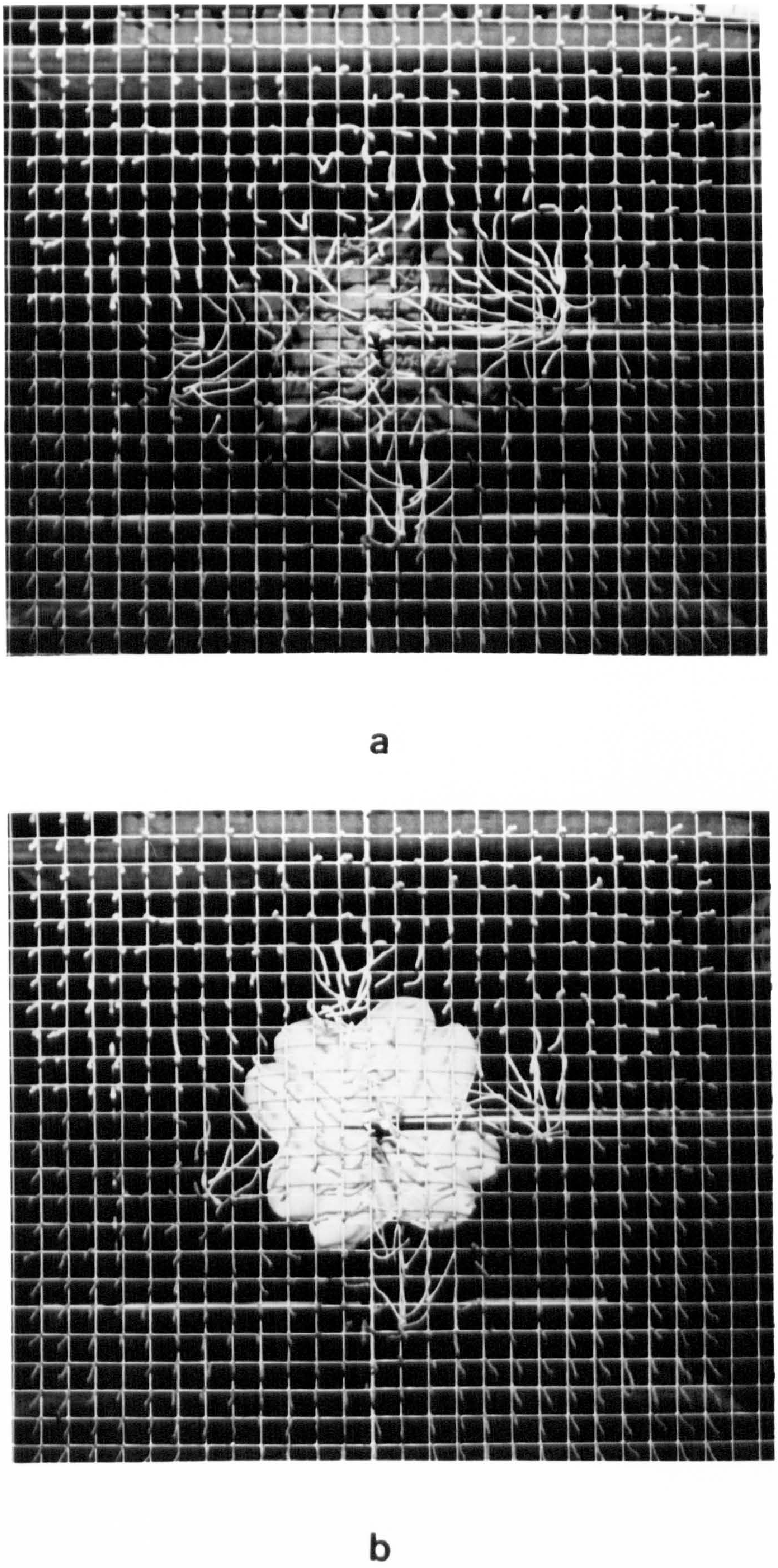

Fig. 4.12 Tuft Patterns 150 mm Downstream of Arm Ratio 3:1 Cross-Shaped Canopy

(a) Fabric Porosity: 0 cu.ft/sq.ft/sec
(b) Fabric Porosity: 23 cu.ft/sq.ft/sec

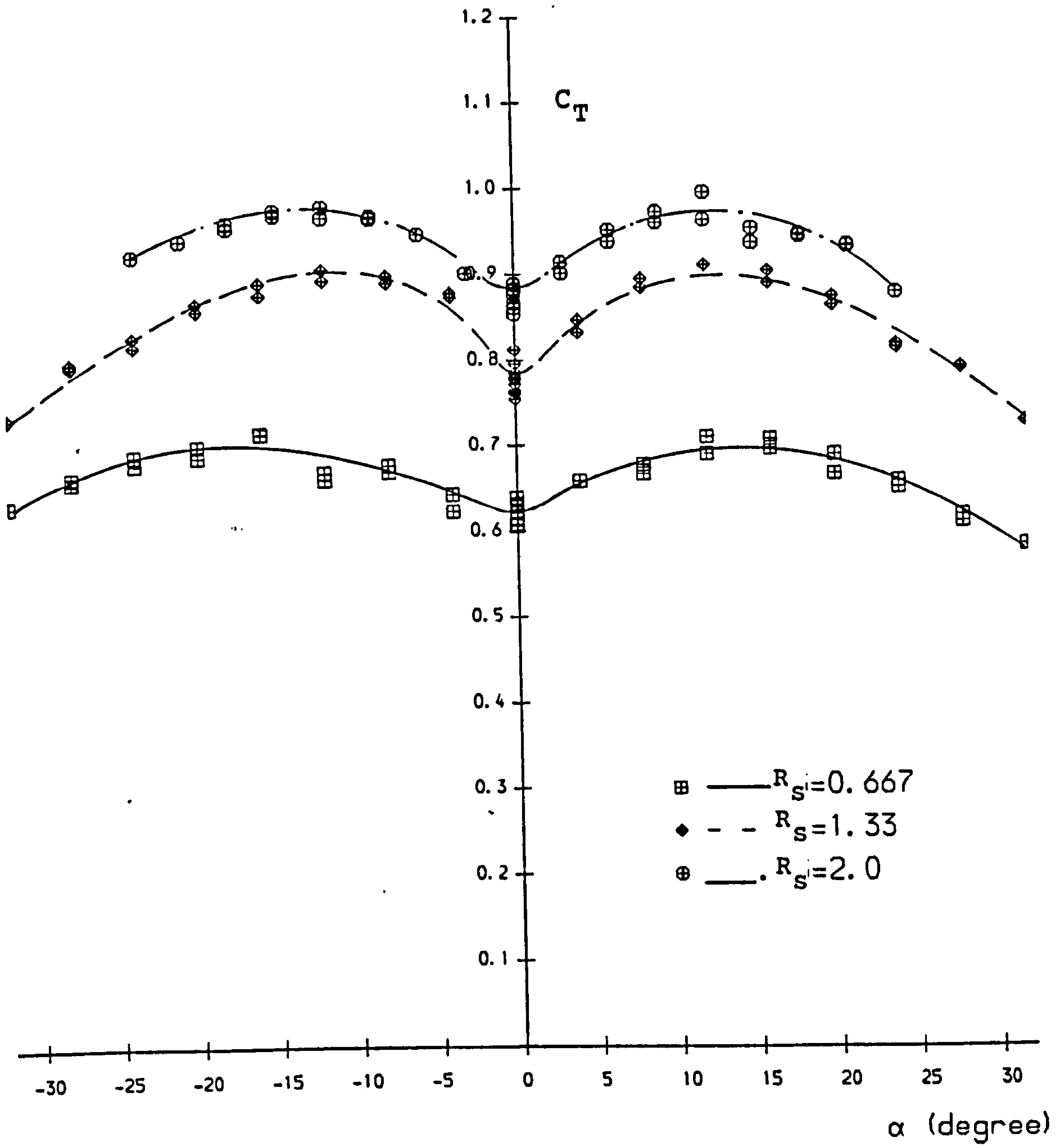

Fig. 4.13 Tangent Force Coefficient versus Angle of Attack for Various Suspension Line Ratios R_S

Arm Ratio R_A=2.4

Nominal Porosity (cu.ft/sq.ft/sec) λ=13

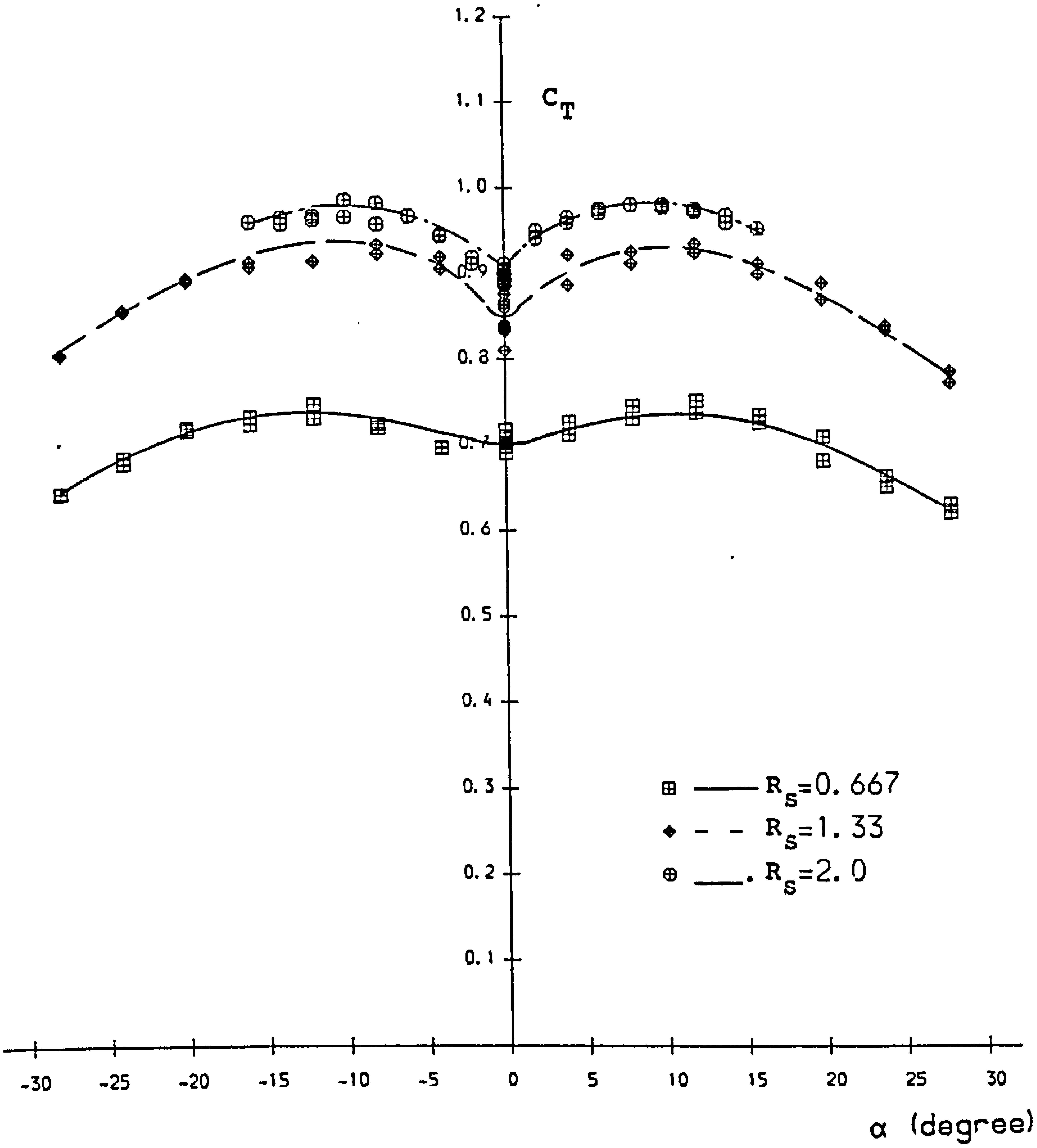

Fig. 4.14 Tangent Force Coefficient versus Angle of Attack for Various Suspension Line Ratios R_s

Arm Ratio R_A=3.0
Nominal Porosity (cu.ft/sq.ft/sec) λ=13

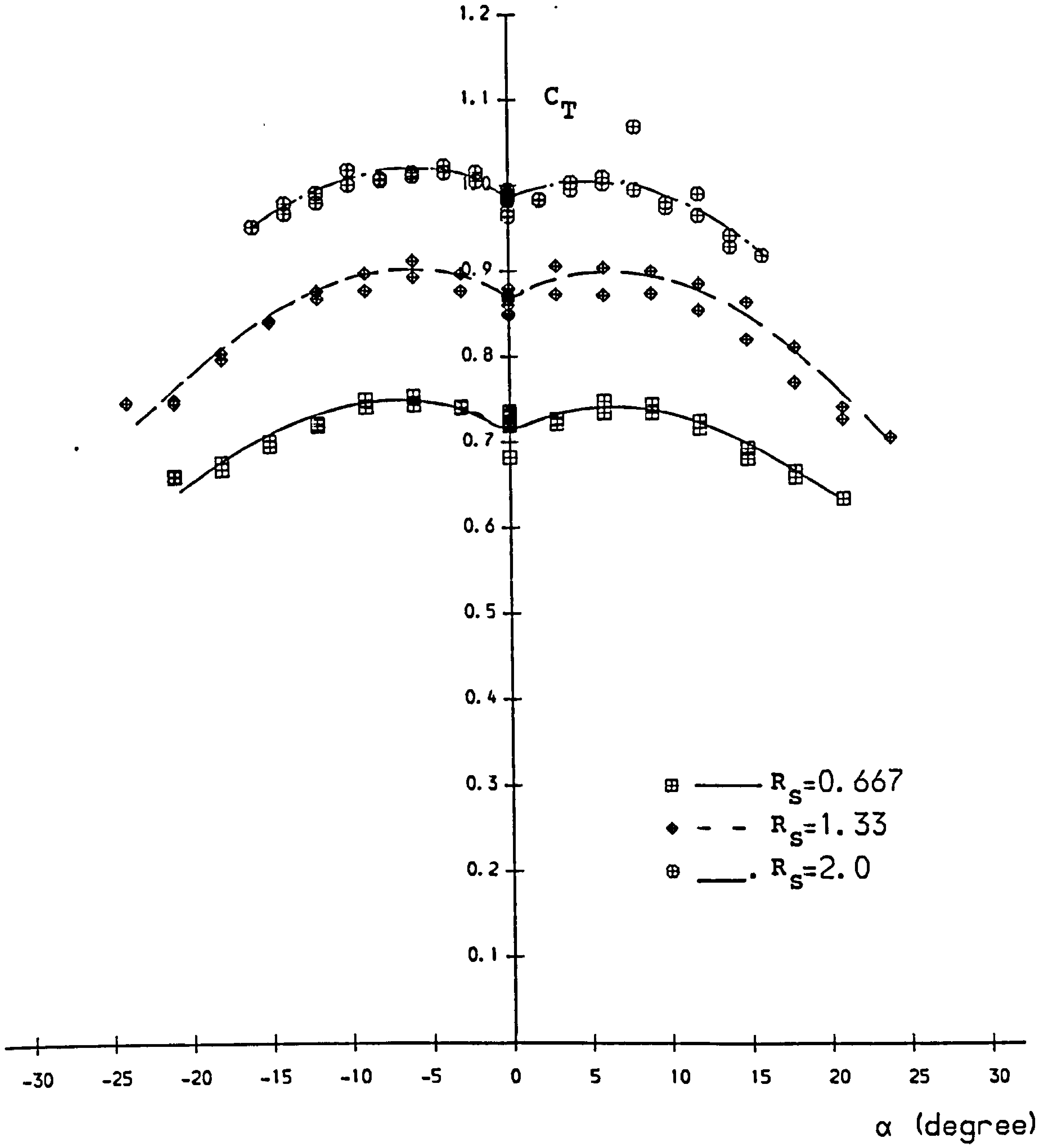

Fig. 4.15 Tangent Force Coefficient versus Angle of Attack for Various Suspension Line Ratios R_s

Arm Ratio R_A=4.0

Nominal Porosity (cu.ft/sq.ft/sec) λ=13

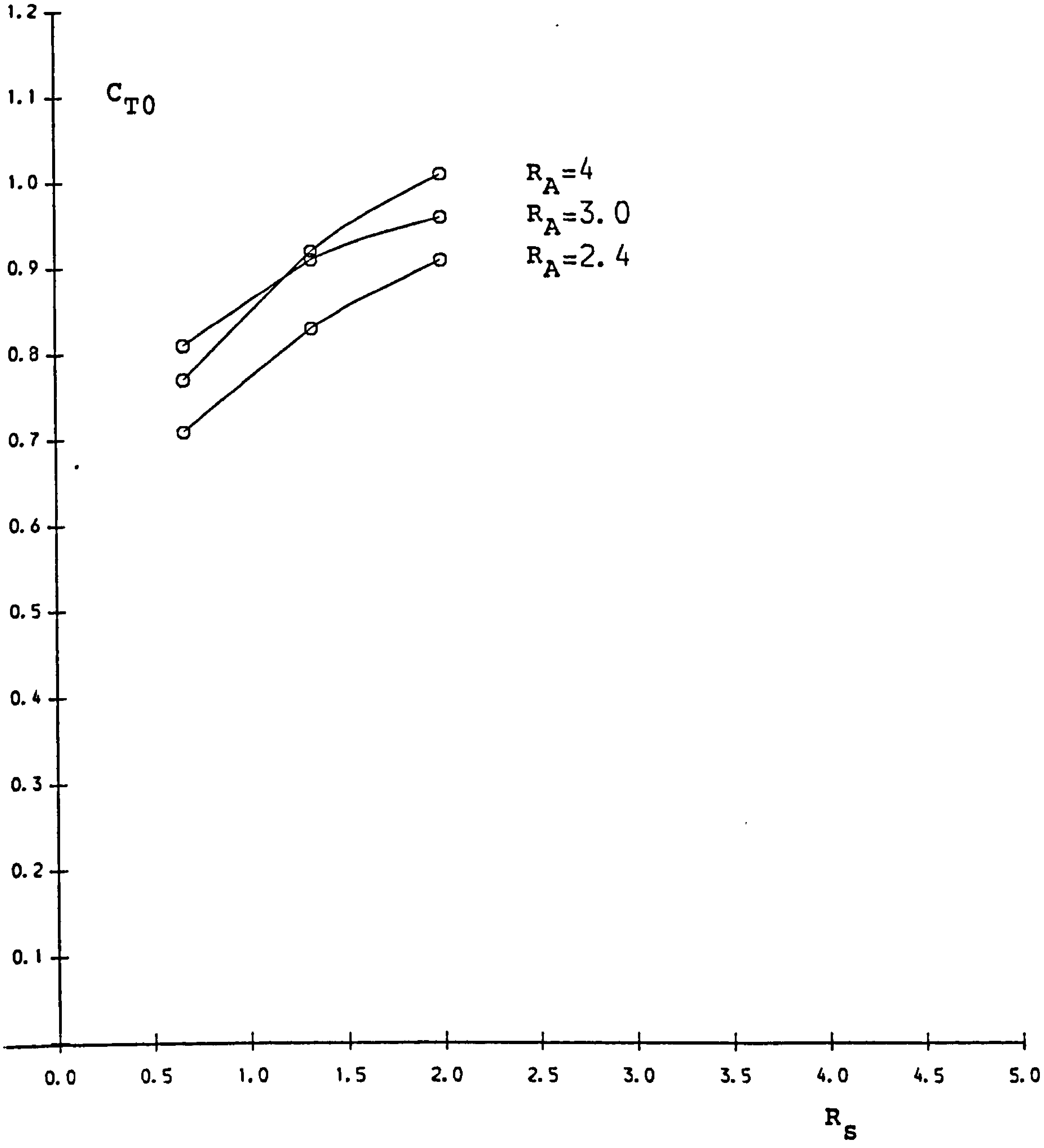

Fig. 4.16 Variation of Tangential Force Coefficient at Zero Angle of Attack C_{T0} with Suspension Line Ratios R_s for Canopies of Varying Arm Ratios R_A

Nominal Porosity (cu.ft/sq.ft/sec) $\lambda=0$

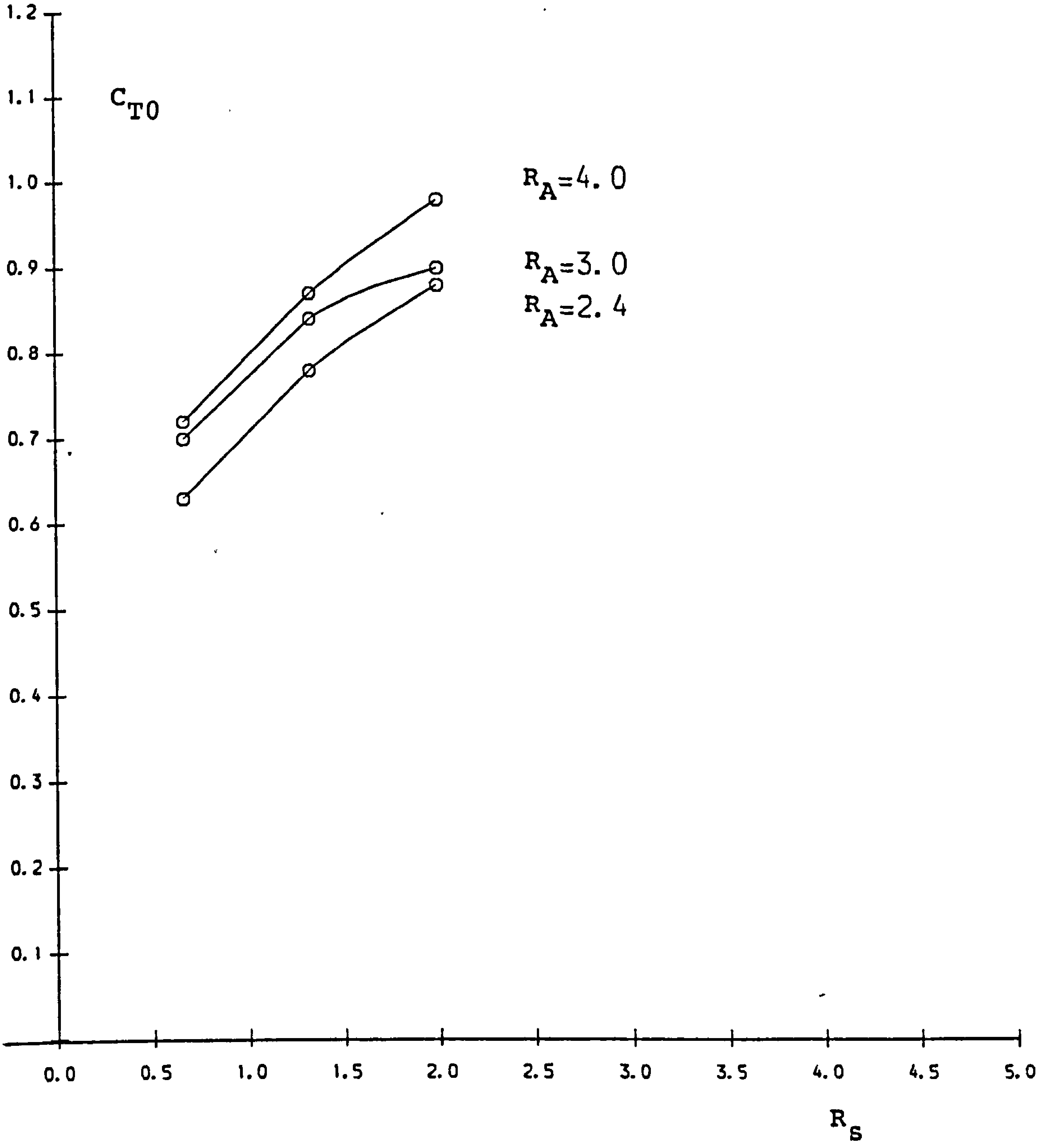

Fig. 4.17 Variation of Tangential Force Coefficient at Zero Angle of Attack C_{T0} with Suspension Line Ratios R_S for Canopies of Varying Arm Ratios R_A

Nominal Porosity (cu.ft/sq.ft/sec) λ=13

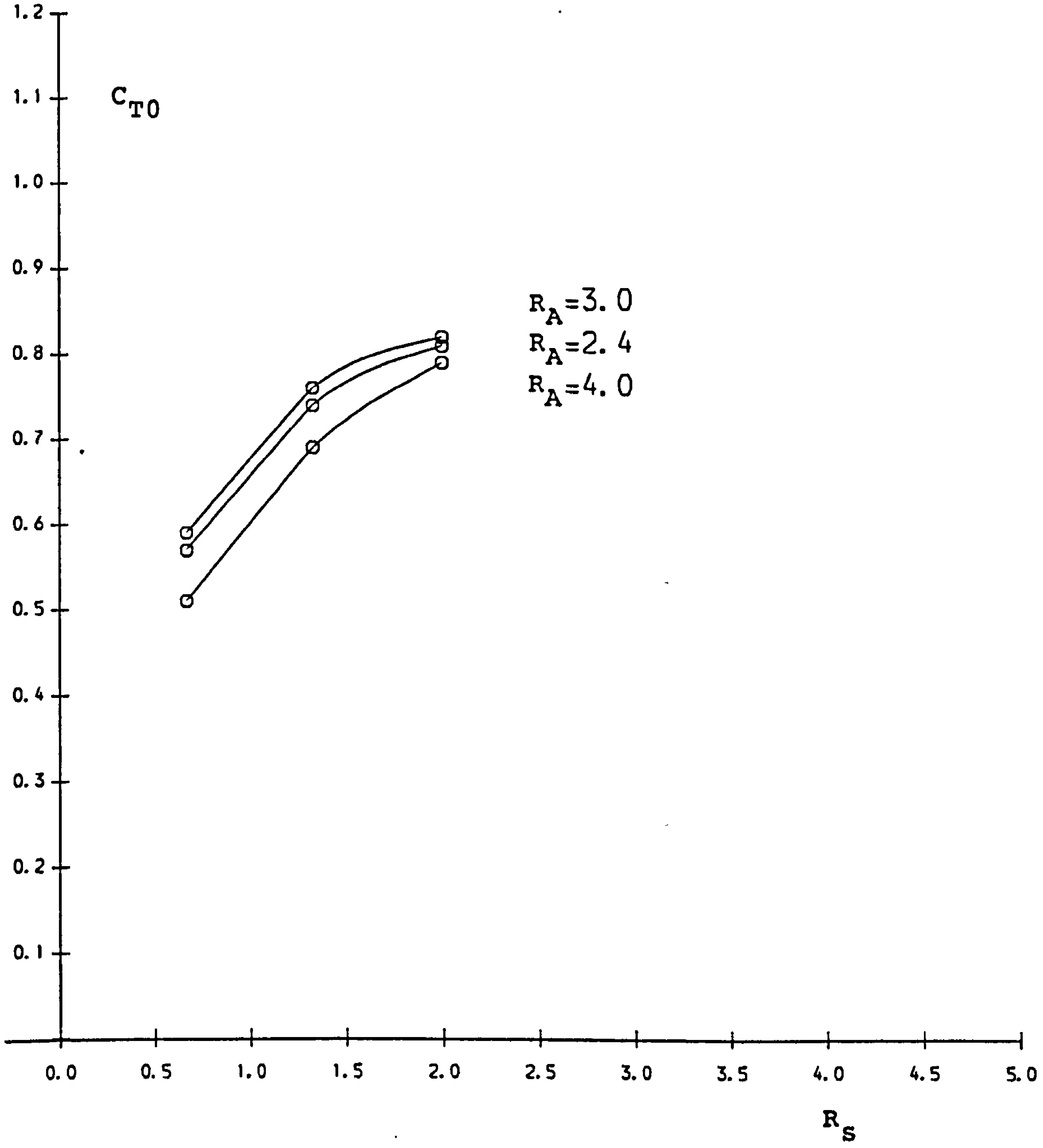

Fig. 4.18 Variation of Tangential Force Coefficient at Zero Angle of Attack C_{T0} with Suspension Line Ratios R_S for Canopies of Varying Arm Ratios R_A

Nominal Porosity (cu.ft/sq.ft/sec) $\lambda=23$

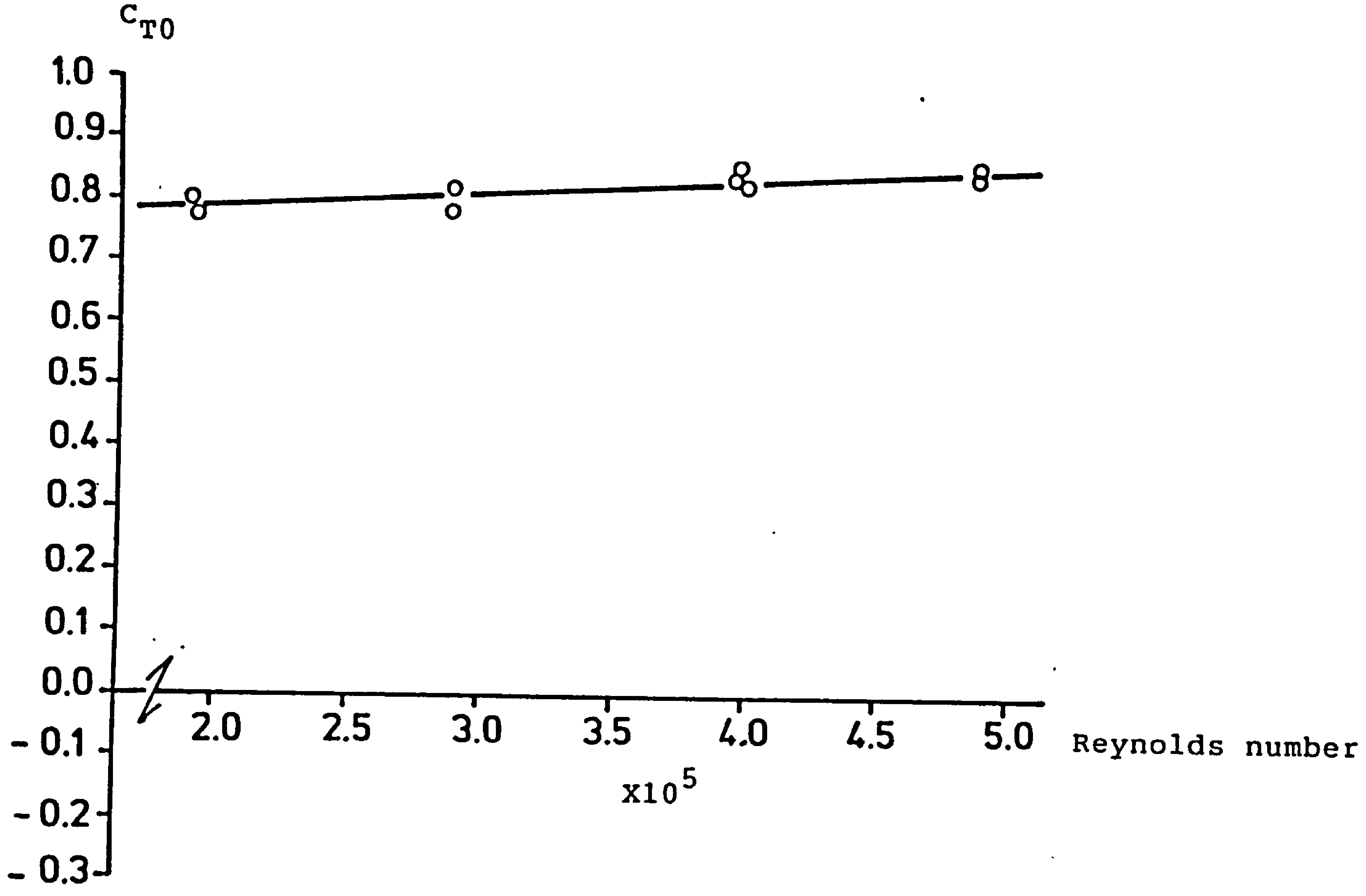

Fig. 4.19 Tangent force coefficient versus Reynolds number for arm ratio 3:1 cross parachute at $\alpha = 0$

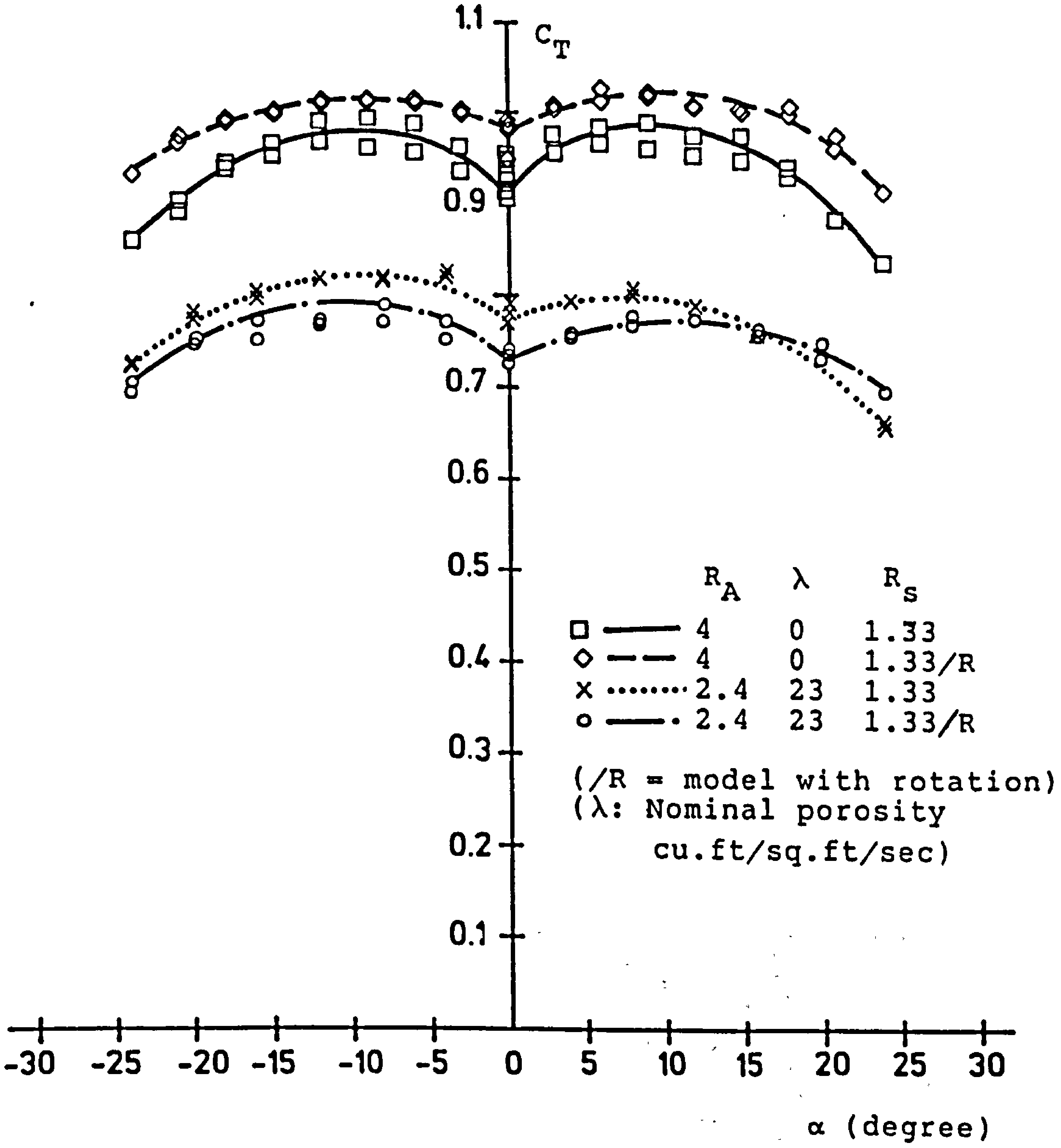

Fig. 4.20 Tangent Force Coefficient versus Angle of Attack

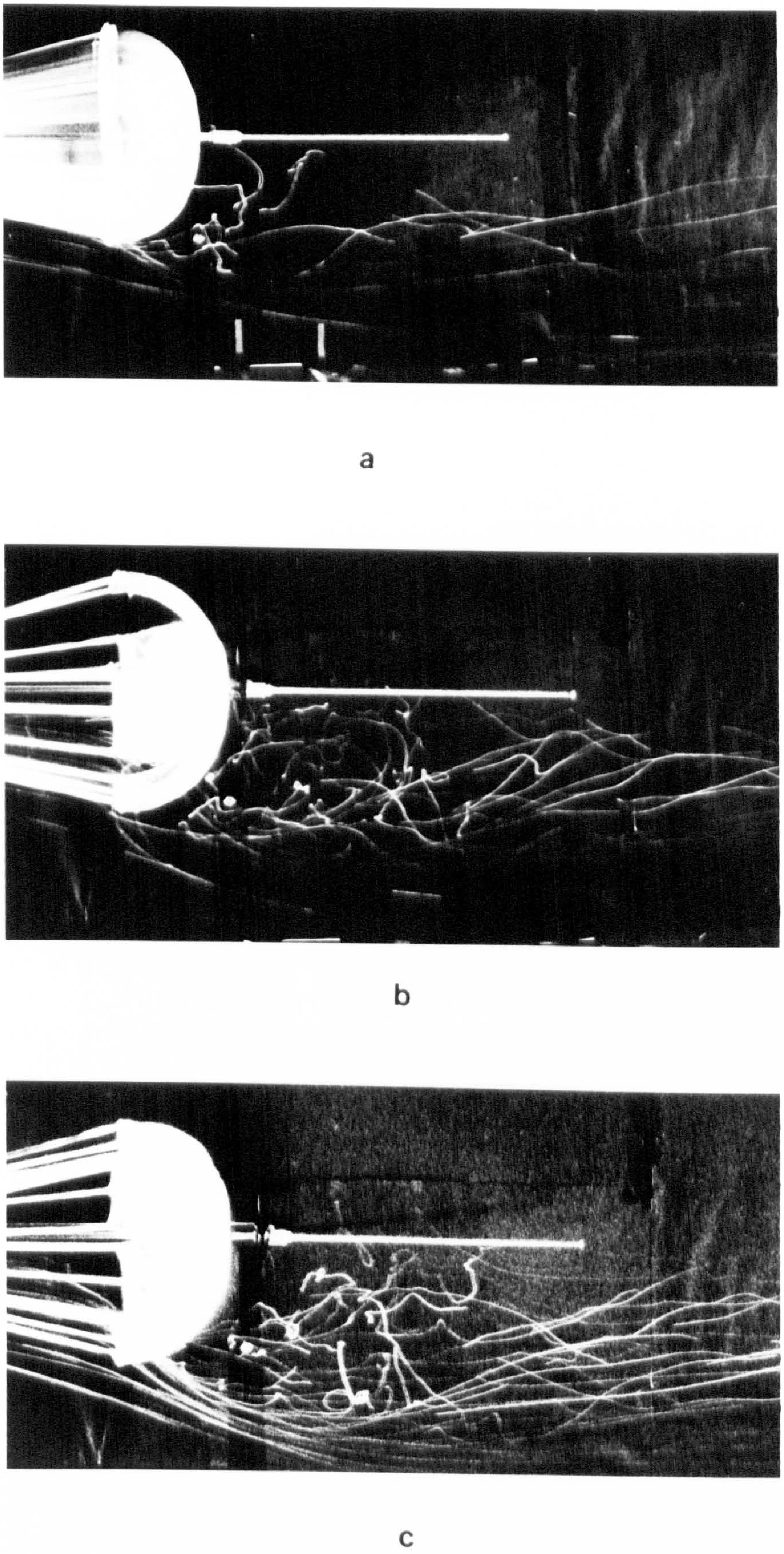

Fig. 4.21 The Flow Field around Cross-Shaped Canopies with 3:1 Arm Ratio

(a) Flow past a Rotating Canopy
(b) Flow over an Arm of Non-Rotating Canopy
(c) Flow though a Gap of Non-Rotating Canopy

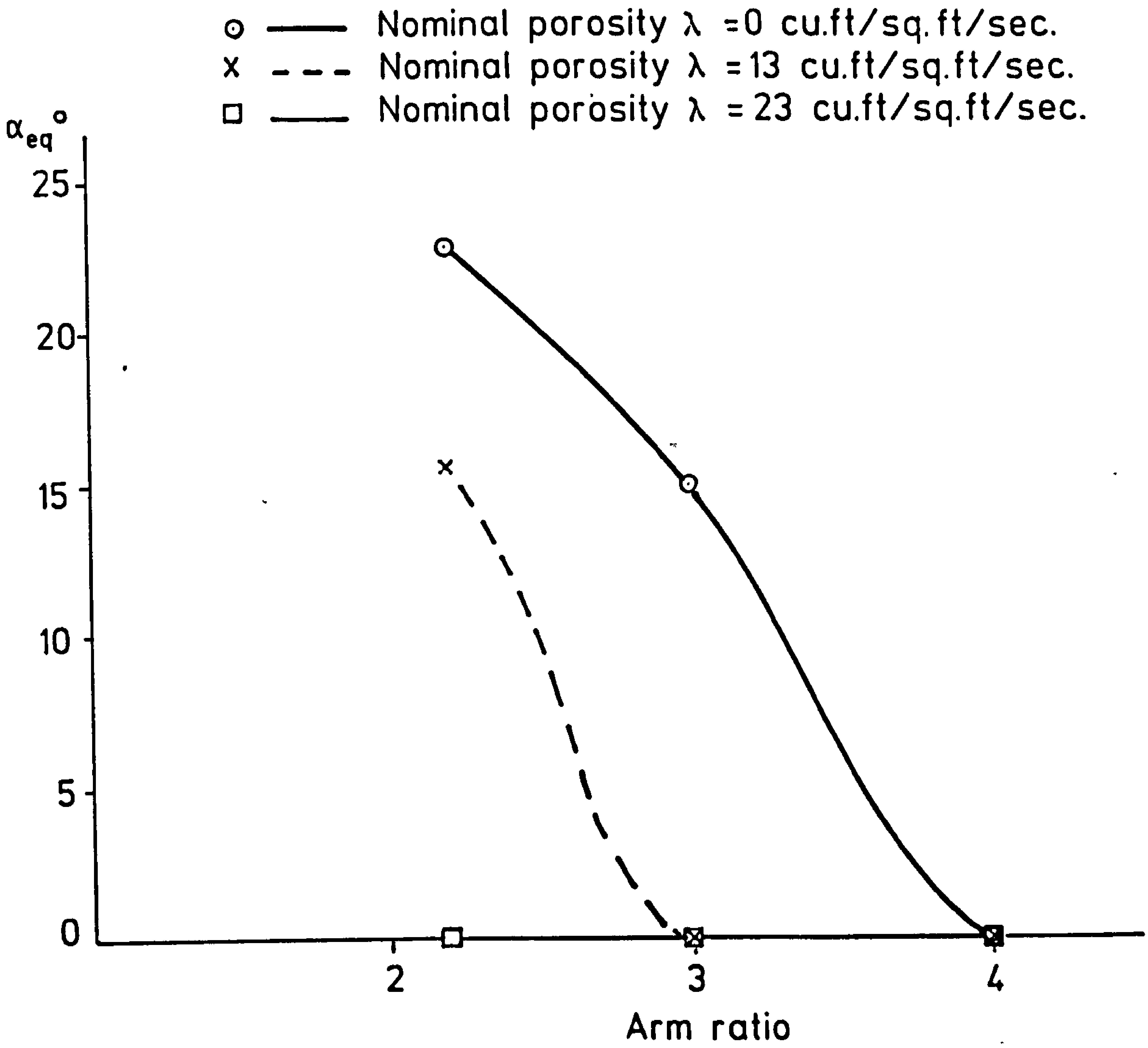

Fig. 4.22 Variation of the statically stable equilibrium angle of attack α_{eq} for cross-shaped canopies with arm ratio and porosity

Suspension line ratio = 1.33:1

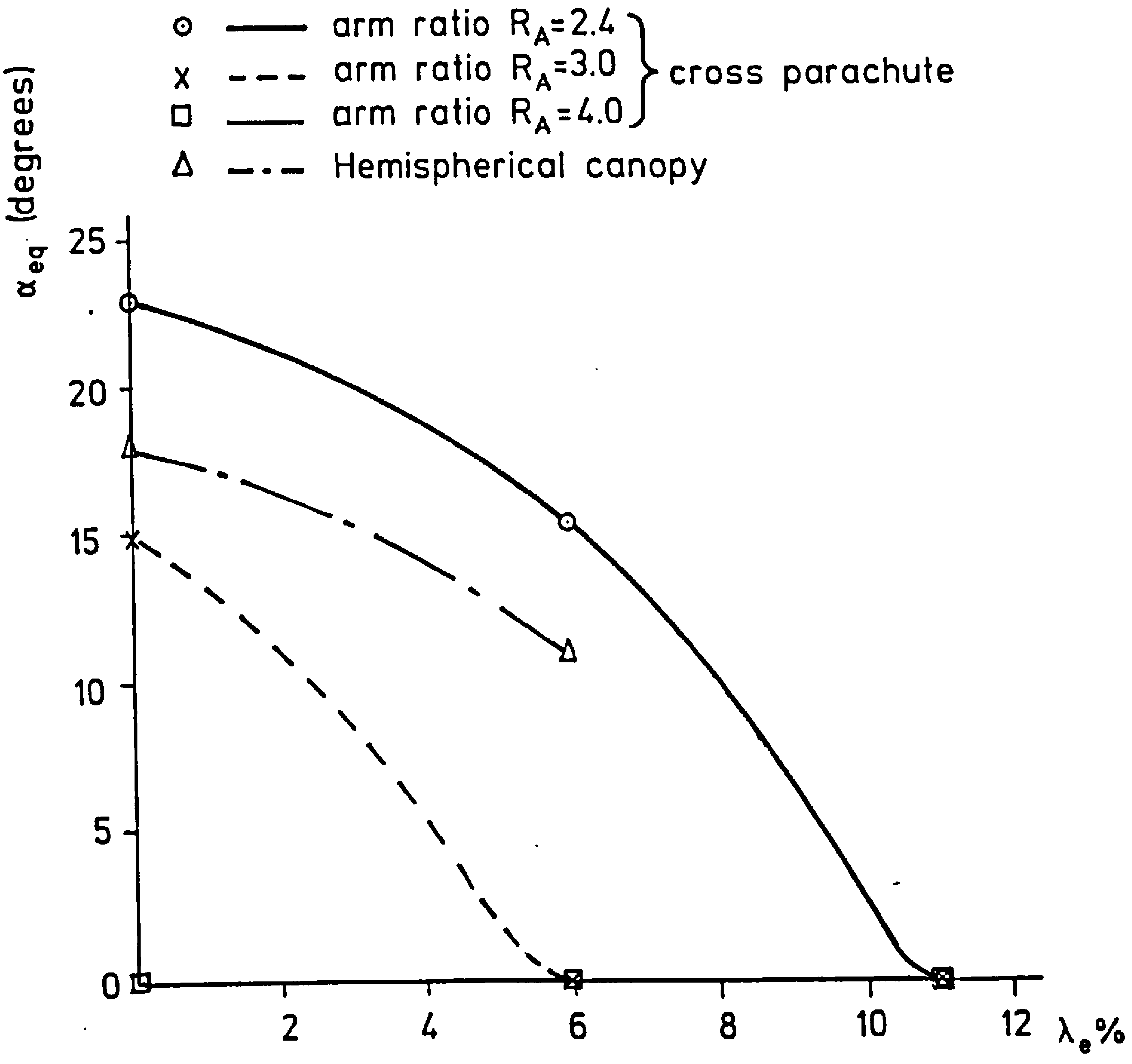

Fig. 4.23 Variation of the statically stable equilibrium angle of attack α_{eq} for various canopies with effective porosity λ_e (or λ_g- geometrical porosity)

Suspension line ratio = 1.33:1

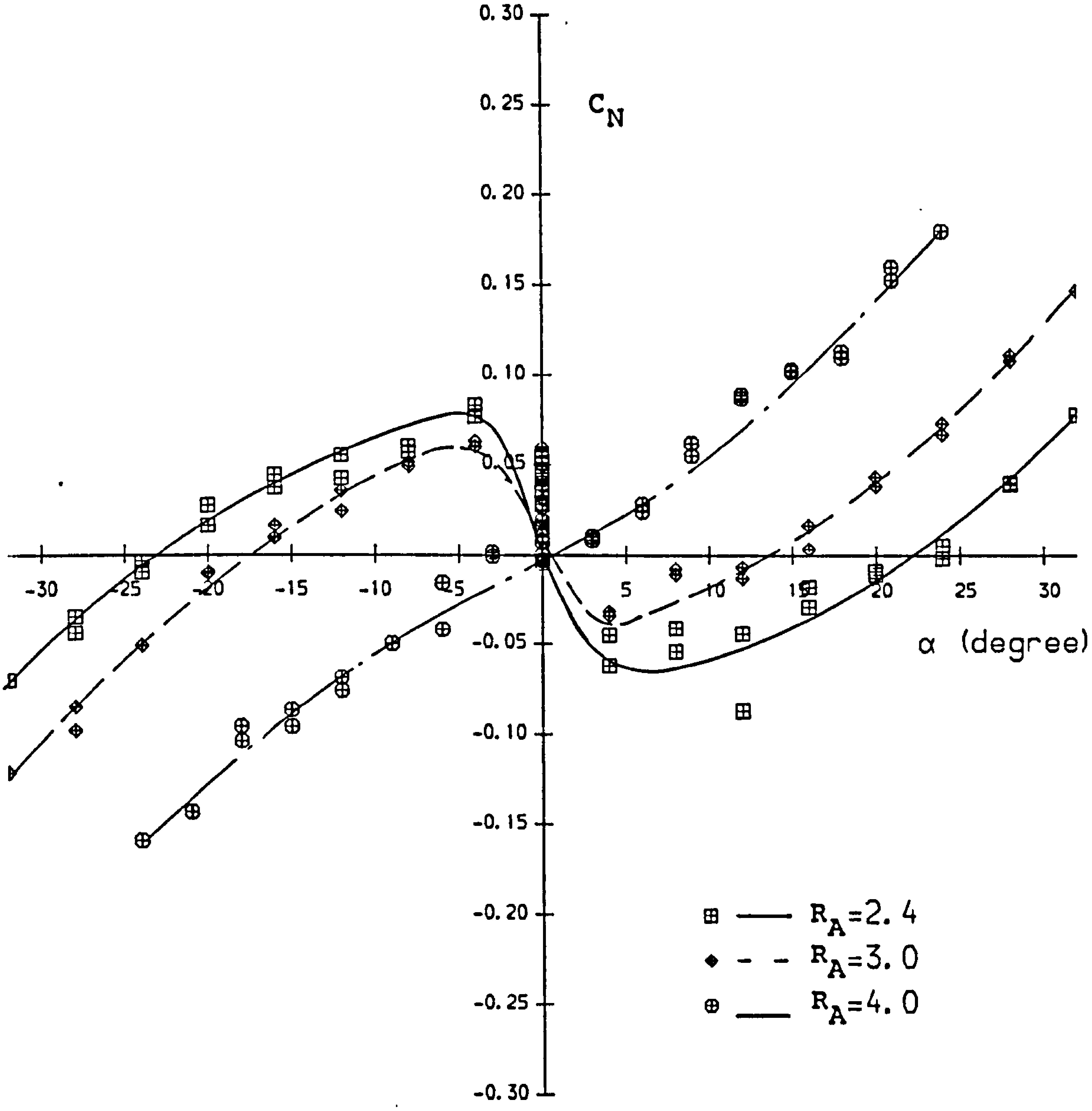

Fig. 4.24 Normal Force Coefficient versus Angle of Attack for Various Arm Ratios R_A

Nominal Porosity (cu.ft/sq.ft/sec) $\lambda=0$
Suspension Line Ratio $R_s=1.33$

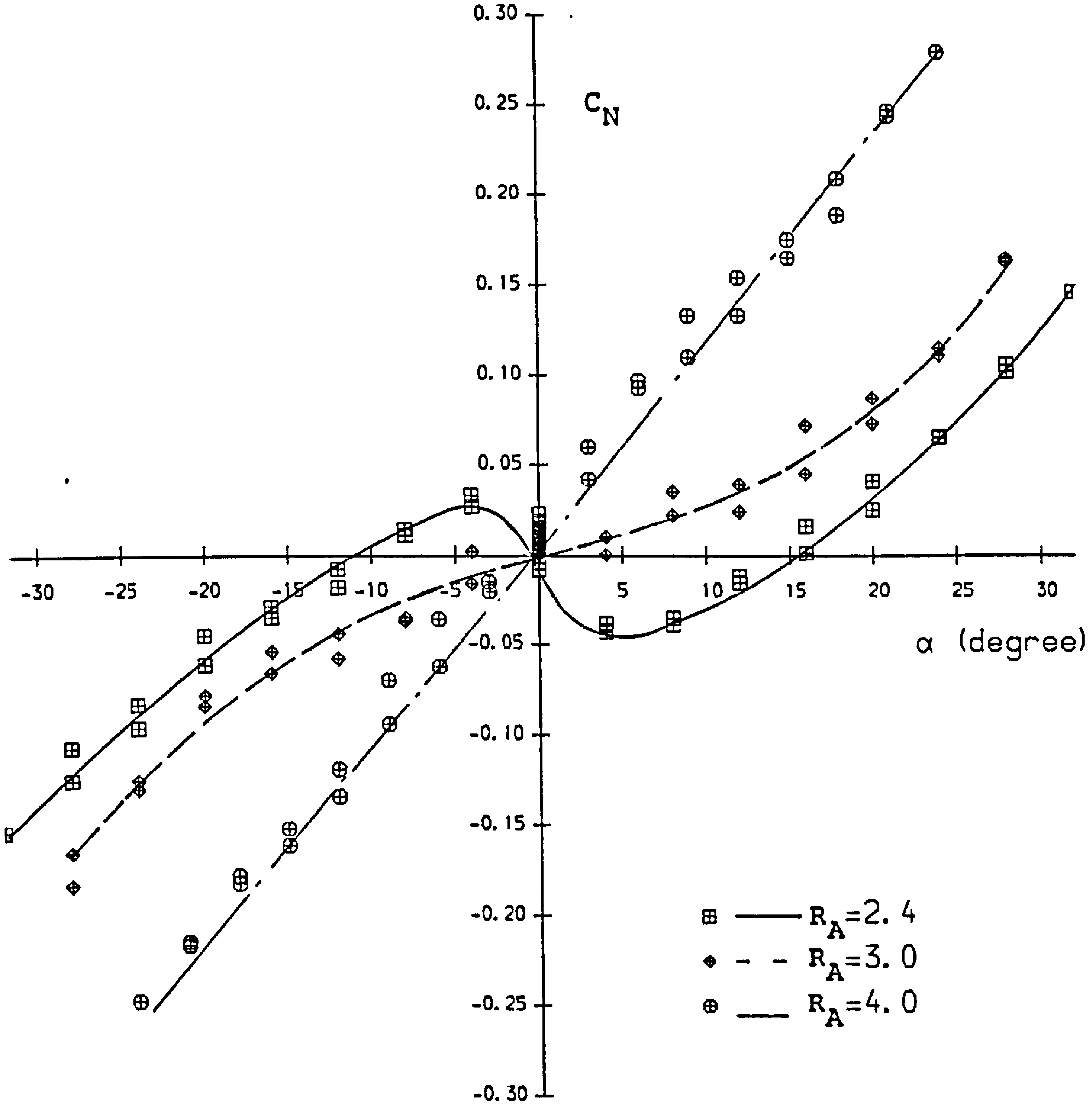

Fig. 4.25 Normal Force Coefficient versus Angle of Attack for Various Arm Ratios R_A

Nominal Porosity (cu.ft/sq.ft/sec) $\lambda=13$
Suspension Line Ratio $R_s=1.33$

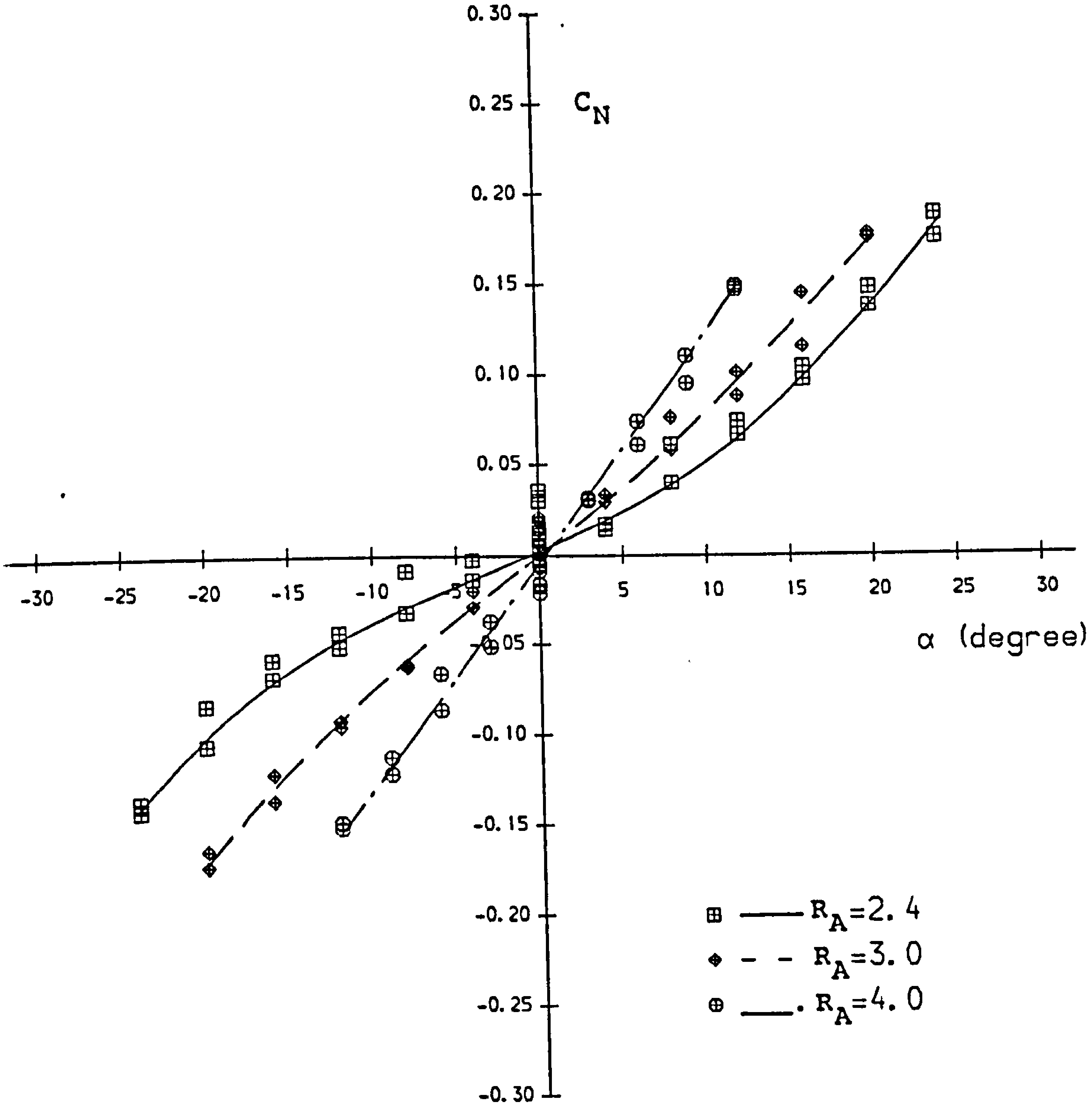

Fig. 4.26 Normal Force Coefficient versus Angle of Attack for Various Arm Ratios R_A

Nominal Porosity (cu.ft/sq.ft/sec) λ=23
Suspension Line Ratio R_s=1.33

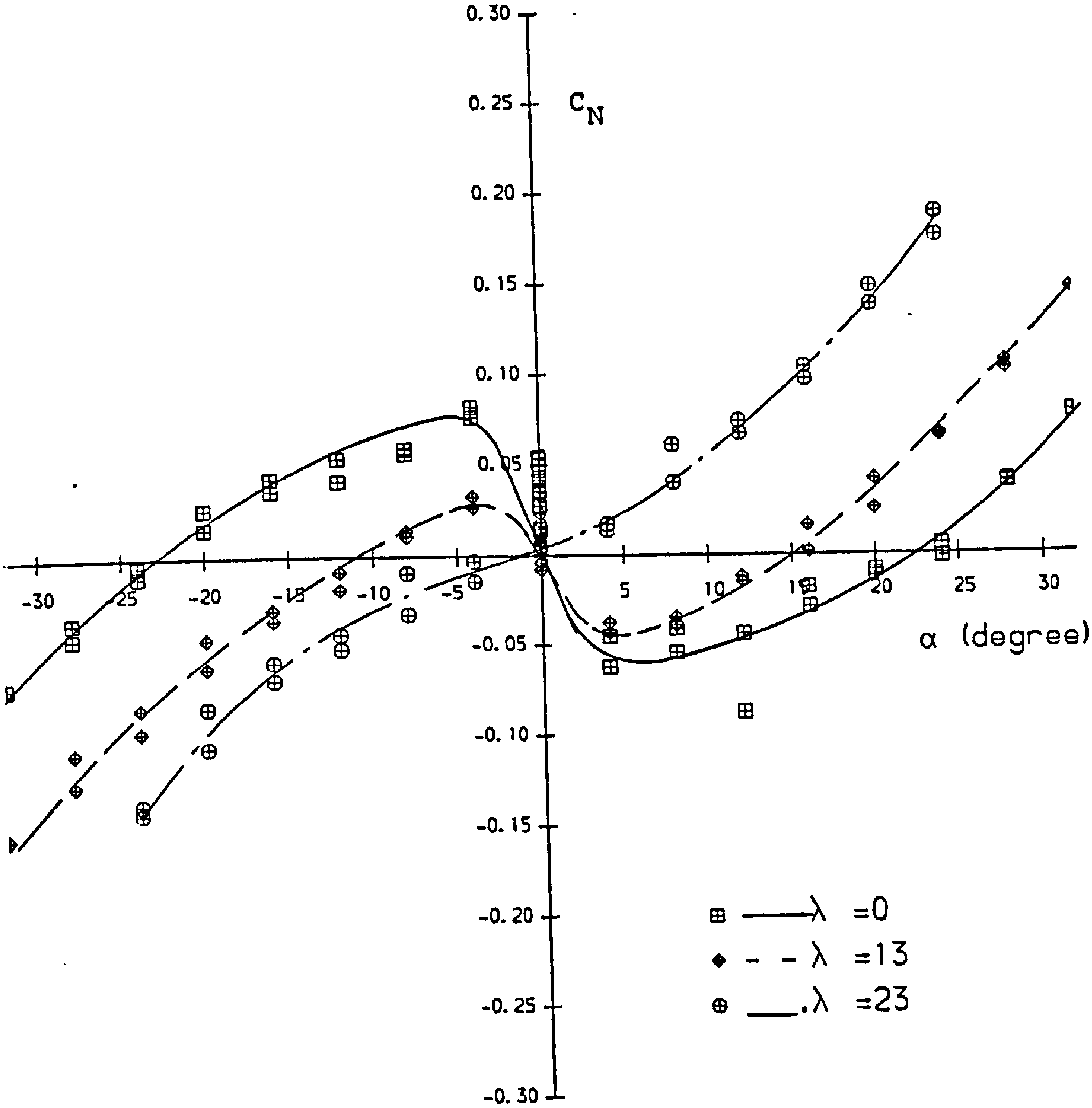

Fig. 4.27 Normal Force Coefficient versus Angle of Attack for Various Nominal Porosities λ(cu.ft/sq.ft/sec)

Arm Ratio R_A=2.4
Suspension Line Ratio R_s=1.33

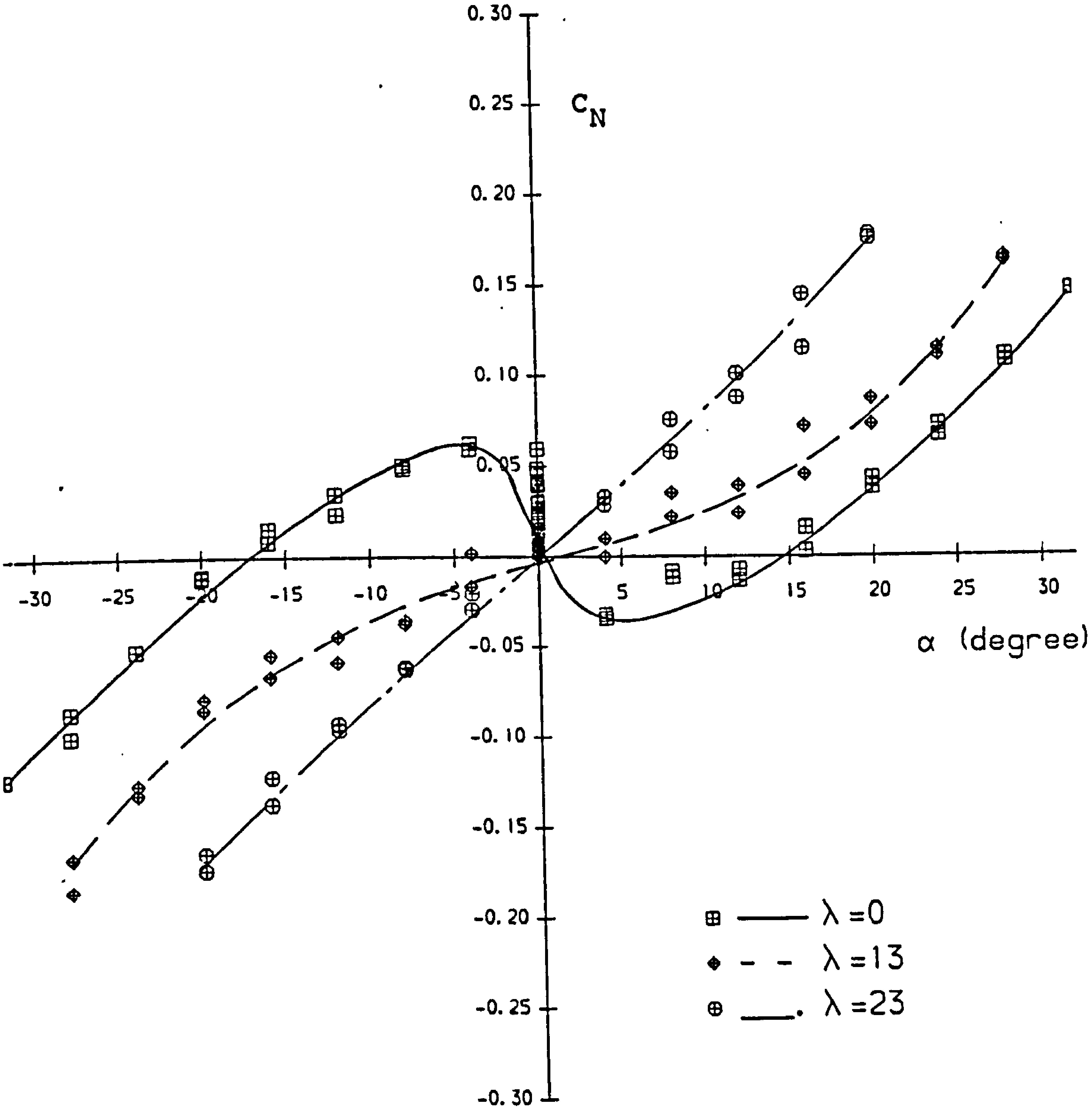

Fig. 4.28 Normal Force Coefficient versus Angle of Attack for Various Nominal Porosities λ(cu.ft/sq.ft/sec)

Arm Ratio R_A=3.0
Suspension Line Ratio R_S=1.33

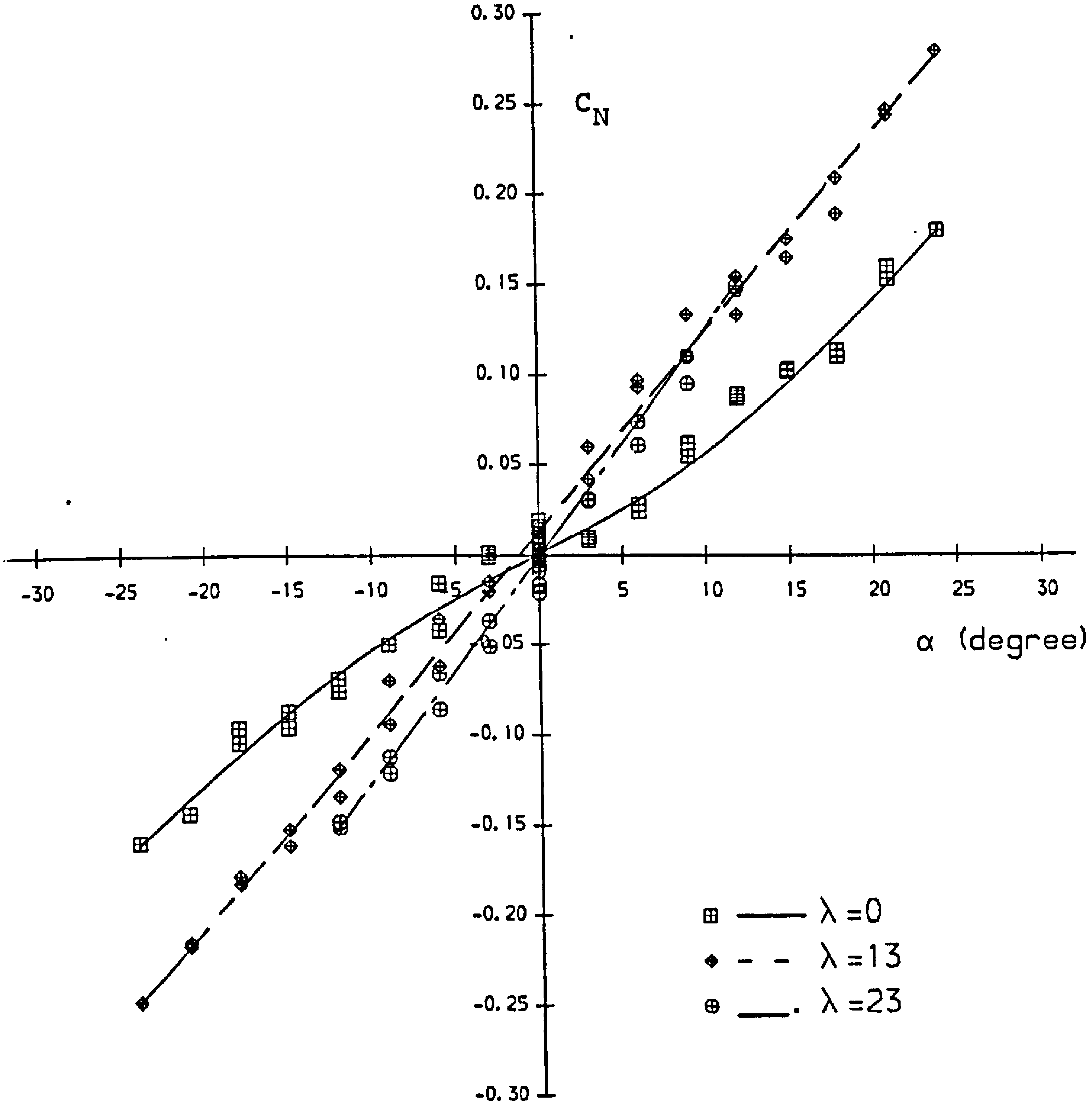

Fig. 4.29 Normal Force Coefficient versus Angle of Attack for Various Nominal Porosities λ(cu.ft/sq.ft/sec)

Arm Ratio R_A=4.0
Suspension Line Ratio R_s=1.33

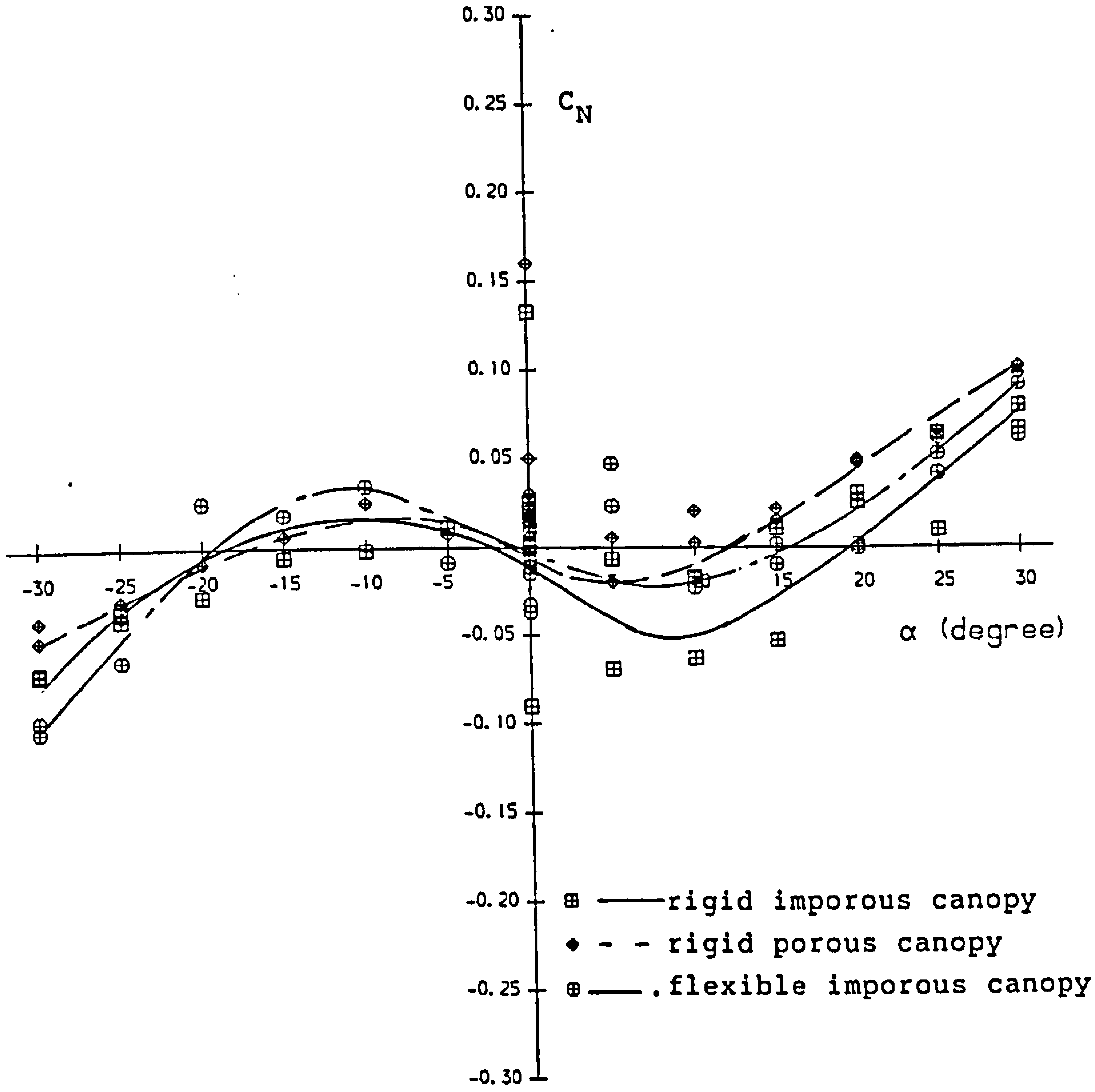

Fig. 4.30 Normal Force Coefficient versus Angle of Attack for Hemispherical Parachutes

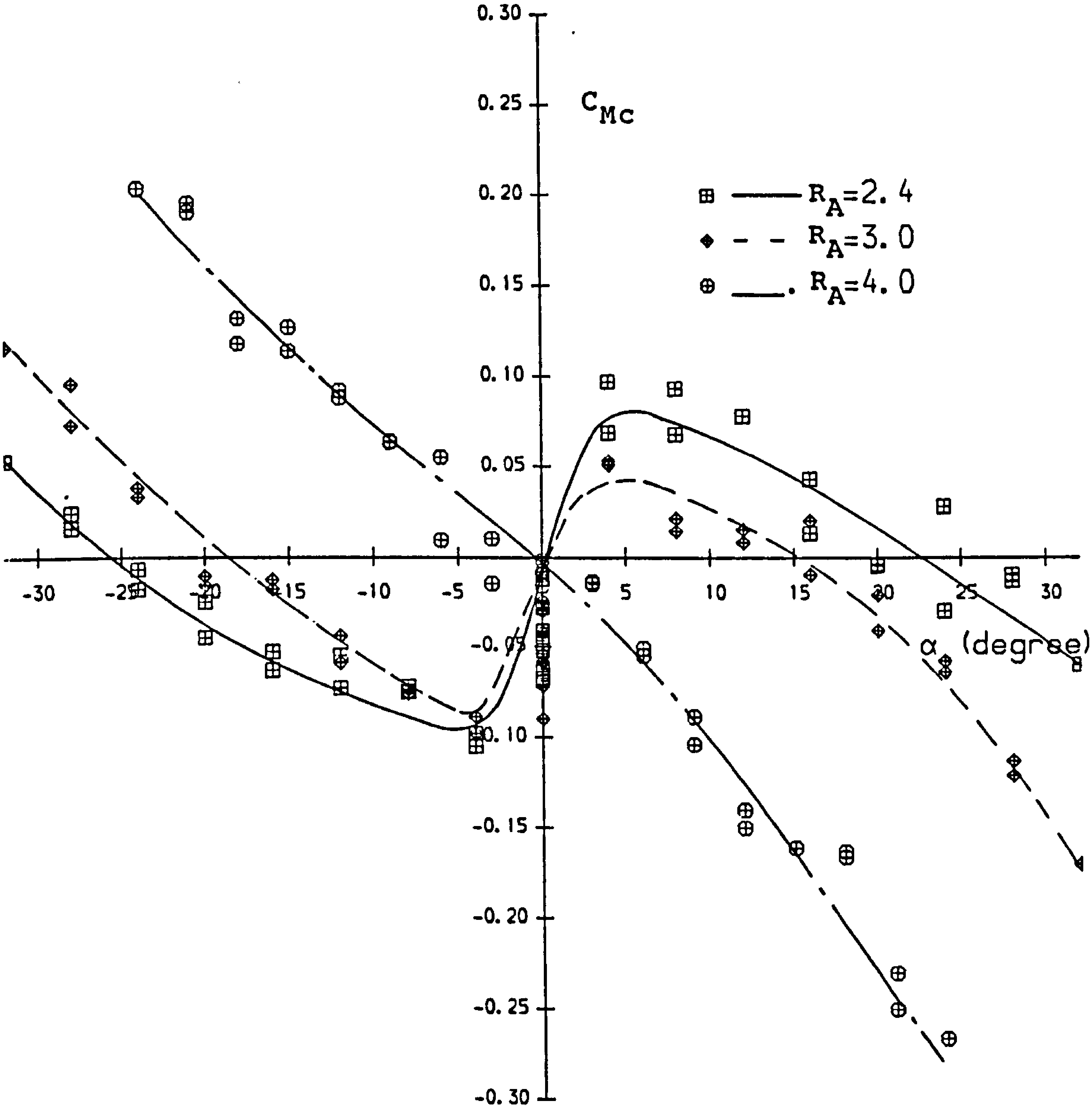

Fig. 4.31 Moment Coefficient versus Angle of Attack for Various Arm Ratios R_A

Nominal Porosity (cu.ft/sq.ft/sec) λ=0
Suspension Line Ratio R_s=1.33

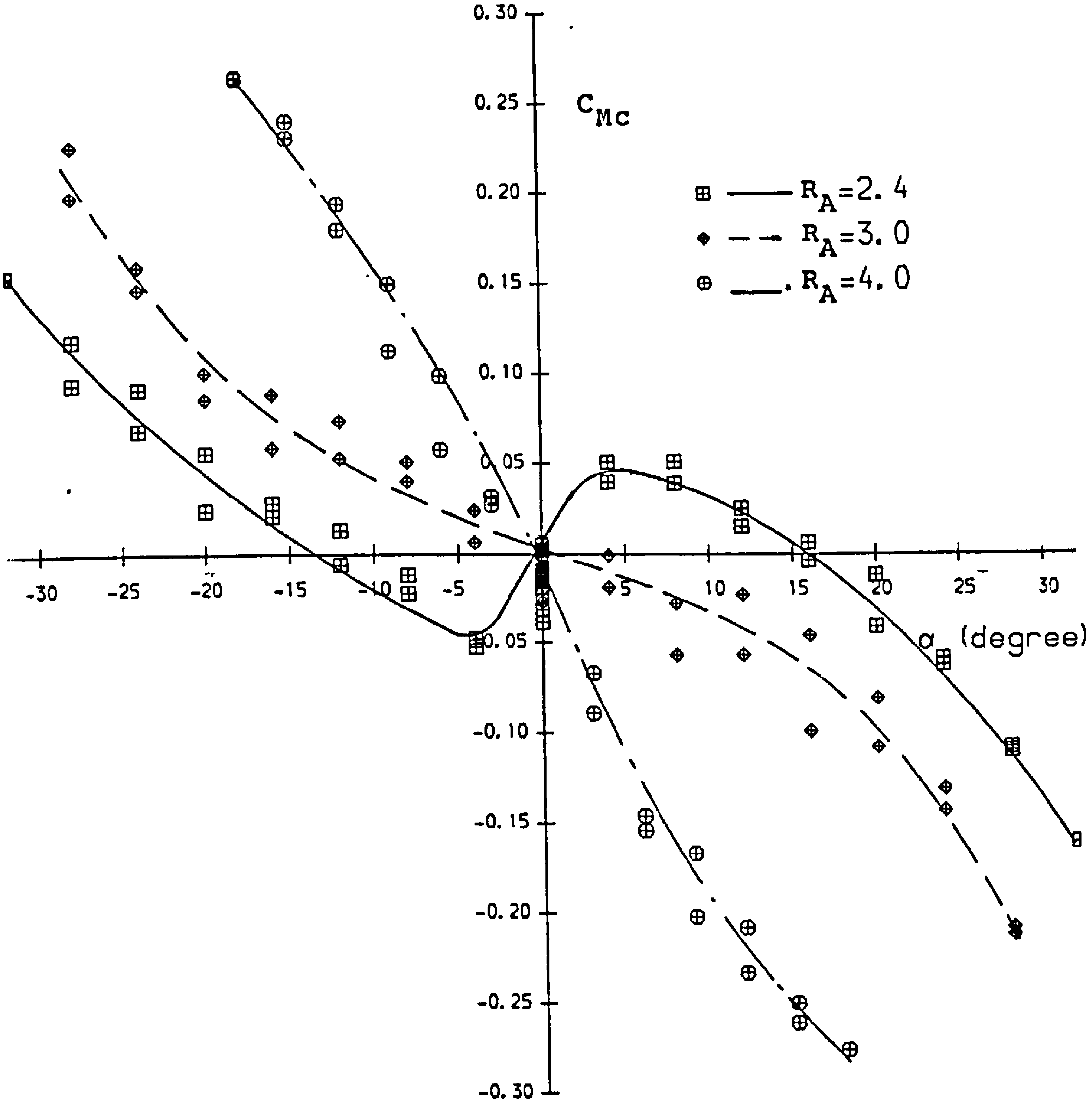

Fig. 4.32 Moment Coefficient versus Angle of Attack for Various Arm Ratios R_A

Nominal Porosity (cu.ft/sq.ft/sec) λ=13
Suspension Line Ratio $R_S=1.33$

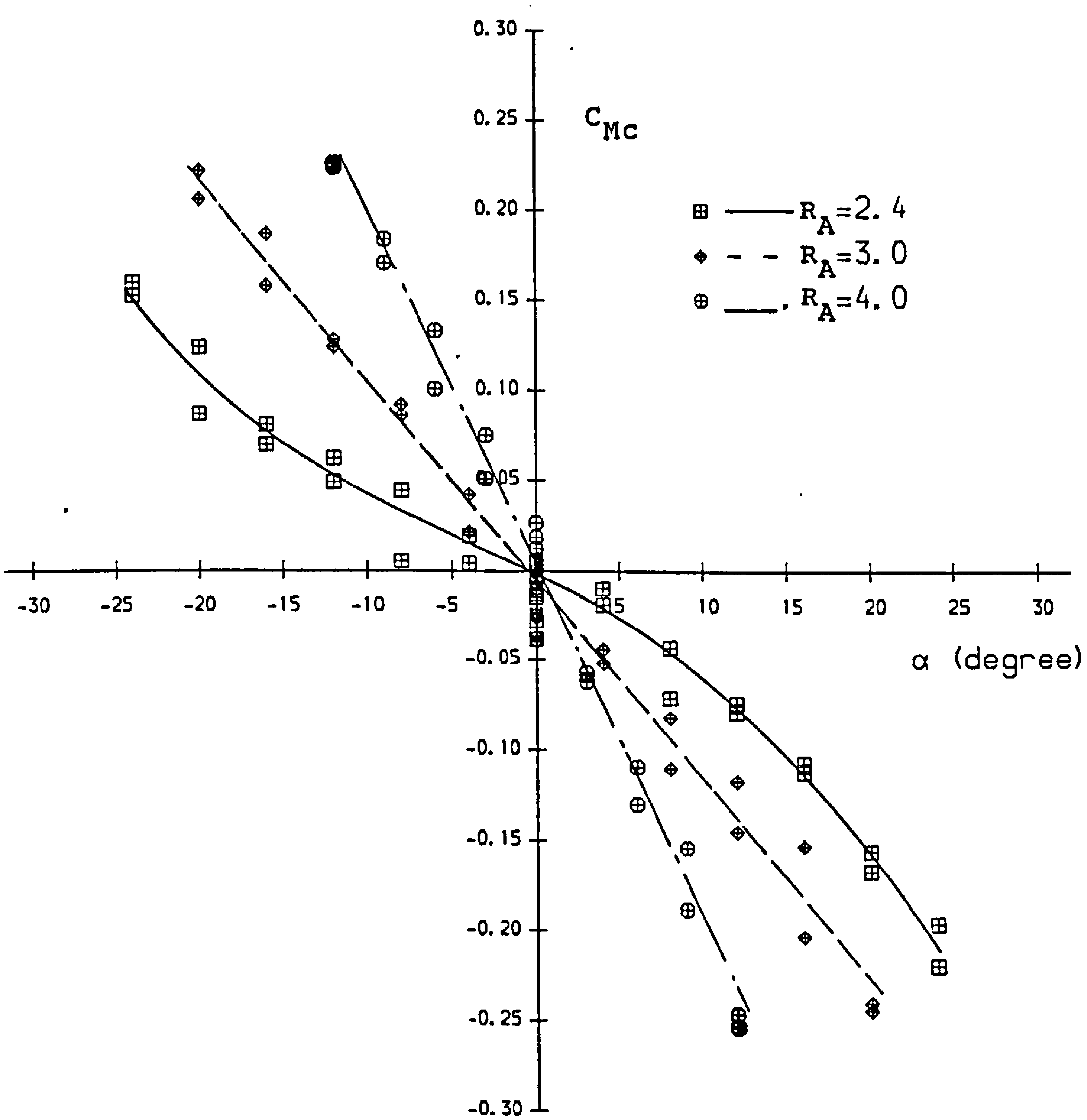

Fig. 4.33 Moment Coefficient versus Angle of Attack for Various Arm Ratios R_A

Nominal Porosity (cu.ft/sq.ft/sec) λ=23
Suspension Line Ratio R_S=1.33

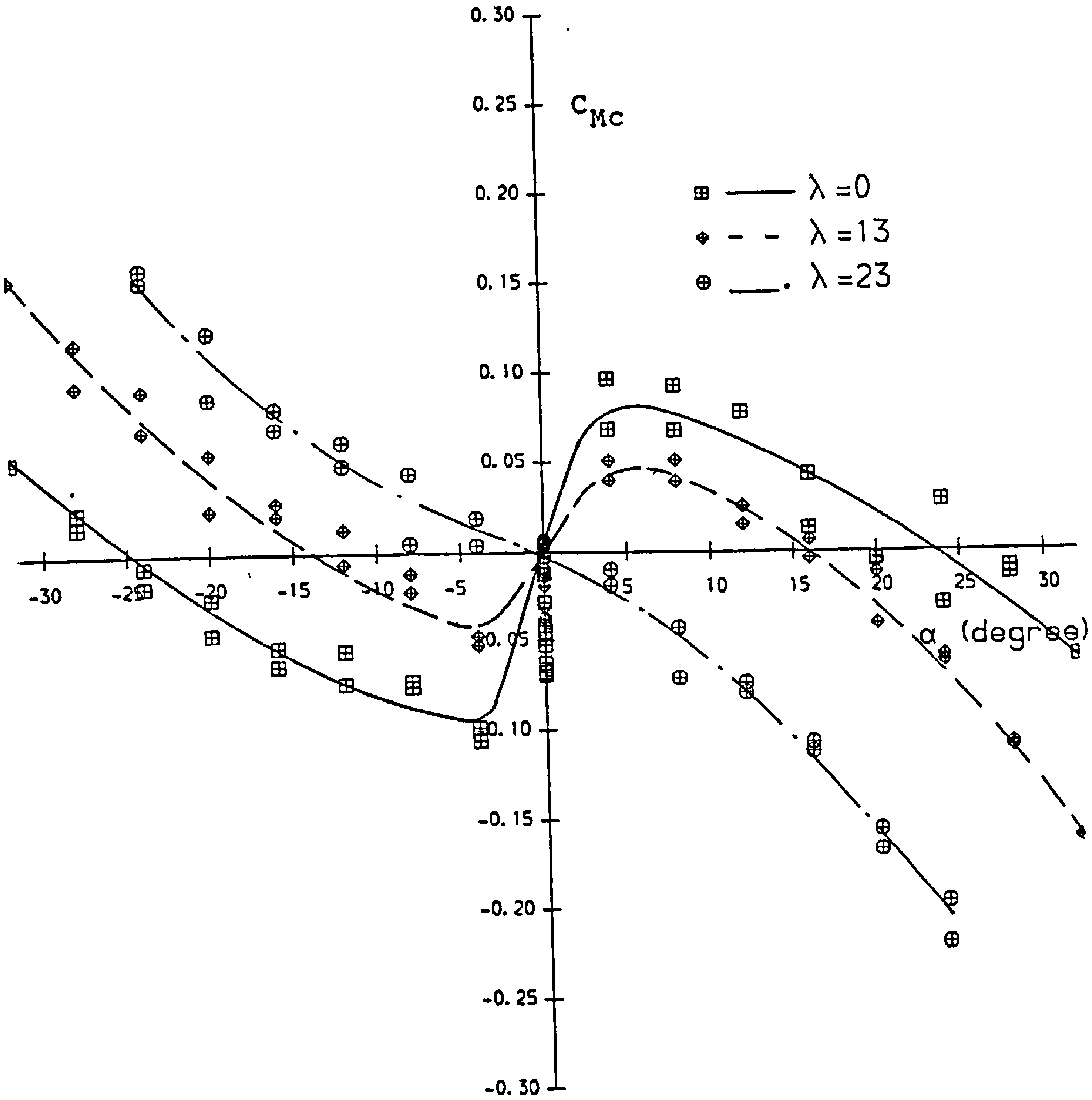

Fig. 4.34 Moment Coefficient versus Angle of Attack
for Various Nominal Porosities λ(cu.ft/sq.ft/sec)

Arm Ratio R_A=2.4
Suspension Line Ratio R_S=1.33

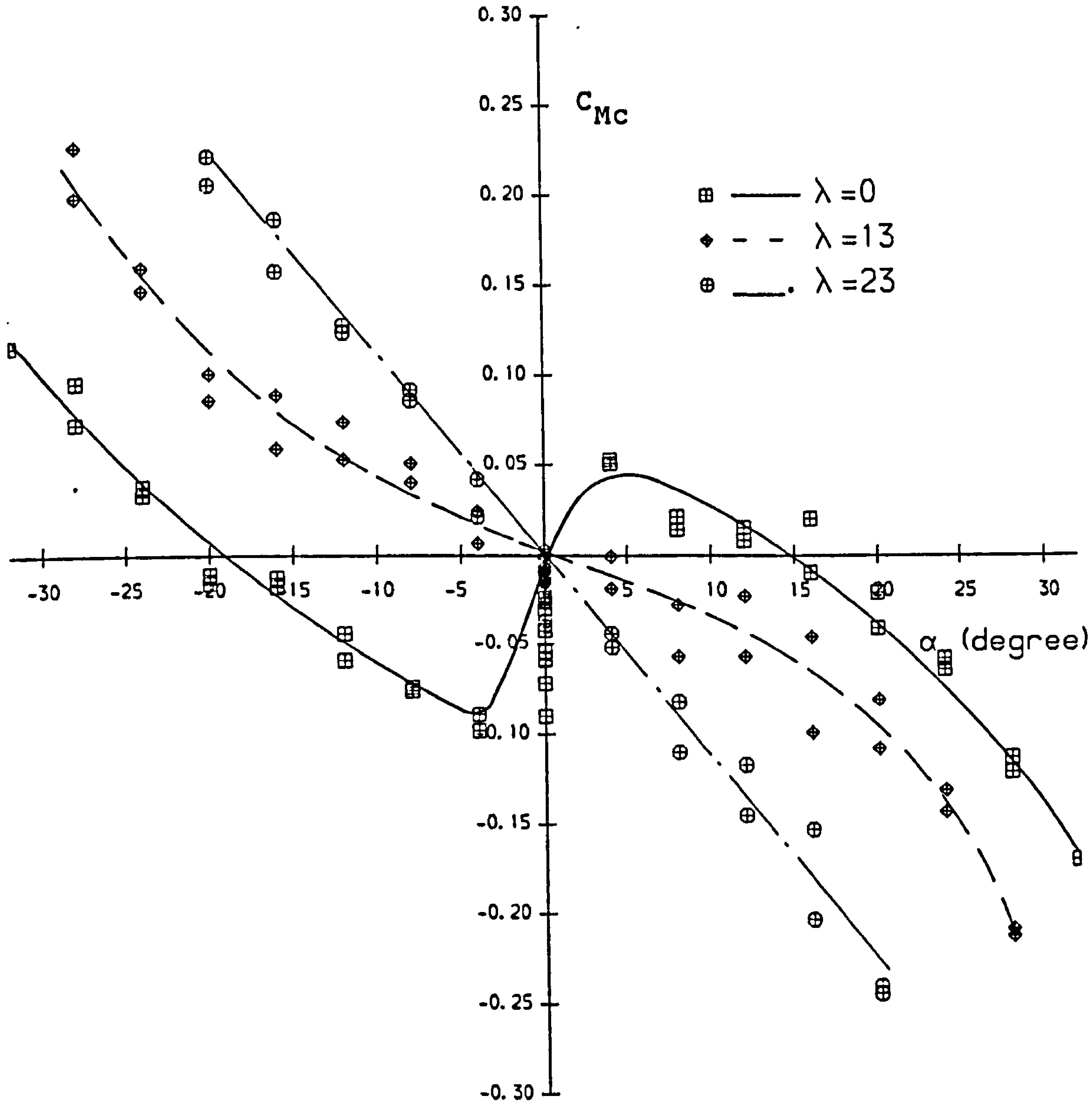

Fig. 4.35 Moment Coefficient versus Angle of Attack for Various Nominal Porosities λ (cu.ft/sq.ft/sec)

Arm Ratio R_A=3.0
Suspension Line Ratio R_S=1.33

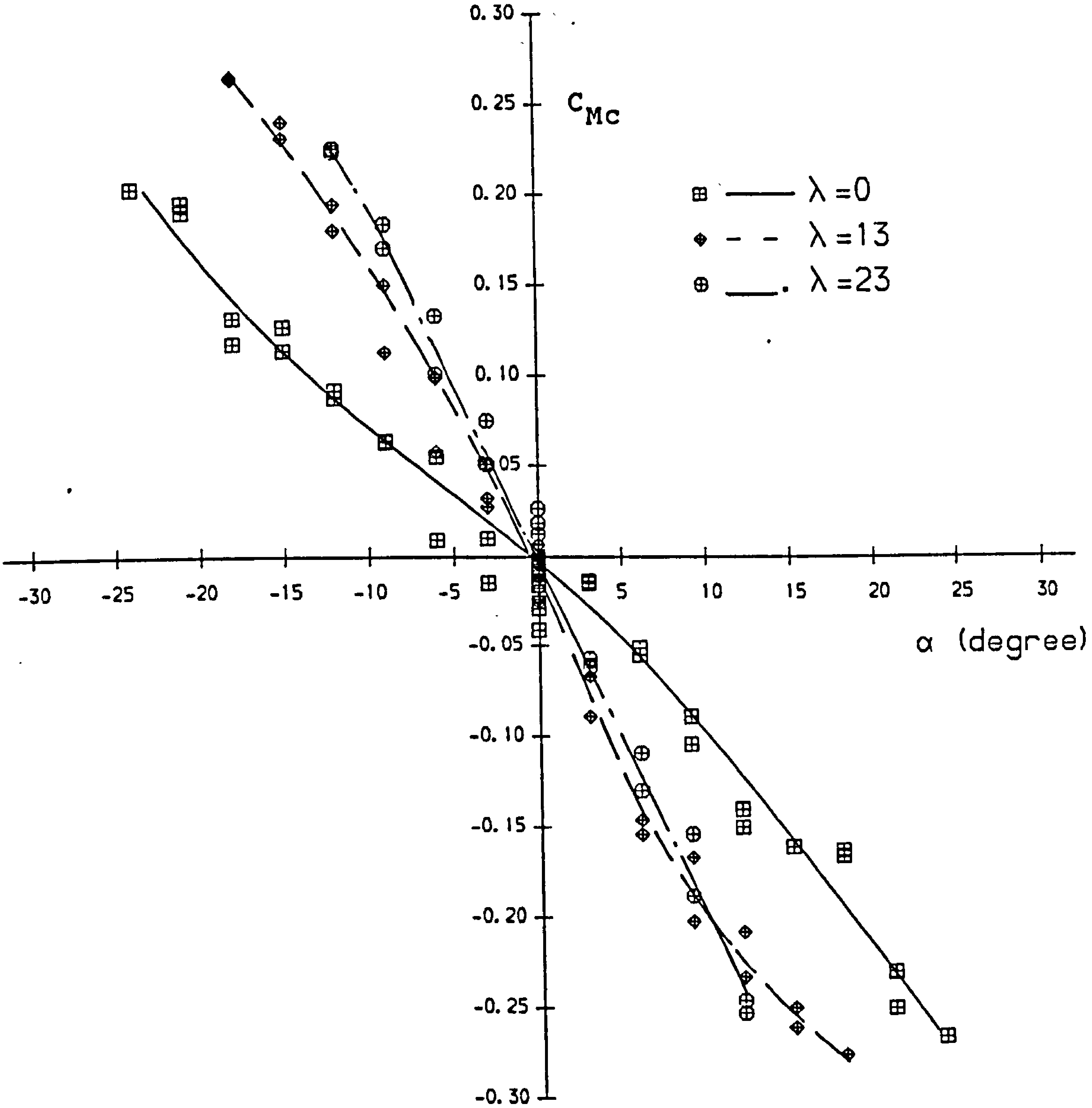

Fig. 4.36 Moment Coefficient versus Angle of Attack for Various Nominal Porosities λ(cu.ft/sq.ft/sec)

Arm Ratio R_A=4.0
Suspension Line Ratio R_S=1.33

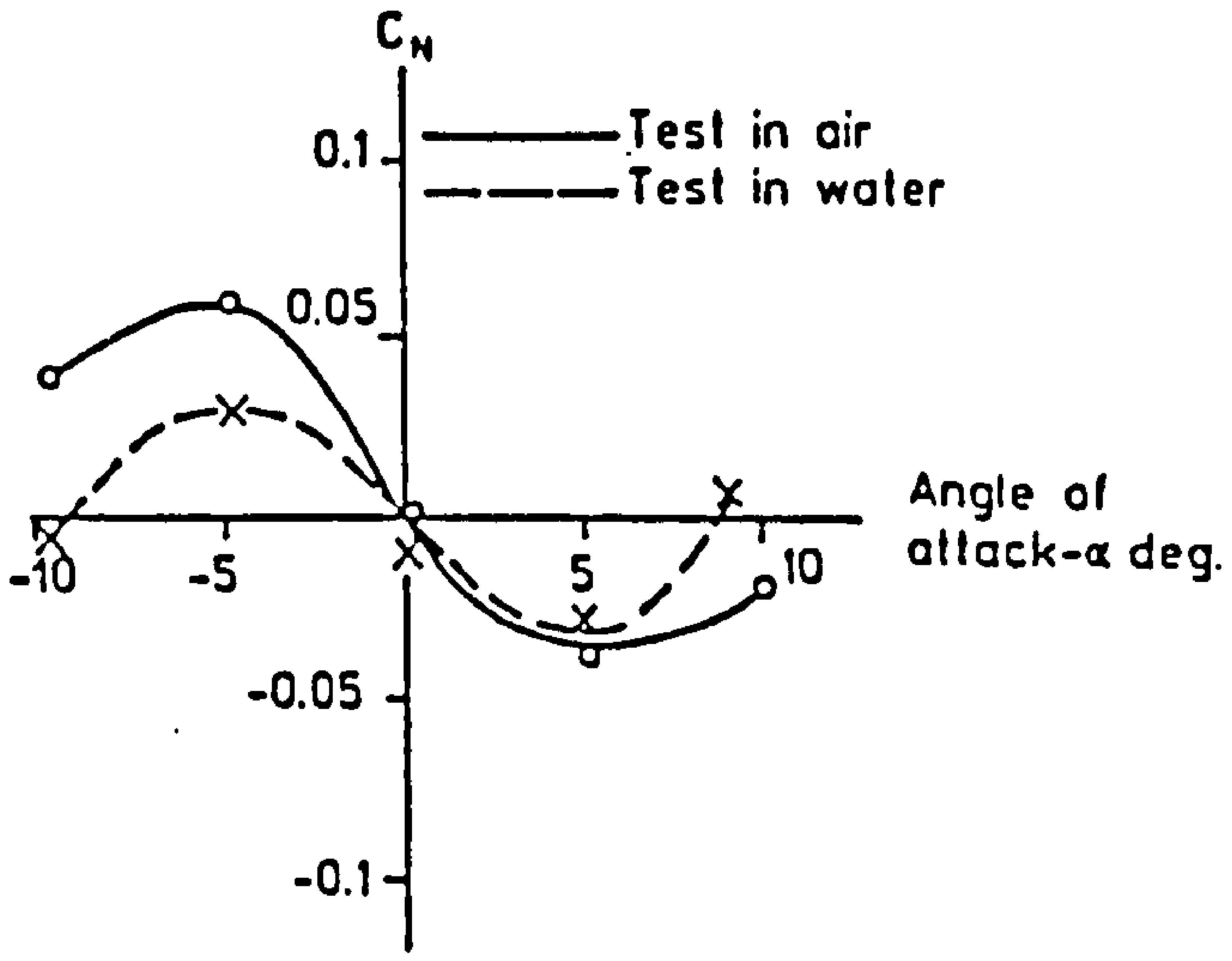

(a) Imporous canopy

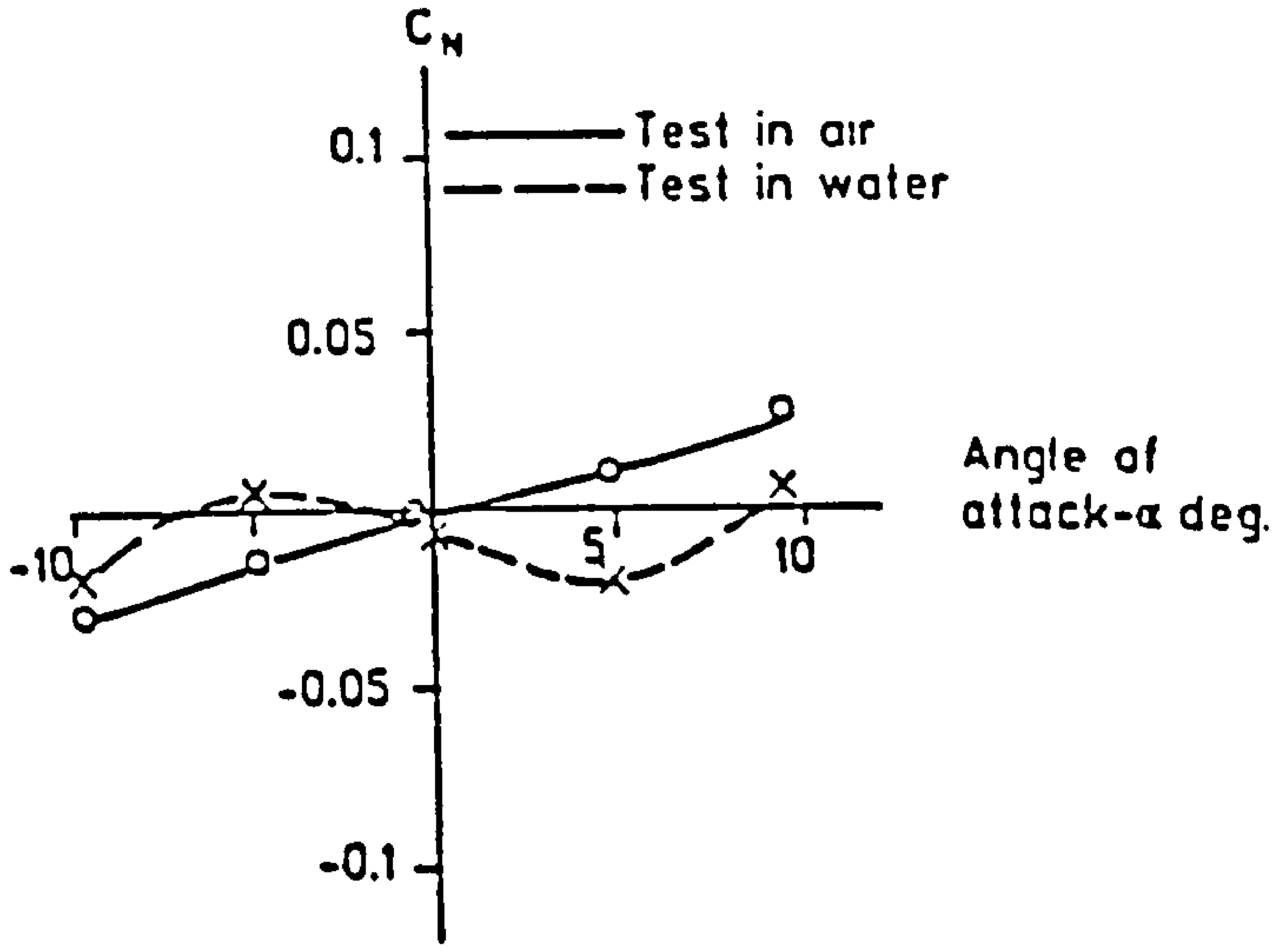

(b) Canopy of medium porosity

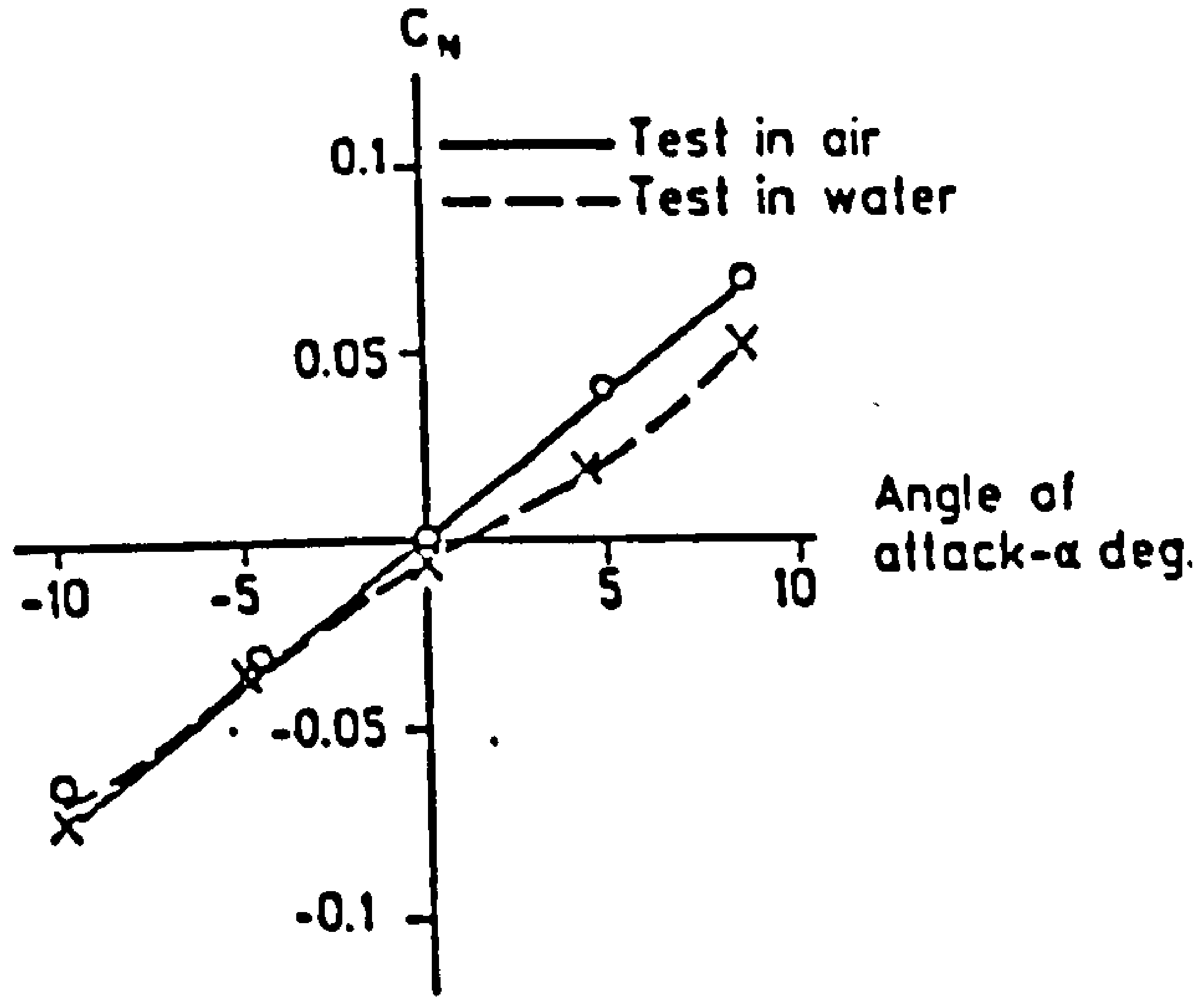

(c) Very porous canopy

Fig. 4.37 Tests on Cross Parachute Canopies in Air and in Water

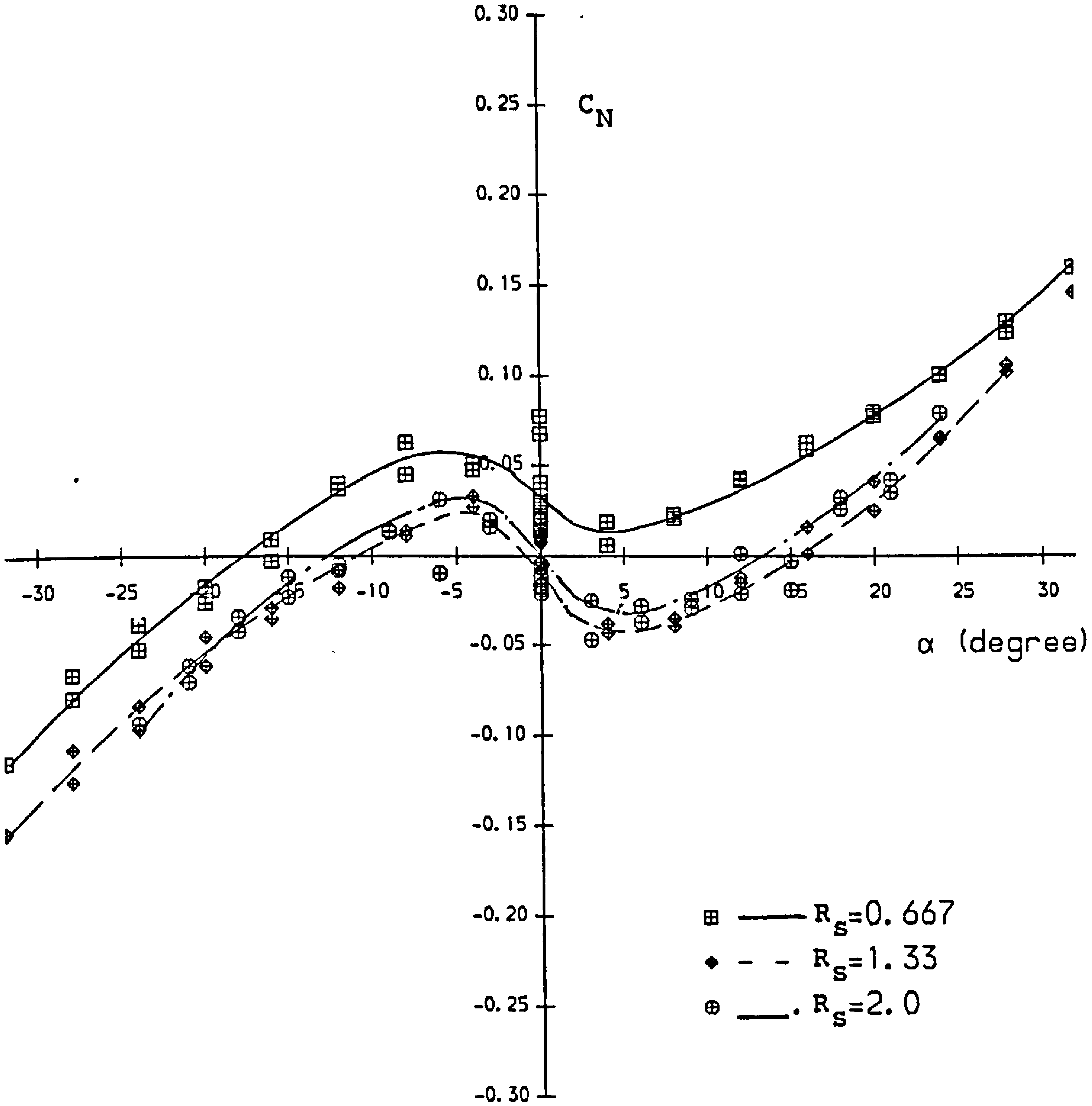

Fig. 4.38 Normal Force Coefficient versus Angle of Attack for Various Suspension Line Ratios R_s

Arm Ratio R_A=2.4

Nominal Porosity (cu.ft/sq.ft/sec) λ=13

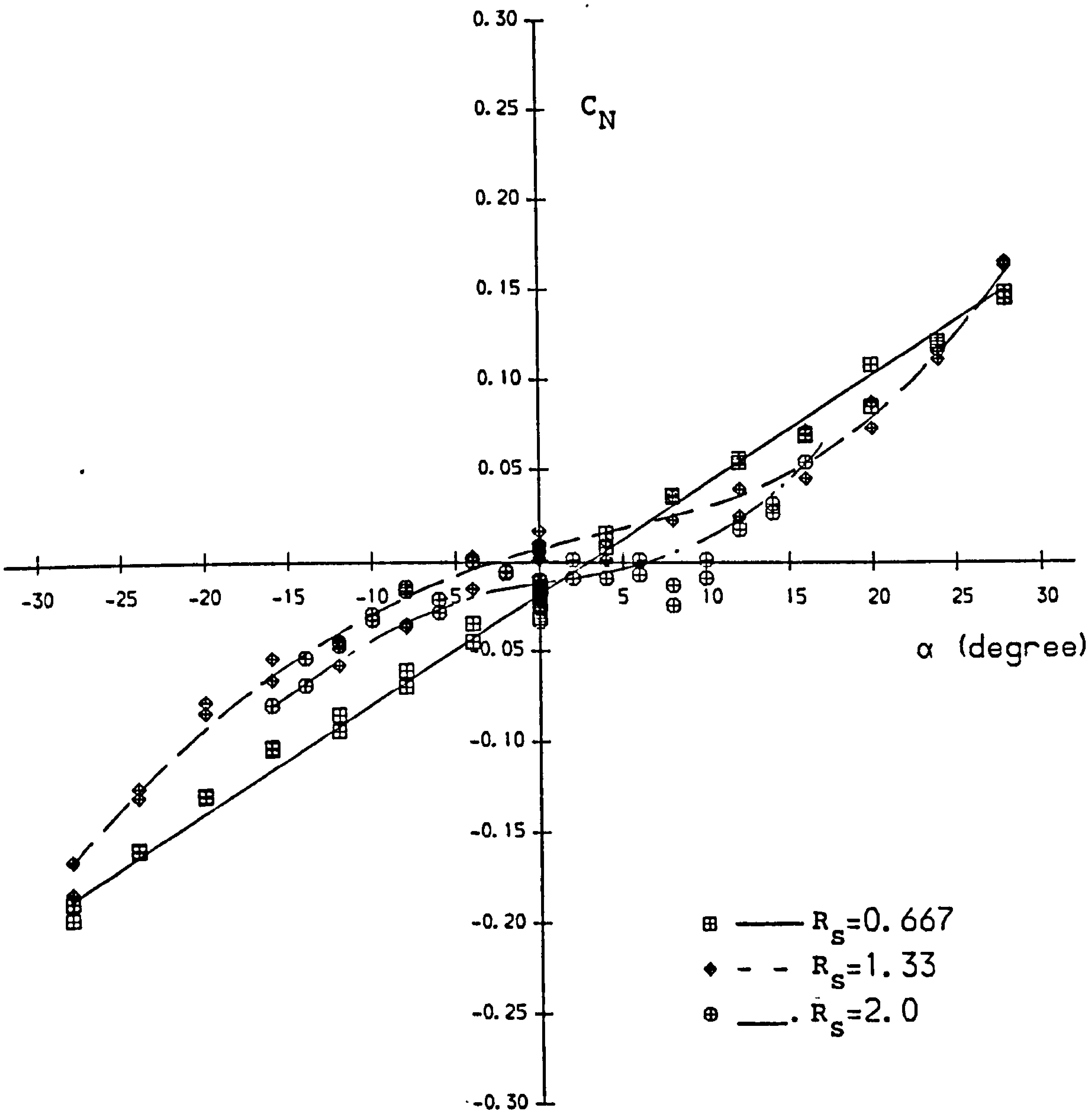

Fig. 4.39 Normal Force Coefficient versus Angle of Attack for Various Suspension Line Ratios R_s

Arm Ratio R_A=3.0
Nominal Porosity (cu.ft/sq.ft/sec) λ=13

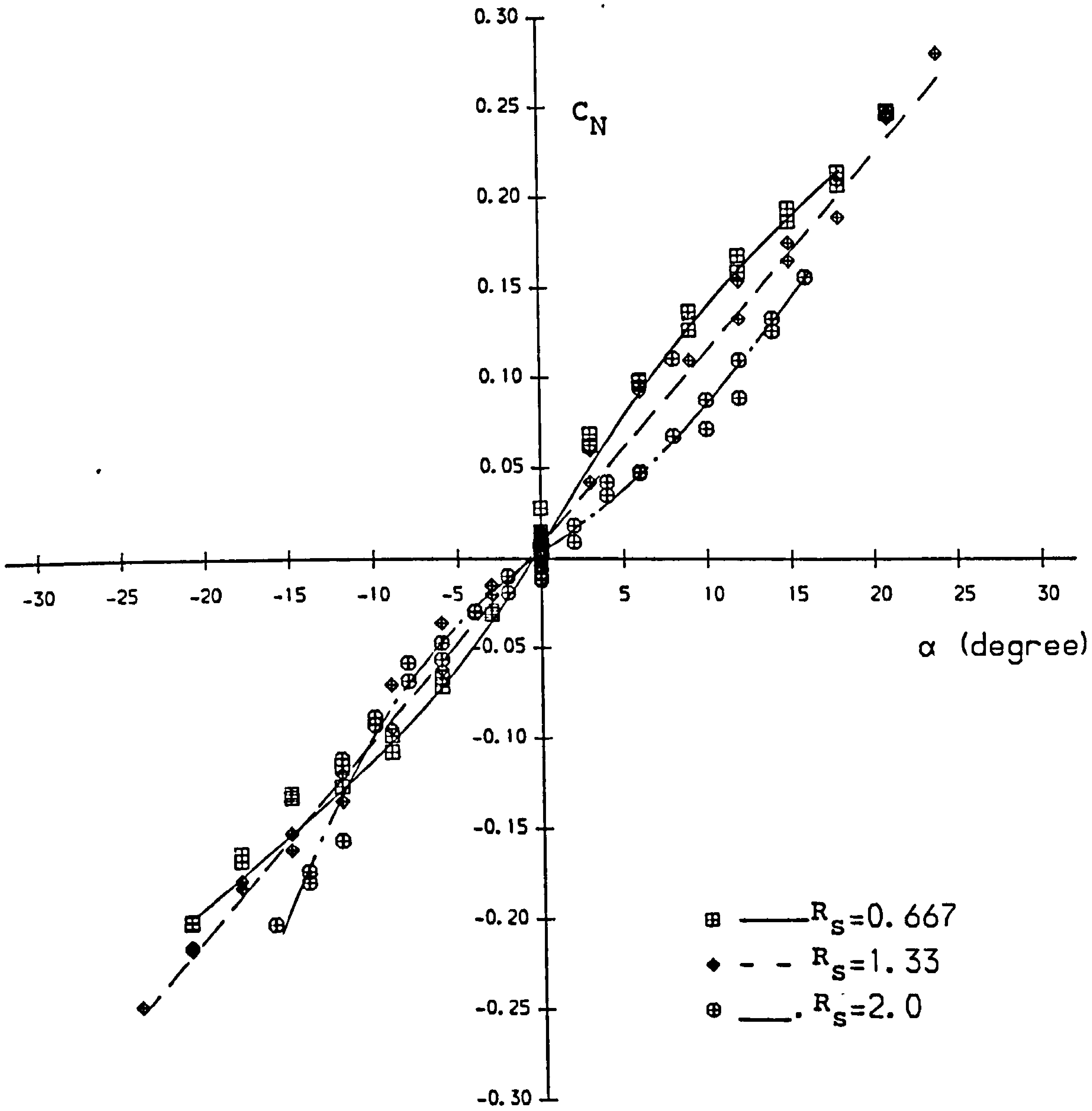

Fig. 4.40 Normal Force Coefficient versus Angle of Attack for Various Suspension Line Ratios R_s

Arm Ratio R_A=4.0

Nominal Porosity (cu.ft/sq.ft/sec) λ=13

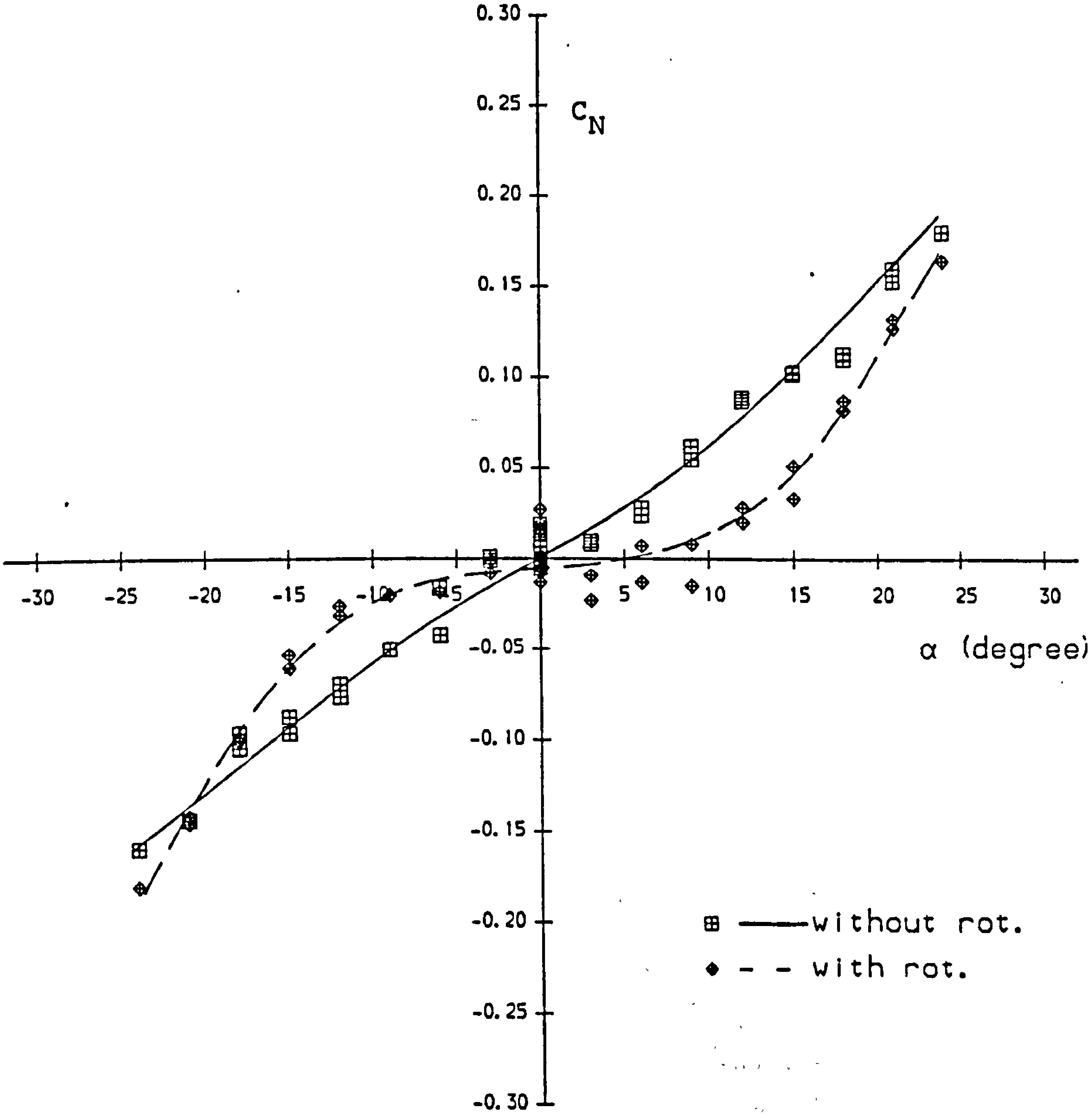

Fig. 4.41 Normal Force Coefficient versus Angle of Attack for Both Rotating and Non-Rotating Cross-Shaped Canopies

Arm Ratio R_A=4.0
Nominal Porosity (cu.ft/sq.ft/sec) λ=0
Suspension Line Ratio R_s=1.33

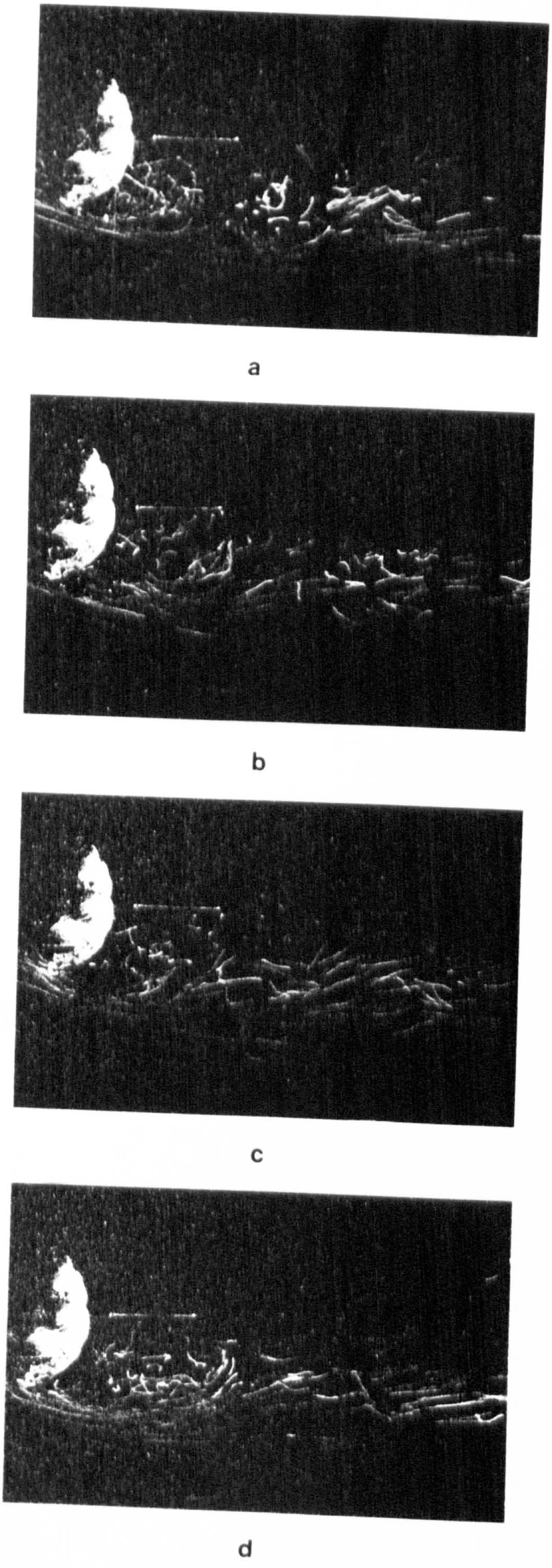

Fig. 4.42 The Wake Formed behind a Cross-Shaped Canopy
(Consecutive frames from a cine film)

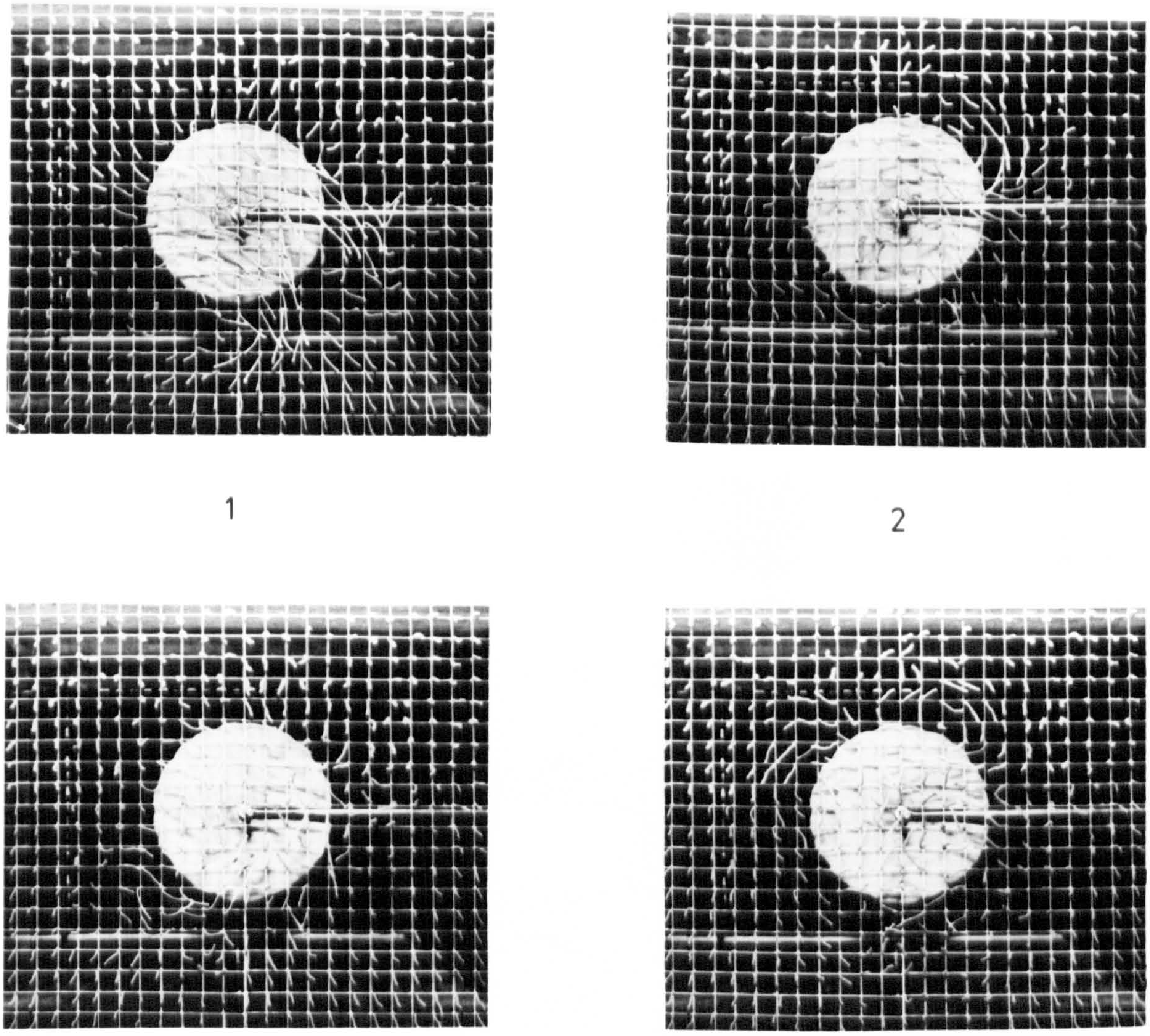

1

2

3

4

Fig. 4.43 The Wake behind a Hemispherical Canopy at Zero Angle of Attack

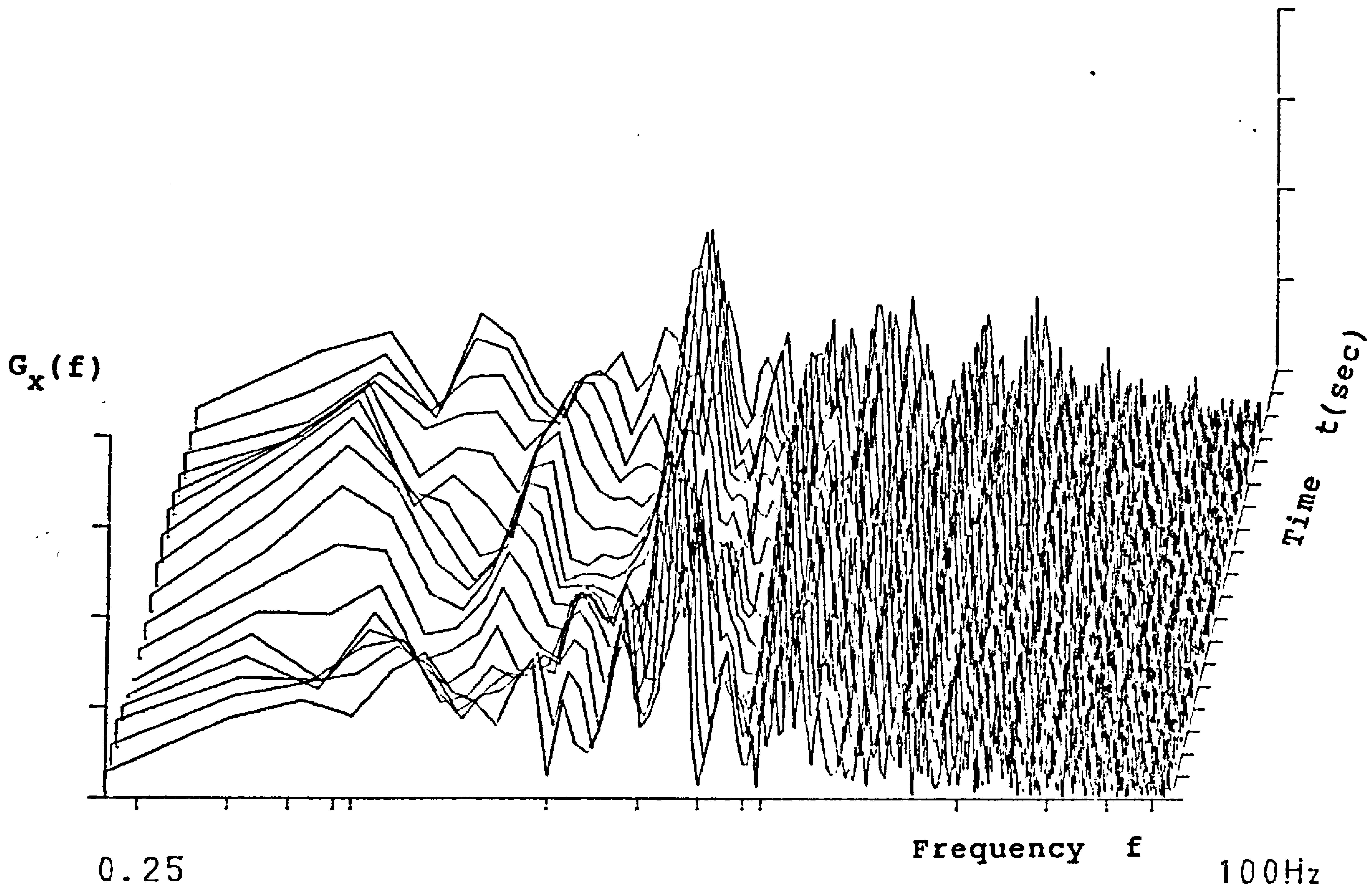

Fig. 4.44 Variation of Frequency Spectra with Time at a Point in the Canopy Wake

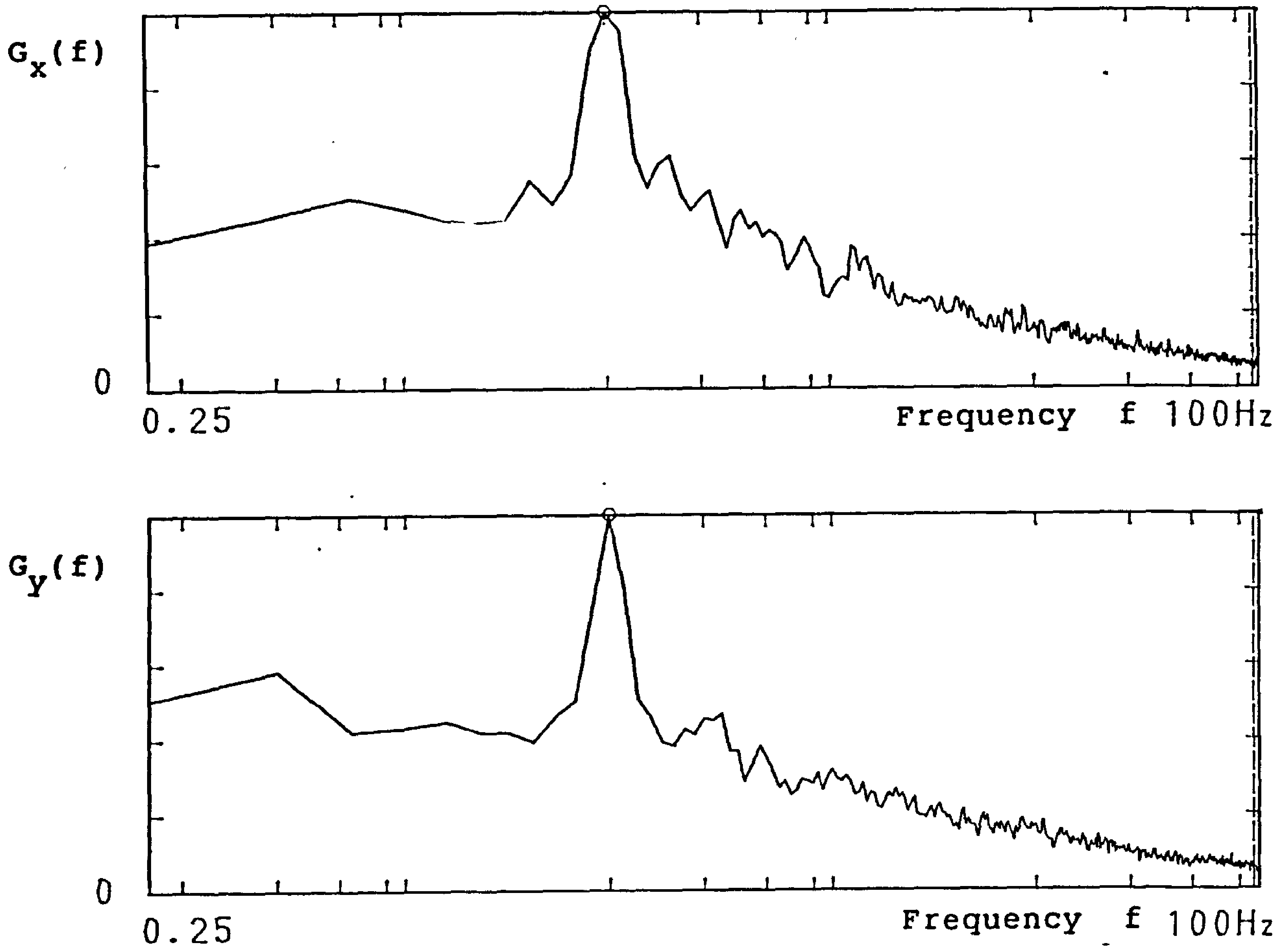

Fig. 4.45 Frequency Spectra at Two Points 180^0 Apart in the Canopy Wake

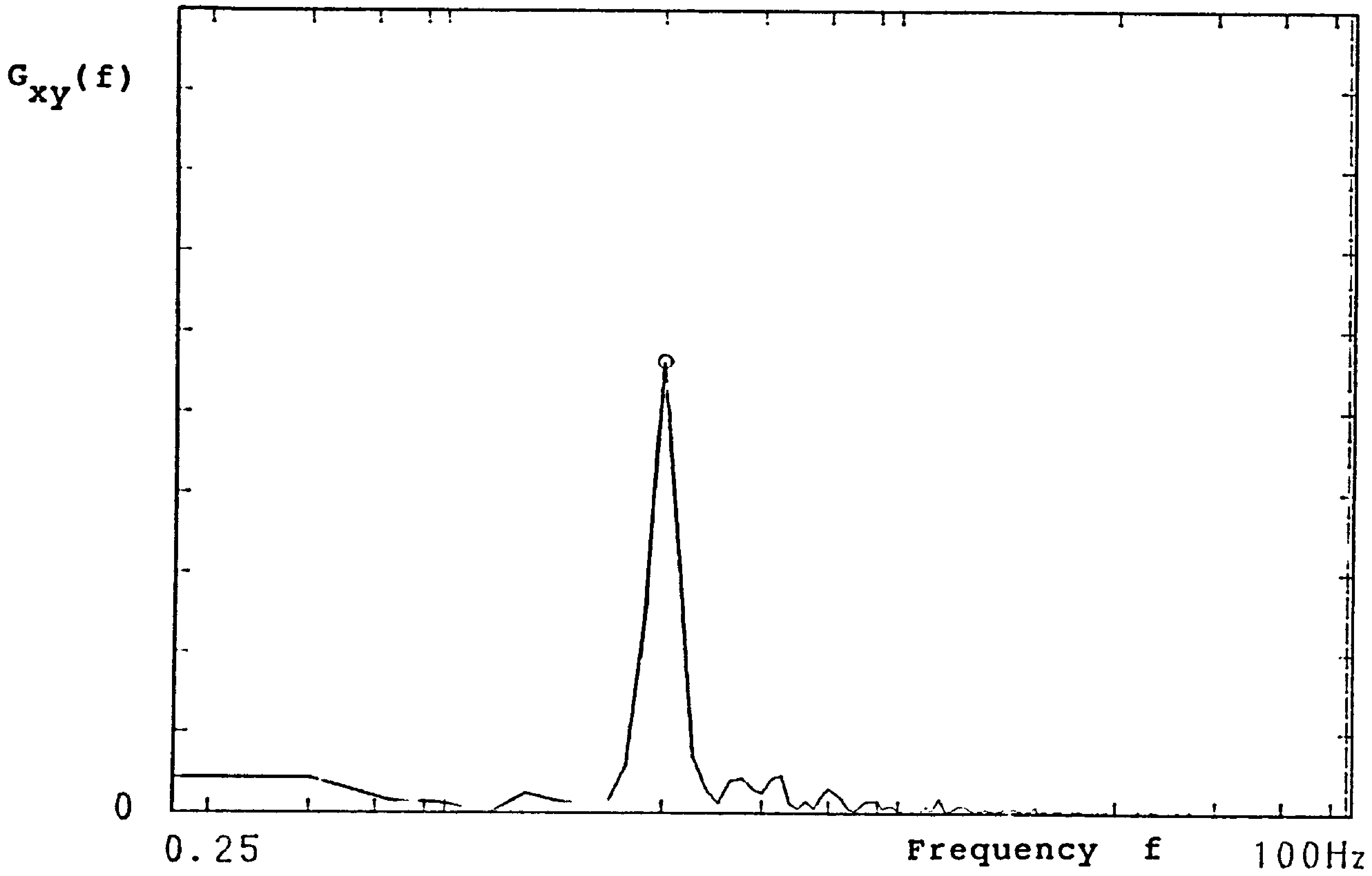

Fig. 4.46 Cross-Spectra from Two Points 180^0 Apart in the Canopy Wake

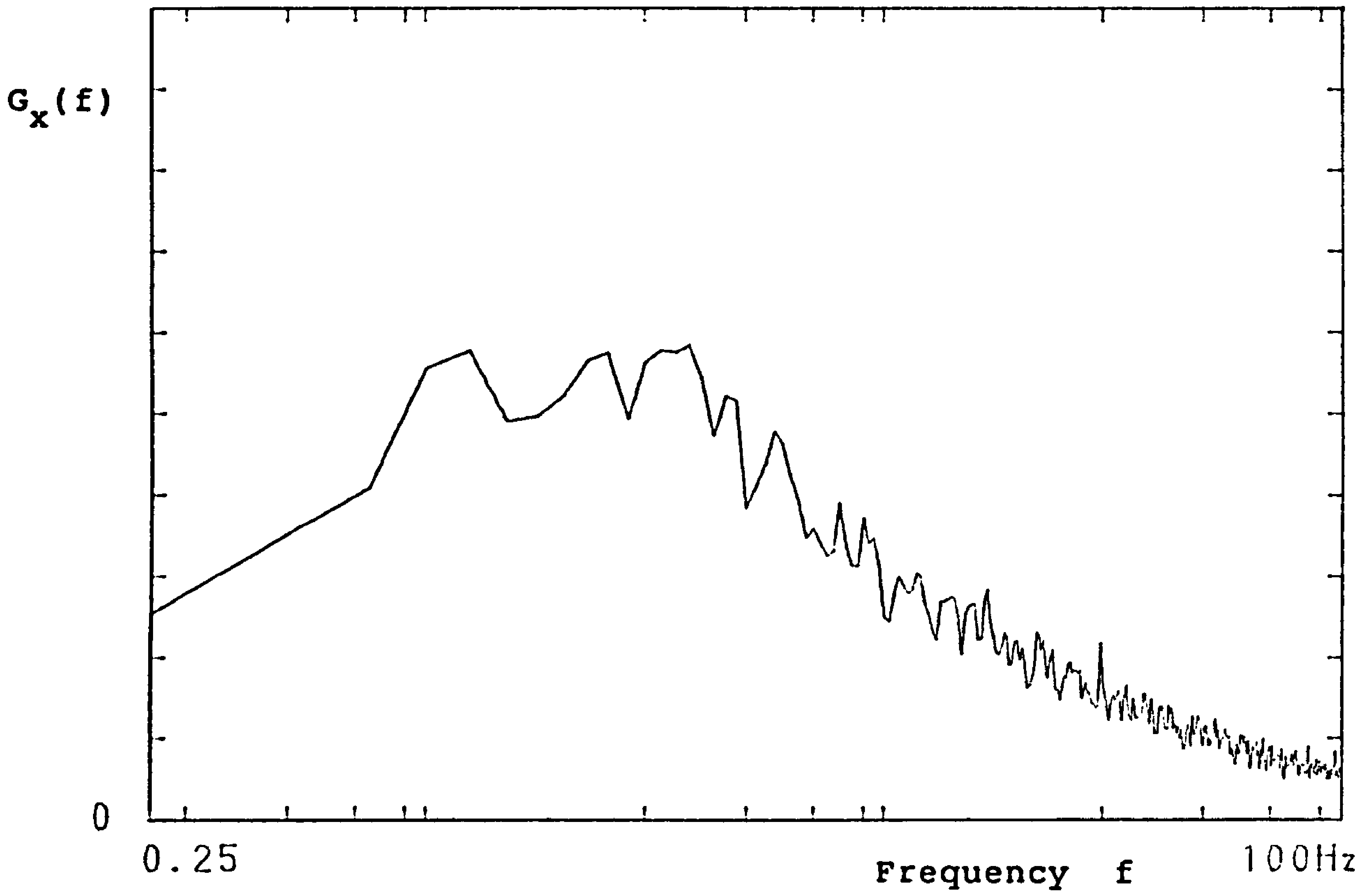

Fig. 4.47 Frequency Spectra on the Axis of Symmetry in the Canopy Wake

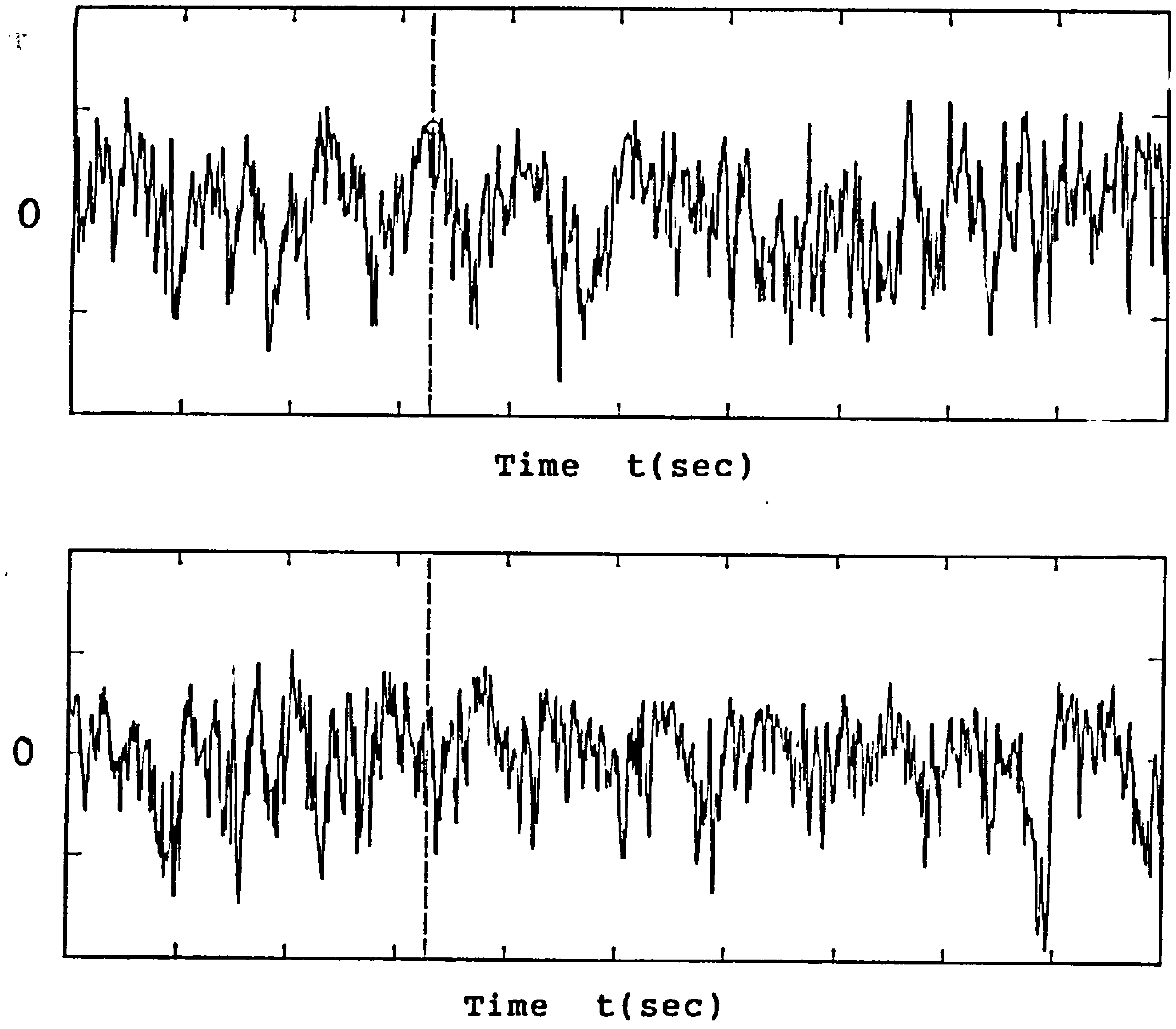

Fig 4.48 Waveforms of Fluctuating Velocity at Two Points 180^0 Apart in the Canopy Wake

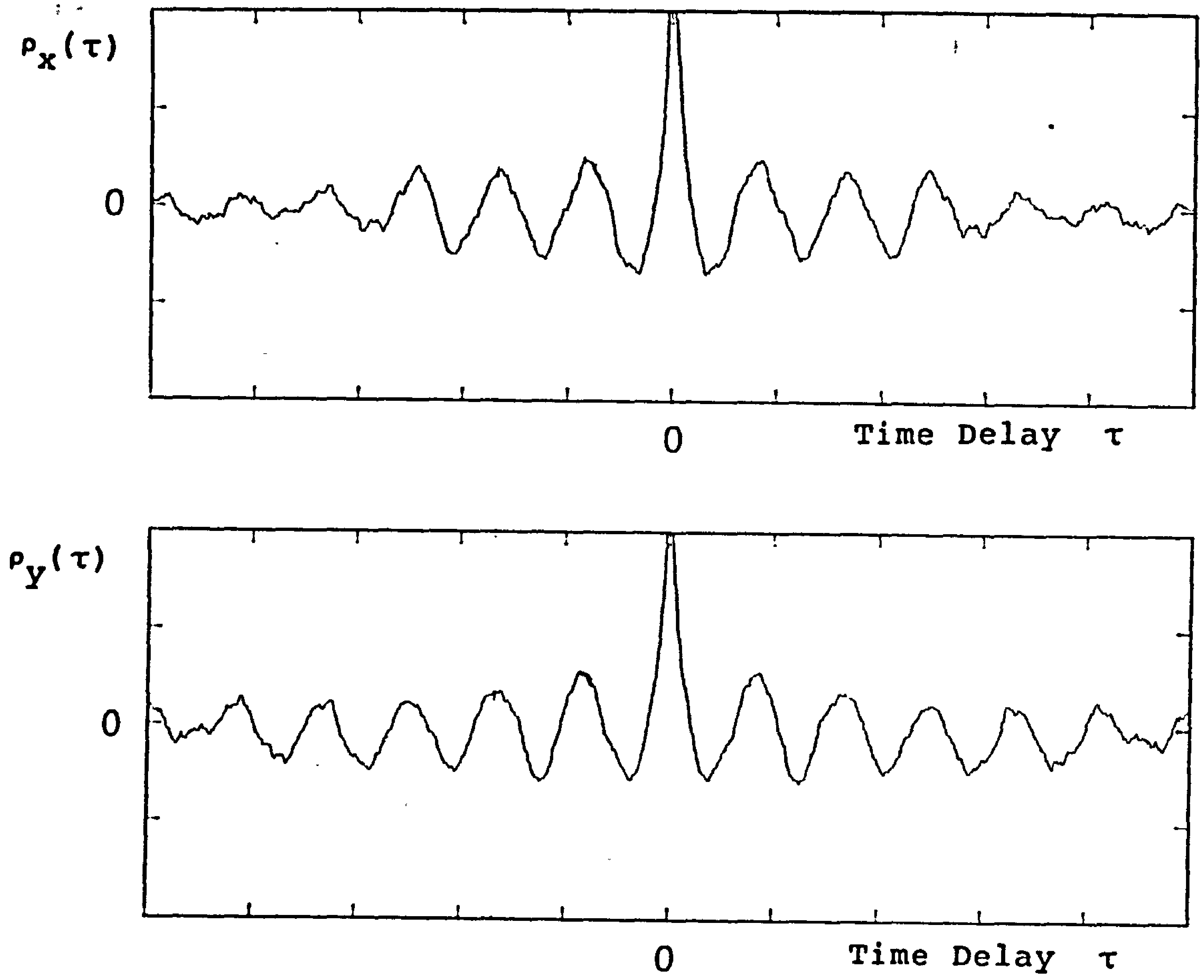

Fig. 4.49 Auto-Correlation Functions at Two Points 180^0 Apart in the Canopy Wake

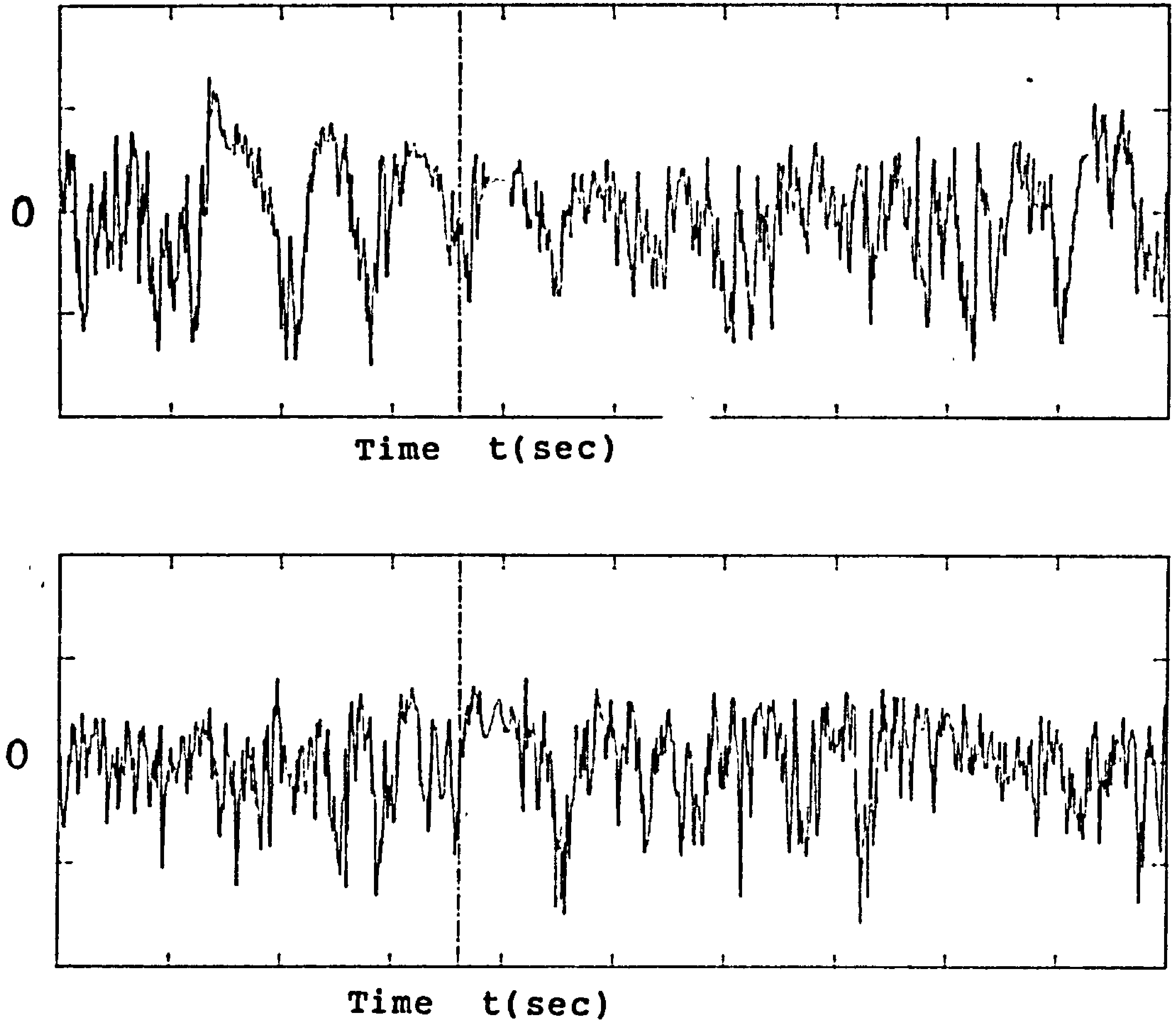

Fig. 4.50 Waveforms of Fluctuating Velocity at Two Points 90^0 Apart in the Canopy Wake

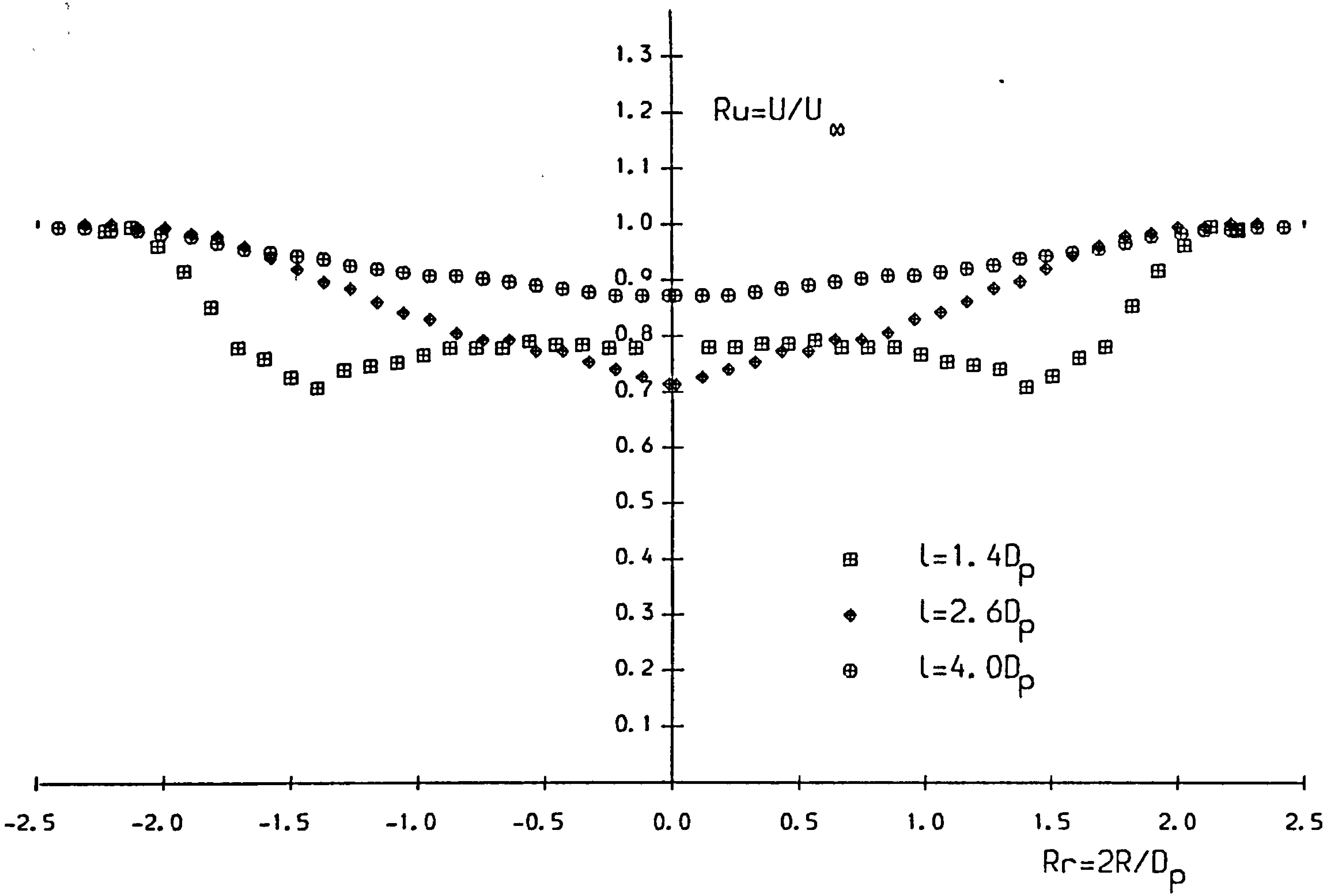

Fig. 4.51 Mean Velocity Distribution along the Radius at various Distance l behind Canopy Skirt

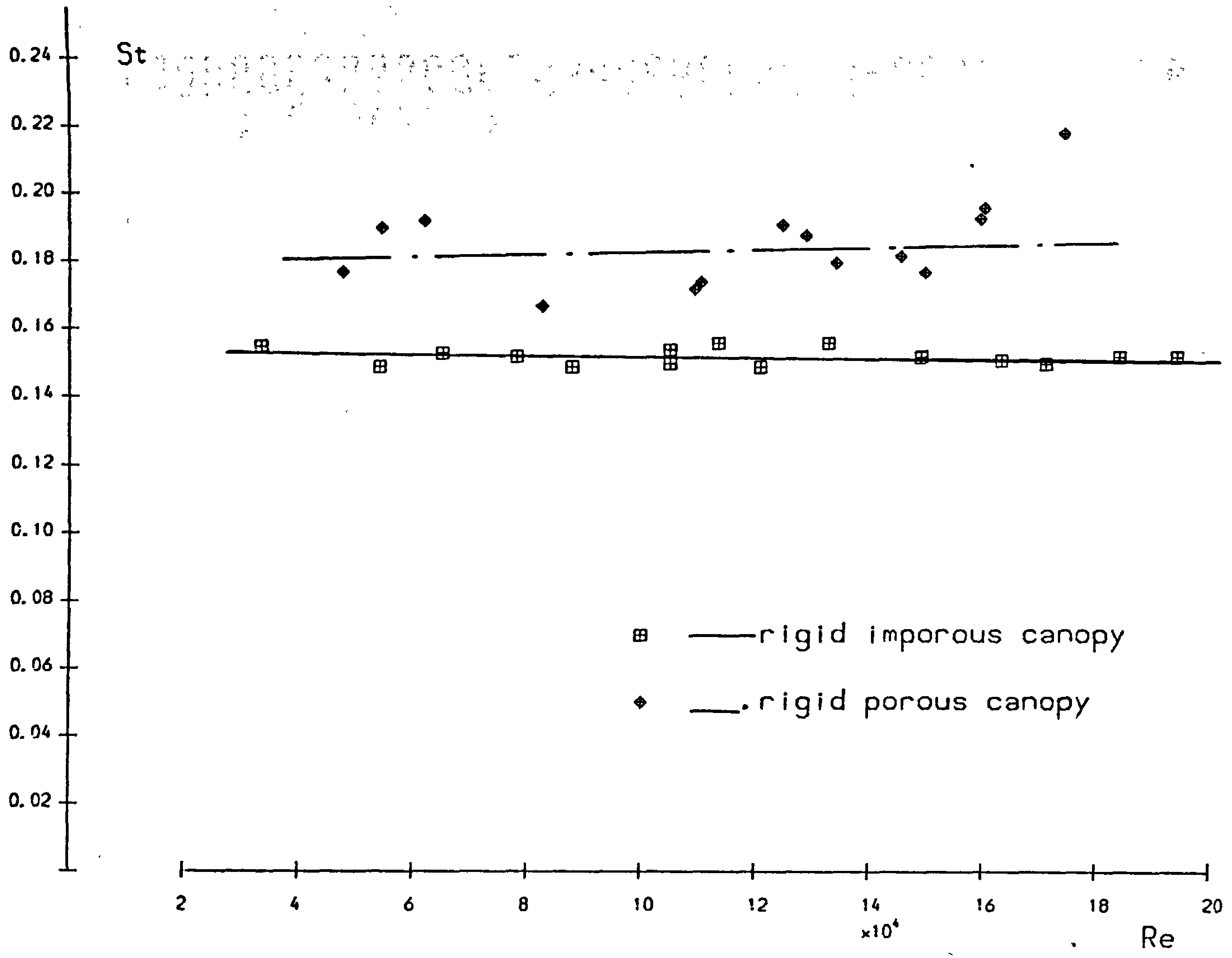

Fig. 4.52 Strouhal Numbers versus Reynolds Numbers in Hemispherical Canopy Wakes

Table 4.1 The Summary of Aerodynamic Force Coefficients of Parachute Canopy Models

Model Name	Tangential Force Coefficient C_{To}		α_{eq} (degrees)		$dC_{Mc}/d\alpha$ (at $\alpha=0$)		Collapse angle α_c (degrees)
	In Wind Tunnel	In Ship Tank	In Wind Tunnel	In Ship Tank	In Wind Tunnel	In Ship Tank	In Wind Tunnel
CS4020	1.01	-	0	-	<0	-	-
CS4013	0.92	0.77	0	0	<0	<0	-
CS4006	0.77	-	0	-	<0	-	-
CM4020	0.98	-	0	-	<0	-	-
CM4013	0.87	-	0	-	<0	-	-
CM4006	0.72	-	0	-	<0	-	21
CL4020	0.79	-	0	-	<0	-	16
CL4013	0.69	-	0	-	<0	-	12
CL4006	0.51	-	0	-	<0	-	10
CS3020	0.96	-	13	-	>0	-	-
CS3013	0.91	0.74	15	10	>0	>0	-
CS3006	0.81	-	20	-	>0	-	-
CM3020	0.90	-	0	-	<0	-	-
CM3013	0.84	0.71	0	8	<0	>0	31
CM3006	0.70	-	0	-	<0	-	30
CL3020	0.82	-	0	-	<0	-	-
CL3013	0.76	0.66	0	0	<0	<0	22
CL3006	0.59	-	0	-	<0	-	20
CS2420	0.91	-	23	-	>0	-	-
CS2413	0.83	-	23	-	>0	-	-
CS2406	0.71	-	14	-	>0	-	-
CM2420	0.88	-	17	-	>0	-	-
CM2413	0.78	-	16	-	>0	-	-
CM2406	0.63	-	20	-	>0	-	-
CL2420	0.81	-	0	-	<0	-	-
CL2413	0.74	-	0	-	<0	-	27
CL2406	0.57	-	0	-	<0	-	25
FHN	0.89	-	± 20	-	>0	-	-
RHN	0.90	-	± 18	-	>0	-	-
RHP	0.79	-	± 12	-	>0	-	-

Table 4.2 Blockage Constraint Effects on C_{To} in Wind Tunnel

Model Name	Projected Area $S_p (m^2)$	Blockage Factor	Tangential Force Coefficient C_{To} (at α=0)		
			Wind Tunnel Test	Corrected by Maskell's method	Ship Tank Test
CS4013	0.078	0.081	0.92	0.74	0.77
CM4013	0.073	0.076	0.87	0.71	-
CL3013	0.060	0.062	0.69	0.61	-
CS3013	0.068	0.071	0.91	0.75	0.74
CM3013	0.067	0.070	0.84	0.70	0.71
CL3013	0.060	0.062	0.76	0.66	0.66
CS2413	0.058	0.060	0.83	0.71	-
CM2413	0.058	0.060	0.78	0.68	-
CL2413	0.058	0.060	0.74	0.65	-

Table 4.3 Aerodynamic Characteristics of Hemisperical Parachute Canopy

Model Name	Characteristics (Rigid or Flexible)	Geometrical (effective) Porosity (%)	$dC_N/d\alpha$ at $\alpha=0$ (rad^{-1})	α_{eq}	Tangential Force Coefficient (at $\alpha=0$) C_{To}
RHN	Rigid	0	-0.34	18^o	0.90
RHP	Rigid	8.6	-0.29	12^o	0.79
FHN	Flexible	0.0	-0.22	20^o	0.89 *

* Based on projected area S_p

Table 4.4 Some of Wake Characteristics Observed by Flow Visualisation and Hot Wire Measurements. (Strouhal Number based on projected diameter D_p)

Model Name	Strouhal Number		Velocity Rate U/UK		Width Rate W/D_p	
	Method		Method		Method	
	Cine camera	Hot wire	Cine camera	Hot wire	Cine Camera	Hot wire
CS4013	0.145 *	0.29			1.74	
CL3013	0.135 *					
CS3013	0.148					
CS2413	0.213	0.28			1.68	
FHN	0.162	0.20	0.76		1.66	1.53
RHN	0.132	0.153	0.60	0.71-0.79	2.00	2.00
RHP	0.171	0.185	0.73		1.76	1.60

* not clear enough

Table 4.5 Strouhal Number Observed on Various Three-Dimensional Bluff Bodies

Body Shape	Strouhal Number	Observer	Method	Date of Observation	Range of Reynolds Numbers
Disc	0.13	Stanton & Marshall	Flow Visualisation	1930	190
Sphere	0.2	Cometta	Hot wire	1957	$4\times10^3-4\times10^4$
Sphere	0.183	Achenbach	Hot wire	1974	$6\times10^3-3\times10^5$
Disc	0.136	Calvert	Hot wire	1967	$3.5\times10^4-5\times10^4$
Cone (conical angle=0)	0.246	Calvert	Hot wire	1967	5×10^4
Cube	0.118	Nakamura & Ohya	Hot wire	1986	$3.4\times10^4-1.47\times10^5$
Square Plate	0.115	Nakamura & Ohya	Hot wire	1986	$3.4\times10^4-1.47\times10^5$
Flexible Hemisph. Canopy	0.61	Jorgensen	Fluctuation Force	1982	6.1×10^5
Rigid Imporous Canopy	0.153	Current Research	Hot wire	1987	$3\times10^4-2\times10^5$
Rigid Porous Canopy	0.185	Current Research	Hot wire	1987	$3\times10^4-2\times10^5$
Flexible Hemisph. Canopy	0.20	Current Research	Hot wire	1987	$8\times10^4-1.4\times10^5$
Flexible Cross Canopy	0.280	Current Research	Hot wire	1987	1.1×10^5

5 DISCUSSION OF THE FLOW FIELD AROUND THE CANOPY

Comparison made between the results of force and moment measurements and flow visualisation leads to a better understanding of the flow field characteristics around parachute canopies, especially of cross parachute canopies.

As will be shown, both the mean velocity distribution determined in the wake as shown in Fig.4.51 and statistical correlation analyses of the two random velocity fluctuations in the wake which had been measured by hot-wire anemometers indicate that the formation of the wakes behind hemispherical or cross-shaped parachute canopies, whether those canopies are rigid or flexible, are essentially similar. One explanation of the experimental evidence is that the wake consists of a chain of irregularly-shaped vortex loops, which move downstream at an average speed of about 0.7 of the undisturbed free stream velocity, possibly overtaking and penetrating one another. However the evidence is not completely conclusive and other descriptions may be possible.

The wake formed behind a cross-shaped parachute canopy is widened by fluid which flows though the large gaps between two of the canopy arms. The large gaps also ensure that the air passes through the canopy freely. This flow field characteristic causes a relatively high drag and good static stability for a cross-shaped parachute canopy.

5.1 The Wake Formed behind Parachute Canopies

5.1.1 General Structure of the Wake

Flow visualisation studies and frequency analyses of power spectra conducted for the field around cross parachute and hemispherical parachute canopies show that these wakes have similar structures, although their detailed shapes and periodicities differ. The flow separates from the canopies somewhere near the hem of the skirt, forming a vortex sheet at the wake boundary. Within this boundary the flow moves at a much lower speed than it does outside. At some distance downstream of the canopy strong vortices can be seen to have been formed from the coalescence of the wake boundary, or vortex sheet, these then move downstream periodically. Over the range of reynolds numbers for which tests were performed, from 3×10^4 to 2×10^5, these vortices diffuse rapidly, so that the visible vortex shedding is only apparent for one to two periods. The strongest periodic vortex shedding for a rigid imporous hemispherical canopy was seen to occur at about 0.8 projected diameters downstream of the skirt, where the wake is widest. It was not possible to analyse periodic motion any nearer than this to the canopy. The periodic motion of the vortex loops does not start immediately downstream of flow separation. There is an interval, during which the vortex loops are formed. The mean velocity distribution which is shown in fig.4.51 differs from that for the disc, which Fail et al[2.38] investigated.

Rosenhead[2.15] suggested, based on the work of both Levy & Forsdyke[2.34,2.35] and Stanton & Marshall[2.38] and on Thomson's Circulation Theory, that the only possible structure of the wake formed behind three-dimensional bluff bodies is a sequence of irregularly-shaped vortex loops, or vortex rings, discharged downstream in some purely randomly-orientated plane which is determined by the location of the point at which the vortex layer starts to roll up.

Wakes formed behind parachute canopies are highly conplex. Frame by frame analyses of the cine and video films of the helium bubble flow visualisation does suggest such a chain of vortex loops in the wake as shown in Fig.5.1. In the frame (a) of the four consecutive frames from a cine film shown in Fig.4.42 there is evidence of at least two vortex rings shed from the canopy. The shapes of the wake in frame (b) and (d) are similar. Although there is less evidence of two vortex rings in frame (c) because of the imperfection of the illumination technique, the first vortex is similar to that in the frame (a). The time interval between the first and third frames is the vortex shedding period. However it is accepted that further experimental investigations with more refined technique are needed to completely confirm this wake description.

Over the range of Reynolds numbers at which tests were conducted the vortex loops in the wake diffused so rapidly that some of the flow visualisation photographs show only one period of the shedding process. Because of this wake diffusion it is easy to confuse the wake structure with that of a closed-bubble wake as was suggested from Jorgensen's[1.26] 1982 observations. However, as flow visualisation indicates, the vortex loops form up in chains periodically. Furthermore, the mean velocity distribution along the radius illustrated in Fig.4.51 shows positive mean velocity everywhere. The flow pattern in the wake formed behind the hemispherical canopy is not as Jorgensen proposed.

The statistical correlation analysis performed with the Fast Fourier Transform Analyser indicate that the velocity fluctuation throughout the wake has the same periodicity, as shown in Fig 4.45. Since the velocity fluctuation is dominated by periodic motion, the two hot-wire anemometer signals, x(t), and y(t), 90° or 180° apart, at the same distance from the canopy skirt can be expressed as Fourier series

$$x(t) = \sum_{n=1}^{\infty} (a_{nx} \cos n\omega_x t + b_{nx} \sin n\omega_x t)$$

$$y(t) = \sum_{n=1}^{\infty} (a_{ny} \cos n\omega_y t + b_{ny} \sin n\omega_y t)$$

As defined in section 4.5, with further detail obtained from Bendat[5.1](1958), the auto-correlation functions $R_x(\tau)$ and $R_y(\tau)$, the cross-correlation function $R_{xy}(\tau)$ and the coherence function $\gamma_{xy}{}^2(f)$ are expressed as follows:

$$R_x(\tau) = \lim_{T\to\infty} \frac{1}{T} \int_0^T x(t)x(t+\tau)dt$$

$$R_y(\tau) = \lim_{T\to\infty} \frac{1}{T} \int_0^T y(t)y(t+\tau)dt$$

$$R_{xy}(\tau) = \lim_{T\to\infty} \frac{1}{T} \int_0^T x(t)y(t+\tau)dt$$

where τ __ time delay

f __ frequency

The auto-correlation functions of the signals x(t) and y(t) at time delay $\tau=0$ are respectively used to normalise these functions, then

$$\rho_x(\tau) = \frac{R_x(\tau)}{R_x(0)}$$

$$\rho_y(\tau) = \frac{R_y(\tau)}{R_y(0)}$$

$$\rho_{xy}(\tau) = \frac{R_{xy}(\tau)}{[R_x(0)R_y(0)]^{1/2}}$$

And the coherence function

$$\gamma_{xy}^2(f) = \frac{|G_{xy}(f)|^2}{G_x(f)G_y(f)} \leqslant 1$$

Where $G_x(f)$, $G_y(f)$ are the power spectral density functions and $G_{xy}(f)$ is the cross-spectral density function.

If the coherence function γ_{xy}^2 is zero at a particular frequency, then x(t) and y(t) are fully independent. If $\gamma_{xy}^2=1$ however, x(t), y(t) are fully coherent that is, they are identical signals. The coherency function of two signals obtained 180° apart behind the parachute canopy is shown in Fig.5.2 to be 0.8.

The normalized cross-correlation function as shown in Fig.5.3 between these two signals 180° apart appears sinusoidal. This indicates that these two signals correlate with each other. The phase angle observed between them was about 180°. The reciprocal value of the time between two successive maxima in the cross-correlation function curve is the periodicity, and this is in good agreement with what was indicated by the power spectra.

The cross-correlation function formed between two signals which are 90° apart is shown in Fig.5.4. At $\tau=0$ its value lies between zero and a negative minimum and this implies that the phase angle of the two signals is in the range from 90° and 180°. From these statistical correlation results it can be concluded that the vortex shedding behind the parachute canopy is not axisymmetrical. The wool tuft visualisation shown in Fig.4.43 also exhibits this asymmetry in the vortex shedding structure but it was not possible to support this technique with helium bubble flow visualisation as in the current research programme not more than one-half of the field can be viewed at any instant.

Results from these statistical analyses of periodic velocity fluctuation in the wake support the flow pattern of a chain of irregularly orientated vortex loops shed from the parachute canopy as shown in Fig.5.1. Similar results would also be obtained if a helical vortex structure was formed in the wake of the canopy. However, such a wake formation would not satisfy Thomson's Circulation Theory, as was demonatrated by Levy & Forsdyke[2.35]. There might also be other explanations. Much more detailed study of wake flow is necessary before the favoured vortex ring explanation can be completely accepted.

In a summary of some theoretical and applied fluid mechanics[5.2] the mechanism of two moving vortex rings was considered by Hicks[5.3](1922). It is shown in Fig.5.5 that if two vortex rings A and B having the same sense move along a common axis, one behind the other. The points 1 and 2 are on the vortex A, and points 3 and 4 are on the vortex B. V_1,V_2, V_3 and V_4 are resultant induced velocities at point 1,2,3 and 4 respectively. For point 1 induced velocity is

$$V_1 = V_{12} + V_{13} + V_{14}$$

Where V_{12} — velocity induced at point 1 by the vortex at 2

V_{13} — velocity induced at point 1 by the vortex at 3

V_{14} — velocity induced at point 1 by the vortex at 4

Similarly for induced velocities at point 2,3 and 4.

Hence the forward one will receive an induced velocity component in the outward direction, while the rear one will receive one in the inward direction. At some point P outside the two vortex rings the velocity induced by the vortex rings, as shown in Fig.5.6, is:

$$V_p = \frac{\Gamma}{4\pi} \int_c \frac{\sin\alpha}{r^2} ds$$

Where Γ _ velocity of the vortex ring

c __ circumference of vortex ring

This relationship shows that as its radius increases, the forward vortex decreases in speed while the rearward vortex increases in speed. Finally, the rear vortex overtakes and passes through the larger forward vortex. The process then repeats itself for the two vortices in their reversed position, which then successively penetrate one another.

The double-dot lines in the schematic presentation of the vortex configuration shown in Fig.5.1 represent the trace of the vortex loops. Although theory predicts predicts this process, there is no obvious evidence in the flow visualisation studies to confirm that it is so.

From his flow visualisation studies conducted on the wake formed behind a sphere Taneda[2.46] concluded that at Reynolds numbers between 10^4 and 10^6 and in a uniform flow the sphere is subjected to a side force. Similarly, the normal force which was measured on a cross parachute canopy at zero angle of attack exhibits fluctuations, as seen in Fig.5.7. This is corroborate evidence that the wake formed behind a three-dimensional parachute canopy does not consist of symmetric vortex loops which roll up randomly from the vortex layer.

The cross-correlation function from the two hot-wire sensors located 180° apart has a 180 degrees phase angle. Achenbach[2.32] made a similar observation for the flow behind a sphere, as did Nakamura & Ohya[2.42] for the flow behind a square prism. The direction of the side force or orientation of the vortex loops do not appear to be completely random, but further work is required to understand the mechanism which determine its behaviour.

5.1.2 The Flow Field around Cross Parachute Canopies

Although the vortex shedding formation in the wake behind a cross parachute canopy is basically the same as that behind a rigid hemispherical canopy, the wake shape and width observed in the flow which occurs through the gap formed between cross canopy arms differ from the flow across these arms, as shown in Fig.4.4.

With a cross canopy the flow through the gap formed between the arms can be seen in Fig.4.4(b). As this fluid flows into the canopy under surface, it decelerates and loses energy by mixing. Then it accelerates through the gaps to the canopy upper surface, where it goes on to join the wake downstream. Since the fluid which it joins has also lost energy by mixing, it does little to raise or lower the speed in the wake but its main effect, which can be observed from the direction of the free streamline in Fig.4.4(b), is to widen the wake in the manner shown by the sketch of Fig.5.8.

The flow over the four arms of the cross canopy will separate from the canopy long before it reaches the apex. The point of flow separation varies with both the canopy arm ratio and the fabric porosity. With the 4:1 arm ratio imporous canopy shown in Fig.4.4(a), some flow attachment can be seen near the hem of the canopy skirt. However, flow around the 3:1 arm ratio imporous canopy shown in Fig.4.11(a) does not appear to be similarly attached. In the photographs of 3:1 arm ratio canopies shown in Fig.4.11(a) and 4.11(b) the position of flow separation, and hence the drag characteristics which result, is strongly dependent on the canopy porosity. As can be seen in Fig.4.12, the earlier separation occurs the wider the wake will be. This is the physical explanation for the variation in drag coefficient with porosity for a cross-shaped canopy.

Although cross-shaped canopies with large arm ratios offer greater open areas between the arms for the air to pass through, the flow separates readily after the skirt hem line. Thus the major physical effect with these large arm ratio canopies is a wider wake and consequentially larger drag coefficient.

5.2 Cross Canopy Stability Characteristics

The flow visualisation photographs shown in Fig.5.9 and in Fig.4.11 reveal that the stability of cross parachute canopies is dependent on the ability of the air otherwise trapped within the canopy to flow out freely, both through the gaps which are formed between the canopy arms and through the canopy fabric. When all these gaps are small, for example when the arm ratio R_A is equal to 2.4:1 or 3:1, and the fabric is imporous, some of this enclosed air spills out, like tea from a cup, around the hem of the canopy skirt and this produces a destabilising moment. Increasing the arm ratio or the porosity of the canopy permits the air to flow out more freely and reduces this destabilising tendency.

When parachutes are disturbed from equilibrium at zero angle of attack the characteristics of the flow around canopies having arm ratios of 2.4:1 and 4:1 are shown in Fig.5.10 and Fig.5.11 respectively. In Fig.5.10 the flow pattern from the 4:1 arm ratio canopy gives an aerodynamic moment which is in a stabilising direction, whereas in Fig.5.11 the direction in which the entrapped air spills out of the 2.4:1 arm ratio canopy results in an increased trailing vortex from the leading arm edge (the bottom arm as seen in Fig.5.11). This trailing vortex results in a destabilising aerodynamic moment. A precisely similar phenomenon was observed with the unstable hemispherical parachute canopy and its existence was confirmed by using the Fast Fourier Transform Analyser.

5.3 Effects of the Fluid Medium on Aerodynamic Characteristics

The static stability characteristics of a 3:1 arm ratio parachute with an average porosity (effective porosity 6%, i.e. nominal porosity 13 cu.ft/sq.ft/sec) are influenced by the fluid medium, as is shown in Fig.4.37. When tested under water the effective porosity of the canopy will differ from its value in air, a phenomenon which has been described by Lingard[2.54] who showed that a reduction of effective porosity for a nylon canopy from 6% in air to 2.5% in the water can be measured at the same pressure difference across the fabric. Such a variation of porosity would have a 4% effect on the tangential force coefficient for a 3:1 arm ratio cross parachute, and this was observed in the ship tank test results given in Table 4.1. However, Fig.5.12 indicates that it causes sufficient variation in the normal force coefficient to result in statically unstable characteristics under water even though the same canopy is statically stable in air.

If a canopy which is selected is either strongly statically stable or strongly statically unstable in air, testing it under water will not affect its stability characteristics. The 3:1 arm ratio cross parachute with an average porosity was only marginally statically stable in air and the reduction in its porosity under water was sufficient to cause it to become unstable.

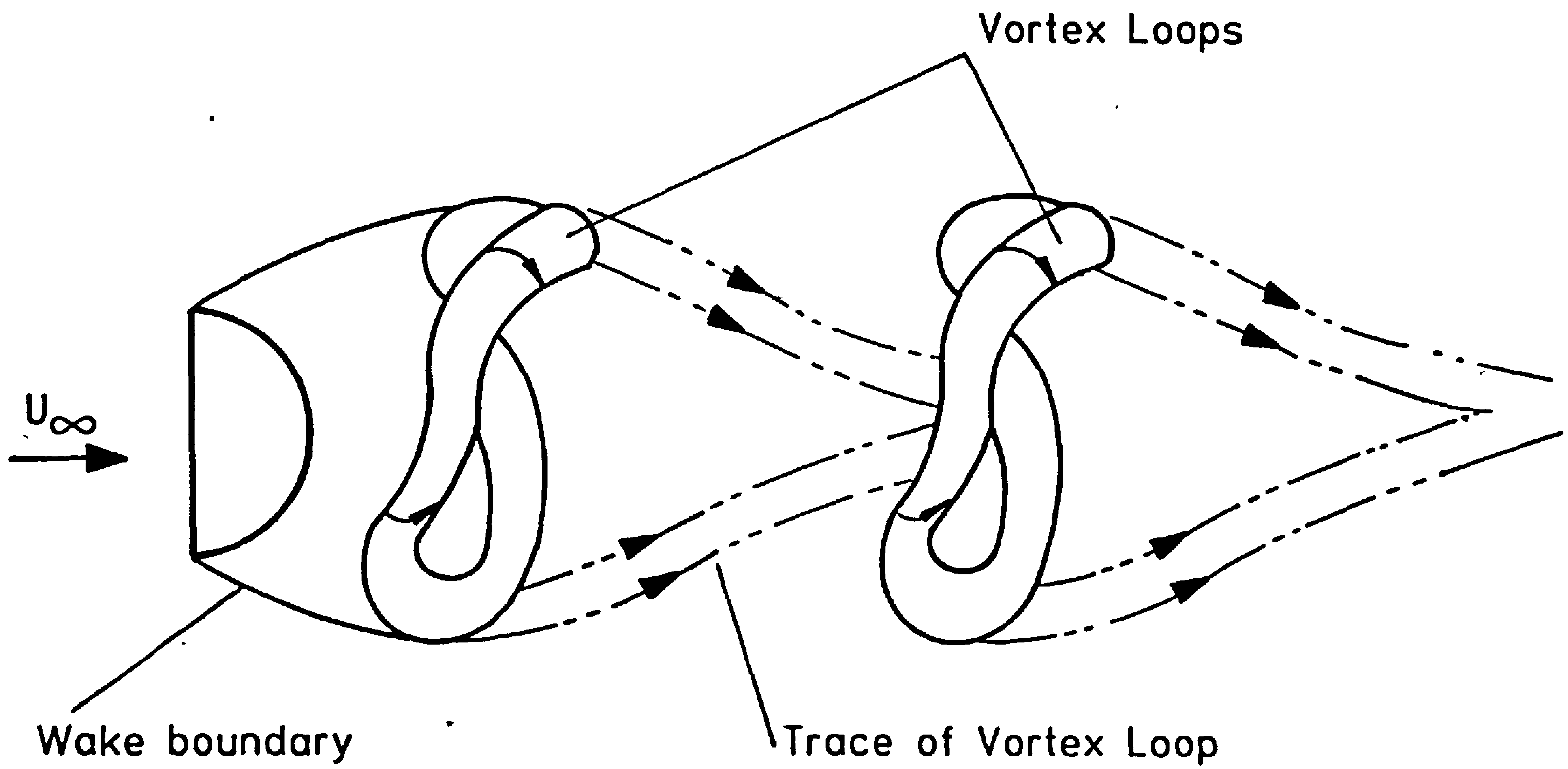

Fig. 5.1 Schematic representation of vortex shedding configuration behind parachute canopy

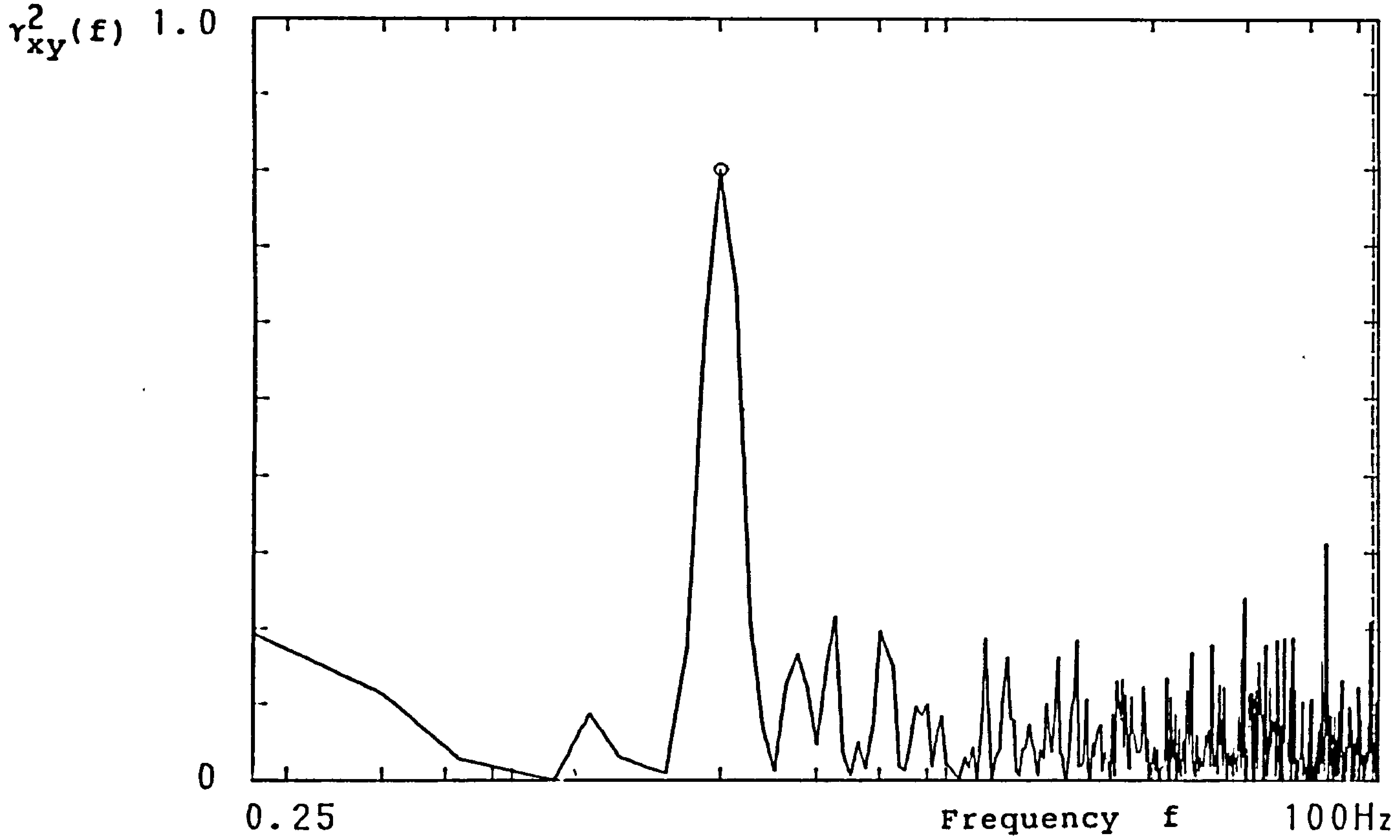

Fig.5.2 Coherency Between Two Points 180° Apart in the Canopy Wake

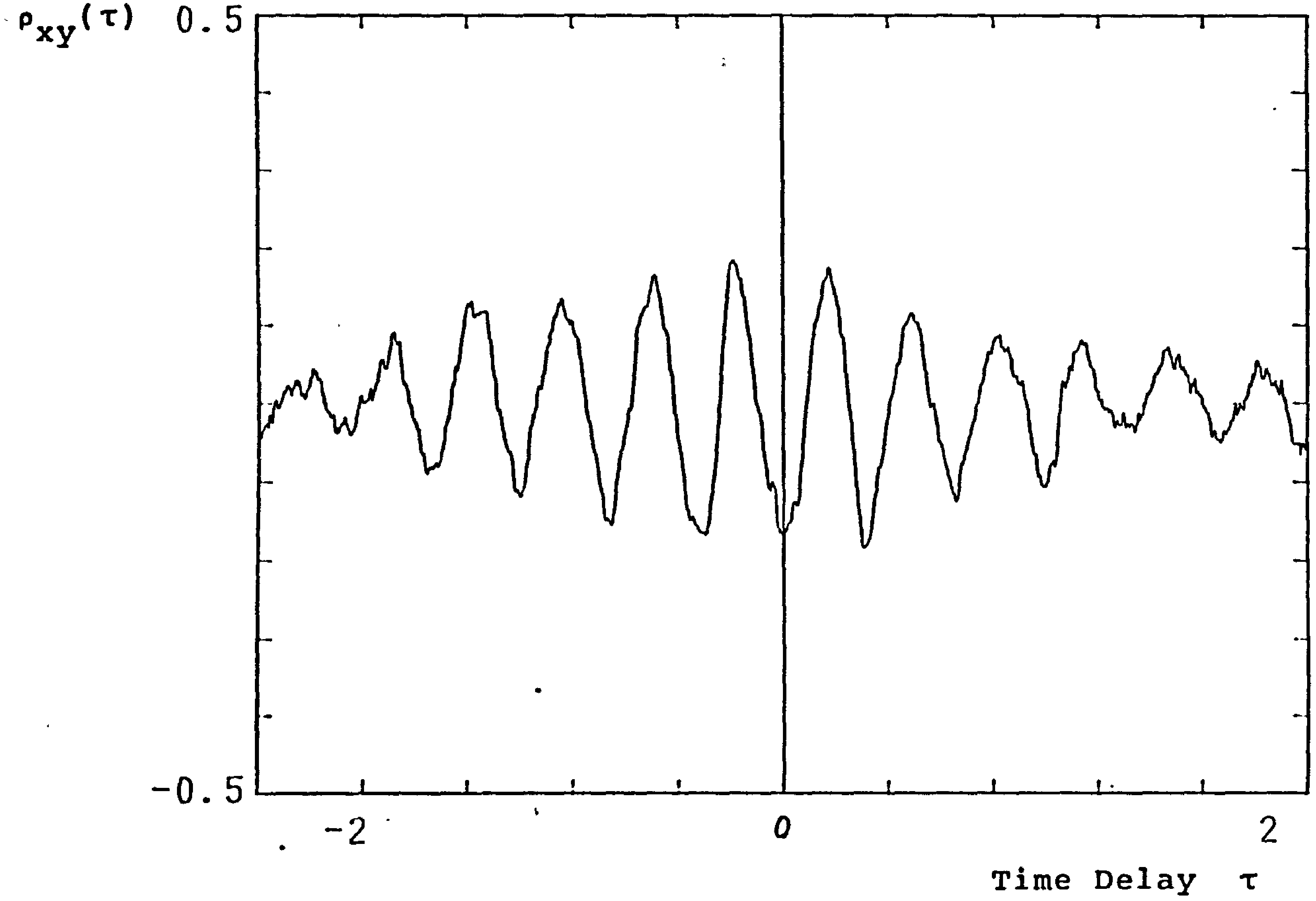

Fig.5.3 Cross-Correlation Function from Two points 180° Apart in the Canopy Wake

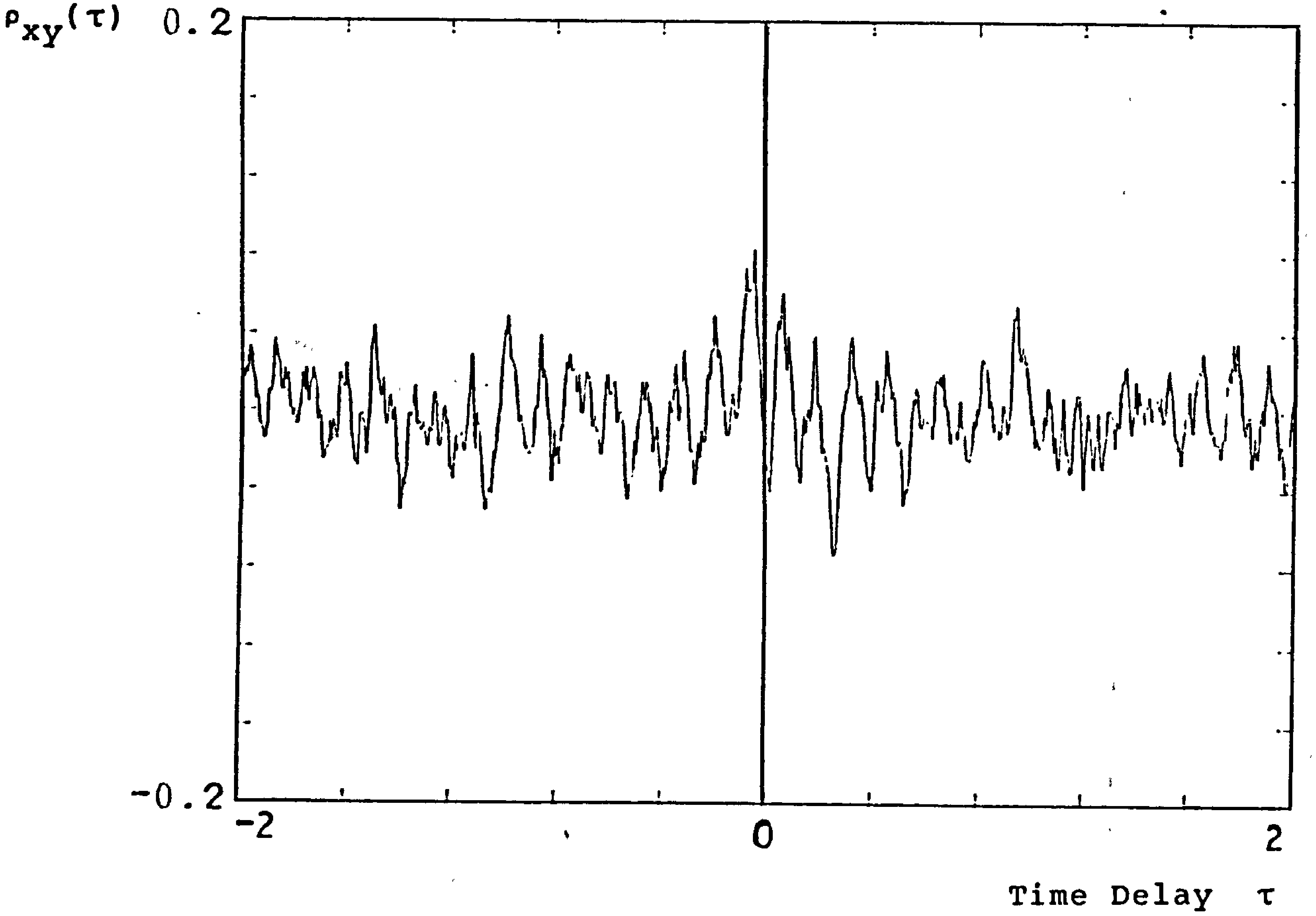

Fig.5.4 Cross-Correlation Function from Two points 90° Apart in the Canopy Wake

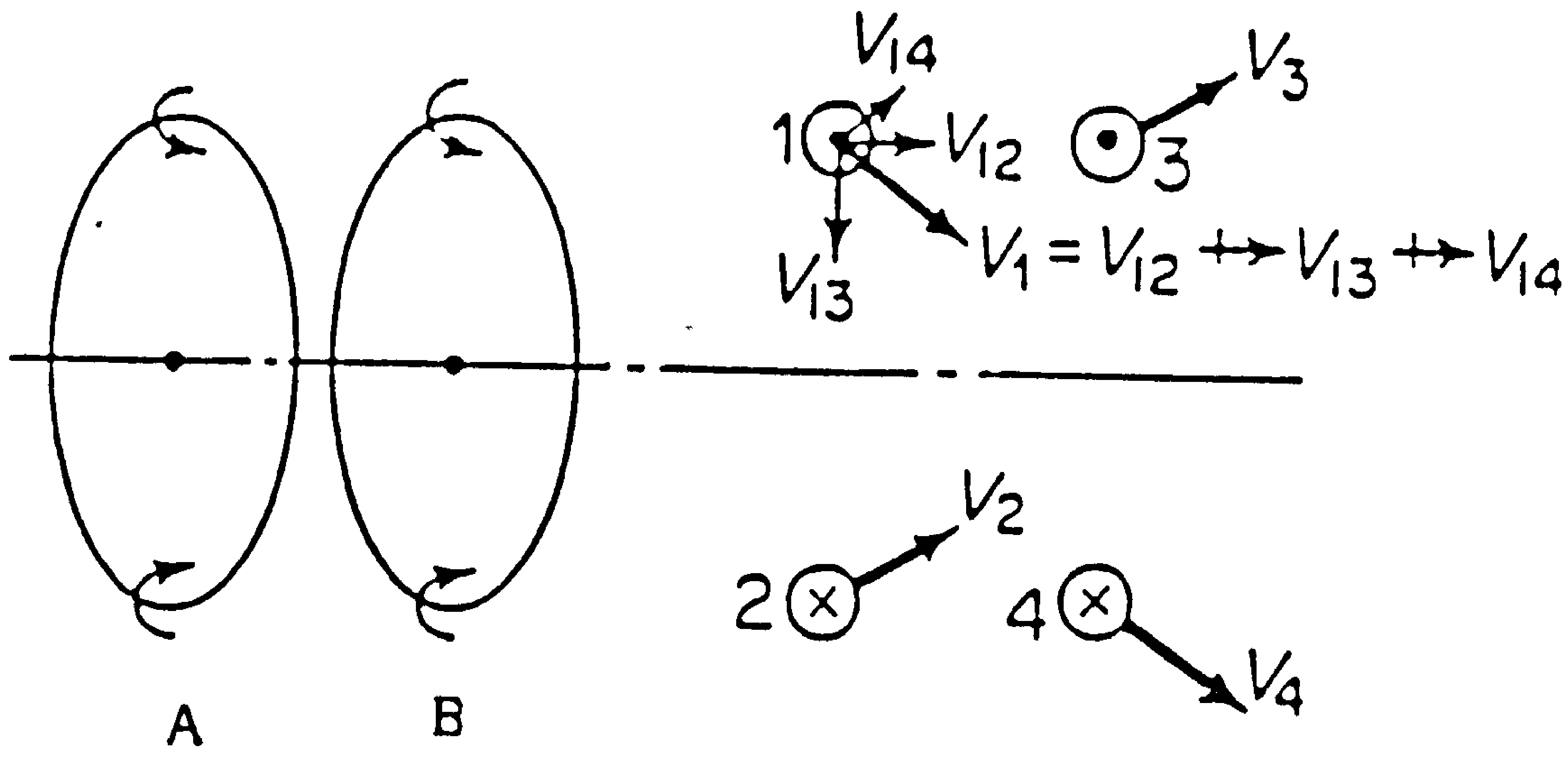

Fig.5.5 Induced Velocity Diagram for Two Vortex Rings with the Same Sense Motion

(after Robertson,J.)

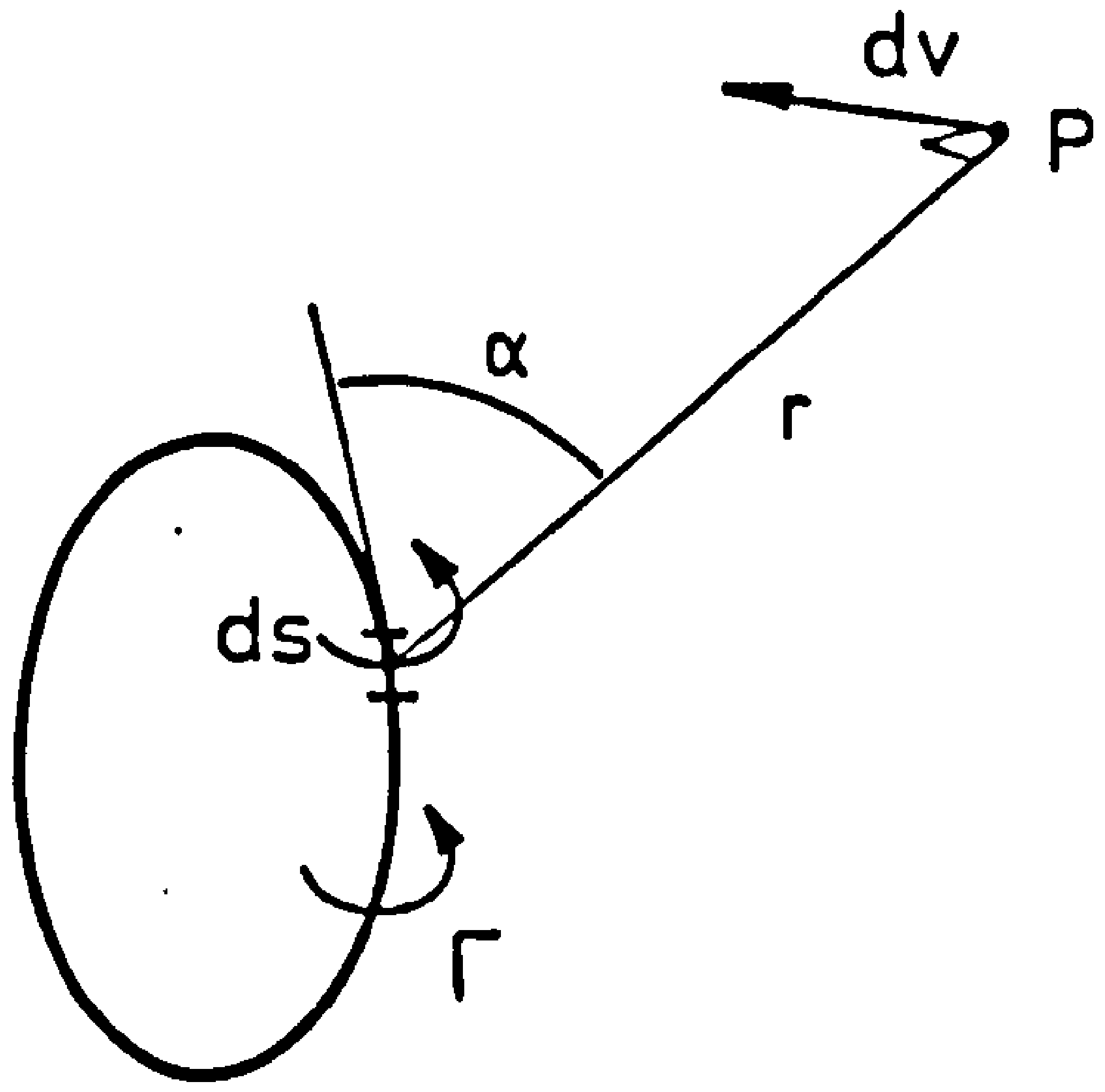

Fig. 5.6 Veocity induced by vortex filament

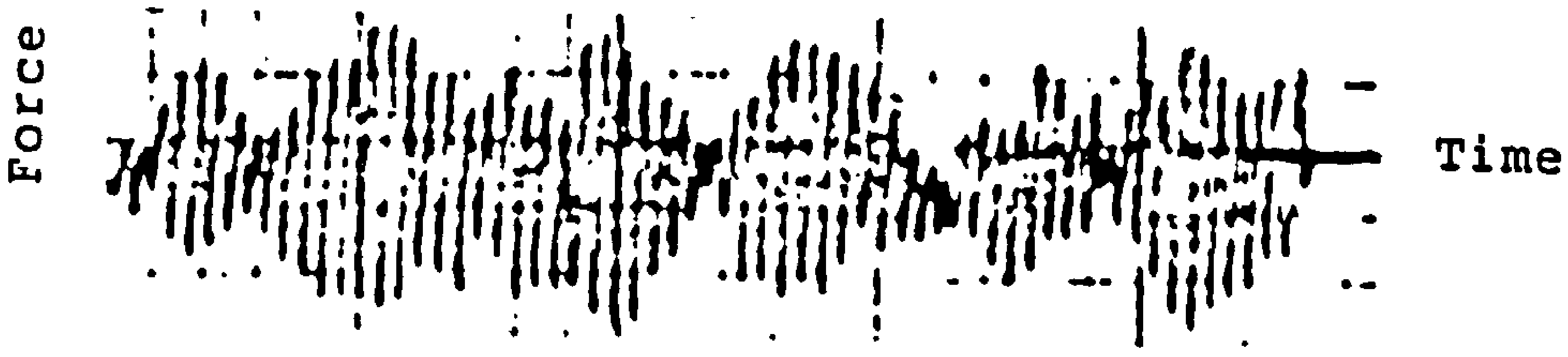

Fig.5.7 Fluctuating Normal Force Observed on A Cross Parachute Canopy

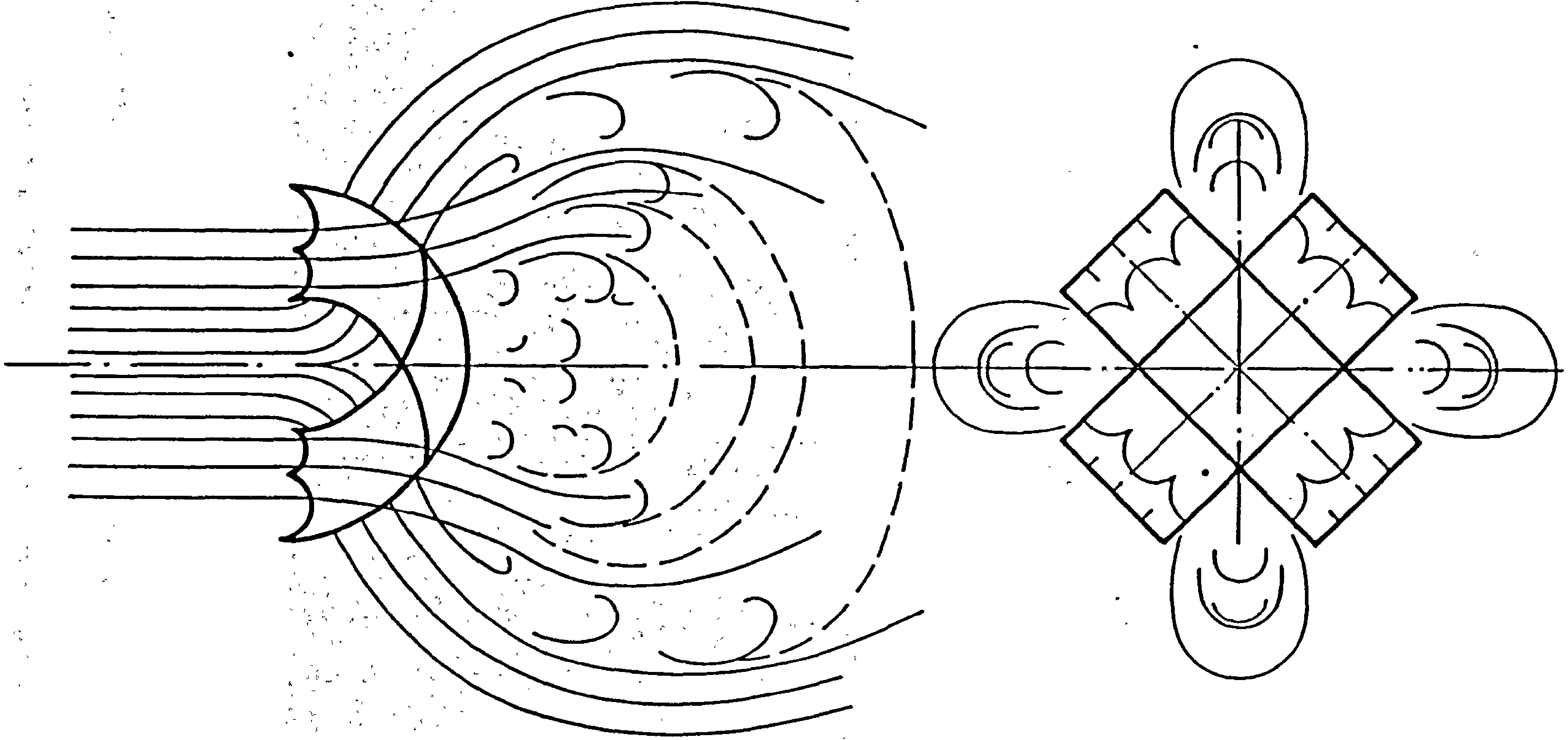

Fig.5.8 Sketch of the Flow Pattern around and Downstream of a Cross Parachute Canopy

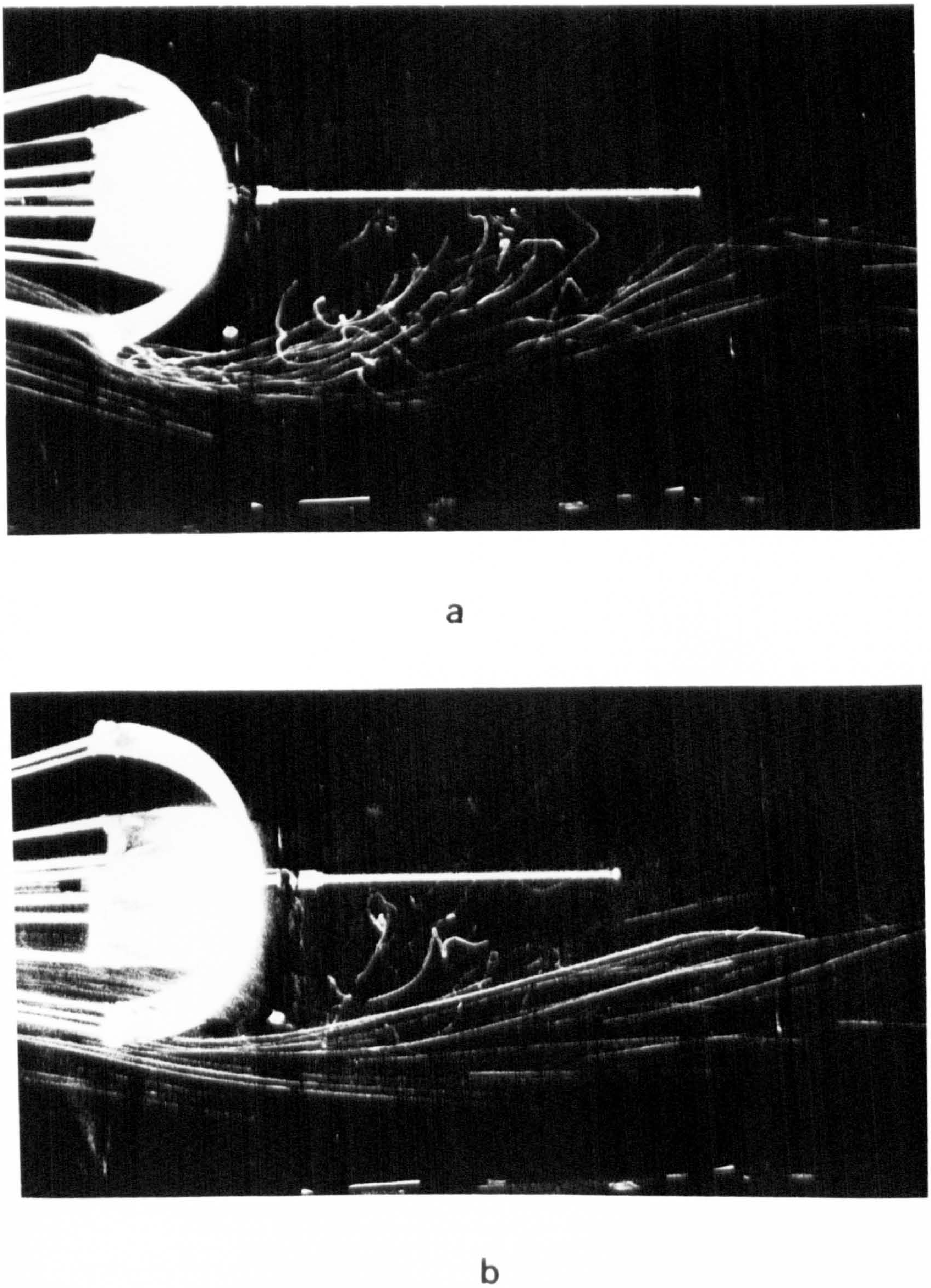

Fig. 5.9 Flow Field over Arm of Cross-Shaped Canopies

(a) Arm Ratio 2.4:1 Imporous Canopy
(b) Arm Ratio 4:1 Imporous Canopy

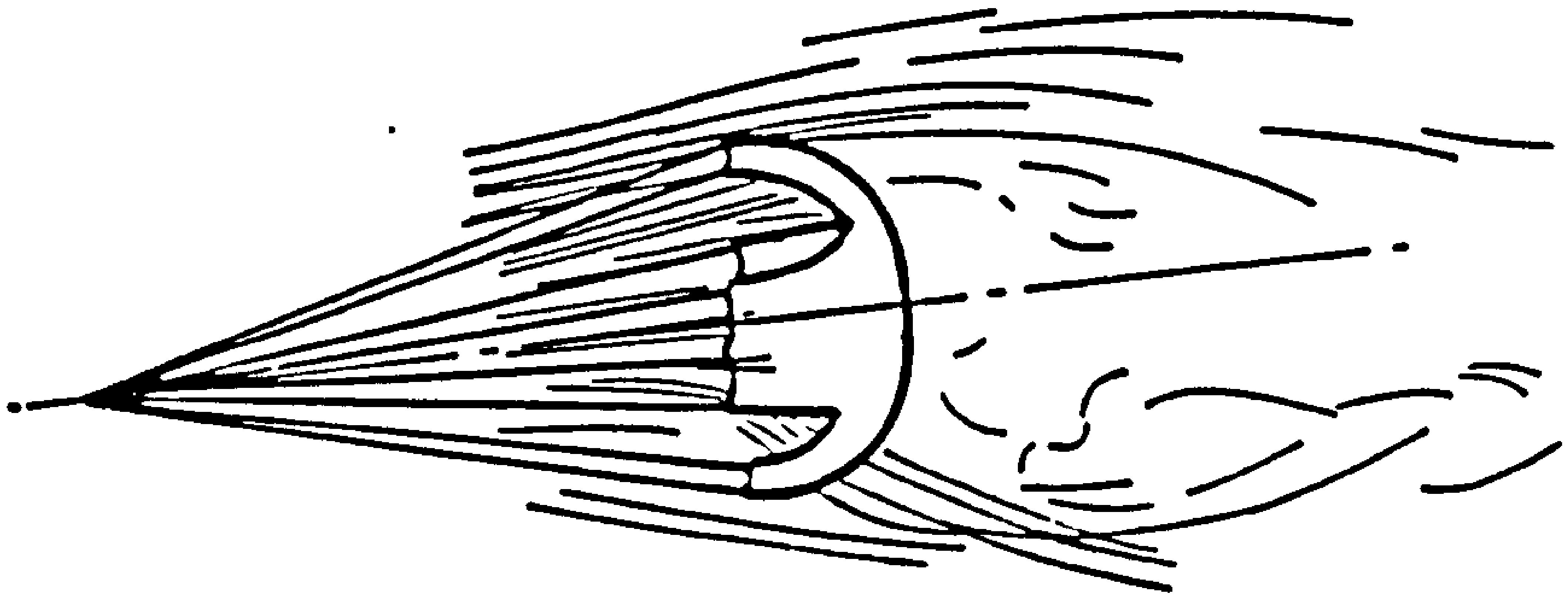

Fig.5.10 Flow Visualisation Past Arm Ratio 4:1
Cross Parachute (α=5)

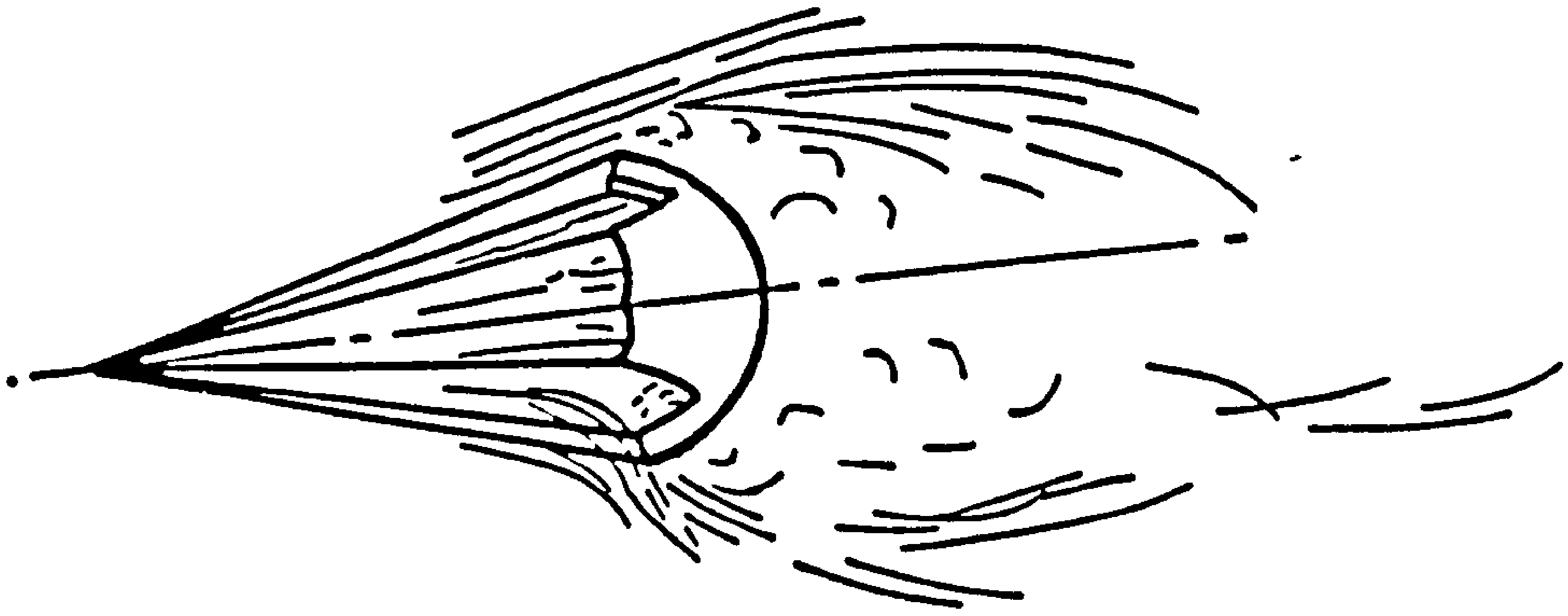

Fig.5.11 Flow Visualisation Past Arm Ratio 2.4:1
Cross Parachute (α=5)

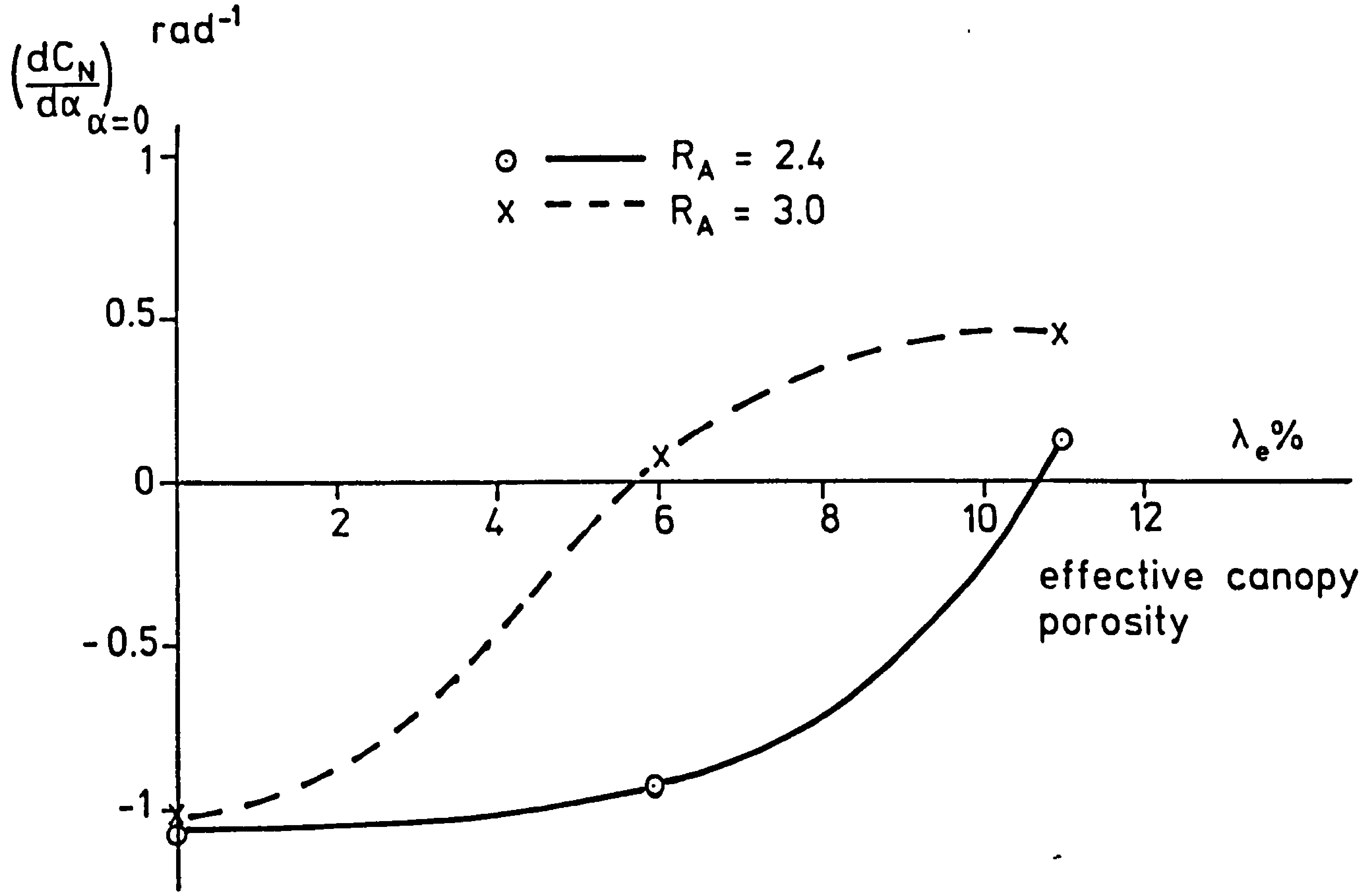

Fig. 5.12 Effect of canopy porosity on stability characteristics

6 EXPERIMENTAL DATA REQUIRED FOR VORTEX SHEET METHODS OF ANALYSIS

The flow in the wakes formed behind bluff parachute canopies is a highly complex phenomenon. There is scope for a great deal of further investigation about the detail of the the wake flow. This will require refinement in flow visualisation techniques and more comprehensive hot wire anemometer investigation with a greater number of simultaneous records.

The probable explanation of the experimental evidence presented is the existence of irregularly-shaped vortex loops in the wakes formed behind bluff parachute canopies. For rigid imporus hemispherical canopies the Strouhal number which is associated with these loops is about 0.15. An increase of about 20% in the Strouhal number was detected as the canopy porosity was increased by about 8.6% and the drag force, based on the canopy projected diameter, decreased by 12% from its imporous value of 0.9 as the wake width decreased from about two projected diameters of the canopy to some 1.6 projected diameters. Over the Reynolds number range from 3×10^4 to 2×10^5 negligible variation was detected in either the drag coefficient or in these accompanying Strouhal numbers.

In any analytical model for flow in the wake shed by parachute canopies these observed phenomena should be faithfully reproduced. Prior to this current investigation such factual data have been almost entirely lacking.

The analytical modelling of bluff body drag forces is relatively straightforward. A more exacting test is to reproduce analytically the experimental pressure distributions determined over the parachute canopies. Although some reliable data exist, e.g. that by Heinrich & Uotila[6.1](1977) and by Pepper & Reed[6.2](1976) it is recommended that further experimental studies are conducted so that pressure distributions over parachute canopies can be obtained for a wide range of varying shapes and fabric porosities. Currently, since analytical modelling methods are restricted to axisymmetric bluff bodies, experimental results are only required at zero angle of attack. However, as these analytical methods advance it will be desirable to extend the range of angles of attack over which the experimentally-obtained pressure distributions are determined.

7 CONCLUSIONS

1. Flow fields in the wakes formed behind parachute canopies are highly complex but they are essentially similar. These wakes appear to consist of chains of irregularly-shaped vortex loops which might penetrate together and move downstream at an average speed of about 0.7 times the undisturbed free stream velocity.

   The wake formed behind a symmetrical parachute canopy is itself asymmetrical. Hidden in the random fluctuations periodic motion can be observed, which is probably caused the vortex rings present in the wake. These result in essentially random fluctuations in the instantaneous aerodynamic forces developed on the canopy which contain a less evident periodic content.

2. In possessing relatively high drag coefficients and desirable static stability characteristics cross parachute canopies differ from other readily-formed canopy shapes. Their arm ratios and their fabric porosities have significant effects on these characteristics. Cross parachute canopies having an arm ratio of 4:1 possess excellent static and dynamic stability characteristics in pitch. Except when they are very porous they also possess high drag characteristics. Cross parachute canopies having arm ratios of 3:1 also possess good stability and drag characteristics, provided that they are not manufactured from an imporous fabric, but further reductions in arm ratio lead to a marked

deterioration in stability characteristics.

3. Over an observed Reynolds number range from 1.0 x 10^5 to 5.0 x 10^5 the observed variation in C_{To} was less than 10%. Extensions of this range to more than 10^6 made by Ludtke indicate that C_{To} shows no significant variation.

4. The values of drag which were obtained when there was a substantial wind tunnel blockage factor of about 7.5% can be compensated for satisfactorily by application of Maskell's bluff body correction factor, but blockage factors much greater than this ratio 8% are not to be recommended.

5. Over the test Reynolds number range from 3 x 10^4 to 2 x 10^5 the observed Strouhal numbers in the wake of a rigid imporous parachute canopy was 0.15, with a wake width of about twice the canopy projected diameter. With porous canopies the Strouhal number is increased, and the width of wake is decreased, resulting in a reduction of drag coefficient. A negligible variation in Strouhal numbers with Reynolds numbers of less than 5% was detected for hemispherical canopies.

REFERENCES

1.1 Cockrell, D.J., The Aerodynamics of Parachutes, AGARDograph, AGARD-AG-295, 1987.

1.2 Ibrahim, S.K., Apparent Added Mass and Moment of Inertia of Cup-Shaped Bodies in Unsteady Incompressible Flow, Ph.D. Thesis, University of Minnesota, USA. 1965.

1.3 Ibrahim, S.K., Potential Flowfield and Added Mass of the Idealized Hemispherical Parachute, J. of Aircraft, Vol.4, 96-100, 1967.

1.4 Klimas, P.C., Internal Parachute Flows, J. of Aircraft, Vol.9, 313-314, April 1972.

1.5 Klimas, P. C., Fluid Mass Associated with an Axisymmetric Parachute Canopy, J. of Aircraft, Vol.14, 577-580, 1977.

1.6 Klimas, P.C., Inflating Parachute Canopy Differential Pressures, J. of Aircraft, Vol.16, 861-862, Dec. 1972.

1.7 Roberts, B.W., Aerodynamic Inflation of Shell Type, Parachute Structures, J. of Aircraft, Vol.11, 390-396, July 1974.

1.8 Reddy, K.R. & Roberts, B.W., Inflation of a Multi-Element Parachute Structure, AIAA-75-1353, Proceeding of AIAA 5th Aerodynamic Deceleration Systems Conference, Albuquerque, N.M., USA, Nov. 1975.

1.9 Ashurst, W.T., Application of Lagrangian Vortex Dynamics to Parachute Flow Fields, Internal Communications, Sandia National Laboratories.

1.10 Meyer, J. & Purvis, J.W., Vortex Lattice Theory Applied to Parachute Canopy Configurations, AIAA-84-0795, Proceedings of the AIAA 8th Aerodynamic Decelerator and Balloon Technology Conference, Hyannis, April 1984.

1.11 Shirayama, S. & Kuwahara, K., Computation of Flow Past a Parachute by a Three-Dimensional Vortex Method, AIAA-86-0350, Proceeding of the AIAA 24th Aerospasce Sciences Meeting, Reno, Jan. 1986.

1.12 Shirayama, S. & Kuwahara, K., Superconductors and Fluid Dynamics, Proceedings of the First Nobeyama Workshop, 1985, Edited by Kuwahara, Mendez and Orszag, Springer-Verlay, 1985.

1.13 Strickland, J.h., On the Utilization of Vortex Methods for Parachute Aerodynamic Predictions, AIAA-86-2455, Proceedings of the AIAA 9th Aerodynamic Decelerator and Balloon Technology Conference, Albuquerque, Oct.1986.

1.14 McCoy, H.H. & Werme, T.d., Axisymmetric Vortex Lattice Method Applied to Parachute Shapes, AIAA-86-2456, Proceedings of the AIAA 9th Aerodynamic Deceletor and Balloon Technology Conference, Albuquerque, Oct. 1986.

1.15 Milne-Thomson, L.M., Theoretical Hydrodynamics, MacMillan and Co. Ltd., London, 1963.

1.16 Thwaites, B.(Editor), Incompressible Aerodynamics, Clarendon Press, Oxford, 1960.

1.17 Doherr, K.-F. & Saliaris, C., On the Influence of Stochastic and Acceleration Dependent Aerodynamic Forces on the Dynamic Stability of Parachutes, AIAA-81-1941, Proceedings of AIAA 7th Aerodynamic Deceletor and Balloon Technology Conference, San Diego, Cal., Oct. 1981.

1.18 White, F.M., and Wolf, D.F., A Theory of Three-Dimensional Parachute Dynamic Stability, J. of Aircraft, Vol.5, No.1, 86-92, Jan.-Feb. 1968.

1.19 Wolf, D.F., The Dynamic Stability of a Non-Rigid Parachute and Payload System, Ph.D. Thesis, University of Rhode Island, Kingston, Rhode Island, 1968.

1.20 Tory, C. & Ayres, R., Computer Model of a Fully Deployed Parachute, J. of Aircraft, Vol.14, No.7, 675-679, July 1977.

1.21 Eaton, J.A., Added Fluid Mass And the Equations of Motion of A Parachute, Aeronautical Quarterly, Vol.34, 226-242, August 1983.

1.22 Heinrich, H.G. & Haak, E. L., Stability and Drag of Parachutes with Varying Effective Porosity, U.S. Air Force Flight Dynamic Laboratory, Air Force System Command, Wright-Patterson Air Force Base, Ohio, AFFDL-TR-71-58, February, 1971.

1.23 Doherr, K.-F. & Schmerwitz, D., Three-Component Measurements for Rigid Models, Symposium on Parachutes and Related Technologies, Royal Aeronautical Society, London, Sep. 1971.

1.24 Hume, R.G., A Two-Dimensional Mathematical Model of a Parachute in Steady Descent, RAE-TR 73040, Royal Aircraft Establishment, U.K., April 1973.

1.25 Yavuz, T., Aerodynamics of Parachutes and Like Bodies in Unsteady Motion, Ph.D. Thesis, University of Leicester, 1982.

1.26 Jorgensen, D.S., Cruciform Parachute Aerodynamics, Ph.D. Thesis, University of Leicester, 1982.

1.27 Cockrell, D.J. & Doherr, K.-F., Preliminary Consideration of Parameter Indentification Analysis from Parachute Aerodynamic Flight Test Data, AIAA-81-1940, Proceedings of the AIAA 7th Aerodynamic Deceletor and Balloon Technology Conference, San Diego, Cal., Oct. 1981.

1.28 Yavuz, T. & Cockrell, D.J., Experimental Determination of Parachute Apparent Mass and the Significance in Predicting Dynamic Stability, AIAA-81-1920, Proceedings of AIAA 7th Aerodynamic Deceletor and Balloon Technology Conference, San Diego, Cal. Oct. 1981.

1.29 Cockrell, D.J., Shen, C.Q., Harwood, R.J. & Baxter, A.C., Aerodynamic Forces Acting on Parachutes in Unsteady Motion and the Consequential Dynamic Stability Characteristics, AIAA-86-2486, Proceedings of AIAA 9th Aerodynamic Decelerator and Balloon Technology Conference, Albuquerque, N.M. Oct. 1986.

1.30 Doherr, K.-F., Theoretical and Experimental Investigation of Parachute-Load-System Dynamic Stability, AIAA-75-1397, AIAA 5th Aerodynamic Deceleration Systems Conference, Albuquerque, N.M. USA, Nov. 1975.

1.31 Doherr, K.-F., Theoretisch-Experimentelle Untersuchung des Dynamischen Verhaltens von Fallschirm-Last-Systemen bei Windkanal-versuchen, Ph.D. Thesis, Technische Universität München, Published as DFVLR-FB 81-29, 1981

1.32 Niccum, R.J., Haak, E.L. & Gutenkauf, R., Drag and Stability of Cross Type Parachutes, University of Minnesota, Minneapolis, Minnesota, FDL-TDR-64-155, Feb. 1965.

1.33 Ludtke, M.P., Effects of Canopy Geometry on the Spinning Characteristics of a Cross Parachute with a W/L Ratio of 0.264, Naval Ordnance Laboratory, White Oak, Silver Spring, Maryland, NOLTR 72-145, June 1972.

2.1 Strouhal, V. Ann. Physik Chem. (Wiedemann's Ann), 5, 216-251, 1878.

2.2 Mallock, A., Proc. Roy. Soc. (London) A79, 262-273, 1907.

2.3 Benard, H., Compt. rend., 147, 839-842, 970-972, 1908; 156, 1003-1005, 1225-1228, 1913.

2.4 Karman, Th.v., Göttinger Nachrichten, 507-517, 1911.

2.5 Karman, Th. v. & Rubach, H. L., Physik. A., 13, 49-59, 1912.

2.6 Fage, A. & Johansen, F.C., On the Flow of Air Behind an Inclined Flat Plate of Infinite Span, A.R.C., R. & M. 1104, 1927.

2.7 Fage, A. & Johansen, F.C., The Structure of Vortex Sheets, A.R.C., R. & M. 1143, 1927.

2.8 Relf, E.F. & Simmons, L.F.G., The Frequency of the Eddies Generated by the Motion of Circular Cylinder Through a Fluid, A.R.C., R. & M. 917, 1924.

2.9 Goldstein, S., Modern Developments in Fluid Dynamics, Oxford University Press, 1938.

2.10 Rubach, Göttingen Dissertation, 1914. (See Goldstein, S., Modern Developments in Fluid Dynamics, pp63. 1938.)

2.11 Homann, F., Einfluss Grosser Zahigheit bei Strömung um Zylinder, Forschung auf dem Gebiete des Ingenieurwesens, 7, 1-10, 1936.

2.12 Fage, Proc. Institution of Mechanical Engineers, 130, 30, 1935. (See Goldstein, S., Modern Developments in Fluid Dynamics, pp63, 1938.)

2.13 Follp, L.,Sitzber. bayer. Akad. Wiss. München Mathphys. Klasse, 1-17, 1913.

2.14 Thom, Proc. Roy. Soc. A, 141, 658, 1933.(See Goldstein, S., Modern Development in Fluid Dynamics pp63, 1938.)

2.15 Rosenhead, L., Vortex Systems in the Wake, Naval Contract, N-5 Ori-76-Project 22, 1950.

2.16 Delany, N.K. & Sorensen, N.E., Low Speed Drag of Cylinders of Various Shapes, NACA TN 3038, 1953.

2.17 Roshko, A., On the Development of Turbulent Wakes from Vortex Streets, Nat. Adv. Comm. Aero., Wash., Rep. No. 1191, 1954.

2.18 Roshko, A., On the Drag and Shedding Frequency of Bluff Cylinders, Nat. Adv. Comm. Aero., Wash., Tech. Note No. 3169, 1955.

2.19 Cometta, C., An Investigation of the Unsteady Flow Pattern in the Wake of Cylinders and Spheres Using a Hot-Wire Probe, Div. Engng., Brown University, Tech. Rep. Wt-21, 1957.

2.20 Abernathy, F.H. & Kronauer, R.E., The Formation of Vortex Streets, J. Fluid Mech. Vol.13, 1-20, 1962.

2.21 Lippisch, A.M., Flow Visualisation, Aero. Eng. Rev.17, 24-32, 1958.

2.22 Eden, C.G., Investigation by Visual and Photographic Methods of the Flow Past Plates and Models, A.R.C. R. & M. 58, 1912.

2.23 Nisi, H. & Porter, A.W., Eddies in Air, Phil. Mag. (6), 46, 754, 1923.

2.24 Ermisch, Abhandlungen aus dem Aero. Inst., Heft 6, 1927.

2.25 Simmons, L.F.G. & Dewey, N. S., Wind Tunnel Experiments with Circular Disc, A.R.C., R. & M. 1334, 1931.

2.26 Karman, Th.v. & Levi-Civita, T., Vortrage aus dem Gebiete der Hydro-and Aerodynamik, Innsbruck, 1922.

2.27 Schiller, von.L. & Schmiedel, H., Zeit. für Flugtechnik und Motorluftschiffahrt, Vol.19, No.21, 497-501, 1928.

2.28 Stanton, Sir.T.E. & Marshall, D., On the Eddy System in the Wake of Flat Circular Plates in Three-Dimensional Flow, A.R.C., R. & M. 1358, 1930.

2.29 Rosenhead, L., Note on "On the Eddy System in the Wake of Flat Circular Plates in Three-Dimensional Flow", Appendix of A.R.C. R. & M. 1358, 1930.

2.30 Moller, W., Experimentell Untersuchung zur Hydrodynamik der Kugel, Phys. Z. 39, 67-80, 1938.

2.31 Taneda, S., Experimental Investigation of the Wake Behind a Sphere at low Reynolds Numbers, J. Phys. Soc. Japan, 11, 1104-1108, 1956.

2.32 Achenbach, E., Vortex Shedding from Spheres, J. Fluid Mech. Vol.62, 209-221, 1974

2.33 Magarvey, R.H. & Maclatchy, C.S., Vortex in Sphere Wake, Can. J. Phys. 43, 1649-1656, 1965.

2.34 Levy, H. & Forsdyke, A. G., The Stability of an Inclined System of Circular Vortices, Proc. Roy. Soc. (London), A114 594-604, 1927.

2.35 Levy, H. & Forsdyke, A.G., Proc. Soc. (London), A120, 760-690, 1928.

2.36 Thomson, Sir. W., Phil. Mag. (5) 10, 155-168, 1880; (or look Kelvin's collected paper 4. 152-165)

2.37 Winny, H.F., The Vortex System Generated Behind a Sphere Moving Through a Viscous Fluid, A.R.C. R. & M. 1531, 1934.

2.38 Fail, R., Lawford, J.A. & Eyer, C.W., Low-Speed Experiments on the Wake Characteristics of Flat Plates Normal to an Air Stream, A.R.C. R. & M. 3120, 1957.

2.39 Carmody, T., Establishment of the Wake Behind a Disc, J. of Basic Engng. Vol.86, 869-882, 1964.

2.40 Bearman, P.W., Review-Bluff Body Flow Applicable to Vehicle Aerodynamics, Trans. ASME I, J. Fluids Engng. Vol.102, 265-274, 1980

2.41 MacLennan, A.S.M. & Vincent, J.H., Transport in the Near Aerodynamic Wakes of Flat Plates J. Fluid Mech. Vol.120, 185-197, 1982

2.42 Nakamura, Y. & Ohya, Y., Vortex Shedding From Square Prisms in Smooth and Turbulent Flows, J. Fluid Mech. Vol.164, 17-89, 1986

2.43 Calvert, J.R., Experiments on the Low-speed Flow past Cones, J. Fluid Mech. Vol.27, 273-289, 1967.

2.44 Calvert, J.R., Experiments on the Flow past an Inclined Disc, J. Fluid Mech. Vol.29, 691-703, 1967.

2.45 Achenbach, E., Experiments on the Flow past Sphere at Very High Reynolds Numbers, J. Fluid Mech. Vol.54, 565-575, 1972.

2.46 Taneda, S., Visual Observation of the Flow past a Sphere at Reynolds Numbers Between 10^4 and 10^6, J. Fluid Mech. Vol.85, 187-192, 1978.

2.47 Pao, H.P. & Kao, T.W., Vortex Structure in the Wake of a Sphere, Phys. of Fluid, Vol.20, No.2, 187-191, 1977.

2.48 Xia, X.J. & Bearman, P.W., An Experimental Investigation of the Wake of an Axisymmetric Body with a Slanted Base, Aero. Quart. Vol.34, 1983.

2.49 Pounder, E., Parachute Inflation Process Wind Tunnel Study, Wright Air Development Center, TR 56-391, Wright-Patterson Air Force Base, Sep. 1956.

2.50 Babish, C.A., III & Hunter, W.C., Visualisation of the Flow Field about Parachute Canopy Models and Approximation of Canopy Pressure Distributions, Tech. Docu. Rep. No. FDL-TDR-64-136, Air Force Flight Dynamic Laboratory, Research and Technology Division, Air Forcce Systems Command, Wright-Patterson Air Force Base, Ohio, 1965.

2.51 Dereng, V.G., Parachute Gore Shape and Flow Visualisation During Transient and Steady-State Conditions, Proceedings of AIAA 4th Aerodynamic Deceleration Systems Conference, Palm Springs Cal., No.73-474, May, 1973.

2.52 Klimas, P.C., Helium Bubble Survey of an Opening Parachute Flowfield, J. of Aircraft, Vol.10. No.9. 556-569, Sep. 1973.

2.53 Klimas, P.C. & Rogers, D.F., Helium Bubble Survey of a Parachute Opening Flowfield Using Computer Graphics Techniques, J. of Aircraft, Vol.14, No.10, 952-958, 1977.

2.54 Lingard, J.S., The Aerodynamics of Parachutes during the Inflation Process, Ph.D. Thesis, Dept. of Aero. Engng., Bristol University, 1977.

2.55 Shen, C.Q. & Cockrell, D.J, Aerodynamic Characteristics and Flow Round Cross Parachute in Steady Motion, AIAA-86-2458 Proceedings of AIAA 9th Aerodynamic Decelerator & Balloon Technology Conference, No. 2458, Oct. 1986.

2.56 Van Dyke, M., A Album of Fluid Motion, the Parabolic Press, Stanford,California, USA, 1982

3.1 Maskell, E.C., A Theory of the Blockage Effects on Bluff Bodies and Stalled Wing in a Closed Wind Tunnel, A.R.C., R. & M. 3120, U.K., Nov. 1965

4.1 Ludtke, W.P., Effects of Canopy Geometry on a Cross Parachute, in the Fully Open and Reefed Conditions, for a W:L Ratio of 0.264., U.S.Naval Ordnance Laboratory, NOLTR 71-111, August 1971

4.2 Shen, C.Q., & Cockrell, D.J.,The Flow Characteristics of Cross Parachutes in Air and in Water, F-117, Proceedings of International Conference on Fluid Mechanics, Beijing, China, July, 1987

5.1 Bendat, J.S., Principles and Applications of Random Noise Theory, John Wiley & Sons Ins., New York, 1958

5.2 Roberson, J.M., Prentice-Hall International Series in Theoretical and Applied Mechanics - Fluid Mechanics Series-, Prentice-Hall, Inc./Englewood Cliffs, N.J., 1965

5.3 Hick, W.M.,On the Mutual Threading of Vortex Rings, Proc. Roy. Soc. London, A102 111-31, 1922

6.1 Heinrich, G.H. & Uotila, J.I., Pressure and Profile Data of 20° Conical Ribbon Parachutes, Sand. 77-7005, Sandia Laboratories, May 1977

6.2 Pepper,B.W. & Reed, J.F., Parametric Study of Parachute Pressure Distribution by Wind Tunnel Testing, J. of Aircraft, Vol.13 No.11 Nov. 895-900 1976.

APPENDIX A

STRUCTURAL AND GEOMETRICAL CHARACTERISTICS OF PARACHUTE CANOPY MODELS

Table A.1 The Configuration Characteristics of Cross Parachute models

Name Of Model	Nominal Surface Area $S_o(m^2) = W(2L-W)$	Actual Arm Length L(m)	Actual Arm Width W(m)	Projected Area $S_p(m^2)$	Arm Ratio $R_A = L/W$	Suspension Line Ratio $R_s = l_s/L$	Fabric Nominal Porosity λ(cu.ft/sq.ft/sec)	Number Of Suspension Line
CS4020	0.108	0.490	0.124	0.078	4	2.00	0	12
CS4013	0.108	0.490	0.124		4	1.33	0	12
CS4006	0.108	0.490	0.124		4	0.67	0	12
CM4020	0.108	0.491	0.124	0.073	4	2.00	13	12
CM4013	0.108	0.491	0.124		4	1.33	13	12
CM4006	0.108	0.491	0.124		4	0.67	13	12
CL4020	0.108	0.495	0.125	0.060	4	2.00	23	12
CL4013	0.108	0.495	0.125		4	1.33	23	12
CL4006	0.108	0.495	0.125		4	0.67	23	12
CS3020	0.108	0.437	0.146	0.068	3	2.00	0	12
CS3013	0.108	0.437	0.146		3	1.33	0	12
CS3006	0.108	0.437	0.146		3	0.67	0	12
CM3020	0.108	0.436	0.147	0.067	3	2.00	13	12
CM3013	0.108	0.436	0.147		3	1.33	13	12
CM3006	0.108	0.436	0.147		3	0.67	13	12
CL3020	0.108	0.440	0.149	0.060	3	2.00	23	12
CL3013	0.108	0.440	0.149		3	1.33	23	12
CL3006	0.108	0.440	0.149		3	0.67	23	12
CS2420	0.108	0.403	0.167	0.058	2.4	2.00	0	12
CS2413	0.108	0.403	0.167		2.4	1.33	0	12
CS2406	0.108	0.403	0.167		2.4	0.67	0	12
CM2420	0.108	0.401	0.168	0.058	2.4	2.00	13	12
CM2413	0.108	0.401	0.168		2.4	1.33	13	12
CM2406	0.108	0.401	0.168		2.4	0.67	13	12
CL2420	0.108	0.401	0.169	0.058	2.4	2.00	23	12
CL2413	0.108	0.401	0.169		2.4	1.33	23	12
CL2406	0.108	0.401	0.169		2.4	0.67	23	12

Table A.2 Fabric Porosity

Material of Model	Nominal Porosity λ (at Δp=10 inches water) cu.ft/sq.ft/sec.	Effective Porosity λ_e (at sea level) %
Nylon 1	0	0
Nylon 2	13	6
Nylon 3	23	11

Table A.3 The Configuration Characteristics of Hemispherical Parachute Models

Name Of Model	Nominal Surface Area S_o (m^2) $=\Pi D_o^2/2$	Projected Diameter of Canopy D_p (m)	Projected Area S_p (m^2)	Geometric Porosity λ_g (or Effective Porosity λ_e)	Canopy Material	Number of Suspension Line
RHN	0.037	0.153	0.018	0.0	Rigid plastic	0
RHP	0.037	0.153	0.018	8.6	Rigid plastic	0
FHN	0.112	0.235	0.043	0.0	Nylon	20

APPENDIX B

THE STRUCTURE DIAGRAM FOR TEST COMPUTER PROGRAM IN THE WIND TUNNEL AND THE FULL PROGRAM LISTING

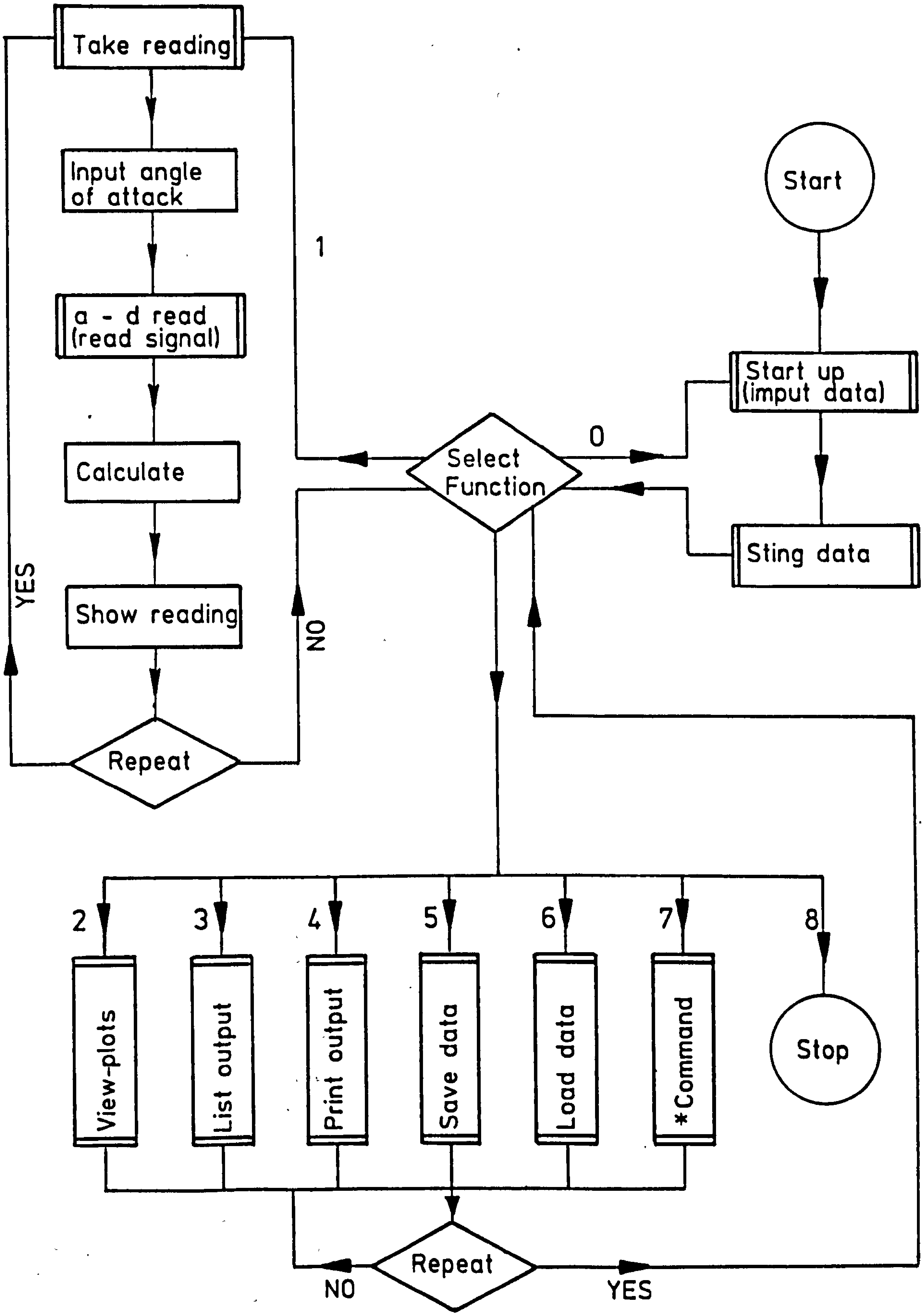

Fig. B.1 Structure diagram of computer program

Title — Subroutine or Procedure

THE BBC MICRO-COMPUTER PROGRAM OF AERODYNAMIC FORCE AND MOMENT MEASUREMENT IN THE WIND TUNNEL

```
 10 maxread=40
 20 DIM ALF(40),CT(40),CN(40),CMC(40),LC(40),REY(40)
 30 DIM CNAS(40),CNFS(40),CDGS(40)
 40 DIM channel(4)
 50 REM DS IS DIAMETER OF STING,apexset IS DISTANCE BETWEEN
    APEX AND CENTRE OF BALANCE
 60 apexset=0.08:DS=0.012
 70 MODE7
 80 PROCstartup
 90 PROCstingdata
100 reading=0
110 FOR I=0 TO 6 :ALF(I)=0:NEXTI
120 FOR I=7 TO 14:ALF(I)=alfmax/8+ALF(I-1):NEXTI
130 FOR I=15 TO 30:ALF(I)=ALF(I-1)-alfmax/8:NEXTI
140 FOR I=31 TO 38:ALF(I)=alfmax/8+ALF(I-1):NEXTI
150 ALF(39)=0

170 REPEAT
180 MODE 7:@%=&90A
190 PRINT'';reading" Readings taken of ";m maximum"
200 PRINT''''"Start-up data    = 0"
210 PRINT"Test & Calculate = 1"
220 PRINT"View plots       = 2"
230 PRINT"List readings    = 3"
240 PRINT"Print readings   = 4"
250 PRINT"Load  data       = 5"
260 PRINT"Save data        = 6"
270 PRINT"  * command      = 8"
280 PRINT"STOP             = 9"
290 PRINT"Which function now ?"
300 REPEAT:a=GET:UNTILa>=&30 AND a<=&39
310 IF a=&30 THEN MODE 7: PROCstartup
320 IF a=&31 THEN MODE 3: PROCtake_readings
330 IF a=&32 THEN MODE 4: PROCview_plots
340 IF a=&33 THEN MODE 3: PROCprint_output
350 IF a=&34 THEN MODE 3:VDU2: PROCprint_output:VDU3
360 IF a=&36 THEN MODE 3: PROCsave
370 IF a=&35 THEN MODE 3:PROCload: PROCprint_output:
    initialised=TRUE
380 IF a=&38 THEN MODE 3: PROCstar
390 IF a=&39 THEN STOP
400 UNTILFALSE

420 DEFPROCtake_readings
430 IF reading>maxread THEN ENDPROC
440 REPEAT
450 CLS :@%=&90A
460 PRINT'''';reading" Readings taken of ";maxread+1;
    "maximum "'"Reading will be taken when RETURN is hit"
470 PRINT"Set Alpha ="ALF(reading)"================Next
    Angle="ALF(reading+1):temp=GET
480 PROCa_dread:PROCread
```

```
490 PRINT"reading   NAP    NFP    GDP     CT     CN      CMC
    LC    ALF      REY"
500 VEL=SQR(2*q/DENS)
510 REY(reading)=(DENS*VEL*D/MU)
520 CL=(NAP+NFP)/(q*S)
530 CD=DGP/(q*S)
450
    CT(reading)=-CL*SIN(ALF(reading)*3.1416/180)+CD*COS(ALF(
    reading)*3.1416/180)
550
    CN(reading)=CD*SIN(ALF(reading)*3.1416/180)+CL*COS(ALF(
    reading)*3.1416/180)
560 NORF=CN(reading)*q*S
570 MOMO=-(NAP-NFP)*0.127/2+NORF*apexset
580 AC=ABS(MOMO/NORF)
590 LC(reading)=AC/0.153
600 MOMC=-NORF*(L-AC)
610 CMC(reading)=MOMC/(q*S*D)
620 PRINT;reading;
630 @%=&20307
640
    PRINT,NAP,NFP,DGP,CT(reading),CN(reading),CMC(reading),
    LC(reading),ALF(reading);"  "REY(reading)
650 reading=reading+1 :PRINT'''
660 IF reading>maxread THEN exit=FNyesno("FULL! No more
    readings! Continue "):exit=TRUE ELSE exit=NOT
    FNyesno("Another reading")
670 UNTIL exit
680 ENDPROC

700 DEFPROCview_plots
710 CLS:PROCplo1:PROCprint_cont
720 CLS:PROCplo2:PROCprint_cont
730 CLS:PROCplo3:PROCprint_cont
740 CLS:PROCplo4:PROCprint_cont
750 CLS:PROCplo5:PROCprint_cont
760 ENDPROC

770 DEFPROCplo1
780 PROCaxes(520,125,0,1040,16,0,1000,8)
790 FOR I=0 TO 38
800 X=1040*ALF(I)/80+520
810 Y=1000*CT(I)/1.6+125
820 PLOT 69,X,Y
830 PRINT TAB(32,29)"40 alpha"
840 PRINT TAB(17,0)"1.4  CT"
850 PRINT TAB(17,29)"0"
860 NEXT I
870 ENDPROC

880 DEFPROCplo2
890 PROCaxes(520,500,0,1040,16,0,1000,10)
900 FOR I=0 TO 38
910 X=1040*ALF(I)/80+520
920 Y=1000*CN(I)/0.5+500
930 PLOT 69,X,Y
940 PRINT TAB(32,17)"40 alpha"
950 PRINT TAB(17,0)"0.25  CN"
```

```
 960 NEXT I
 970 ENDPROC

 980 DEFPROCplo3
 990 PROCaxes(520,500,0,1040,16,0,1000,10)
1000 FOR I=0 TO 38
1010 X=1040*ALF(I)/80+520
1020 Y=1000*CMC(I)/0.5+500
1030 PLOT 69,X,Y
1040 PRINT TAB(32,17)"40 alpha"
1050 PRINT TAB(17,0)"0.25  CM"
1060 NEXT I
1070 ENDPROC

1080 DEFPROCplo4
1090 PROCaxes(100,100,100,1000,3,100,1000,6)
1100 FOR I=0 TO 6
1110 X=900*(REY(I)-180000)/300000+100
1120 Y=900*CT(I)/1.2+100
1130 PLOT 69,X,Y
1140 PRINT TAB(1,30)"1.8       2.8       3.8      4.8  REY"
1150 PRINT TAB(0,0)"CT    1.2 "
1160 PRINT TAB(27,27)"X100000"
1170 NEXT I
1180 ENDPROC

1190 DEFPROCplo5
1200 PROCaxes(520,118,0,1040,16,0,1059,9)
1210 FOR I=0 TO 38
1220 X=1040*ALF(I)/80+520
1230 Y=1000*LC(I)/1.7+118
1240 PLOT 69,X,Y
1250 NEXT I
1260 PRINT TAB(32,29)"40 alpha"
1270 PRINT TAB(17,2)"1.4  LC"
1280 ENDPROC

1290 DEFPROCprint_cont
1300 LOCAL key%
1310 REPEAT key%=GET:UNTILkey%=&20 OR key%=&50
1320 IF key%=&50 THEN *GRDUMP
1330 ENDPROC

1350 DEFPROCaxes(xc%,yc%,fx%,lx%,nx%,fy%,ly%,ny%)
1360 MOVE 0,yc%:DRAW 1239,yc%
1370 FOR I%=0 TO nx%
1380 xt%=(fx%+I%*(lx%-fx%)/nx%)
1390 MOVE xt%,yc%:DRAW xt%,yc%+20
1400 NEXTI%
1410 MOVE xc%,0:DRAW xc%,1023
1420 FOR I%=0 TO ny%
1430 yt%=(fy%+I%*(ly%-fy%)/ny%)
1440 MOVE xc%,yt%:DRAW xc%+20,yt%
1450 NEXTI%
1460 ENDPROC

1480 DEFFNyesno(prompt$)
1490 PRINTprompt$;" ? (Y/N) ";
```

```
1500 REPEAT
1510 a$=GET$
1520 UNTILa$="y" OR a$="Y" OR a$="n" OR a$="N"
1530 IF (a$="y" OR a$="Y")THEN = TRUE ELSE =FALSE
1540 STOP

1550 DEFPROCread
1560 B1A=-0.02144:B2A=0.87412
1570 NA=(channel(2)-B1A)*9.81/B2A-1.052*9.81
1580 NAP=NA-CNAS(reading)*q*3.1416*DS^2/4
1590 B1F=-0.02144:B2F=0.87412
1600 NF=(channel(4)-B1F)*9.81/B2F-1.052*9.81
1610 NFP=NF-CNFS(reading)*q*3.1416*DS^2/4
1620 B1G=-0.00356:B2G=0.85862
1630 DG=(channel(3)-B1G)*9.81/B2G
1640 DGP=DG-CDGS(reading)*q*3.1416*DS^2/4
1650 ENDPROC

1660 DEFPROCa_dread
1670 no_ad_read=100
1680 FOR I%=1 TO 4:channel(I%)=0:NEXTI%
1690 FOR I%=1 TO no_ad_read
1700 FOR J%=1 TO 4
1710 channel(J%)=channel(J%)+ADVAL(J%)
1720 NEXTJ%
1730 NEXTI%
1740 PRINT'''"                      Q        AFT    DRAG
     FORE"
1750 @%=&407
1760 PRINT"Readings in V =";:
1770 FOR J%=1 TO 4
1780 channel(J%)=(channel(J%)/no_ad_read)*1.8/(4096*16)
1790 PRINT,channel(J%);: NEXTJ%
1800 PRINT''''
1810 B1Q=0.00086:B2Q=0.00484
1820 q=(channel(1)-B1Q)/B2Q
1830 ENDPROC

1840 DEFPROCprint_output
1850 VDU14
1860 PROCheader
1870 PRINT'';reading" Readings taken of ";maxread+1;"
     maximum"
1880 PRINT"reading          ALF       CT         CN         CMC
     LC         REY"
1890 IF reading=0 THEN1960
1900 FOR K%=0 TO reading-1
1910 @%=&0405
1920 PRINT K%;
1930 @%=&2030A
1940 PRINT,ALF(K%),CT(K%),CN(K%),CMC(K%),LC(K%);"
     "REY(K%)
1950 NEXTK%
1960 REPEAT:UNTIL FNyesno("Continue")
1970 ENDPROC

1980 DEFPROCstartup
1990 REPEAT:CLS
```

```
2000 PRINT''''
2010 INPUT"Date as text string ";date$
2020 INPUT"Model name";model$
2030 INPUT"with rotation or not";rotation$
2040 INPUT"Maximum Aipha(degrees)=";alfmax
2050 INPUT"Arm length m ";arm
2060 INPUT"Arm width  m ";width
2070 AR=arm/width
2080 S=width*(arm+arm-width)
2090 D=SQR(4*S/3.1416)
2100 INPUT"Model rigging line length ratio ";LR
2110 INPUT"Length of flying parachute m ";L
2120 INPUT"Canopy porosity (cu ft/sq ft/sec!) ",porosity
2130 PRINT''
2140 INPUT"Air pressure mm Hg";P
2150 INPUT"Air temperature deg C";T: T=T+273
2160 DENS=1.2*293*P/(760*T):MU=1.458/(T+110.4)*T^1.5*1E-6
2170 PRINT''
2180 PROCheader
2190 PRINT'"Arm length = ";arm;" m"
2200 PRINT"Arm width = ";width;" m"
2210 PRINT"Length of flying parachute =";L;" m"
2220 UNTILFNyesno("O.K. ")

2240 DEFPROCheader
2250 CLS :@%=&90A
2260 PRINT''date$'model$'rotation$'"Area = "S;" sq.m."
2270 PRINT"Maximum Alpha(degrees)=";alfmax
2280 PRINT"Arm ratio ="AR'"Line length ratio = "LR
2290 PRINT"Porosity = "porosity" (cu ft/sq ft/sec!)"
2300 PRINT'"Air pressure mm Hg ="P
2310 PRINT"Air temperature deg C ="T-273''
2320 ENDPROC

2340 DEFPROCstar
2350 INPUT"  *"text$
2360 OSCLItext$
2370 REPEAT:UNTILFNyesno("Continue")
2380 ENDPROC

2390 DEFPROCsave:CLS
2400 INPUT"Save data in what file? c."filename$
     :filename$="c."+filename$
2410 outfile%=OPENOUTfilename$
2420 PRINT#outfile%,reading
2430 PRINT#outfile%,date$,model$,rotation$,S,AR,LR,porosity
2440 PRINT#outfile%,P,T
2450 FOR K%=0 TO reading-1
2460
     PRINT#outfile%,ALF(K%),CT(K%),CN(K%),CMC(K%),LC(K%),REY
     (K%)
2470 NEXTK%
2480 CLOSE#outfile%
2490 ENDPROC

2500 DEFPROCload
2510 CLS
2520 IF NOT FNyesno("LOAD will destroy all
```

```
     readings"+CHR$(10)+CHR$(13)+"go ahead"):ENDPROC
2530 CLS
2540 INPUT"Load data from what file? c."filename$ :
     filename$="c."+filename$
2550 infile%=OPENINfilename$
2560 INPUT#infile%,reading
2570 INPUT#infile%,date$,model$,rotation$,S,AR,LR,porosity
2580 INPUT#infile%,P,T
2590 IF reading>=0 FOR K%=0 TO reading-1:
     INPUT#infile%,ALF(K%),CT(K%),CN(K%),CMC(K%),LC(K%),REY(
     K%):NEXTK%
2600 CLOSE#infile%
2610 ENDPROC

2620 DEFPROCstingdata
2630 CLS
2640 PRINT"Loading sting data"
2650 INPUT"Load data from what file? c."filename$ :
     filename$="c."+filename$
2660 infile%=OPENINfilename$
2670 INPUT#infile%,Z%
2680 INPUT#infile%,temp$,temp$
2690 INPUT#infile%,temp,temp
2700 IF Z%>=0 FOR K%=0 TO Z%-1:
     INPUT#infile%,temp,CNAS(K%),CNFS(K%),CDGS(K%),temp:NEXT
     K%
2710 CLOSE#infile%
2720 ENDPROC
```

APPENDIX C

THE TOTAL RESULTS FOR FORCE MEASUREMENTS IN THE WIND TUNNEL

Conducted on: 28.8.85
Model name: CS4020
Parachute status: No Rotation
Measured surface area (sq.m): 0.106
Arm ratio: 4.0:1
Fabric porosity (cu.ft/sq.ft/sec): 0
Suspension line ratio: 2.0

Angle of Atack (degrees)	C_T	C_N	C_{Mc}	Reynolds Numbers Re
0.000	0.982	0.006	-0.018	212693.095
0.000	0.998	0.015	-0.042	303534.707
0.000	1.044	0.029	-0.084	371121.591
0.000	1.004	0.032	-0.092	427882.600
0.000	1.045	0.023	-0.067	370957.920
0.000	1.009	0.023	-0.065	303084.962
0.000	1.005	0.031	-0.091	211121.183
2.000	1.074	0.034	-0.092	301351.462
4.000	1.075	0.030	-0.078	302454.794
6.000	1.091	0.045	-0.117	303011.684
8.000	1.094	0.051	-0.117	301392.064
10.000	1.089	0.049	-0.103	303379.389
12.000	1.082	0.073	-0.155	301393.568
14.000	1.073	0.101	-0.225	303661.591
16.000	1.062	0.124	-0.274	302211.957
14.000	1.097	0.113	-0.260	301793.279
12.000	1.087	0.087	-0.205	303588.452
10.000	1.084	0.067	-0.156	303525.748
8.000	1.087	0.060	-0.144	303171.675
6.000	1.076	0.021	-0.044	303439.136
4.000	1.077	0.037	-0.097	303510.817
2.000	1.065	0.019	-0.047	303512.310
0.000	1.009	0.002	-0.007	303123.836
-2.000	1.065	0.009	-0.022	302683.962
-4.000	1.080	0.004	0.003	301934.404
-6.000	1.096	-0.010	0.006	301902.881
-8.000	1.103	-0.007	-0.013	302193.961
-10.000	1.097	-0.034	0.050	301225.109
-12.000	1.093	-0.057	0.097	302442.807
-14.000	1.084	-0.083	0.153	302424.825
-16.000	1.069	-0.095	0.170	302138.467
-14.000	1.079	-0.073	0.128	302130.967
-12.000	1.083	-0.058	0.102	301357.477
-10.000	1.097	-0.030	0.038	300559.380
-8.000	1.102	-0.019	0.021	301976.428
-6.000	1.087	-0.012	0.008	301085.157
-4.000	1.073	-0.004	-0.009	301337.927
-2.000	1.056	0.017	-0.050	302962.324
0.000	1.006	0.022	-0.064	302992.240

Conducted on: 1.9.85
Model name: CS4013
Parachute status: No Rotation
Measured surface area (sq.m): 0.106
Arm ratio: 4.0:1
Fabric porosity (cu.ft/sq.ft/sec): 0
Suspension line ratio: 1.33

Angle of Atack (degrees)	C_T	C_N	C_{Mc}	Reynolds Numbers Re
0.000	0.878	-0.005	-0.002	215321.618
0.000	0.946	0.016	-0.029	303517.335
0.000	0.913	0.010	-0.016	371491.578
0.000	0.928	0.007	-0.010	427655.628
0.000	0.908	-0.000	-0.008	374563.825
0.000	0.948	-0.003	-0.002	304727.034
0.000	0.911	-0.003	-0.010	216030.952
3.000	0.977	0.010	-0.014	304845.052
6.000	0.984	0.028	-0.055	304200.628
9.000	0.989	0.055	-0.089	305461.286
12.000	0.977	0.089	-0.150	303943.075
15.000	0.975	0.102	-0.161	304682.205
18.000	0.941	0.113	-0.166	304577.579
21.000	0.884	0.160	-0.250	305174.959
24.000	0.836	0.180	-0.266	306183.368
21.000	0.884	0.153	-0.230	305800.952
18.000	0.930	0.110	-0.163	304735.999
15.000	0.948	0.103	-0.161	304068.884
12.000	0.954	0.087	-0.140	304414.590
9.000	0.962	0.062	-0.104	304462.449
6.000	0.967	0.024	-0.051	302603.878
3.000	0.957	0.008	-0.015	302506.059
0.000	0.952	0.019	-0.041	302642.997
-3.000	0.963	0.001	0.010	301969.750
-6.000	0.987	-0.016	0.009	303050.434
-9.000	0.994	-0.050	0.064	303020.383
-12.000	0.991	-0.069	0.088	301532.164
-15.000	0.967	-0.087	0.114	303346.272
-18.000	0.945	-0.096	0.118	302963.280
-21.000	0.902	-0.143	0.191	304549.175
-24.000	0.860	-0.159	0.204	305456.814
-21.000	0.890	-0.143	0.196	302391.646
-18.000	0.939	-0.104	0.132	302522.615
-15.000	0.953	-0.096	0.127	303208.150
-12.000	0.968	-0.076	0.092	302369.059
-9.000	0.962	-0.050	0.063	303376.290
-6.000	0.958	-0.042	0.055	304336.803
-3.000	0.937	-0.001	-0.015	303994.004
0.000	0.943	0.014	-0.026	303299.738

Conducted on:	31.10.85
Model name:	CS4006
Parachute status:	No Rotation
Measured surface area (sq.m):	0.106
Arm ratio:	4.0:1
Fabric porosity (cu.ft/sq.ft/sec):	0
Suspension line ratio:	0.667

Angle of Atack (degrees)	C_T	C_N	C_{Mc}	Reynolds Numbers Re
0.000	0.781	0.011	-0.004	210907.827
0.000	0.763	-0.007	-0.008	299125.120
0.000	0.775	-0.010	-0.001	366447.249
0.000	0.770	-0.014	0.002	423244.106
0.000	0.750	-0.010	0.000	366601.195
0.000	0.777	-0.008	-0.004	298172.892
0.000	0.778	0.018	-0.017	211691.849
3.000	0.822	0.044	-0.050	300448.661
6.000	0.829	0.077	-0.081	300140.508
9.000	0.832	0.105	-0.101	299860.640
12.000	0.815	0.132	-0.122	300024.680
15.000	0.789	0.162	-0.143	299604.619
18.000	0.757	0.181	-0.159	301781.356
21.000	0.737	0.194	-0.168	302301.441
24.000	0.699	0.209	-0.174	303291.312
21.000	0.723	0.202	-0.174	302437.293
18.000	0.758	0.184	-0.162	302834.048
15.000	0.786	0.164	-0.145	301606.299
12.000	0.806	0.138	-0.129	301517.983
9.000	0.824	0.107	-0.103	301195.937
6.000	0.816	0.086	-0.084	301452.104
3.000	0.803	0.053	-0.061	300233.739
0.000	0.780	0.009	0.002	303032.231
-3.000	0.803	-0.019	-0.001	302613.361
-6.000	0.816	-0.050	0.025	302011.619
-9.000	0.818	-0.074	0.043	303268.987
-12.000	0.816	-0.091	0.054	301836.695
-15.000	0.790	-0.105	0.065	302884.724
-18.000	0.784	-0.125	0.081	302710.304
-21.000	0.771	-0.149	0.094	302825.104
-24.000	0.745	-0.165	0.105	304587.860
-21.000	0.771	-0.149	0.095	303420.770
-18.000	0.770	-0.120	0.076	303615.597
-15.000	0.777	-0.109	0.064	303347.864
-12.000	0.809	-0.091	0.051	304099.890
-9.000	0.810	-0.081	0.046	302784.855
-6.000	0.811	-0.051	0.021	302395.499
-3.000	0.798	-0.018	-0.007	303026.273
0.000	0.774	0.013	-0.002	303332.983

Conducted on: 28.8.85
Model name: CM4020
Parachute status: No Rotation
Measured surface area (sq.m): 0.106
Arm ratio: 4.0:1
Fabric porosity (cu.ft/sq.ft/sec): 13
Suspension line ratio: 2

Angle of Atack (degrees)	C_T	C_N	C_{Mc}	Reynolds Numbers Re
0.000	0.964	-0.012	0.030	213175.951
0.000	0.995	-0.005	0.011	303266.620
0.000	0.986	0.000	0.006	374044.282
0.000	0.990	0.006	-0.009	429613.644
0.000	0.984	-0.005	0.011	369550.568
0.000	0.982	-0.011	0.031	302660.873
0.000	0.988	0.008	-0.025	212045.712
2.000	0.984	0.018	-0.041	304268.541
4.000	1.003	0.042	-0.099	304256.597
6.000	1.009	0.048	-0.109	303041.855
8.000	1.068	0.111	-0.285	303874.148
10.000	0.980	0.072	-0.146	303369.955
12.000	0.990	0.089	-0.181	305293.957
14.000	0.941	0.133	-0.284	305555.720
16.000	0.918	0.156	-0.329	304784.661
14.000	0.928	0.126	-0.263	305485.840
12.000	0.965	0.110	-0.240	304635.583
10.000	0.974	0.088	-0.194	304475.989
8.000	0.995	0.068	-0.152	304751.870
6.000	1.002	0.047	-0.100	305238.899
4.000	0.995	0.035	-0.080	305888.549
2.000	0.982	0.009	-0.014	304032.564
0.000	0.983	-0.008	0.022	304498.367
-2.000	1.015	-0.010	0.024	302959.400
-4.000	1.023	-0.030	0.074	304043.023
-6.000	1.011	-0.047	0.113	302692.390
-8.000	1.008	-0.058	0.133	303528.635
-10.000	1.018	-0.088	0.203	301409.561
-12.000	0.991	-0.111	0.249	303115.297
-14.000	0.979	-0.179	0.401	301766.533
-16.000	0.952	-0.202	0.453	303241.155
-14.000	0.967	-0.173	0.382	302330.501
-12.000	0.980	-0.156	0.360	301762.017
-10.000	1.001	-0.092	0.203	302932.409
-8.000	1.006	-0.068	0.155	303067.337
-6.000	1.015	-0.056	0.139	302011.800
-4.000	1.015	-0.029	0.066	302378.578
-2.000	1.005	-0.019	0.049	303155.757
0.000	0.969	0.010	-0.021	303690.222

Conducted on: 1.9.85
Model name: CM4013
Parachute status: No Rotation
Measured surface area (sq.m): 0.106
Arm ratio: 4.0:1
Fabric porosity (cu.ft/sq.ft/sec): 13
Suspension line ratio: 1.33

Angle of Atack (degrees)	C_T	C_N	C_{Mc}	Reynolds Numbers Re
0.000	0.850	0.002	-0.001	216015.028
0.000	0.872	0.013	-0.026	305589.514
0.000	0.880	0.006	-0.005	375514.373
0.000	0.879	0.004	-0.004	432829.083
0.000	0.870	0.003	-0.000	375245.684
0.000	0.866	-0.005	0.006	317477.581
0.000	0.848	0.002	-0.005	216761.643
3.000	0.906	0.042	-0.067	304438.889
6.000	0.904	0.093	-0.146	304164.432
9.000	0.900	0.110	-0.167	305217.419
12.000	0.885	0.133	-0.208	306037.219
15.000	0.863	0.165	-0.250	304567.783
18.000	0.811	0.189	-0.276	305363.920
21.000	0.741	0.247	-0.384	307377.907
24.000	0.705	0.280	-0.442	308031.989
21.000	0.727	0.244	-0.375	308168.266
18.000	0.770	0.209	-0.313	307345.241
15.000	0.820	0.175	-0.261	308227.498
12.000	0.854	0.154	-0.233	305311.607
9.000	0.874	0.133	-0.202	305658.204
6.000	0.872	0.097	-0.154	304734.066
3.000	0.873	0.060	-0.089	304203.441
0.000	0.860	0.015	-0.024	305009.507
-3.000	0.897	-0.015	0.032	304507.839
-6.000	0.912	-0.036	0.058	304366.924
-9.000	0.897	-0.070	0.113	303665.876
-12.000	0.876	-0.119	0.181	304425.397
-15.000	0.840	-0.152	0.232	305220.410
-18.000	0.804	-0.178	0.265	306426.191
-21.000	0.746	-0.216	0.324	306520.006
-24.000	0.747	-0.247	0.379	306863.752
-21.000	0.750	-0.214	0.317	306691.183
-18.000	0.797	-0.182	0.266	306022.306
-15.000	0.842	-0.161	0.241	306854.829
-12.000	0.868	-0.134	0.195	306168.422
-9.000	0.877	-0.094	0.150	305319.081
-6.000	0.893	-0.062	0.099	307016.900
-3.000	0.877	-0.020	0.027	306653.979
0.000	0.872	0.009	-0.018	305256.294

Conducted on: 31.10.85
Model name: CM4006
Parachute status: No Rotation
Measured surface area (sq.m): 0.106
Arm ratio: 4.0:1
Fabric porosity (cu.ft/sq.ft/sec): 13
Suspension line ratio: 0.667

Angle of Atack (degrees)	C_T	C_N	C_{Mc}	Reynolds Numbers Re
0.000	0.683	0.005	-0.005	215296.131
0.000	0.723	0.004	-0.004	302566.176
0.000	0.723	0.008	-0.007	373268.137
0.000	0.720	0.015	-0.013	427629.496
0.000	0.730	0.011	-0.008	372593.576
0.000	0.732	0.005	-0.004	303389.017
0.000	0.736	0.004	-0.004	213250.011
3.000	0.728	0.063	-0.056	302625.985
6.000	0.749	0.098	-0.080	302778.447
9.000	0.745	0.127	-0.101	302657.381
12.000	0.725	0.159	-0.125	302591.596
15.000	0.693	0.187	-0.150	303166.727
18.000	0.666	0.207	-0.164	303725.871
21.000	0.634	0.247	-0.199	302903.946
21.000	0.634	0.247	-0.199	302903.946
21.000	0.634	0.248	-0.200	303205.527
18.000	0.659	0.214	-0.170	302762.009
15.000	0.681	0.194	-0.153	303062.239
12.000	0.717	0.168	-0.135	301967.427
9.000	0.735	0.137	-0.110	302394.157
6.000	0.735	0.099	-0.077	303239.847
3.000	0.722	0.069	-0.055	303290.573
0.000	0.737	0.006	-0.006	303572.396
-3.000	0.742	-0.031	0.023	303236.863
-6.000	0.754	-0.066	0.050	303330.849
-9.000	0.750	-0.098	0.072	302839.708
-12.000	0.722	-0.114	0.082	302738.097
-15.000	0.701	-0.132	0.093	304450.482
-18.000	0.676	-0.167	0.120	304530.722
-21.000	0.661	-0.201	0.151	306160.678
-21.000	0.661	-0.201	0.151	306160.678
-21.000	0.660	-0.200	0.148	305229.705
-18.000	0.668	-0.163	0.114	305462.344
-15.000	0.695	-0.130	0.085	306513.676
-12.000	0.719	-0.126	0.086	304166.497
-9.000	0.741	-0.107	0.074	303658.828
-6.000	0.744	-0.071	0.046	304766.864
-3.000	0.740	-0.029	0.011	303840.555
0.000	0.733	0.028	-0.033	305201.539

Conducted on: 29.8.85
Model name: CL4020
Parachute status: No Rotation
Measured surface area (sq.m): 0.108
Arm ratio: 4.0:1
Fabric porosity (cu.ft/sq.ft/sec): 23
Suspension line ratio: 2

Angle of Atack (degrees)	CT	CN	CMC	Reynolds Numbers Re
0.000	0.763	0.018	-0.054	219762.094
0.000	0.791	0.018	-0.045	309057.844
0.000	0.786	0.014	-0.034	377185.938
0.000	0.777	0.013	-0.026	435710.063
0.000	0.783	0.013	-0.030	373174.656
0.000	0.784	0.011	-0.023	306365.281
0.000	0.820	0.033	-0.089	216471.125
2.000	0.811	0.048	-0.141	304890.375
4.000	0.811	0.074	-0.204	304523.906
6.000	0.827	0.089	-0.236	304019.406
8.000	0.807	0.119	-0.294	306538.344
10.000	0.794	0.135	-0.323	306614.219
12.000	0.785	0.166	-0.390	304716.375
14.000	0.733	0.207	-0.492	307129.656
16.000	0.669	0.245	-0.583	307860.406
14.000	0.723	0.212	-0.501	305780.156
12.000	0.781	0.189	-0.458	305145.063
10.000	0.801	0.154	-0.376	305871.406
8.000	0.809	0.141	-0.365	305263.938
6.000	0.806	0.086	-0.214	306160.250
4.000	0.820	0.072	-0.190	304581.969
2.000	0.806	0.042	-0.115	305268.531
0.000	0.794	0.013	-0.034	305971.781
-2.000	0.805	0.002	0.014	306333.438
-4.000	0.811	-0.016	0.011	306382.031
-6.000	0.804	-0.054	0.109	306819.000
-8.000	0.809	-0.080	0.167	306714.375
-10.000	0.799	-0.119	0.252	307901.219
-12.000	0.788	-0.143	0.306	307225.063
-14.000	0.760	-0.175	0.375	307548.938
-16.000	0.695	-0.190	0.409	309333.219
-14.000	0.725	-0.162	0.339	308494.406
-12.000	0.739	-0.136	0.286	309051.875
-10.000	0.771	-0.112	0.230	308360.156
-8.000	0.790	-0.085	0.171	308271.156
-6.000	0.793	-0.060	0.117	310584.938
-4.000	0.800	-0.024	0.028	309363.281
-2.000	0.791	-0.001	-0.024	308308.875
0.000	0.778	0.023	-0.063	308749.156

Conducted on:	1.9.85
Model name:	CL4013
Parachute status:	No Rotation
Measured surface area (sq.m):	0.108
Arm ratio:	4.0:1
Fabric porosity (cu.ft/sq.ft/sec):	23
Suspension line ratio:	1.33

Angle of Atack (degrees)	C_T	C_N	C_{Mc}	Reynolds Numbers Re
0.000	0.696	-0.021	0.026	219956.383
0.000	0.702	-0.003	-0.011	305747.023
0.000	0.693	-0.009	0.003	377785.237
0.000	0.684	-0.006	-0.001	434524.910
0.000	0.684	-0.007	-0.000	378440.272
0.000	0.689	-0.016	0.018	306062.394
0.000	0.699	-0.017	0.012	216999.130
3.000	0.726	0.030	-0.062	306743.578
6.000	0.698	0.074	-0.130	306722.408
9.000	0.706	0.095	-0.154	306372.899
12.000	0.666	0.149	-0.253	307598.213
12.000	0.666	0.149	-0.253	307598.213
12.000	0.666	0.149	-0.253	307598.213
12.000	0.666	0.149	-0.253	307598.213
12.000	0.666	0.149	-0.253	307598.213
12.000	0.666	0.149	-0.253	307598.213
12.000	0.666	0.149	-0.253	307598.213
12.000	0.666	0.149	-0.253	307598.213
12.000	0.664	0.147	-0.246	307178.743
9.000	0.688	0.110	-0.188	307536.385
6.000	0.700	0.061	-0.109	307632.892
3.000	0.710	0.031	-0.057	306066.940
0.000	0.684	0.009	-0.006	306289.624
-3.000	0.723	-0.037	0.051	306726.944
-6.000	0.714	-0.066	0.101	307858.963
-9.000	0.708	-0.112	0.171	306571.154
-12.000	0.690	-0.148	0.226	307587.658
-12.000	0.690	-0.148	0.226	307587.658
-12.000	0.690	-0.148	0.226	307587.658
-12.000	0.690	-0.148	0.226	307587.658
-12.000	0.690	-0.148	0.226	307587.658
-12.000	0.690	-0.148	0.226	307587.658
-12.000	0.690	-0.148	0.226	307587.658
-12.000	0.690	-0.148	0.226	307587.658
-12.000	0.694	-0.151	0.224	307837.870
-9.000	0.694	-0.121	0.184	305358.427
-6.000	0.709	-0.086	0.133	305979.034
-3.000	0.715	-0.051	0.075	307470.019
0.000	0.690	-0.002	-0.011	306557.538

Conducted on: 31.10.85
Model name: CL4006
Parachute status: No Rotation
Measured surface area (sq.m): 0.108
Arm ratio: 4.0:1
Fabric porosity (cu.ft/sq.ft/sec): 23
Suspension line ratio: 0.667

Angle of Atack (degrees)	C_T	C_N	C_{Mc}	Reynolds Numbers Re
0.000	0.501	0.003	0.002	219289.629
0.000	0.519	0.003	-0.001	310152.921
0.000	0.512	0.001	0.006	379789.916
0.000	0.507	0.004	0.001	438374.713
0.000	0.511	0.002	0.004	373164.923
0.000	0.515	0.003	0.001	304655.979
0.000	0.507	0.001	0.002	215658.271
3.000	0.504	0.032	-0.032	305359.940
6.000	0.495	0.059	-0.051	305971.025
9.000	0.474	0.088	-0.071	304661.990
9.000	0.474	0.088	-0.071	304661.990
9.000	0.474	0.088	-0.071	304661.990
9.000	0.474	0.088	-0.071	304661.990
9.000	0.474	0.088	-0.071	304661.990
9.000	0.474	0.088	-0.071	304661.990
9.000	0.474	0.088	-0.071	304661.990
9.000	0.474	0.088	-0.071	304661.990
9.000	0.474	0.088	-0.071	304661.990
9.000	0.474	0.088	-0.071	304661.990
9.000	0.445	0.093	-0.073	304795.700
6.000	0.459	0.063	-0.051	304752.138
3.000	0.476	0.019	-0.016	306270.130
0.000	0.498	-0.011	0.002	305496.342
-3.000	0.513	-0.047	0.031	304343.253
-6.000	0.521	-0.068	0.042	303988.040
-9.000	0.534	-0.104	0.071	304424.472
-9.000	0.534	-0.104	0.071	304424.472
-9.000	0.534	-0.104	0.071	304424.472
-9.000	0.534	-0.104	0.071	304424.472
-9.000	0.534	-0.104	0.071	304424.472
-9.000	0.534	-0.104	0.071	304424.472
-9.000	0.534	-0.104	0.071	304424.472
-9.000	0.534	-0.104	0.071	304424.472
-9.000	0.534	-0.104	0.071	304424.472
-9.000	0.534	-0.104	0.071	304424.472
-9.000	0.525	-0.110	0.075	304882.805
-6.000	0.522	-0.075	0.049	305503.835
-3.000	0.519	-0.043	0.023	304400.410
0.000	0.512	0.003	0.005	305148.472

Conducted on: 30.8.85
Model name: CS3020
Parachute status: No Rotation
Measured surface area (sq.m): 0.106
Arm ratio: 3.0:1
Fabric porosity (cu.ft/sq.ft/sec): 0
Suspension line ratio: 2:1

Angle of Atack (degrees)	C_T	C_N	C_{Mc}	Reynolds Numbers Re
0.000	0.960	0.003	0.007	210478.314
0.000	0.973	0.009	-0.011	302649.725
0.000	0.975	-0.010	0.022	367692.183
0.000	0.946	0.009	-0.014	423127.326
0.000	0.950	-0.015	0.040	369950.640
0.000	0.974	0.017	-0.034	300395.050
0.000	0.947	-0.002	0.005	213446.963
2.000	1.010	-0.033	0.082	300809.798
4.000	1.031	-0.051	0.129	299759.798
6.000	1.056	-0.039	0.099	299708.558
8.000	1.058	-0.053	0.142	301361.906
10.000	1.072	-0.041	0.107	300611.512
12.000	1.067	-0.020	0.031	300202.509
14.000	1.059	-0.011	-0.013	299440.158
16.000	1.057	0.016	0.014	301042.467
14.000	1.064	-0.004	-0.032	300479.248
12.000	1.066	-0.013	0.009	298922.281
10.000	1.072	-0.029	0.070	301537.229
8.000	1.074	-0.035	0.093	301507.266
6.000	1.062	-0.039	0.102	302666.143
4.000	1.025	-0.039	0.103	303208.912
2.000	1.002	-0.029	0.072	302898.878
0.000	0.958	-0.003	0.006	302144.825
-2.000	1.007	0.061	-0.132	300812.801
-4.000	1.045	0.070	-0.159	300859.349
-6.000	1.062	0.057	-0.125	299875.809
-8.000	1.089	0.053	-0.126	299957.141
-10.000	1.091	0.040	-0.102	300000.810
-12.000	1.091	0.021	-0.054	299645.250
-14.000	1.077	0.018	-0.036	300573.943
-16.000	1.074	-0.004	-0.021	301573.180
-14.000	1.076	0.010	-0.010	300271.718
-12.000	1.089	0.034	-0.091	300689.640
-10.000	1.091	0.036	-0.089	300985.442
-8.000	1.084	0.052	-0.119	301051.470
-6.000	1.060	0.056	-0.122	300775.257
-4.000	1.036	0.062	-0.143	302228.535
-2.000	0.996	0.055	-0.118	303103.119
0.000	0.992	0.011	-0.013	306227.103

Conducted on: 31.8.85
Model name: CS3013
Parachute status: No Rotation
Measured surface area (sq.m): 0.106
Arm ratio: 3.0
Fabric porosity (cu.ft/sq.ft/sec): 0
Suspension line ratio: 1.33

Angle of Atack (degrees)	C_T	C_N	C_{Mc}	Reynolds Numbers Re
0.000	0.895	0.025	-0.030	211720.023
0.000	0.929	0.030	-0.042	300704.924
0.000	0.924	0.040	-0.054	365515.042
0.000	0.907	0.041	-0.058	425989.639
0.000	0.927	0.031	-0.042	367315.047
0.000	0.897	0.060	-0.090	300115.379
0.000	0.893	0.019	-0.024	211512.383
4.000	0.969	-0.034	0.051	301425.731
8.000	0.983	-0.011	0.021	299638.419
12.000	0.994	-0.007	0.008	298791.779
16.000	0.981	0.016	-0.010	299313.533
20.000	0.969	0.043	-0.041	299168.193
24.000	0.936	0.067	-0.058	299001.789
28.000	0.918	0.111	-0.121	300449.845
32.000	0.865	0.147	-0.170	301226.341
28.000	0.911	0.108	-0.113	300682.557
24.000	0.936	0.073	-0.064	300427.460
20.000	0.961	0.038	-0.021	299838.865
16.000	0.981	0.003	0.020	299353.976
12.000	0.987	-0.013	0.015	300064.579
8.000	0.995	-0.008	0.014	299883.722
4.000	0.956	-0.032	0.053	300339.393
0.000	0.867	0.049	-0.072	303362.171
-4.000	0.957	0.060	-0.089	300381.191
-8.000	0.990	0.051	-0.076	298796.281
-12.000	0.986	0.035	-0.059	299359.967
-16.000	0.969	0.009	-0.013	300658.698
-20.000	0.945	-0.011	-0.011	301703.763
-24.000	0.918	-0.051	0.038	300089.980
-28.000	0.872	-0.098	0.096	301537.272
-32.000	0.846	-0.121	0.116	301761.716
-28.000	0.876	-0.085	0.073	301519.428
-24.000	0.920	-0.051	0.033	302691.900
-20.000	0.954	-0.010	-0.016	301696.332
-16.000	0.958	0.016	-0.018	301186.150
-12.000	0.977	0.024	-0.044	299425.861
-8.000	0.980	0.049	-0.074	299391.418
-4.000	0.951	0.063	-0.098	300928.499
0.000	0.896	0.042	-0.059	304982.162

Conducted on: 11.11.85
Model name: CS3006
Parachute status: No Rotation
Measured surface area (sq.m): 0.106
Arm ratio: 3.0:1
Fabric porosity (cu.ft/sq.ft/sec): 0
Suspension line ratio: 0.667

Angle of Atack (degrees)	C_T	C_N	C_{Mc}	Reynolds Numbers Re
0.000	0.824	0.043	-0.040	215911.182
0.000	0.810	0.033	-0.025	302700.363
0.000	0.813	0.037	-0.027	372765.111
0.000	0.815	0.034	-0.026	425288.152
0.000	0.803	0.038	-0.028	370040.953
0.000	0.828	0.030	-0.023	300174.079
0.000	0.795	0.037	-0.037	214623.477
4.000	0.794	-0.002	-0.006	301632.815
8.000	0.828	-0.006	-0.001	301580.679
12.000	0.864	0.054	-0.039	300317.728
16.000	0.861	0.076	-0.056	300296.783
20.000	0.835	0.089	-0.061	301454.026
24.000	0.826	0.111	-0.075	301172.218
28.000	0.803	0.126	-0.083	300528.589
32.000	0.763	0.137	-0.087	300993.156
28.000	0.788	0.133	-0.087	301275.131
24.000	0.810	0.111	-0.072	301239.339
20.000	0.823	0.086	-0.056	302164.087
16.000	0.843	0.076	-0.052	300533.073
12.000	0.842	0.060	-0.046	302790.887
8.000	0.830	-0.002	0.000	301285.570
4.000	0.791	-0.015	0.009	303965.239
0.000	0.814	0.028	-0.017	302936.261
-4.000	0.793	0.046	-0.032	302905.115
-8.000	0.859	0.005	-0.003	300636.205
-12.000	0.861	-0.005	0.003	300721.374
-16.000	0.839	-0.014	0.004	303143.818
-20.000	0.827	-0.038	0.016	302850.232
-24.000	0.790	-0.057	0.024	302397.432
-28.000	0.759	-0.086	0.041	303780.428
-32.000	0.732	-0.124	0.053	304424.562
-28.000	0.764	-0.101	0.046	303397.142
-24.000	0.784	-0.072	0.032	303336.423
-20.000	0.814	-0.044	0.018	302256.257
-16.000	0.831	-0.020	0.002	302891.766
-12.000	0.853	-0.013	0.005	301608.983
-8.000	0.852	-0.003	-0.002	301903.776
-4.000	0.811	0.044	-0.036	302991.130
0.000	0.811	0.025	-0.018	303063.777

Conducted on: 30.8.85
Model name: CM3020
Parachute status: No Rotation
Measured surface area (sq.m): 0.107
Arm ratio: 3.0:1
Fabric porosity (cu.ft/sq.ft/sec): 13
Suspension line ratio: 2.0

Angle of Atack (degrees)	C_T	C_N	C_{Mc}	Reynolds Numbers Re
0.000	0.891	-0.034	0.073	213433.813
0.000	0.905	-0.024	0.051	302712.619
0.000	0.898	-0.018	0.033	368892.491
0.000	0.888	-0.018	0.035	428044.952
0.000	0.887	-0.026	0.054	371592.431
0.000	0.891	-0.026	0.052	300690.400
0.000	0.911	0.008	-0.002	211829.811
2.000	0.950	-0.010	0.016	300776.249
4.000	0.965	-0.010	0.023	301456.144
6.000	0.975	-0.008	0.022	301786.513
8.000	0.980	-0.025	0.065	300287.942
10.000	0.980	-0.010	0.012	300414.616
12.000	0.972	0.017	-0.015	300129.524
14.000	0.967	0.026	-0.019	299366.439
16.000	0.952	0.054	-0.079	300532.195
14.000	0.959	0.031	-0.036	300806.365
12.000	0.975	0.020	-0.016	299656.791
10.000	0.977	-0.000	-0.016	300182.340
8.000	0.980	-0.014	0.035	298818.236
6.000	0.971	0.000	0.003	300773.237
4.000	0.960	-0.000	-0.000	301555.293
2.000	0.941	-0.000	-0.006	302300.867
0.000	0.902	-0.021	0.040	302851.740
-2.000	0.912	-0.007	0.014	301969.562
-4.000	0.944	-0.000	-0.011	300887.664
-6.000	0.968	-0.022	0.043	300411.601
-8.000	0.983	-0.017	0.023	299720.269
-10.000	0.987	-0.030	0.053	299193.909
-12.000	0.964	-0.047	0.082	300587.953
-14.000	0.959	-0.054	0.088	300974.961
-16.000	0.961	-0.080	0.144	300315.091
-14.000	0.966	-0.069	0.124	301311.870
-12.000	0.968	-0.045	0.070	301840.539
-10.000	0.967	-0.033	0.055	299943.843
-8.000	0.958	-0.015	0.022	300649.727
-6.000	0.967	-0.029	0.057	300295.484
-4.000	0.946	-0.001	-0.014	302321.843
-2.000	0.919	-0.006	0.005	302227.442
0.000	0.899	-0.011	0.016	302411.721

Conducted on: 1.9.85
Model name: CM3013
Parachute status: No Rotation
Measured surface area (sq.m): 0.107
Arm ratio: 3.0:1
Fabric porosity (cu.ft/sq.ft/sec): 13
Suspension line ratio: 1.33

Angle of Atack (degrees)	C_T	C_N	C_{Mc}	Reynolds Numbers Re
0.000	0.836	0.008	-0.014	214952.361
0.000	0.876	0.009	-0.016	306743.875
0.000	0.833	0.008	-0.015	374638.730
0.000	0.841	0.004	-0.007	430118.156
0.000	0.838	0.005	-0.009	372205.197
0.000	0.859	0.009	-0.010	304032.908
0.000	0.810	0.016	-0.027	214082.260
4.000	0.922	0.010	-0.019	302431.905
8.000	0.925	0.035	-0.057	300802.755
12.000	0.934	0.039	-0.057	302609.045
16.000	0.911	0.072	-0.099	303280.636
20.000	0.888	0.087	-0.108	302616.549
24.000	0.838	0.115	-0.143	303624.849
28.000	0.784	0.163	-0.212	304822.062
28.000	0.784	0.163	-0.212	304822.062
28.000	0.771	0.165	-0.208	307016.170
24.000	0.833	0.111	-0.131	303211.746
20.000	0.869	0.073	-0.081	303880.510
16.000	0.899	0.045	-0.046	304252.406
12.000	0.924	0.024	-0.023	301964.537
8.000	0.912	0.022	-0.028	303626.344
4.000	0.887	-0.000	-0.001	303500.677
0.000	0.864	0.001	-0.001	304953.141
-4.000	0.920	-0.016	0.024	304418.044
-8.000	0.934	-0.037	0.051	301808.086
-12.000	0.915	-0.058	0.074	301290.013
-16.000	0.914	-0.066	0.089	301359.342
-20.000	0.895	-0.084	0.101	301508.495
-24.000	0.858	-0.130	0.160	301068.356
-28.000	0.806	-0.183	0.227	306383.898
-28.000	0.806	-0.183	0.227	306383.898
-28.000	0.807	-0.165	0.199	303925.341
-24.000	0.856	-0.125	0.147	304116.545
-20.000	0.891	-0.078	0.086	304689.437
-16.000	0.908	-0.054	0.059	302424.397
-12.000	0.915	-0.044	0.053	303488.707
-8.000	0.923	-0.035	0.040	303211.746
-4.000	0.906	0.002	0.006	304107.585
0.000	0.868	0.000	0.003	304725.207

Conducted on: 29.10.85
Model name: CM3006
Parachute status: No Rotation
Measured surface area (sq.m): 0.107
Arm ratio: 3.0
Fabric porosity (cu.ft/sq.ft/sec): 13
Suspension line ratio: 0.667

Angle of Atack (degrees)	C_T	C_N	C_{Mc}	Reynolds Numbers Re
0.000	0.703	-0.022	0.010	216770.847
0.000	0.704	-0.014	0.004	305500.039
0.000	0.698	-0.015	0.006	376030.777
0.000	0.708	-0.014	0.006	434593.762
0.000	0.699	-0.015	0.006	376161.472
0.000	0.707	-0.012	0.003	304863.308
0.000	0.691	-0.032	0.020	216208.527
4.000	0.727	0.015	-0.015	304696.002
8.000	0.746	0.036	-0.028	303416.314
12.000	0.752	0.054	-0.040	304765.347
16.000	0.735	0.069	-0.048	305690.950
20.000	0.709	0.085	-0.055	306693.157
24.000	0.662	0.121	-0.081	306820.448
28.000	0.629	0.148	-0.097	307140.689
28.000	0.629	0.148	-0.097	307140.689
28.000	0.619	0.145	-0.088	306289.968
24.000	0.650	0.119	-0.071	307161.628
20.000	0.681	0.108	-0.067	307266.300
16.000	0.726	0.070	-0.037	306597.279
12.000	0.738	0.056	-0.034	305992.858
8.000	0.731	0.035	-0.021	304229.773
4.000	0.713	0.007	-0.006	307505.417
0.000	0.702	-0.021	0.017	308169.486
-4.000	0.698	-0.045	0.034	306357.453
-8.000	0.725	-0.070	0.052	306892.307
-12.000	0.748	-0.094	0.071	306619.753
-16.000	0.733	-0.103	0.075	306306.466
-20.000	0.720	-0.129	0.089	306586.790
-24.000	0.685	-0.159	0.105	307686.126
-28.000	0.645	-0.188	0.122	307258.825
-28.000	0.645	-0.188	0.122	307258.825
-28.000	0.644	-0.197	0.129	307780.172
-24.000	0.679	-0.160	0.104	308241.031
-20.000	0.717	-0.130	0.086	308535.976
-16.000	0.724	-0.104	0.068	306463.899
-12.000	0.731	-0.085	0.060	306417.427
-8.000	0.720	-0.061	0.040	306762.050
-4.000	0.696	-0.035	0.021	307584.584
0.000	0.717	-0.019	0.008	307550.231

Conducted on: 30.8.85
Model name: CL3020
Parachute status: No Rotation
Measured surface area (sq.m): 0.109
Arm ratio: 3.0:1
Fabric porosity (cu.ft/sq.ft/sec): 23
Suspension line ratio: 2

Angle of Atack (degrees)	C_T	C_N	C_{MC}	Reynolds Numbers Re
0.000	0.826	-0.016	0.042	215727.402
0.000	0.820	-0.010	0.024	308453.647
0.000	0.822	-0.005	0.012	378120.384
0.000	0.815	-0.001	0.003	434474.153
0.000	0.814	0.002	-0.005	376845.054
0.000	0.816	-0.003	0.008	304895.959
0.000	0.851	0.018	-0.044	216151.845
2.000	0.860	0.002	0.003	304631.674
4.000	0.860	0.019	-0.033	304608.880
6.000	0.862	0.031	-0.061	305131.192
8.000	0.845	0.043	-0.085	305817.643
10.000	0.842	0.051	-0.090	305382.918
12.000	0.831	0.077	-0.141	305485.975
14.000	0.827	0.094	-0.168	306011.328
16.000	0.796	0.121	-0.225	307012.601
14.000	0.808	0.103	-0.195	305965.944
12.000	0.825	0.096	-0.188	305664.727
10.000	0.838	0.068	-0.134	306661.094
8.000	0.851	0.052	-0.098	306413.439
6.000	0.852	0.039	-0.073	305729.839
4.000	0.853	0.025	-0.047	305664.727
2.000	0.862	0.016	-0.028	306070.318
0.000	0.827	-0.001	-0.001	307161.833
-2.000	0.841	-0.016	0.040	306274.423
-4.000	0.869	-0.029	0.063	305661.698
-6.000	0.867	-0.045	0.101	306564.472
-8.000	0.868	-0.062	0.130	306712.412
-10.000	0.861	-0.083	0.174	305810.075
-12.000	0.839	-0.105	0.212	306630.903
-14.000	0.823	-0.119	0.239	307342.622
-16.000	0.816	-0.153	0.304	306538.801
-14.000	0.827	-0.130	0.256	306229.078
-12.000	0.847	-0.106	0.208	306041.581
-10.000	0.837	-0.087	0.179	306715.430
-8.000	0.840	-0.055	0.110	306182.214
-6.000	0.853	-0.054	0.114	305875.156
-4.000	0.859	-0.030	0.061	306971.889
-2.000	0.838	-0.012	0.024	307193.479
0.000	0.819	0.001	-0.002	306843.687

Conducted on: 1.9.85
Model name: CL3013
Parachute status: No Rotation
Measured surface area (sq.m): 0.109
Arm ratio: 3.0:1
Fabric porosity (cu.ft/sq.ft/sec): 23
Suspension line ratio: 1.33

Angle of Atack (degrees)	C_T	C_N	C_{MC}	Reynolds Numbers Re
0.000	0.758	0.019	-0.027	220249.752
0.000	0.764	0.021	-0.037	309915.802
0.000	0.762	0.013	-0.022	378582.813
0.000	0.755	0.013	-0.024	437586.943
0.000	0.758	0.015	-0.026	377705.564
0.000	0.764	0.021	-0.040	309257.802
0.000	0.766	0.005	-0.008	216434.386
4.000	0.809	0.033	-0.052	308757.328
8.000	0.812	0.076	-0.110	307688.651
12.000	0.795	0.101	-0.145	307794.927
16.000	0.755	0.145	-0.203	308793.644
20.000	0.702	0.176	-0.244	308852.647
20.000	0.702	0.176	-0.244	308852.647
20.000	0.702	0.176	-0.244	308852.647
20.000	0.702	0.176	-0.244	308852.647
20.000	0.702	0.176	-0.244	308852.647
20.000	0.702	0.176	-0.244	308852.647
20.000	0.688	0.178	-0.240	310545.328
16.000	0.744	0.115	-0.153	309002.374
12.000	0.785	0.088	-0.117	308714.955
8.000	0.796	0.058	-0.082	311121.025
4.000	0.777	0.029	-0.044	308805.748
0.000	0.775	0.006	-0.011	308510.573
-4.000	0.801	-0.029	0.042	307387.844
-8.000	0.802	-0.061	0.092	308381.819
-12.000	0.781	-0.092	0.124	306445.537
-16.000	0.740	-0.136	0.187	308904.077
-20.000	0.685	-0.172	0.222	308043.772
-20.000	0.685	-0.172	0.222	308043.772
-20.000	0.685	-0.172	0.222	308043.772
-20.000	0.685	-0.172	0.222	308043.772
-20.000	0.685	-0.172	0.222	308043.772
-20.000	0.685	-0.172	0.222	308043.772
-20.000	0.697	-0.163	0.206	309951.982
-16.000	0.742	-0.121	0.158	306602.536
-12.000	0.764	-0.095	0.128	307671.948
-8.000	0.781	-0.062	0.086	308398.484
-4.000	0.786	-0.020	0.021	307462.314
0.000	0.766	-0.000	-0.002	307681.059

Conducted on: 30.10.85
Model name: CL3006
Parachute status: No Rotation
Measured surface area (sq.m): 0.107
Arm ratio: 3.0:1
Fabric porosity (cu.ft/sq.ft/sec): 23
Suspension line ratio: 0.667

Angle of Atack (degrees)	C_T	C_N	C_{MC}	Reynolds Numbers Re
0.000	0.583	0.008	-0.009	215037.337
0.000	0.578	0.006	-0.003	306529.414
0.000	0.581	0.009	-0.008	373751.294
0.000	0.589	0.006	-0.003	432375.211
0.000	0.586	0.006	-0.000	373330.628
0.000	0.590	0.010	-0.007	304504.901
0.000	0.586	0.012	-0.010	214863.585
4.000	0.617	0.053	-0.043	302919.756
8.000	0.630	0.083	-0.060	303528.098
12.000	0.630	0.125	-0.091	302496.953
16.000	0.600	0.169	-0.122	302933.288
16.000	0.600	0.169	-0.122	302933.288
16.000	0.600	0.169	-0.122	302933.288
16.000	0.600	0.169	-0.122	302933.288
16.000	0.600	0.169	-0.122	302933.288
16.000	0.600	0.169	-0.122	302933.288
16.000	0.600	0.169	-0.122	302933.288
16.000	0.600	0.169	-0.122	302933.288
16.000	0.529	0.217	-0.149	306284.146
12.000	0.571	0.155	-0.112	305253.357
8.000	0.589	0.122	-0.088	304304.403
4.000	0.589	0.069	-0.047	305324.969
0.000	0.591	0.019	-0.011	304003.408
-4.000	0.602	-0.032	0.019	305891.307
-8.000	0.634	-0.078	0.053	304832.297
-12.000	0.631	-0.114	0.076	304539.302
-16.000	0.607	-0.152	0.099	304995.116
-16.000	0.607	-0.152	0.099	304995.116
-16.000	0.607	-0.152	0.099	304995.116
-16.000	0.607	-0.152	0.099	304995.116
-16.000	0.607	-0.152	0.099	304995.116
-16.000	0.607	-0.152	0.099	304995.116
-16.000	0.607	-0.152	0.099	304995.116
-16.000	0.607	-0.152	0.099	304995.116
-16.000	0.608	-0.148	0.094	305775.144
-12.000	0.625	-0.112	0.074	304956.286
-8.000	0.630	-0.075	0.048	304765.052
-4.000	0.606	-0.026	0.013	305769.186
0.000	0.612	0.010	-0.010	306376.330

Conducted on: 27.8.85
Model name: CS2420
Parachute status: No Rotation
Measured surface area (sq.m): 0.108
Arm ratio: 2.4:1
Fabric porosity (cu.ft/sq.ft/sec): 0
Suspension line ratio: 2

Angle of Atack (degrees)	C_T	C_N	C_{MC}	Reynolds Numbers Re
0.000	0.924	-0.048	0.118	216549.136
0.000	0.905	-0.043	0.107	308667.294
0.000	0.931	-0.033	0.081	377119.445
0.000	0.895	-0.033	0.079	430269.732
0.000	0.936	-0.047	0.114	373389.965
0.000	0.908	-0.028	0.069	303926.410
0.000	0.902	-0.034	0.083	215235.274
3.000	0.979	-0.093	0.212	304576.010
6.000	1.027	-0.098	0.232	302312.949
9.000	1.043	-0.108	0.263	302499.033
12.000	1.061	-0.079	0.200	302479.371
15.000	1.051	-0.078	0.180	301608.422
18.000	1.047	-0.042	0.067	301180.358
21.000	1.047	-0.038	0.044	302402.223
24.000	1.029	-0.007	-0.053	302759.057
21.000	1.045	-0.032	0.027	301857.088
18.000	1.051	-0.052	0.097	301878.306
15.000	1.054	-0.065	0.143	301700.937
12.000	1.055	-0.072	0.176	303376.474
9.000	1.036	-0.093	0.228	303272.401
6.000	1.030	-0.100	0.232	304236.346
3.000	0.968	-0.085	0.199	304909.295
0.000	0.922	-0.055	0.131	305588.247
-3.000	0.942	0.006	0.001	305493.913
-6.000	0.976	0.031	-0.053	305129.782
-9.000	1.031	0.018	-0.029	305116.288
-12.000	1.032	0.007	-0.011	305582.258
-15.000	1.052	0.011	-0.025	305252.707
-18.000	1.047	-0.005	-0.003	304281.456
-21.000	1.039	-0.029	0.035	306013.135
-24.000	1.035	-0.039	0.031	306922.268
-21.000	1.044	-0.024	0.022	306774.662
-18.000	1.040	-0.003	-0.010	304919.798
-15.000	1.038	0.001	0.004	306240.298
-12.000	1.040	0.010	-0.021	306895.436
-9.000	1.024	0.012	-0.016	306737.376
-6.000	0.961	0.011	-0.013	307824.258
-3.000	0.905	-0.005	0.001	309369.055
0.000	0.936	-0.063	0.153	307306.608

Conducted on: 30.8.85
Model name: CS2413
Parachute status: No Rotation
Measured surface area (sq.m): 0.107
Arm ratio: 2.4:1
Fabric porosity (cu.ft/sq.ft/sec): 0
Suspension line ratio: 1.33

Angle of Atack (degrees)	C_T	C_N	C_{MC}	Reynolds Numbers Re
0.000	0.832	0.054	-0.067	213264.818
0.000	0.823	0.042	-0.048	302237.170
0.000	0.830	0.044	-0.052	368842.827
0.000	0.859	0.015	-0.012	422435.328
0.000	0.859	0.051	-0.062	371612.644
0.000	0.811	0.036	-0.041	303029.454
0.000	0.792	0.028	-0.028	213114.436
4.000	0.914	-0.045	0.069	302992.199
8.000	0.955	-0.041	0.068	300763.466
12.000	0.965	-0.044	0.078	299517.781
16.000	0.975	-0.029	0.043	300082.591
20.000	0.958	-0.009	-0.004	301155.060
24.000	0.947	-0.002	-0.030	299752.871
28.000	0.923	0.039	-0.010	302222.230
32.000	0.881	0.078	-0.060	303435.981
28.000	0.922	0.040	-0.013	302559.705
24.000	0.947	0.005	0.028	301698.845
20.000	0.955	-0.011	-0.005	300360.839
16.000	0.955	-0.018	0.013	300788.988
12.000	0.962	0.087	0.154	300347.309
8.000	0.957	-0.054	0.093	302465.668
4.000	0.895	-0.062	0.097	302825.240
0.000	0.823	0.055	-0.069	302986.238
-4.000	0.899	0.083	-0.105	302368.615
-8.000	0.967	0.060	-0.075	299255.347
-12.000	0.968	0.055	-0.073	300469.061
-16.000	0.968	0.044	-0.063	300816.009
-20.000	0.969	0.027	-0.045	301927.751
-24.000	0.953	-0.004	-0.018	301763.196
-28.000	0.929	-0.035	0.016	301538.658
-32.000	0.893	-0.070	0.053	301203.037
-28.000	0.924	-0.044	0.024	302371.602
-24.000	0.942	-0.010	-0.007	301005.084
-20.000	0.953	0.016	-0.025	300769.472
-16.000	0.966	0.037	-0.053	299673.021
-12.000	0.966	0.042	-0.055	300025.405
-8.000	0.959	0.057	-0.072	298929.247
-4.000	0.904	0.077	-0.098	301727.281
0.000	0.825	0.035	-0.043	303343.704

Conducted on: 28.10.85
Model name: CS2406
Parachute status: No Rotation
Measured surface area (sq.m): 0.107
Arm ratio: 2.4:1
Fabric porosity (cu.ft/sq.ft/sec): 0
Suspension line ratio: 0.667

Angle of Atack (degrees)	C_T	C_N	C_{MC}	Reynolds Numbers Re
0.000	0.698	0.097	-0.050	217773.680
0.000	0.694	0.062	-0.032	307401.132
0.000	0.711	0.056	-0.031	374554.920
0.000	0.692	0.032	-0.014	431590.550
0.000	0.747	0.037	-0.017	372681.870
0.000	0.705	0.053	-0.025	305656.288
0.000	0.717	0.099	-0.049	216242.654
4.000	0.756	0.008	0.000	304145.974
8.000	0.777	-0.008	0.007	305411.427
12.000	0.803	-0.019	0.019	304847.958
16.000	0.817	0.016	-0.000	304115.416
20.000	0.816	0.032	-0.013	305152.665
24.000	0.796	0.055	-0.024	305671.490
28.000	0.765	0.078	-0.039	305304.904
32.000	0.752	0.112	-0.061	306395.762
28.000	0.765	0.085	-0.043	307735.023
24.000	0.786	0.059	-0.025	305911.586
20.000	0.799	0.037	-0.013	306833.745
16.000	0.813	0.019	-0.001	306574.668
12.000	0.804	-0.006	0.000	306470.066
8.000	0.761	-0.017	0.017	306598.919
4.000	0.754	0.015	-0.001	306642.868
0.000	0.708	0.053	-0.023	307204.557
-4.000	0.743	0.078	-0.071	308984.273
-8.000	0.809	0.132	-0.079	306927.626
-12.000	0.837	0.088	-0.045	305938.926
-16.000	0.828	0.071	-0.040	306515.550
-20.000	0.816	0.037	-0.017	307831.647
-24.000	0.807	0.017	-0.008	308853.407
-28.000	0.803	-0.010	0.008	306683.780
-32.000	0.788	-0.042	0.027	307346.709
-28.000	0.806	-0.018	0.014	308878.983
-24.000	0.797	0.006	0.002	308839.866
-20.000	0.814	0.031	-0.016	307366.363
-16.000	0.824	0.065	-0.037	306289.582
-12.000	0.824	0.087	-0.051	307381.481
-8.000	0.806	0.123	-0.067	307358.804
-4.000	0.742	0.106	-0.059	308057.992
0.000	0.710	0.063	-0.034	308772.152

Conducted on: 27.8.85
Model name: CM2420
Parachute status: No Rotation
Measured surface area (sq.m): 0.107
Arm ratio: 2.4:1
Fabric porosity (cu.ft/sq.ft/sec): 13
Suspension line ratio: 2

Angle of Atack (degrees)	C_T	C_N	C_{MC}	Reynolds Numbers Re
0.000	0.861	-0.021	0.047	215331.694
0.000	0.882	-0.017	0.037	305981.601
0.000	0.883	-0.017	0.040	373496.910
0.000	0.888	-0.012	0.024	431196.499
0.000	0.889	-0.017	0.035	372818.967
0.000	0.882	-0.019	0.041	305618.736
0.000	0.866	-0.010	0.015	216836.337
3.000	0.901	-0.047	0.098	304224.496
6.000	0.951	-0.037	0.075	302251.784
9.000	0.972	-0.029	0.074	301816.360
12.000	0.995	-0.021	0.048	301243.910
15.000	0.953	-0.003	-0.023	301233.299
18.000	0.944	0.032	-0.021	302704.685
21.000	0.932	0.035	-0.019	301412.123
24.000	0.877	0.079	-0.102	301374.245
21.000	0.933	0.042	-0.032	300101.822
18.000	0.946	0.026	-0.011	302339.398
15.000	0.936	-0.019	0.004	302805.740
12.000	0.963	0.001	0.020	301084.703
9.000	0.960	-0.024	0.057	301586.299
6.000	0.938	-0.028	0.062	302120.316
3.000	0.914	-0.025	0.054	302233.654
0.000	0.877	-0.005	0.008	304517.051
-3.000	0.902	0.016	-0.036	302307.678
-6.000	0.948	0.031	-0.074	300536.691
-9.000	0.967	0.014	-0.022	301127.167
-12.000	0.968	-0.008	-0.005	300506.301
-15.000	0.976	-0.012	-0.012	299664.797
-18.000	0.962	-0.042	0.052	300074.431
-21.000	0.942	-0.070	0.099	301810.307
-24.000	0.924	-0.093	0.126	300352.784
-21.000	0.941	-0.061	0.071	301274.226
-18.000	0.956	-0.034	0.029	299289.697
-15.000	0.971	-0.023	0.017	299091.283
-12.000	0.980	-0.005	-0.012	300570.116
-9.000	0.969	0.013	-0.020	300655.183
-6.000	0.948	-0.010	0.019	301575.700
-3.000	0.902	0.020	-0.041	303146.365
0.000	0.854	-0.007	0.014	303960.204

Conducted on: 30.8.85
Model name: CM2413
Parachute status: No Rotation
Measured surface area (sq.m): 0.107
Arm ratio: 2.4:1
Fabric porosity (cu.ft/sq.ft/sec): 13
Suspension line ratio: 1.33

Angle of Atack (degrees)	C_T	C_N	C_{MC}	Reynolds Numbers Re
0.000	0.785	0.010	-0.014	214009.436
0.000	0.762	0.018	-0.031	306763.548
0.000	0.796	-0.008	0.005	371121.657
0.000	0.778	0.008	-0.012	428665.014
0.000	0.772	0.023	-0.038	373322.938
0.000	0.780	0.007	-0.009	304471.854
0.000	0.755	-0.004	0.002	212670.063
4.000	0.846	-0.038	0.040	302632.259
8.000	0.894	-0.035	0.039	301226.115
12.000	0.910	-0.015	0.025	299714.144
16.000	0.903	0.001	0.006	298407.542
20.000	0.873	0.041	-0.041	299878.009
24.000	0.817	0.066	-0.059	301104.898
28.000	0.790	0.102	-0.108	300579.059
32.000	0.726	0.146	-0.161	299992.210
28.000	0.789	0.106	-0.110	299675.044
24.000	0.813	0.065	-0.062	300959.672
20.000	0.863	0.025	-0.012	298504.187
16.000	0.889	0.016	-0.004	299544.172
12.000	0.909	-0.012	0.015	300549.069
8.000	0.884	-0.039	0.051	299754.743
4.000	0.832	-0.043	0.051	300411.076
0.000	0.812	0.012	-0.019	302043.431
-4.000	0.879	0.033	-0.052	298637.025
-8.000	0.899	0.014	-0.022	297472.688
-12.000	0.907	-0.008	-0.006	297581.754
-16.000	0.891	-0.029	0.021	297787.659
-20.000	0.868	-0.045	0.024	298285.179
-24.000	0.829	-0.083	0.069	298056.937
-28.000	0.799	-0.107	0.095	298484.559
-32.000	0.735	-0.153	0.155	300020.753
-28.000	0.795	-0.125	0.119	298855.775
-24.000	0.818	-0.096	0.092	299113.545
-20.000	0.859	-0.061	0.056	299005.037
-16.000	0.877	-0.035	0.028	299081.901
-12.000	0.894	-0.018	0.013	298032.742
-8.000	0.891	0.011	-0.012	299607.359
-4.000	0.874	0.027	-0.047	300508.577
0.000	0.764	0.013	-0.019	302056.860

Conducted on: 28.10.85
Model name: CM2406
Parachute status: No Rotation
Measured surface area (sq.m): 0.107
Arm ratio: 2.4:1
Fabric porosity (cu.ft/sq.ft/sec): 13
Suspension line ratio: 0.667

Angle of Atack (degrees)	C_T	C_N	C_{MC}	Reynolds Numbers Re
0.000	0.609	0.078	-0.050	216221.164
0.000	0.631	0.041	-0.029	306245.582
0.000	0.630	0.030	-0.024	373313.488
0.000	0.633	0.028	-0.024	430781.216
0.000	0.640	0.021	-0.018	372506.023
0.000	0.624	0.037	-0.027	306683.780
0.000	0.609	0.068	-0.043	216629.106
4.000	0.659	0.006	-0.003	307851.270
8.000	0.678	0.021	-0.020	306497.357
12.000	0.710	0.043	-0.033	306146.940
16.000	0.707	0.063	-0.043	305502.702
20.000	0.689	0.078	-0.050	306720.142
24.000	0.657	0.101	-0.062	306368.462
28.000	0.617	0.124	-0.077	307724.453
32.000	0.582	0.160	-0.098	305391.647
28.000	0.610	0.130	-0.081	306548.900
24.000	0.650	0.100	-0.057	306927.626
20.000	0.666	0.080	-0.048	307408.691
16.000	0.696	0.059	-0.035	306470.066
12.000	0.690	0.042	-0.029	306848.889
8.000	0.667	0.023	-0.017	305536.163
4.000	0.659	0.019	-0.016	306310.821
0.000	0.607	0.014	-0.005	307661.024
-4.000	0.644	0.048	-0.031	307092.604
-8.000	0.678	0.063	-0.044	305266.852
-12.000	0.670	0.037	-0.024	306917.028
-16.000	0.716	0.009	-0.007	306451.871
-20.000	0.701	-0.017	0.004	305574.182
-24.000	0.690	-0.038	0.013	304957.687
-28.000	0.660	-0.066	0.031	306651.960
-32.000	0.633	-0.114	0.062	306997.260
-28.000	0.665	-0.079	0.043	306206.129
-24.000	0.680	-0.052	0.027	305724.692
-20.000	0.688	-0.026	0.007	304347.578
-16.000	0.714	-0.003	-0.005	305926.775
-12.000	0.661	0.040	-0.030	306918.542
-8.000	0.670	0.045	-0.032	306965.473
-4.000	0.624	0.051	-0.038	307473.682
0.000	0.615	0.015	-0.011	306715.597

Conducted on: 27.8.85
Model name: CL2420
Parachute status: No Rotation
Measured surface area (sq.m): 0.107
Arm ratio: 2.4:1
Fabric porosity (cu.ft/sq.ft/sec): 23
Suspension line ratio: 2

Angle of Atack (degrees)	C_T	C_N	C_{MC}	Reynolds Numbers Re
0.000	0.800	0.006	-0.006	214167.075
0.000	0.828	-0.040	0.093	305766.586
0.000	0.823	-0.037	0.085	377017.969
0.000	0.832	-0.031	0.072	430490.652
0.000	0.814	-0.031	0.073	370926.489
0.000	0.824	-0.036	0.085	306261.171
0.000	0.767	-0.024	0.057	214569.297
3.000	0.869	-0.291	0.654	305515.991
6.000	0.826	-0.010	0.023	305223.119
9.000	0.830	-0.007	-0.001	305266.692
12.000	0.823	0.025	-0.024	305534.004
15.000	0.802	0.50	0.450	305024.708
18.000	0.779	0.079	-0.109	306723.559
21.000	0.790	0.018	0.046	306178.795
24.000	0.712	0.160	-0.262	307510.559
21.000	0.746	0.114	-0.177	306737.016
18.000	0.779	0.079	-0.110	307805.724
15.000	0.800	0.051	-0.062	306445.312
12.000	0.813	0.034	-0.041	306186.285
9.000	0.775	-0.030	0.284	307368.839
6.000	0.806	-0.010	0.244	308671.696
3.000	0.809	-0.025	0.063	308658.323
0.000	0.791	-0.027	0.066	308964.267
-3.000	0.811	-0.044	0.095	307435.977
-6.000	0.824	-0.052	0.110	308069.344
-9.000	0.812	-0.045	0.086	307758.040
-12.000	0.812	-0.063	0.121	307626.870
-15.000	0.818	-0.074	0.133	306388.434
-18.000	0.791	-0.108	0.199	307315.117
-21.000	0.761	-0.136	0.243	309361.839
-24.000	0.732	-0.169	0.293	306817.747
-21.000	0.768	-0.131	0.231	308450.227
-18.000	0.781	-0.103	0.184	308913.792
-15.000	0.801	-0.085	0.154	308222.646
-12.000	0.811	-0.059	0.104	306762.434
-9.000	0.815	-0.047	0.089	307068.773
-6.000	0.817	-0.069	0.146	307556.790
-3.000	0.811	-0.055	0.119	309304.015
0.000	0.798	-0.038	0.084	309643.390

Conducted on: 25.10.85
Model name: CL2413
Parachute status: No Rotation
Measured surface area (sq.m): 0.107
Arm ratio: 2.4:1
Fabric porosity (cu.ft/sq.ft/sec): 23
Suspension line ratio: 1.33

Angle of Atack (degrees)	C_T	C_N	C_{MC}	Reynolds Numbers Re
0.000	0.738	0.036	-0.038	307373.045
0.000	0.735	0.013	-0.013	307585.738
0.000	0.736	0.005	-0.003	307205.826
0.000	0.738	-0.002	-0.002	307245.359
0.000	0.739	0.002	0.004	308235.062
0.000	0.739	0.015	-0.015	308524.389
0.000	0.726	0.030	-0.028	307687.475
4.000	0.758	0.017	-0.019	306479.646
8.000	0.777	0.040	-0.043	306266.184
12.000	0.779	0.067	-0.074	305815.903
16.000	0.762	0.097	-0.107	306380.557
20.000	0.749	0.138	-0.156	306414.099
24.000	0.696	0.189	-0.219	308527.417
24.000	0.696	0.189	-0.219	308527.417
24.000	0.696	0.189	-0.219	308527.417
24.000	0.696	0.189	-0.219	308527.417
24.000	0.694	0.176	-0.196	308350.219
20.000	0.733	0.148	-0.167	307553.844
16.000	0.759	0.104	-0.112	307546.249
12.000	0.774	0.074	-0.079	308118.345
8.000	0.767	0.061	-0.071	307625.223
4.000	0.755	0.014	-0.010	308698.461
0.000	0.736	0.004	0.005	308934.436
-4.000	0.774	-0.003	0.004	308601.598
-8.000	0.790	-0.009	0.005	307945.463
-12.000	0.774	-0.043	0.049	309378.668
-16.000	0.775	-0.058	0.070	310844.340
-20.000	0.747	-0.083	0.087	310567.703
-24.000	0.706	-0.136	0.153	310982.566
-24.000	0.706	-0.136	0.153	310982.566
-24.000	0.706	-0.136	0.153	310982.566
-24.000	0.706	-0.136	0.153	310982.566
-24.000	0.696	-0.141	0.160	310593.273
-20.000	0.749	-0.105	0.124	310633.878
-16.000	0.754	-0.068	0.081	311708.746
-12.000	0.770	-0.051	0.062	310524.081
-8.000	0.773	-0.032	0.044	309921.760
-4.000	0.754	-0.014	0.019	309312.225
0.000	0.731	-0.005	0.006	310430.797

Conducted on: 28.10.85
Model name: CL2406
Parachute status: No Rotation
Measured surface area (sq.m): 0.107
Arm ratio: 2.4:1
Fabric porosity (cu.ft/sq.ft/sec): 23
Suspension line ratio: 0.667

Angle of Atack (degrees)	C_T	C_N	C_{MC}	Reynolds Numbers Re
0.000	0.573	0.054	-0.031	217743.278
0.000	0.575	0.033	-0.021	308191.069
0.000	0.577	0.021	-0.014	376362.490
0.000	0.575	0.018	-0.011	432483.065
0.000	0.577	0.021	-0.013	374926.255
0.000	0.571	0.031	-0.021	308112.314
0.000	0.572	0.054	-0.030	217762.568
4.000	0.578	0.039	-0.025	309947.248
8.000	0.614	0.080	-0.049	307182.380
12.000	0.632	0.119	-0.076	307457.253
16.000	0.610	0.153	-0.096	307174.784
20.000	0.586	0.187	-0.119	307747.047
24.000	0.508	0.242	-0.151	307762.212
24.000	0.508	0.242	-0.151	307762.212
24.000	0.508	0.242	-0.151	307762.212
24.000	0.508	0.242	-0.151	307762.212
24.000	0.503	0.237	-0.145	309431.848
20.000	0.558	0.193	-0.122	307423.857
16.000	0.592	0.156	-0.097	308113.828
12.000	0.619	0.126	-0.078	308343.980
8.000	0.601	0.086	-0.052	308406.031
4.000	0.557	0.042	-0.025	308921.632
0.000	0.563	0.021	-0.010	309335.304
-4.000	0.576	0.005	-0.001	309896.047
-8.000	0.594	-0.024	0.019	308912.567
-12.000	0.585	-0.060	0.043	309774.036
-16.000	0.602	-0.086	0.052	309243.256
-20.000	0.601	-0.132	0.088	309633.890
-24.000	0.562	-0.172	0.105	309814.712
-24.000	0.562	-0.172	0.105	309814.712
-24.000	0.562	-0.172	0.105	309814.712
-24.000	0.562	-0.172	0.105	309814.712
-24.000	0.555	-0.174	0.107	309463.520
-20.000	0.590	-0.138	0.088	309199.487
-16.000	0.600	-0.097	0.062	308578.498
-12.000	0.583	-0.060	0.039	309871.950
-8.000	0.581	-0.036	0.025	309324.742
-4.000	0.569	0.000	-0.000	310666.169
0.000	0.561	0.019	-0.013	310374.590

Conducted on: 31.10.85
Model name: CS4013R
Parachute status: With Rotation
Measured surface area (sq.m): 0.106
Arm ratio: 4.0:1
Fabric porosity (cu.ft/sq.ft/sec): 0
Suspension line ratio: 1.33

Angle of Atack (degrees)	C_T	C_N	C_{MC}	Reynolds Numbers Re
0.000	0.978	0.001	0.008	208266.925
0.000	0.980	-0.005	0.001	299943.382
0.000	0.985	-0.013	0.008	366092.881
0.000	0.982	0.019	-0.038	365474.865
0.000	0.993	0.002	0.003	295070.071
0.000	0.985	0.016	-0.027	208734.669
3.000	1.002	-0.023	0.041	302647.724
6.000	1.025	-0.013	0.026	302129.024
9.000	1.014	-0.015	0.029	302517.018
12.000	1.004	0.020	-0.026	302109.685
15.000	1.002	0.033	-0.038	301812.015
18.000	0.994	0.087	-0.117	300927.691
21.000	0.973	0.127	-0.184	303244.097
24.000	0.913	0.164	-0.239	304669.448
21.000	0.961	0.132	-0.189	303870.359
18.000	1.003	0.082	-0.109	303239.651
15.000	1.000	0.051	-0.067	302934.189
12.000	1.007	0.028	-0.035	302689.301
9.000	1.018	0.008	-0.007	302466.503
6.000	1.012	0.007	-0.007	301528.956
3.000	1.003	-0.009	0.014	302456.102
0.000	0.979	-0.008	0.012	302579.408
-3.000	0.997	-0.008	0.000	302963.859
-6.000	1.010	-0.018	0.019	303005.392
-9.000	1.011	-0.020	0.008	302974.243
-12.000	1.007	-0.026	0.012	303569.974
-15.000	1.001	-0.053	0.051	302790.249
-18.000	0.990	-0.100	0.125	302546.729
-21.000	0.969	-0.145	0.200	304108.385
-24.000	0.933	-0.180	0.244	304213.294
-21.000	0.975	-0.141	0.187	305163.213
-18.000	0.987	-0.098	0.132	304635.518
-15.000	0.995	-0.060	0.068	303655.829
-12.000	1.010	-0.031	0.018	303979.786
-9.000	1.012	-0.020	0.006	304163.060
-6.000	1.011	-0.018	0.010	302993.526
-3.000	0.998	-0.001	-0.013	303393.748
0.000	0.976	0.000	0.012	302953.475

Conducted on: 25.10.85
Model name: CL2413R
Parachute status: With Rotation
Measured surface area (sq.m): 0.106
Arm ratio: 2.4:1
Fabric porosity (cu.ft/sq.ft/sec): 23
Suspension line ratio: 1.33

Angle of Atack (degrees)	C_T	C_N	C_{MC}	Reynolds Numbers Re
0.000	0.799	0.094	-0.153	213155.698
0.000	0.776	0.058	-0.094	302612.430
0.000	0.779	0.045	-0.074	370117.720
0.000	0.767	0.035	-0.057	427511.161
0.000	0.788	0.044	-0.070	371702.014
0.000	0.789	0.064	-0.104	302990.160
0.000	0.785	0.130	-0.210	214325.599
4.000	0.792	0.071	-0.114	302886.216
8.000	0.804	0.093	-0.143	301284.339
12.000	0.787	0.124	-0.180	302145.350
16.000	0.760	0.151	-0.212	303046.703
20.000	0.728	0.192	-0.262	304015.456
24.000	0.656	0.270	-0.355	304234.712
24.000	0.656	0.270	-0.355	304234.712
24.000	0.656	0.270	-0.355	304234.712
24.000	0.656	0.270	-0.355	304234.712
24.000	0.652	0.274	-0.357	303310.937
20.000	0.728	0.195	-0.263	303330.784
16.000	0.753	0.160	-0.222	305186.039
12.000	0.781	0.124	-0.179	304045.917
8.000	0.795	0.101	-0.150	304467.499
4.000	0.792	0.079	-0.123	305481.773
0.000	0.785	0.073	-0.118	305540.886
-4.000	0.823	0.055	-0.090	306249.347
-8.000	0.816	0.046	-0.081	304797.357
-12.000	0.816	-0.001	-0.021	305586.349
-16.000	0.802	-0.032	0.013	306610.515
-20.000	0.771	-0.071	0.059	305783.280
-24.000	0.725	-0.163	0.178	306566.714
-24.000	0.725	-0.163	0.178	306566.714
-24.000	0.725	-0.163	0.178	306566.714
-24.000	0.725	-0.163	0.178	306566.714
-24.000	0.723	-0.161	0.175	306583.329
-20.000	0.779	-0.076	0.065	305525.730
-16.000	0.794	-0.031	0.009	305716.640
-12.000	0.816	0.005	0.014	306022.455
-8.000	0.814	0.037	-0.059	306763.015
-4.000	0.818	0.065	-0.108	306043.638
0.000	0.784	0.076	-0.123	305913.487